

中国科学技术大学

博士学位论文



低 Q^2 下质子 g_2 结构函数的 测量

作者姓名 : 朱鹏佳
学科专业 : 粒子物理
导师姓名 : 叶云秀 教授, 陈剑平教授
完成时间 : 二〇一五年十月

University of Science and Technology of China
A dissertation for doctor degree



A measurement of the proton's
spin structure function g_2 at low Q^2

Author's Name : Pengjia Zhu
Speciality : Partical Physics
Supervisor : Prof. Yunxiu Ye
Prof. Jian-ping Chen
Finished Time : October, 2015

低 Q^2 下质子 g_2 结构函数的测量 四系 朱鹏佳 中国科学技术大学

中国科学技术大学学位论文原创性声明

本人声明所呈交的学位论文，是本人在导师指导下进行研究工作所取得的成果。除已特别加以标注和致谢的地方外，论文中不包含任何他人已经发表或撰写过的研究成果。与我一同工作的同志对本研究所做的贡献均已在论文中作了明确的说明。

作者签名: 朱鹏程 签字日期: 2015.10.21

中国科学技术大学学位论文授权使用声明

作为申请学位的条件之一，学位论文著作权拥有者授权中国科学技术大学拥有学位论文的部分使用权，即：学校有权按有关规定向国家有关部门或机构送交论文的复印件和电子版，允许论文被查阅和借阅，可以将学位论文编入《中国学位论文全文数据库》等有关数据库进行检索，可以采用影印、缩印或扫描等复制手段保存、汇编学位论文。本人提交的电子文档的内容和纸质论文的内容相一致。

保密的学位论文在解密后也遵守此规定。

公开 保密 _____ 年

作者签名: 朱鹏程 导师签名: 叶云秀
签字日期: 2015.10.21 签字日期: 2015.10.21

摘要

JLab E08-027 实验在 2012 年 3 月至 5 月期间成功获取了数据，其目的是测量质子的极化结构函数 g_2 以及自旋极化率 δ_{LT} 。当前不管对于理论物理还是对于实验物理来说对核子自旋结构的研究都是一个热门的领域。近二十年来在此领域已经出了许多令人振奋及惊讶的结果。近年来 JLab 在低 Q^2 共振区获得了大量关于核子结构的精确数据，其覆盖了禁闭区以及从渐进自由到禁闭区的过渡区间。对实验结果与手征微扰理论（一个在低能领域公认比较有效 QCD 理论）的比较显示了非常好的相似性，但对于中子的自旋极化率的比较却显示出了相当大的不同。本实验精确测量了在低 Q^2 共振区间的质子的极化结构函数 g_2 以及自旋极化率 δ_{LT} 。

本实验第一次在 JLab A 大厅使用了极化质子靶（固态氮靶）。散射电子由一对高精度谱仪测量，并且加了一对额外的切隔磁铁以获取小散射角度的散射电子。为了避免靶上大量的退极化，束流强度被限制在了 50-100 纳安区间。由于原有的束流强度探测器 (BCM)，束流位置探测器 (BPM) 以及相应的刻度方法在这个低束流强度的情况下无法工作，设计了新的 BCM 和 BPM 的电子学接收器。一对超级 harp 以及一个钨质量能器被用于刻度 BCM 和 BPM。为了补偿 2.5/5 特斯拉的靶区间的强磁场，一对 chicane 偶极磁场被放置于靶前。一套标准的 A 大厅数据获取系统以及一套改进过的高精度数据获取系统被分别用来记录探测器信息以及和螺旋度相关的束流信息。

为获取在靶上必要精度的位置和角度信息，对于 BPM 以及 harp 的数据进行了非常仔细的分析，以得到在靶区域重建每个事例的位置及角度信息。使用钨质量能器刻度以后的 BCM 可以达到 1% 以下的不准确度，这对非对称性的测量至关重要。在对谱仪的接收率以及靶的稀释因子的分析结束前，前人拟合得到的物理模型用来得到非极化截面以及靶的稀释因子。在对从物理模型得到的非对称性进行反辐射修正以后，将其与实验得到的横向及纵向极化的非对称性进行了对比。结合测量得到的非对称性以及从物理模型中得到的非极化截面，我们得到了原始的 g_1 和 g_2 结果。

关键词： 极化结构函数, g_2 , 非对称性, 自旋极化率

ABSTRACT

JLab E08-027, a measurement of g_{2p} and the longitudinal-transverse (LT) spin polarizability, successfully collected data from March to May, 2012. Nucleon spin structure study has been an active research area, which has attracted a very large effort from both experimentalists and theorists. The spin structure study for the last 2 decades has provided us with many exciting and often surprising results. Recently, new precision results in the low-to-intermediate momentum transfer Q^2 region from JLab have provided extensive information on the nucleon structure in the confinement region and the transition region between asymptotic free to confinement. In particular, the extensive comparisons of experimental results with Chiral Perturbation Theory (the effective theory of QCD at low energy) calculations show general good agreements, but strong disagreement in the case of the neutron LT spin polarizability. This experiment completed the measurements of g_2^p and the LT spin polarizability on the proton in the low-to-intermediate Q^2 region.

The experiment used a polarized proton (NH_3) target for the first time in Hall A. Scattered electrons were detected by a pair of Hall A high resolution spectrometer (HRS) with a pair of septum magnets. To avoid too much depolarization of the target, beam current was limited to 50-100 nA during the experiment. Since the existing beam current monitors (BCMs), beam position monitors (BPMs) and calibration methods did not work at such a low current range, new BPM and BCM receivers were designed and used for current condition. A pair of super-harps and a tungsten calorimeter were installed to calibrate the BPMs and BCMs. To compensate for the effect of the 2.5/5T transverse magnet field, two chicane dipole magnets were installed. A pair of slow rasters were installed for the first time in Hall A, combining with a pair of fast raster. The standard Hall A DAQ system and the improved high resolution DAQ system were used to record the detector information and the helicity dependent beam information, respectively.

In order to achieve the required accuracy of the beam position and angle and reconstruct them event by event at the target location, the data of the BPMs and harps were carefully analyzed. The final uncertainty of BCM after the calibration using the tungsten calorimeter is below 1%, which is important for the asymmetry extraction. Before the acceptance and the dilution factor are available, the models from fitting to the world data were used instead to extract the unpolarized cross section and the dilution factor. The longitudinal and transverse physics asymmetries were extracted and compared with the model, with the study of the radiative correction. The preliminary g_1 and g_2 results were then extracted using the measured asymmetry and the model.

Keywords: g2, E08-027, structure function, asymmetry, spin polarizability

Contents

摘要	I
ABSTRACT	III
Contents	V
List of Tables	IX
List of Figures	XIII
Chapter 1 Overview	3
Chapter 2 Nucleon Spin	5
2.1 The Naive Quark-Parton Model	5
2.1.1 Spin structure in the naive quark-parton model	5
2.1.2 Structure functions in the naive quark-parton model	6
2.1.3 First moment of g_1 in the naive quark-parton model and Ellis-Jaffe sum rule	7
2.2 The quark-parton model corrected by QCD	8
2.3 Chiral Perturbation Theory	11
2.4 Sum rules	11
2.4.1 The Bjorken sum rule	12
2.4.2 The Gerasimov-Drell-Hearn sum rule	12
2.5 The g_2 Structure Function and the Spin Polarizabilities	13
2.5.1 The generalized forward spin polarizability γ_0 and The longitudinal-transverse polarizability δ_{LT}	14
2.5.2 The Burkhardt-Cottingham Sum Rule	15
2.5.3 Higher twist moments d_2	16
Chapter 3 History and Recent Results on the Measurement of Spin Structure function	17
3.1 History for the spin structure measurement	17
3.2 Results for g_2	18
3.3 Results for B-C sum rule	22
3.4 Results for spin polarizabilities γ_0 and δ_{LT}	22
3.5 Results for d_2	25

Chapter 4 Inclusive Lepton-Nucleon Scattering	27
4.1 Kinematic variables	27
4.2 Types of the inclusive electron scattering	28
4.3 Differential cross section and structure functions	30
4.4 Virtual photoabsorption cross section	33
Chapter 5 The E08-027 (g2p) Experiment	37
5.1 Motivation	37
5.2 Experiment Overview	37
5.3 The Beamline System	41
5.3.1 Beam Charge and Current	41
5.3.2 Beam polarization	48
5.3.3 Chicane dipole magnet	49
5.3.4 Beam Position and Angle	49
5.3.5 Local beam dump	68
5.4 The Polarized Target System	70
5.4.1 Polarized NH_3 target	70
5.4.2 Polarized 3He target	77
5.5 The Hall A High Resolution Spectrometers	84
5.5.1 Septum magnet	84
5.5.2 Detector package in HRS	84
5.5.3 Simulation package	88
5.5.4 Spectrometer optics	88
5.6 The Data Acquisition System	99
5.6.1 Single arm HRS DAQ	99
5.6.2 Helicity	100
5.6.3 HAPPEX DAQ	103
5.6.4 Third arm DAQ	104
Chapter 6 Results	109
6.1 Extract asymmetry from data	109
6.1.1 Asymmetry method	109
6.1.2 Charge asymmetry	110
6.1.3 False asymmetry	110
6.1.4 Packing fraction	110

6.1.5 Dilution	113
6.1.6 Radiative correction	116
6.1.7 Acceptance cut	119
6.1.8 Asymmetry result	120
6.1.9 Asymmetry with different acceptance cuts	120
6.2 Model prediction	121
6.2.1 MAID	121
6.2.2 Peter Bosted Model	121
6.2.3 Asymmetry from the models	121
6.3 Asymmetry Comparison	122
6.4 g_1 and g_2	122
6.5 Conclusion	122
Chapter 7 Summary	137
参考文献	145

List of Tables

3.1	Summary of spin structure function g_2 measurement before E08-027	20
4.1	The properties of the nucleon resonance	30
5.1	Summary of the Møller measurements for g2p experiment	48
5.2	Characteristics of the Hall A HRS	84
5.3	Performance summary of RMS values for optics study without target field	89
5.4	Helicity configuration	101
6.1	Parameters used in dilution calculation	116
6.2	comparison of the asymmetries with and without the acceptance cut . .	120

List of Figures

2.1	QCD quark parton model diagram	9
3.1	Result of g_2 for the proton and deuteron in DIS region	19
3.2	g_2^n extracted from the experiment E97-103 at JLab for $x \approx 0.2$	21
3.3	g_2^n extracted from experiments at JLab and SLAC	21
3.4	g_2^n extracted from the experiment E94-010 for the different Q^2	23
3.5	Proton's g_2 result and the approximation g_2^{WW} from RSS	24
3.6	Verification of BC sum rule	24
3.7	Spin polarizabilities of proton and neutron	25
3.8	d_2 data for proton and neutron	26
4.1	Feynman diagram for deep-inelastic lepton-hadron scattering	27
4.2	Spectrum of the electron scattering	29
4.3	Spectrum of electron-nucleus scattering and electron-nucleon scattering	29
4.4	The interaction between the virtual photon and the polarized nucleon	34
5.1	Kinematic coverage during the experimental run period	38
5.2	Schematic of components for g2p experiment	39
5.3	Projected uncertainties for Γ_2 and δ_{LT} for the E08-027 (g2p) experiment	40
5.4	BPM and BCM receiver used for g2p experiment	41
5.5	DAQ system for BCM	42
5.6	Tungsten Calorimeter	43
5.7	BCM Calibration	45
5.8	Tungsten calorimeter heat capacity determination	46
5.9	T-Settle signal from helicity control board	46
5.10	Comparing of the charge calculated from upstream and downstream	48
5.11	Chicane dipole magnet upstream of the target	49
5.12	BPM Chamber	50
5.13	Harp diagram	51
5.14	1H05A harp scan data	52
5.15	Fast raster pattern	53
5.16	Slow raster pattern	54
5.17	None-zero t_0 caused slow raster non-uniformity	54
5.18	Coordinate system used for the BPM calibration	55
5.19	Position for 2 BPMs and 2 Harps	55
5.20	Signal for each antenna of BPM	56
5.21	BPM non-linearity correction	57
5.22	ADC value of BPM raw signal V.S. beam current	58
5.23	Harp scan data combined with BPM data	59
5.24	Software filter applied to BPM signal	60
5.25	Transporting beam position from BPM to target	61

5.26	Reconstructed beam position at the target	62
5.27	Converting the raster current to beam position shift	62
5.28	The shape of carbon hole in raster ADC	63
5.29	Beam shape formed by the fast raster at the BPM A location	64
5.30	Slow raster phase reconstruction	64
5.31	fast clock frequency change during experiment	65
5.32	Using RMS to check if beam move	66
5.33	Pedestal change during experiment for left arm	67
5.34	The local beam dump and the septum magnet	69
5.35	Polarized NH_3 target system	71
5.36	1K refrigerator	72
5.37	NH_3 beads before and after the irradiation.	73
5.38	Target insert	74
5.39	Microwave system	74
5.40	NMR system for NH_3 target	75
5.41	NMR signal for the Q-meter	76
5.42	Target polarization	78
5.43	Ground state energy levels for ^{85}Rb	79
5.44	3He target setup	80
5.45	Laser optics	80
5.46	Frequency modulation sweep	83
5.47	Schematic diagram of the septum magnet	85
5.48	Layout of the detector package	85
5.49	Schematic diagram of the VDC	86
5.57	Schematic of the components related in the optics study	88
5.50	VDC track efficiencies for left arm	90
5.51	VDC track efficiencies for right arm	91
5.52	Detector efficiency for gas Cherenkov detector	92
5.53	Layout for the lead glass calorimeters for two arms	93
5.54	Detector efficiency for lead glass calorimeter	94
5.55	Cut efficiency for gas Cherenkov detector	95
5.56	Pion suppression	96
5.58	Target coordinate system	97
5.59	Sieve slit and its reconstructed histogram	97
5.60	Reconstructed momentum after calibration	98
5.61	Reconstructed y after calibration	98
5.63	Hall A standard DAQ system	99
5.64	DAQ deadtime during production run	100
5.65	Helicity signal	101
5.66	Ringbuffer	102
5.67	HAPPEX DAQ diagram	103
5.68	Timing board signals	104
5.70	The slow raster current histogram in third arm DAQ	105
5.62	Trigger efficiency	106
5.69	Charge asym comparison between HAPPEX and scaler	107
6.1	Charge asymmetries for the production runs	111

6.2	False asymmetries for different beam energy settings	112
6.3	Diagram for the comparison of the l_{tg} and l_{tot}	113
6.4	Fit to elastic and quasi-elastic peak in order to extract the yield ratio	114
6.5	Dilution factors	123
6.6	Next to leading order internal radiative correction	124
6.7	Internal and external bremsstrahlung emission	124
6.8	Acceptance cut for E=2.2GeV, Field=5T, longitudinal	125
6.9	Acceptance cut for E=2.2GeV, Field=5T, transverse	126
6.10	Acceptance cut for E=3.3GeV, Field=5T, transverse	127
6.11	Physics asymmetry	128
6.12	Physics Asymmetries with the different acceptance cuts	129
6.13	Unradiated P.Bosted model compare with σ_{rad} , σ_{inrad} and σ_{elrad}	130
6.14	Radiated P.Bosted model compared with the unradiated P.Bosted model	131
6.15	Radiated $\Delta\sigma_{ /\perp}$ compared with the unradiated $\Delta\sigma_{ /\perp}$ from MAID	132
6.16	Radiated $A_{ /\perp}$ compared with the unradiated $A_{ /\perp}$ from Model	133
6.17	Physics asymmetry compared with model	134
6.18	$\Delta\sigma_{ /\perp}$ from data compared with the model	135
6.19	g_1 and g_2 compared with model	136

LIST OF FIGURES

Acknowledgments

First of all, I would like to thank my parents and my girlfriend. Without them I could not stick to the end.

I would like to thank Prof. Yunxiu Ye, my supervisor, who gave me the support and the chance to work with a group of smart people at Jefferson Lab. Also I would like to thank for her guidance and patient in correcting my papers and my draft thesis.

Prof. Jian-ping Chen, my research advisor at Jefferson Lab, who gave me the most help when I was working at Jefferson Lab. His profound knowledge and rich experience impressed me. The experiment will not success without him. He is also very patient on answering any questions and helping me correcting my papers.

I would also like to thank Haijiang Lu, who supported me the place and gave me help in Huangshan University for studying my thesis. Also I would like to thank Xinhu Yan for his friendship and help when I was in Huangshan.

I would like to thank for the friendship from the E08-027 group, Alexandre Camsonne, Melissa Cummings, Chao Gu, Min Huang, Jie liu, Jixie Zhang, Kalyan Allada, Toby Badman, Ryan Zielinski. Alexandre helped me a lot for the beamline study. Melissa was very patient to correct my paper. Chao, Min, Jie and Jixie are the best friends when I was in JLab. Kalyan ,Toby and Ryan are also very nice. I had two years full of memories when I was in JLab.

This work was supported by US DOE contract DE-AC05-84ER40150 under which the Southeastern Universities Research Association (SURA) operates the Thomas Jefferson National Accelerator Facility, and by the National Natural Science Foundation of China (11135002, 11275083), the Natural Science Foundation of Anhui Education Committee (KJ2012B179).

Chapter 1

Overview

Since the birth of mankind, we use our eyes to understand the structure of world. Eyes detect the light and convert it into a set of electrical signals and transmit it to our brain. With the progress of civilization, we learned to use the tools like microscope and telescope to get more detailed information. We never stop exploring the world. We launched space telescopes as our eyes to detect the light ten billion years ago from the ancient stars. We built large accelerator to find the fundamental structure of universe.

Nucleons, neutron and proton, give 99.9% of the mass of the atom. Unraveling the internal structure of the nucleon is one of the most challenging fundamental question in the modern physics. The nucleons were thought to be point like particles until the 1960's. In the later 1960's, Jerome Friedman, Henry Kendall and Richard Taylor used a new high-energy electron beam to bombard a liquid-hydrogen target at SLAC [1]. The form factors gotten from the ratio of the differential cross section and the Mott cross section exhibited approximate scaling at large Q^2 [2]. The remarkable observation awarded them the Nobel prize in physics 1990.

The strong force, one of the four fundamental interactions, tightly glue quarks together mediated by gluons. It is explained by an acceptable theory - Quantum Chromodynamics (QCD). Due to the strong and non-linear nature of the strong force, the mystery of it is still looming. Leptons do not undergo the strong interaction. They only interact with nucleus and hadron, or quarks in hadron via the electromagnetic interaction which is well understood through the Quantum Electrodynamics theory (QED). A lepton beam was proved as a clean probe for the nucleon's substructure. The lepton-nucleon scattering was used as an important tool to study the internal structure of the nucleon.

Spin is one of the fundamental property of particles. The study of the spin structure reveals a lot of exciting phenomenon for the last half century. The spin of the nucleon is known as $\frac{1}{2}$. In naive quark parton model, the spin of the nucleon is carried by the spin of the quarks [3]. The first polarized electron-proton scattering experiments were carried out at SLAC from the middle 1970's to the 1980's [4–6]. The uncertainty was large due to the technology limitation at that time. The result matched the results of the Ellis-Jaffe sum rule which based on the $SU(3)$ symmetry and ignored the strange (sea) quark contribution [7].

Later on the EMC collaboration group at CERN used the muon beam with much higher beam energy to extend the x coverage down to 0.01 [8, 9]. Combining the results from SLAC, the results indicated that only a small part of the nucleon spin came from the quark, which violated the theory prediction from the naive quart model. This puzzling result was termed the “spin crisis”. Later on the spin structure of the nucleon became a productive area for both experiment and theory.

In the last 30 years, many experiments were carried out the study of the spin structure of the nucleon at SLAC, CERN, DESY and JLAB. With the progress of experimental technology, physicists got more accuracy results and extended the kinematic regions. SLAC improved their results on the proton, and also the neutron's spin structure. The SMC group and the COMPASS group at CERN extended the measurements of the semi-inclusive lepton scattering. The COMPASS group at CERN and the HERMES group from DESY tried to measure the gluon contributions indirectly and directly. The Brookhaven National Lab (BNL) and the Jefferson Lab are now productively extending the measurement to larger kinematic range and higher resolution with the higher energy proton beam and the higher luminosity electron beam. The measurement was not only taken with longitudinally polarized target, but also with transversely polarized target. The longitudinal spin-dependent structure function g_1 which is related to the polarized quark distributions and the transverse spin-dependent structure function g_2 which is related to the higher-twist quark-gluon correlations were measured more and more precisely in the DIS region. Further studies were covered from the total quark spin contribution to the individual quark spin contribution, the strange (sea) quark spin contribution, and the gluon spin contribution. The scientists were not only focused on the asymptotic-free deep inelastic region where the interaction is relatively weak but also on the resonance region where the interaction is truly strong. So far the measurements for the longitudinal spin structure function g_1 have been achieved to a reasonable precision, covering the large ranges of Q^2 and x . Now some people focus on the measurements of the transverse spin structure function g_2 , which are still scarce. The further experimental results on nucleon spin will bring us more consideration.

This thesis describes the theoretical basis and the experimental details for the E08-027 experiment in Hall A at Jefferson Lab.

Chapter 2

Nucleon Spin

As known from QCD, the nucleon is consisted of the quarks and gluons. The total nucleon spin can be expressed as [10]:

$$J_Z^N = \frac{1}{2} = \left(\frac{1}{2} \Delta \Sigma + L_q \right) + (\Delta G + L_g). \quad (2.1)$$

The spin of the nucleon is equal to $\frac{1}{2}$. It includes the quark and gluon angular momentum contributions: L_q and L_g respectively, and the intrinsic quark and gluon spin contribution: $\frac{1}{2} \Delta \Sigma$ and ΔG , respectively.

The format of the relationship wasn't like this before the QCD corrected the quark-parton model. The naive quark-parton model [11] was invented long before the QCD in order to describe the nucleon structures. Later on the spin crisis between the experiment and the prediction from the naive quark-parton model activated the enthusiasm for the study of the nucleon spin.

2.1 The Naive Quark-Parton Model

2.1.1 Spin structure in the naive quark-parton model

When proton is considered to be comprised by only the valence u and d quarks, a simple non-relativistic wave function for proton can be expressed as [12]:

$$|p \uparrow\rangle = \frac{1}{\sqrt{6}} (2|u \uparrow u \uparrow d \downarrow\rangle - |u \uparrow u \downarrow d \uparrow\rangle - |u \downarrow u \uparrow d \uparrow\rangle), \quad (2.2)$$

where \uparrow, \downarrow indicate the spin of the quarks or the anti-quarks are parallel or anti-parallel to the spin of the proton, respectively. The color indices and permutations were suppressed in the equation. The contribution of the u quark can be determined by using the following matrix element and projection operator:

$$u^\uparrow = \langle p^\uparrow | \hat{O}_{u\uparrow} | p^\uparrow \rangle, \quad (2.3)$$

$$\hat{O}_{u\uparrow} = \frac{1}{4} (1 + \hat{\tau}_3) (1 + \hat{\sigma}_3), \quad (2.4)$$

where the matrix element gives the number of the u quark which polarized along the polarization of proton. Similar expression can be taken for the d quark. The quark spin contributions can be defined using the matrix elements above:

$$\Delta u = u^\uparrow - u^\downarrow, \quad (2.5)$$

$$\Delta d = d^\uparrow - d^\downarrow, \quad (2.6)$$

so that:

$$\Delta u = \frac{1}{2}(\langle \sigma_3 \rangle + \langle \sigma_3 \tau_3 \rangle) = \frac{4}{3}, \quad (2.7)$$

$$\Delta d = \frac{1}{2}(\langle \sigma_3 \rangle - \langle \sigma_3 \tau_3 \rangle) = -\frac{1}{3}. \quad (2.8)$$

The proton's spin can then be expressed as:

$$J_Z^N = \frac{1}{2}\Delta\Sigma = \frac{1}{2}(\Delta u + \Delta d + \Delta s) = \frac{1}{2}\langle \sigma_3 \rangle = \frac{1}{2}, \quad (2.9)$$

which indicates all of the nucleon spin is carried by the quarks.

2.1.2 Structure functions in the naive quark-parton model

The quark-parton was considered as a mass-less and point-like particle which interact electromagnetically like lepton in the naive model. The spin-averaged structure functions of hadron, F_1 and F_2 , are presented in the naive quark-parton model (QPM) as:

$$F_1(x) = \frac{1}{2}\sum_i e_i^2 [q_i(x) + \bar{q}_i(x)], \quad (2.10)$$

$$F_2(x) = \sum_i e_i^2 x [q_i(x) + \bar{q}_i(x)], \quad (2.11)$$

where $q_i(x)$ and $\bar{q}_i(x)$ are the number density of the quarks and anti-quarks, e_i is the charge of the quark, x is the momentum fraction of the nucleon's total momentum carried by a quark or anti-quark in the parton model. The equations (2.10) and (2.11) lead to Callan-Gross relation [13]:

$$F_2(x) = 2xF_1(x). \quad (2.12)$$

For the polarized scattering the results become more interesting by the spin contribution. Spin plays an essential role for the more detailed structure of the nucleon. The longitudinal spin-dependent structure function g_1 is presented in the naive QPM as:

$$g_1(x) = \frac{1}{2}\sum_i e_i^2 \Delta q_i(x), \quad (2.13)$$

where Δq_i is the difference of the number density of the quarks (anti-quarks) when the helicity parallel and anti-parallel to the nucleon spin, represented as:

$$\Delta q_i(x) = q_i^+(x) + \bar{q}_i^+(x) - q_i^-(x) - \bar{q}_i^-(x). \quad (2.14)$$

where the helicity is defined as:

$$h = \frac{\vec{\sigma} \cdot \vec{p}}{|\vec{p}|}, \quad (2.15)$$

where \vec{p} is the particle's momentum, and $\vec{\sigma}$ is the Pauli spin matrix.

The g_1 structure function represents the charge-weighted quark helicity distributions at the Bjorken limit. Another spin-dependent structure function g_2 cannot be leaded to simple results by using the naive quark-parton model [14] and will discussed later.

2.1.3 First moment of g_1 in the naive quark-parton model and Ellis-Jaffe sum rule

The first moment of g_1 is defined as the integration of g_1 from $x = 0$ to $x = 1$. For proton it is:

$$\Gamma_1^p(x) = \int_0^1 g_1(x) dx. \quad (2.16)$$

The equation (2.13) can be rewritten in terms of linear combinations of quark densities under the group of flavor transformations $SU(3)_F$:

$$\Delta q_3 = \Delta u - \Delta d, \quad (2.17)$$

$$\Delta q_8 = \Delta u + \Delta d - 2\Delta s, \quad (2.18)$$

$$\Delta \Sigma = \Delta u + \Delta d + \Delta s, \quad (2.19)$$

where Δq_3 is the third component of an isotopic spin triplet, Δq_8 is the eighth component of an $SU(3)_F$ octet, and $\Delta \Sigma$ is a flavor singlet. Then g_1 becomes as:

$$g_1(x) = \frac{1}{9}[\frac{3}{4}\Delta q_3(x) + \frac{1}{4}\Delta q_8(x) + \Delta \Sigma(x)]. \quad (2.20)$$

The first moment for the proton is then expressed as:

$$\Gamma_1^p(x) = \int_0^1 g_1(x) dx = \frac{1}{9}(\frac{3}{4}a_3 + \frac{1}{4}a_8 + a_0), \quad (2.21)$$

where a_0, a_3, a_8 are three weak axial-vector couplings [7]:

$$a_0 = \Delta \sum \equiv \int_0^1 \Delta \Sigma(x) dx, \quad (2.22)$$

$$a_3 = \int_0^1 \Delta q_3(x) dx = \left| \frac{g_A}{g_V} \right| = F + D, \quad (2.23)$$

$$a_8 = \int_0^1 \Delta q_8(x) dx = 3F - D, \quad (2.24)$$

where F and D are the symmetric and antisymmetric weak $SU(3)_F$ couplings, which assuming that $SU(3)_F$ is symmetry. g_A and g_V are the axial and vector weak coupling constants of neutron $\beta - decay$. When assuming the strange (sea) quark in the nucleon is not polarized, the equation (2.22) and (2.24) leads to $a_0 = a_8$, and the form:

$$\begin{aligned}\Gamma_1^p(x) &= \frac{1}{12}(F + D) + \frac{5}{36}(3F - D) \\ &= \frac{1}{12} \left| \frac{g_A}{g_V} \right| \left(1 + \frac{5}{3} \frac{3(F/D) - 1}{(F/D) + 1} \right),\end{aligned}\quad (2.25)$$

which is the Ellis-Jaffe sum rules [7]. The ratio of F/D can be measured from hyperon decays, and implying that: $a_0 = a_8 \approx 0.59$. The result of the first moment can be obtained [7]:

$$\Gamma_1^p(x) = 0.186 \pm 0.004. \quad (2.26)$$

Also the a_0 is equal to the spin from all of the quarks from the equation (2.22):

$$a_0 = 2S_z^{quarks}, \quad (2.27)$$

where S_z^{quarks} is the spin combining of all flavor quarks. In the naive quark-parton model all quarks move parallel to the parent hadron, thus there is no orbital angular momentum contributed to the J_z carried by the quarks. The total spin is expected as [15]:

$$S_z^{quark} = J_z = \frac{1}{2}. \quad (2.28)$$

In 1988 the European Muon Collaboration (EMC) published their final results from their study of deep inelastic muon-proton scattering experiment [8], the value implied that:

$$\int_0^1 g_1(x)dx = 0.114 \pm 0.012 \pm 0.026, \quad (2.29)$$

$$S_z^{quark} = 0.006 \pm 0.058 \pm 0.117, \quad (2.30)$$

which indicating that the quark spins carry only a little part of the proton spin, and the Ellis-Jaffe sum rule in the naive quark-parton model is invalid. The large disagreement with the naive quark-parton model result, which terms the spin crisis in the parton model [16].

2.2 The quark-parton model corrected by QCD

The spin crisis was believed to be resolved by considering a large contribution of the polarized gluon. Once the QCD theory is accepted as a valid theory for the strong interaction, it is introduced to the naive quark-parton model to complement the gluon distribution, which describes the strong force between the quarks. After introducing the gluon vector potential, it is much more complicated to describe the nucleon structure. The operator product expansion (OPE) [17] is a fundamental understanding originally within QCD that provide the QCD prediction for the moments of the structure functions via the sum rules. The OPE expresses the product of the two operators in the small distance limit $d \rightarrow 0$ as:

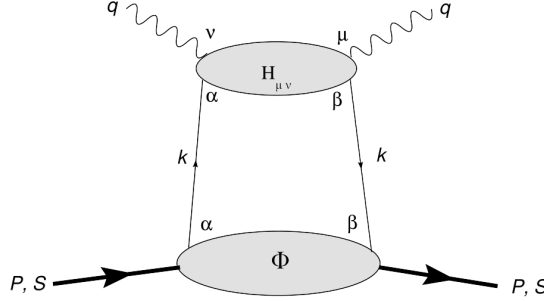


Figure 2.1 QCD quark parton model diagram [18]

$$\lim_{d \rightarrow 0} \sigma_a(d) \sigma_b(0) = \sum_k C_{abk}(d) \sigma_k(0), \quad (2.31)$$

where C_{abk} are the Wilson coefficients, which are calculable perturbatively in QCD. The σ_k are quark and gluon operators of dimension d and spin n , which are not calculable in perturbative QCD. The twist is defined as: $\tau \equiv d - n$. The contribution of any operator, i.e., the differential cross section, is of order:

$$x^{-n} \left(\frac{M}{Q}\right)^{\tau-2}, \quad (2.32)$$

where $Q = \sqrt{Q^2}$, and Q^2 is the squared four-momentum transfer, $Q^2 = -q^2$.

The OPE describes the quark-parton reaction as shown in figure 2.1 [18]. The interaction is splitted to two part: The hard interaction (top “blob”) and the non-perturbative soft interaction (down “blob”). Unfortunately even if for the simplest QCD correction terms, a vertex correction and a gluon radiative correction are infinite because of the masslessness of the quarks. The solution is referring to a factorization scale μ^2 , and splitting the interaction terms of the form $\alpha_s \ln \frac{Q^2}{m_q^2}$ into two parts:

$$\alpha_s \ln \frac{Q^2}{m_q^2} = \alpha_s \ln \frac{Q^2}{\mu^2} + \alpha_s \ln \frac{\mu^2}{m_q^2}, \quad (2.33)$$

where α_s is the strong coupling constant. The first term $\alpha_s \ln \frac{Q^2}{\mu^2}$ was absorbed into the hard part, which can be dealt with the perturbative QCD. The second term $\alpha_s \ln \frac{\mu^2}{m_q^2}$ was absorbed into the soft part, which cannot be calculated and need to be parametrized. The μ^2 is an arbitrary number that we can take a choice. One optimal choice is $\mu^2 = Q^2$. The quark-parton densities which are only depend on x in the naive quark-parton model are now depend on both x and Q^2 : $q(x, Q^2)$ and $\Delta q(x, Q^2)$, which break the Bjorken scaling. The main effect for the QCD correction is that it introduces a calculable logarithmic relation with Q^2 for quark-parton densities, and generates the gluon contribution for g_1 .

At present there are three different factorization schemes in use for handling the quark-gluon interactions and the gluon contributions to nucleon spin, which are the \overline{MS} scheme [19], the AB scheme [20], and the JET scheme [21]. If considering all orders in perturbation theory there is no difference to choose the scheme, but it becomes important when working to leading order (LO), next to leading order (NLO), and NNLO.

In the AB scheme and the JET scheme, a_0 can be implied as:

$$a_0 = \Delta \sum + a_0^{gluon}, \quad (2.34)$$

where $\Delta \Sigma$ is the quark spin contribution, which is independent with Q^2 . a_0^{gluon} is the gluon contribution [21]:

$$a_0^{gluon} = -3 \frac{\alpha_s(Q^2)}{2\pi} \Delta G(Q^2), \quad (2.35)$$

where α_s is the run coupling constant in the QCD, $\Delta G(Q^2) \equiv \int_0^1 dx \Delta G(x, Q^2)$, and parameter 3 correspond to three flavor quarks: u , d , s . The equations (2.34) and (2.35) show that the small measured a_0 does not imply the small $\Delta \Sigma$. The gluon's contribution to the first moment is:

$$\Gamma_1^{gluon}(Q^2) = -3 \frac{\alpha_s(Q^2)}{2\pi} \Delta G(Q^2). \quad (2.36)$$

In the \overline{MS} scheme, $\Delta \Sigma$ is not the pure quark spin contribution anymore, which includes the interaction of quark-gluon. In the NLO of the \overline{MS} scheme, a_0 became to:

$$a_0(Q^2) = \Delta \Sigma(Q^2). \quad (2.37)$$

The first moment for proton in equation (2.21) is corrected as [22, 23]:

$$\Gamma_1^p(Q^2) = \int_0^1 g_1(x) dx = \left(\frac{1}{12} a_3 + \frac{1}{36} a_8 \right) C_{ns}(Q^2) + \frac{1}{9} a_0 C_s(Q^2). \quad (2.38)$$

In the \overline{MS} scheme, the non-singlet coefficient function $C_{ns}(Q^2)$ was calculated in the α_s^3 approximation:

$$C_{ns} = 1 - \frac{\alpha_s(Q^2)}{\pi} - 3.58 \left(\frac{\alpha_s(Q^2)}{\pi} \right)^2 - 20.2153 \left(\frac{\alpha_s(Q^2)}{\pi} \right)^3. \quad (2.39)$$

The singlet part $\frac{1}{9} a_0 C_s(Q^2)$ exists in two forms, one yields a Q^2 dependent $a_0(Q^2)$ [24]:

$$\frac{1}{9} a_0 C_s(Q^2) = \frac{1}{9} a_0(Q^2) \left[1 - \frac{a_s(Q^2)}{\pi} - 1.10 \left(\frac{a_s(Q^2)}{\pi} \right)^2 \right], \quad (2.40)$$

another one yields the a_0^{inv} [22]:

$$\begin{aligned} \frac{1}{9} a_0 C_s(Q^2) &= \frac{1}{9} C_s^{inv}(Q^2) a_0^{inv} \\ &= \frac{1}{9} \left[1 - 0.3333 \left(\frac{\alpha_s(Q^2)}{\pi} \right) - 0.5495 \left(\frac{\alpha_s(Q^2)}{\pi} \right)^2 + O(\alpha_s^3) \right] a_0^{inv}, \end{aligned} \quad (2.41)$$

where a_0^{inv} is the asymptotic high Q^2 limit of $a_0(Q^2)$.

2.3 Chiral Perturbation Theory

In the low Q^2 region with low energy interactions, since α_s becomes large, the QCD becomes highly non-perturbative. The strong force in the nucleon is relatively strong in the resonance region, the quarks and the gluons cannot be escaped to become the free particles. The QCD cannot be easily solved in this region, the usual perturbative expansion does not work. It is better to deal the composite hadrons as the degrees of freedom than directly deal with the quarks and gluons in QCD, which called Chiral Perturbation Theory (χPT) [25].

Considering the complete QCD Lagrangian [26]:

$$\mathcal{L}_{QCD} = -\frac{1}{4g^2}G_{\mu\nu}^a G^{\mu\nu,a} + \bar{q}i\gamma^\mu D_\mu q - \bar{q}\mathcal{M}q, \quad (2.42)$$

where G is the strength of the gluon field, q is the quark spinor, and $\mathcal{M} = \text{diag}(m_u, m_d, m_s, \dots)$ is the quark mass matrix. The masses of u and d are small compared with the proton's mass, i.e., $m_u/m_e \approx 0.006$. If the quark mass is set to 0, the left and right handed quarks are defined as:

$$q_{R,L} = \frac{1}{2}(1 \pm \gamma_5)q, \quad (2.43)$$

where the chirality is identical to helicity h for a massless fermion. The main idea of χPT is that the left and right handed quarks do not interact each other so that the theory admits the $U(3)_L \times U(3)_R$ symmetry. The existed small quark mass breaks the symmetry. In the low energy, the χPT splits the Lagrangian into two parts:

$$\mathcal{L}_{QCD} = \mathcal{L}_{QCD}^0 + \mathcal{L}'_{QCD} \quad (2.44)$$

where \mathcal{L}_{QCD}^0 is the chiral symmetric part, and $\mathcal{L}'_{QCD} = -\bar{q}\mathcal{M}q$ is regarded as a perturbation to the \mathcal{L}_{QCD}^0 .

The low-energy expansion in small momenta and quark masses involves pion loops of the effective theory. In the presence of baryons, it becomes more complex since the baryon mass is non-vanishing in the chiral limit. Two main approaches were considered for dealing of it: heavy baryon χPT ($HB\chi PT$) and relativistic baryon χPT ($RB\chi PT$). The $HB\chi PT$ considers the baryons as very heavy and the theory is expanded in inverse powers of the baryon mass [27], while the $RB\chi PT$ performs the calculation in a fully relativistic treatment [28].

The χPT is available as high as $Q^2 = 0.2 \text{ GeV}^2$, the calculation of it became very productive over the past 15 years. The applicability range of it should be resolved by the benchmark tests of measurements of the quantities calculable in χPT .

2.4 Sum rules

The first moment of the spin structure function is important since it can extract the quark spin distribution to the nucleon spin. Peoples built several sum rules to study QCD by involving the spin structure of the nucleon. Including the Ellis-Jaffe sum rule discussed above, there are several sum rules related to the first moment of g_1 and g_2 . Here we

discuss the Bjorken sum rule and the Gerasimov-Drell-Hearn (GDH) sum rule for g_1 . The Burkhardt-Cottingham sum rule for g_2 will be discussed in the next section.

2.4.1 The Bjorken sum rule

The most fundamental of the definite prediction for the x dependence of spin-dependent structure functions is the Bjorken sum rule, which was derived from light cone current algebra and isospin invariance [29]. In the naive quark-parton model it has the form of :

$$\Gamma_1^p - \Gamma_1^n = \int_0^1 [g_1^p(x) - g_1^n(x)] dx = \frac{1}{6} \left| \frac{g_A}{g_V} \right|, \quad (2.45)$$

which is the difference between the first moment of proton and neutron. For the finite Q^2 range, it is corrected by the QCD radiative corrections:

$$\Gamma_1^p - \Gamma_1^n = \frac{1}{6} \left| \frac{g_A}{g_V} \right| \left[1 - \frac{\alpha_s(Q^2)}{\pi} - 3.25 \left(\frac{\alpha_s(Q^2)}{\pi} \right)^2 - 13.8 \left(\frac{\alpha_s(Q^2)}{\pi} \right)^3 + \dots \right]. \quad (2.46)$$

It is clear from equation (2.46) that the Γ_1 is independent with Q^2 when a_s becomes to 0, which is the case at $Q^2 \rightarrow \infty$, otherwise, the bjorken scaling breaks down when the Q^2 are in the region of finite values. The Bjorken sum rule is one of the sum rule which the right hand side is accurately known. Measuring the $\Gamma_1^p - \Gamma_1^n$ at different Q^2 provides a sensitive test for the QCD.

Many experiments from SLAC, HERMES, and JLab supported the result of the Bjorken sum rule. The sum rule is rigorous with only the assumption of isospin invariance.

2.4.2 The Gerasimov-Drell-Hearn sum rule

The Bjorken sum rule describes the region of $Q^2 \rightarrow \infty$, while the GDH sum rule describes the region of $Q^2 \rightarrow 0$. With the assumptions of Lorentz and gauge invariance, unitarity and causality, the GDH sum rule is derived from the calculation of the forward Compton amplitude for real photon scattering from a nucleon [30]. The GDH sum rule relates to the particle's static properties from the ground state to all of its excited states. It relates to an energy-weighted integral over its photoabsorption cross section to an anomalous magnetic moment κ [31]:

$$I(0) = \int_{\nu_0}^{\infty} \frac{d\nu}{\nu} [\sigma_{1/2}(\nu) - \sigma_{3/2}(\nu)] = -2\pi^2 \alpha \frac{\kappa^2}{M^2}, \quad (2.47)$$

where ν_0 is the threshold energy for pion production: $\nu_0 = m_\pi (1 + \frac{m_\pi}{2M}) \approx 150 \text{ MeV}$, which ignored the elastic scattering below ν_0 . Since the right hand side of the equation (2.47) is given by the nucleon's ground state properties that are known exactly, the sum rule provides an ideal study for the nucleon's internal structure.

The original GDH sum rule pertains strictly to the real photon case for $Q^2 = 0$. For the $Q^2 > 0$ it is useful to generalize the “GDH integral”:

$$\begin{aligned}
 I(Q^2) &= \int_{\nu_0}^{\infty} \frac{d\nu}{\nu} (1-x)[\sigma_{1/2}(\nu, Q^2) - \sigma_{3/2}(\nu, Q^2)] \\
 &= 2 \int_{\nu_0}^{\infty} \frac{d\nu}{\nu} (1-x) \sigma'_{TT},
 \end{aligned} \tag{2.48}$$

which is valid in all Q^2 range, where we can connect it with the Bjorken sum rule. Study of the connection of these two sum rules can help us to understand the transition from the resonance region to the DIS region.

Near $Q^2 = 0$, several calculation have been performed using chiral perturbation theory. For large Q^2 , OPE technology is used to predict. The GDH sum rule is not investigated until this century at Mainz [32]. After that several experiments at Jefferson Lab tried to extract the GDH integral [33–35]. Now the data below $Q^2 < 0.2 \text{ GeV}^2$ is still lacking, which is necessary to extend the integration to $Q^2 = 0$. The data from E97-110 and E03-006 at Jefferson Lab hopefully can extend the GDH integral at low Q^2 and test predictions of chiral perturbation theory.

2.5 The g_2 Structure Function and the Spin Polarizabilities

There is no definition for the structure function g_2 in the naive quark-parton model [14]. The later progress shows that it is related to the higher-twist quark-gluon correlations and needed to be fixed by using QCD. The first reliable result is decomposed by the Wandzura-Wilczek relation [36], which is known as the leading twist-2 term of g_2 , depends only on g_1 :

$$g_2^{WW}(x, Q^2) = -g_1(x, Q^2) + \int_x^1 \frac{g_1(y, Q^2)}{y} dy. \tag{2.49}$$

With the help of the operator product expansion (OPE) [37–39], g_2 can be expanded into leading (twist-2) and higher-twist components if ignoring quark mass effect:

$$g_2(x, Q^2) = g_2^{WW}(x, Q^2) + \bar{g}_2(x, Q^2), \tag{2.50}$$

where the higher twist part $\bar{g}_2(x, Q^2)$ can be expressed as:

$$\bar{g}_2(x, Q^2) = - \int_x^1 \frac{\partial}{\partial y} \left[\frac{m_q}{M} h_T(y, Q^2) + \zeta(y, Q^2) \right] \frac{dy}{y}, \tag{2.51}$$

where m_q is the quark mass, $h_T(y, Q^2)$ is from the quark transverse polarization distribution which suppressed in DIS by m_q/M , and ζ is the twist-3 part which from quark-gluon interactions.

It is a good approximation of g_2 for equation (2.49) while the $Q^2 \rightarrow \infty$. In the low Q^2 g_2 exhibits large deviations from leading twist behavior. While the higher twist is more sensitive to the quark-gluon interaction, the study of g_2 provides a good test for

the quark-gluon interaction, especially for the study of the difference between g_2 and g_2^{WW} .

2.5.1 The generalized forward spin polarizability γ_0 and The longitudinal-transverse polarizability δ_{LT}

Assuming an appropriate high-energy behavior, the spin-flip forward doubly-virtual Compton scattering (VVCS) amplitude g_{TT} satisfies an unsubtracted dispersion relation as [40, 41]:

$$\begin{aligned} Re[g_{TT}(\nu, Q^2) - g_{TT}^{pole}(\nu, Q^2)] &= \frac{\nu}{2\pi^2} \mathcal{P} \int_{\nu_0}^{\infty} \frac{K(\nu', Q^2) \sigma_{TT}(\nu', Q^2)}{\nu'^2 - \nu^2} d\nu' \\ &= \frac{2\alpha}{M^2} I_A(Q^2) \nu + \gamma_0(Q^2) \nu^3 + \mathcal{O}(\nu^5), \end{aligned} \quad (2.52)$$

where the g_{TT}^{pole} is the nucleon pole (elastic) contribution, \mathcal{P} denotes the principle value integral. The $I_A(Q^2)$ is the coefficient of the $\mathcal{O}(\nu)$ term of the Compton amplitude, it can be expressed as the GDH integral by expanding a Taylor series [41]:

$$\begin{aligned} I_A(Q^2) &= \frac{M^2}{4\pi^2 \alpha} \int_{\nu_0}^{\infty} \frac{K(\nu, Q^2)}{\nu} \frac{\sigma_{TT}(\nu, Q^2)}{\nu} d\nu \\ &= \frac{2M^2}{Q^2} \int_0^{x_0} \{g_1(x, Q^2) - \frac{4M^2}{Q^2} x^2 g_2(x, Q^2)\} dx. \end{aligned} \quad (2.53)$$

Similarly the $\mathcal{O}(\nu^3)$ term yields a generalization of the forward spin polarizability [41]:

$$\begin{aligned} \gamma_0(Q^2) &= \left(\frac{1}{2\pi^2}\right) \int_{\nu_0}^{\infty} \frac{K(\nu, Q^2)}{\nu} \frac{\sigma_{TT}(\nu, Q^2)}{\nu^3} d\nu \\ &= \frac{16\alpha M^2}{Q^6} \int_0^{x_0} \{g_1(x, Q^2) - \frac{4M^2}{Q^2} x^2 g_2(x, Q^2)\} x^2 dx. \end{aligned} \quad (2.54)$$

In a similar way with $I(0)$ expressed as the photoabsorption cross section in equation (2.47), the forward spin polarizability γ_0 can be expressed as:

$$\gamma_0 = \frac{1}{4\pi^2} \int_{\nu_0}^{\infty} \frac{d\nu}{\nu^3} [\sigma_{1/2}(\nu) - \sigma_{3/2}(\nu)]. \quad (2.55)$$

The longitudinal-transverse interference amplitude g_{LT} can be expressed by using the same assumption:

$$Re[g_{LT}(\nu, Q^2) - g_{LT}^{pole}(\nu, Q^2)] = \frac{2\alpha}{M^2} Q I_3(Q^2) + Q \delta_{LT}(Q^2) \nu^2 + \mathcal{O}(\nu^4), \quad (2.56)$$

where the $\mathcal{O}(1)$ term yields an integral by using a similar procedure:

$$\begin{aligned} I_3(Q^2) &= \frac{M^2}{4\pi\alpha^2} \int_{\nu_0}^{\infty} \frac{K(\nu, Q^2)}{\nu} \frac{\sigma_{LT}(\nu, Q^2)}{Q} d\nu \\ &= \frac{2M^2}{Q^2} \int_0^{x_0} \{g_1(x, Q^2) - g_2(x, Q^2)\} x^2 dx, \end{aligned} \quad (2.57)$$

and the $\mathcal{O}(\nu^2)$ term yields a generalized longitudinal-transverse polarizability [41]:

$$\begin{aligned} \delta_{LT}(Q^2) &= \left(\frac{1}{2\pi^2}\right) \int_{\nu_0}^{\infty} \frac{K(\nu, Q^2)}{\nu} \frac{\sigma_{LT}(\nu, Q^2)}{Q\nu^2} d\nu \\ &= \frac{16\alpha M^2}{Q^6} \int_0^{x_0} \{g_1(x, Q^2) + g_2(x, Q^2)\} x^2 dx. \end{aligned} \quad (2.58)$$

At large ν , the unmeasured region enlarges the uncertainty for the χPT calculation. The extra $\frac{1}{\nu^2}$ weighting for γ_0 and δ_{LT} in equation (2.54) and (2.58) compared with the first moment leads the value of γ_0 converge quickly in the large- ν region. Measurements of the generalized spin polarizability provide a benchmark tests of the χPT calculation. The value of γ_0 and δ_{LT} have been evaluated in $HB\chi PT$ [42] and $RB\chi PT$ [43]. Compared with the γ_0 , a measurement of the δ_{LT} is expected to be a good test of it since it is insensitive to the $\pi - \Delta$ contribution, which is usually the main high-order correction [44].

2.5.2 The Burkhardt-Cottingham Sum Rule

The spin-flip amplitude g_{TT} and g_{LT} are also related to the covariant spin-dependent VVCS amplitude S_1 and S_2 , as expressed as:

$$S_1(\nu, Q^2) = \frac{\nu M}{\nu^2 + Q^2} [g_{TT}(\nu, Q^2) + \frac{Q}{\nu} g_{LT}(\nu, Q^2)], \quad (2.59)$$

$$S_2(\nu, Q^2) = -\frac{M^2}{\nu^2 + Q^2} [g_{TT}(\nu, Q^2) - \frac{\nu}{Q} g_{LT}(\nu, Q^2)]. \quad (2.60)$$

For the S_2 the unsubtracted dispersion with νS_2 lead to the Burkhardt-Cottingham (B-C) sum rule [45] which is valid for any value of Q^2 :

$$\int_0^1 g_2(x, Q^2) = 0. \quad (2.61)$$

The test of the B-C sum rule can be taken either at DIS region or at low region. The validity of the B-C sum rule depends on the integral at low x . It will be failed if g_2 exhibits non-Regge behavior at low x [46].

2.5.3 Higher twist moments d_2

The moments d_2 is expressed as:

$$\begin{aligned} d_2(Q^2) &= \int_0^1 x^2 [2g_1(x, Q^2) + 3g_2(x, Q^2)] dx \\ &= 3 \int_0^1 x^2 [g_2(x, Q^2) - g_2^{WW}(x, Q^2)] dx. \end{aligned} \quad (2.62)$$

At large Q^2 , the higher twist moments d_2 is related to the color polarizability, which describes color electric and magnetic polarizabilities. It can be calculated from Lattice QCD at high Q^2 , which provides a benchmark test for the Lattice QCD. At lower Q^2 , it provides the study of the transition from perturbative to non-perturbative region. Since it is the x^2 moment of the difference between g_2 and g_2^{WW} , it represents a measure of QCD complexity.

Chapter 3

History and Recent Results on the Measurement of Spin Structure function

3.1 History for the spin structure measurement

After the discovery of the “spin crisis” from the EMC group, more collaboration groups participated in the study of the spin structures besides the groups at SLAC and CERN, like the groups at DESY, at Brookhaven Nation Lab (BNL) and Jefferson Lab (JLab).

The E142 [47], E143 [48], E154 [49] and E155/E155x [50] collaborations at SLAC used a polarized electron beam with the polarization around 36% to hit the fixed polarized target in order to measure the spin structure functions g_1 and g_2 for proton, deuteron and neutron in the DIS region. The polarized 3He target system was used for the neutron target with about 33% polarization. A polarized target system with 1K refrigerator and 5T magnet field was used to extract the spin structure functions for proton and deuteron with the materials of NH_3 , ND_3 , LiD , C_4H_9OH and C_4D_9OD .

Unlike the external polarized target at SLAC, HERMES collaboration used the polarized e^+, e^- beam in one of the HERA rings at DESY to hit the internal gas target fed from atomic beam sources like the hydrogen gas and 3He gas [51, 52]. The gas was polarized in the atomic beam source (ABS) [53], with up to 95% polarization for the proton and up to 46% for the 3He . The advantage of the internal targets is with no dilution and windowless storage cell. They measured the spin structure functions $g_1^{p,d}$ in inclusive [54], the spin contributions from each type of quarks in semi-inclusive scattering experiments [55], and the gluon polarization for the first time [56].

The SMC (Spin Muon Collaboration) at CERN took the measurements [57] with the polarized hydrogen and deuteron targets over a period of ten years after the EMC measurements. They measured the structure functions in the kinematic range of $1 < Q^2 < 60 \text{ GeV}^2$ and $0.003 < x < 0.7$ in the DIS region. The semi-inclusive lepton scattering allowed them to distinguish the contributions from quark and anti-quark densities. The neutron spin structure functions were also extracted from the hydrogen and deuteron data. Results of them are shown in [58–68].

The COMPASS at CERN used the secondary muon beam with naturally polarized to hit the polarized deuteron and hydrogen targets to extract information on the gluon polarization. The first result are shown in [69–71].

The relativistic heavy ion collider (RHIC) at BNL provides an approach using polarized proton collisions with the high energies up to 250GeV to study the spin structures. Two collaborations, PHENIX and STAR, at BNL are trying to study the gluon helicity contribution ΔG by probing the quark-gluon, gluon-gluon interactions in the initial state. The first results were published in [72–75]. The most recent results from them can be found from [76–81].

The continuous electron beam accelerator facility (CEBAF) at JLab provides the polarized electron beam with high luminosity (up to $10^{36} \text{ s}^{-1} \text{ cm}^{-2}$), which significantly

increased the precision and extended the kinematic ranges of the measurement. All of the three experiment halls (Hall A, B and C) measured the spin structures for the last 17 years. Combining with the polarized target system, the experiments at JLab not only measured the total spin contributions of quarks to the nucleon, but also measured the contributions from each type of quarks. Both longitudinal and transverse spin structures were studied. Hall A has two high resolution spectrometers (HRS) with momentum up to $4 \text{ GeV}/c$ and resolution up to 10^{-4} [82]. With the polarized ${}^3\text{He}$ target, Hall A collected the most precisely data on the $g_{1,2}^n$ and $A_{1,2}^n$ at the wide Q^2 range of $0.02 < Q^2 < 5 \text{ GeV}^2$ with a series of experiments. Hall B has the CEBAF Large Acceptance Spectrometer (CLAS) with almost 2π in azimuth and 6 to 140 degrees in polar angle acceptance for all of the particles produced in the electron-proton collisions [83]. The EG1-EG4 series of experiments took the most detailed study on the asymmetry A_1 and the longitudinal spin structure function g_1 on both NH_3 and ND_3 targets over a continuous coverage in Q^2 from 0.015 to 5 GeV^2 . Hall C has the High Momentum Spectrometer (HMS) with the momentum up to $7.5 \text{ GeV}/c$ and resolution up to 10^{-3} [84]. The RSS and the SANE experiments in Hall C collected the precise data of g_{12}^p on both resonances and the DIS region [85].

With the data collected from the experiments over the latest 30 years, peoples get much clearer pictures for the spin structures. The longitudinal spin structure function g_1 was confirmed to have a strong dependence on the Bjorken scaling variable x . The Bjorken sum rule is verified to an accuracy of better than 10%, while the Ellis-Jaffe sum rule is broken. The experiments concluded that the quarks carry about 30% of the nucleon spin. The results from the semi-inclusive show that the distribution of $\Delta u(x)$ is positive, while $\Delta d(x)$ is negative. The distribution of the non-strange sea quark is consistent with zero in the range of uncertainty. The spin contributions for each type of quark are calculated by assuming the $SU(3)$ flavor symmetry in the inclusive measurements and by assuming sea quark flavor symmetry in the semi-inclusive measurements. Most results in the inclusive measurements show a small negative helicity Δs of the strange sea quark, while it is consistent with zero in the semi-inclusive measurements [23].

3.2 Results for g_2

In order to extract the spin structure function g_2 , one can either use the longitudinal and the transverse asymmetry $A_{||}$, A_{\perp} via the equations (4.48-4.52) combining existed F_1 result, or the longitudinal and the transverse differential cross section $\Delta\sigma_{||}$, $\Delta\sigma_{\perp}$ via the equations (4.31-4.32). The earliest results for g_2 are from SLAC in the DIS region by measuring both the longitudinal and the transverse asymmetry [47]. During the same period with SLAC, the SMC group at CERN used a muon beam instead of using an electron beam to extract the $g_{1,2}$ from the longitudinal and transverse asymmetries at the proton and deuteron target in the DIS region [59, 60, 62, 86]. Since g_2 is relatively small, it needs more beam time and larger luminosity than g_1 . Several experiments only focused on the transverse polarized target to get enough statistics on g_2 , and using existed data g_1 or A_1 from other experiments [50, 59, 87]. Some experiments only used the transverse polarized data to reduce the systematic error on g_1 due to g_2 , yielding the very rough result on g_2 [47, 59, 86, 88]. Recently JLab collected a massive precise data set over a wide Q^2 range using the high luminosity electron beam on both DIS region

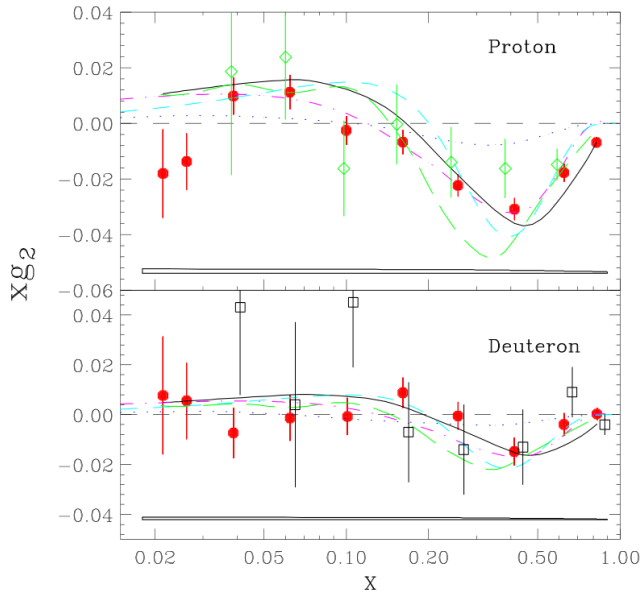


Figure 3.1 Result of g_2 for the proton and deuteron in DIS region [101]. The solid circle is from E155x, the open diamond is from E143, and the open square is from E155. The solid line is the g_2^{WW} at the average Q^2 of E155x. Also the models calculated from Stratmann [102] (dash-dot-dot), Song [103] (dot), Weigel [104] (dash-dot) and Wakamatsu [105] (dash) are compared.

and the resonance region. A summary of experiments for the g_2 measurement is shown in table 3.1.

In the DIS region, g_2 was precisely measured for both neutron and proton. The most precise g_2 data for the proton and deuteron is from SLAC E155x [50, 87]. The g_2 for neutron was extracted by the difference of the proton and deuteron data from E155x, as well. Also, the SLAC E143 [24] and E155 [101] contributed precise data to g_2 . Figure 3.1 shows the g_2 results from SLAC E143, E155 and E155x. The curve is mostly matched the g_2^{WW} from equation (2.49), but with some deviation, especially at the small x . The difference between the g_2 data and the g_2^{WW} is because of the high-twist effect, which is sensitive to the quark-gluon interaction.

With the high luminosity polarized beam, JLab extracted extremely precised g_2 data for the neutron in the DIS region. The experiment E97-103 measured dedicated g_2^n data at low Q^2 DIS region in order to study the Q^2 dependence of g_2 [96], as shown in figure 3.2. It covered five Q^2 values in the Q^2 range of $0.58 < Q^2 < 1.36 \text{ GeV}^2$ at $x \approx 0.2$. The result shows that the g_2 consistently higher than g_2^{WW} in this kinematic range. This is the first time that shows the difference between g_2 and g_2^{WW} significantly positive, while the higher-twist effects predicted from the bag model [102] and Chiral Soliton model [104, 105] are negative or close to zero. Figure 3.3 shows the xg_2^n results from the experiments E97-103 [96], E99-117 [95] from JLab and E155 from SLAC [101]. The precision from JLab is much higher than the one from E155.

Comparing with the DIS region, the resonance region has stronger effect of the quark-gluon interaction. Many of the experiments collects the g_2 data in the region of $W < 2\text{GeV}$. The study in the resonance region can reveal important information on the internal structure of the nucleon resonances. Using the data from neutron, proton

Lab	Exp.	Year	$Q^2(GeV^2)$	x	$W(GeV)$	Beam (GeV)	Target	Measured	Region
SLAC	E142 [47]	1992	~ 2	$0.03 - 0.6$	$19 - 26$	e^-	3He	A_{\parallel} A_{\perp}	DIS
SLAC	E143 [24, 89, 90]	1993	$0.5, 1.2,$ $1.3 - 10$	$0.03 - 0.8$	$9.7 - 29$	e^-	NH_3 ND_3	A_{\parallel} A_{\perp}	DIS Resonance
SLAC	E154 [49, 88]	1995	$1 - 17$	$0.014 - 0.7$	48	e^-	3He	A_{\parallel} A_{\perp}	DIS
SLAC	E155 [91]	1997	$1 - 30$	$0.02 - 0.8$	48	e^-	NH_3 LiD	A_{\perp}	DIS
SLAC	E155x [87]	1999	$0.7 - 20$	$0.02 - 0.8$	30	e^-	NH_3 LiD	A_{\perp}	DIS
CERN	SMC [59, 60, 62, 86]	1992 -1996	$1 - 60$	$0.004 - 0.5$	$100, 190$	μ^+	$C_4^* H_9 OH$ $C_4^* D_9 OD$ NH_3	A_{\parallel} A_{\perp}	DIS
JLab	E94-010 [33, 92-94]	1998	$0.1 - 0.9$	$0.5 - 2.5$	$2.6 - 5.0$	e^-	3He	$\Delta\sigma_{\parallel}$ $\Delta\sigma_{\perp}$	Resonance
JLab	E99-117 [95]	2001	$2.7, 3.5, 4.8$	$0.33, 0.47, 0.6$	$4.0, 4.9, 6.4$	e^-	3He	A_{\parallel} A_{\perp}	DIS
JLab	E97-103 [96]	2001	$0.57 - 1.34$	0.2	> 3.8	e^-	3He	$\Delta\sigma_{\parallel}$ $\Delta\sigma_{\perp}$	DIS
JLab	E97-110 (saGDH) [34]	2003	$0.02 - 0.5$	$0.8 - 2.6$	$1.6 - 6.0$	e^-	3He	$\Delta\sigma_{\parallel}$ $\Delta\sigma_{\perp}$	Resonance
JLab	E01-012 [97]	2004	$1.0 - 5.4$	$0.2 - 0.87$	$1 - 2.1$	e^-	3He	$\Delta\sigma_{\parallel}$ $\Delta\sigma_{\perp}$	Resonance
JLab	E06-014 (d2n) [98]	2009	$2 - 6$	$0.2 - 0.7$	$1.79 - 2.86$	e^-	3He	A_{\parallel} A_{\perp}	DIS
JLab	RSS [99]	2002	$0.6 - 2$	$0.3 - 0.8$	$0.8 - 1.9$	e^-	NH_3 ND_3	A_{\parallel} A_{\perp}	Resonance
JLab	SANE [100]	2008	$2.5 - 6.5$	$0.3 - 0.8$	$4.8 - 6$	e^-	NH_3	A_{\parallel} A_{\perp}	DIS

 Table 3.1 Summary of spin structure function g_2 measurement before E08-027

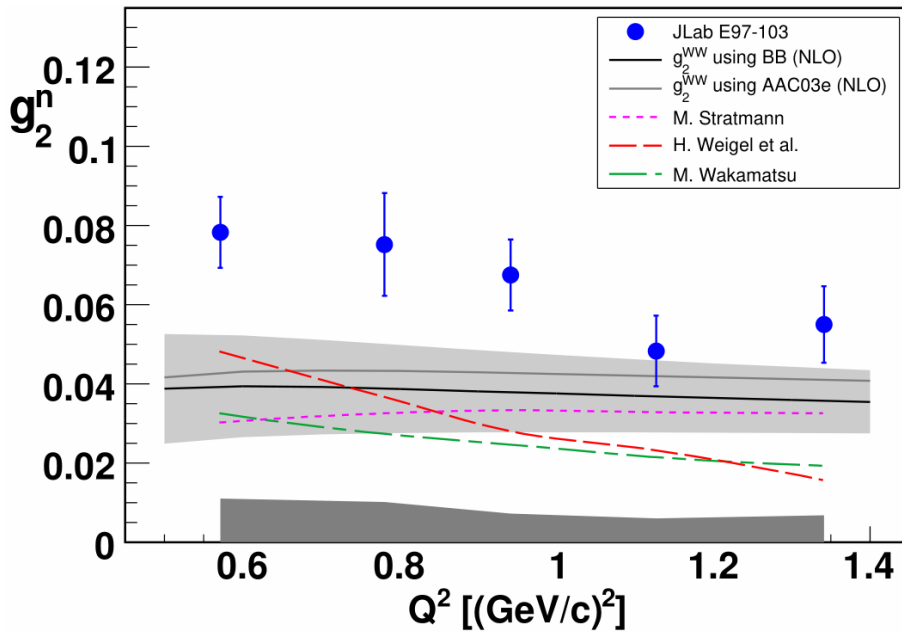


Figure 3.2 g_2^n extracted from the experiment E97-103 at JLab for $x \approx 0.2$ [96]. The low-dark gray band is the systematic uncertainties. The error bar is the statics. The light gray line and the dark solid line with gray uncertainty band are g_2^{WW} from the fit of world g_1 data.

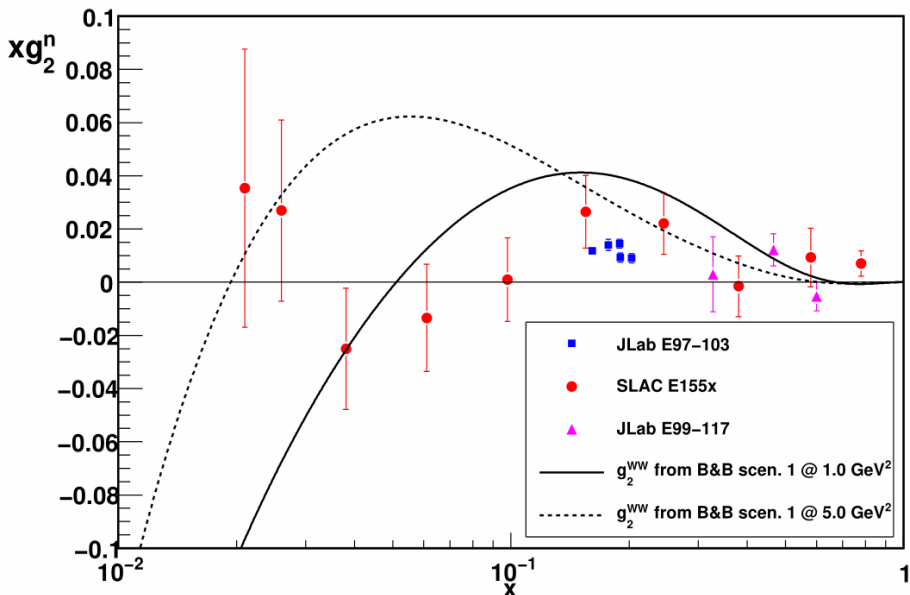


Figure 3.3 g_2^n extracted from the experiment E97-103 [96] (blue square), E99-117 [95] (red square) at JLab and the E155x [101] (pink triangle) at SLAC, compared with the g_2^{WW} from model.

and deuteron, several spin-isospin channels that lead to the different excited resonances can be extracted. The first experiment to measure the g_2 in the resonance region is E143 experiment at SLAC, with the beam energy of 9.7 GeV and the Q^2 value of 0.5 GeV^2 and 1.2 GeV^2 [90]. JLab E94-010 collected a vast data for the neutron [92] at low Q^2 , as shown in Figure 3.4. The structure function g_2 was directly extracted from the measurement of cross section difference for the polarized electron beam scattering of the longitudinal and transverse polarized ${}^3\text{He}$ target. The data shows a significantly positive response of g_2 in the $\Delta(1232)$ resonance region, and a large deviation with g_2^{WW} .

Currently the lowest momentum transfer investigated for proton's g_2 is 1.3 GeV^2 by the RSS collaboration [106] in JLab Hall B. The result is shown in figure 3.5. The comparison of g_2 and g_2^{WW} provides strong evidence of the significance of higher-twist terms in this Q^2 range. It is clearly that g_2^{WW} insufficient to describe the data in the low Q^2 region.

3.3 Results for B-C sum rule

The first moment of g_2 is expected to be 0 in all of the Q^2 ranges as the result of the B-C sum rule. The first measurement for the first moment of g_2 is from E155 at SLAC, which included the result of proton, deuteron and neutron. JLab Hall A extensively extracted the neutron's g_2 integral in a wide kinematic range in several experiments: E94-010 [92], E99-117 [95], E97-103 [96], E97-110 [107] and E01-012 [108]. The RSS experiment from Hall C in JLab provided the proton's g_2 integral in the average Q^2 of 1.3 GeV^2 [106]. The unmeasured low x DIS contribution mostly uses the assumption of $g_2 = g_2^{WW}$, and the elastic contribution ($x=1$) is mostly from the well known elastic form factors. The results for the B-C sum rule are shown in figure 3.6.

The neutron data from E155x shows agreement with the B-C sum rule with a large error bar. The data from RSS also agree with the B-C sum rule. Other extensive data from JLab Hall A was extracted by using a longitudinal and transverse polarized ${}^3\text{He}$ target. The results from E94-010 in the measured region shows a significantly positive value, but consistent with 0 after extended to the elastic and DIS region. The total integral exhibits a significant cancellation of the inelastic and elastic contribution. Most precise data is from E97-110, E94-010 and E01-012, which are consistent with 0.

The proton data from E155 shows large deviation with the B-C sum rule, while the error bar is large [101]. For the $x \rightarrow 0$ extrapolation, they assumed $g_2 = g_2^{WW}$, which is difficult to quantify. The preliminary result from RSS in the measured resonance region is negative, while it consistent with 0 after adding the contributions from elastic scattering and the data in small- x region. The proton data of the B-C sum rule is mostly unmeasured.

3.4 Results for spin polarizabilities γ_0 and δ_{LT}

The experimental results compared with the χPT calculation is shown in figure 3.7. Since the forward spin polarizability γ_0 can be expressed as the photoabsorption cross section from equation (2.55), it can be measured by the real photon Compton scattering experiment with $Q^2 = 0$. An experiment at MAMI (Mainz) measured the γ_0 by using

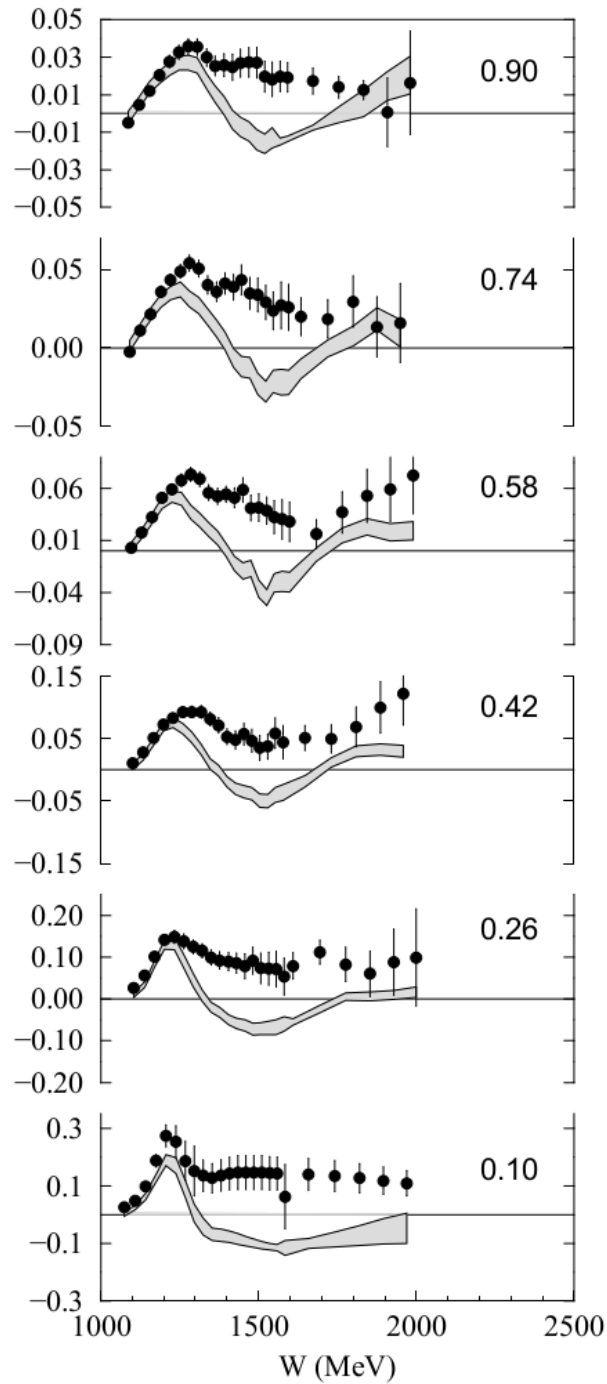


Figure 3.4 g_2^n extracted from the experiment E94-010 for the different Q^2 in the resonance region, compared with g_2^{WW} (grey band) [92]. The unit for the constant Q^2 in each panel is GeV^2 .

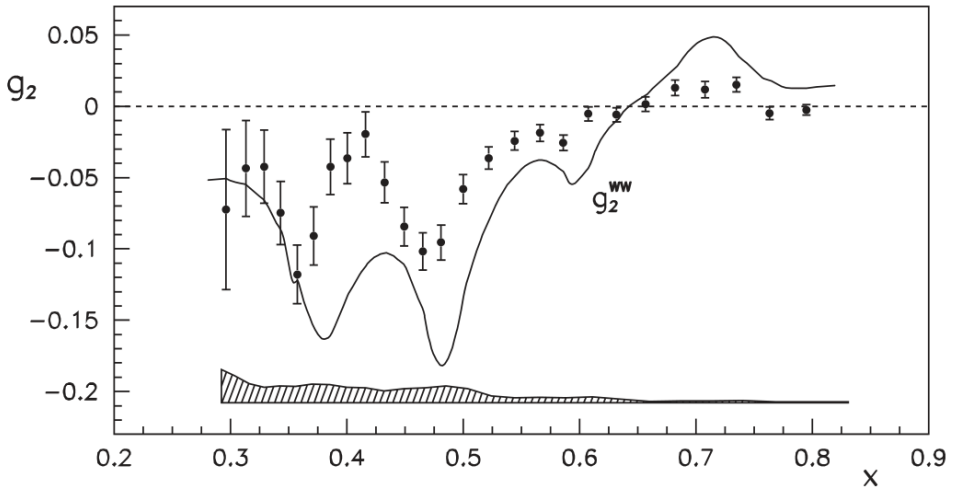


Figure 3.5 Proton's g_2 result and the approximation g_2^{WW} in resonance region, from RSS collaboration [106]. The $\Delta(1232)$ resonance region is at large x around 0.7.

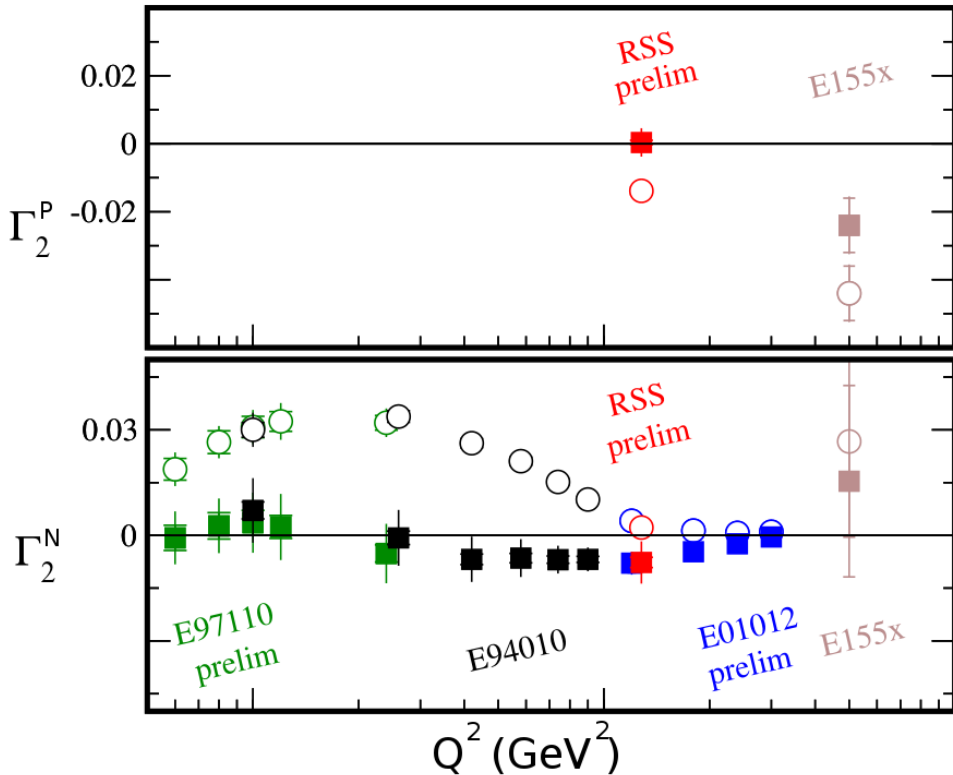


Figure 3.6 Verification of BC sum rule [109]. The top plot is for proton and the bottom one is for neutron. The open circle are the measured values, while the solid square are the total integral in $0 < x < 1$. The proton data is from JLab RSS experiment (red) [85] and SLAC E155 experiment (brown) [101]. The neutron data is from JLab E97-110 [107], E94-010 [92], E01-012 [108] and RSS experiment and SLAC E155 experiment. The neutron data from RSS and E155x is extracted from proton and deuteron data, while others are from 3He data.

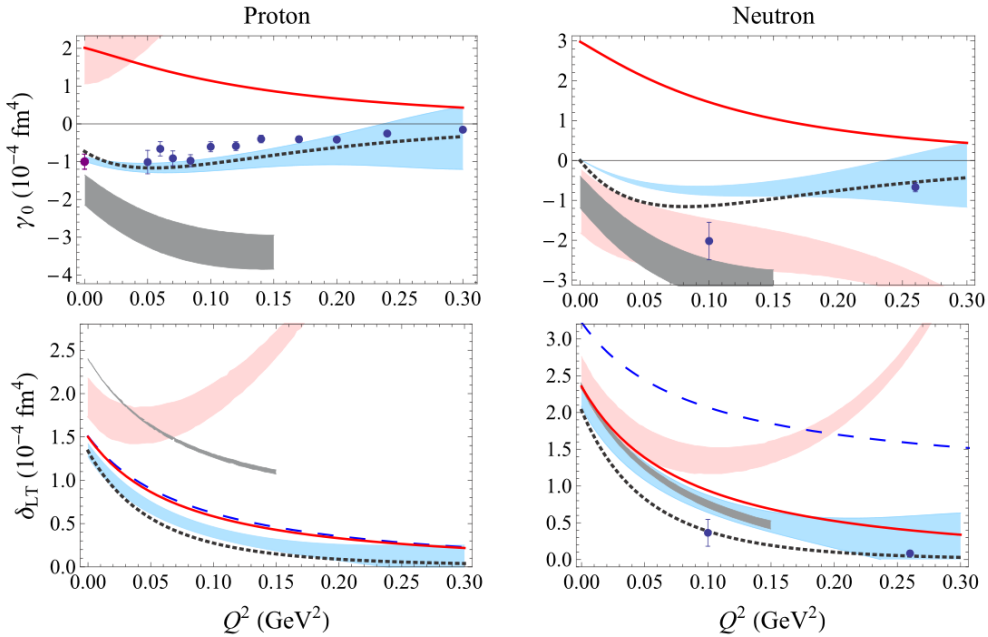


Figure 3.7 Spin polarizabilities of proton and neutron. The neutron data points (blue dots) are from E94-010 experiment [93]. The proton γ_0 data points are from Mainz ($Q^2 = 0$, purple dot) [110] and EG1 in JLab Hall B (finite Q^2 , blue dot) [111] calculated from Ref.[112]. Red solid lines and blue bands are the baryon χPT LO and NLO results calculated from Vadim [112]. Black dotted lines are from MAID 2007. Grey band are the covariant $B\chi PT$ [44]. Blue dashed line is the $\mathcal{O}(p^4)$ HB calculation [42]. Red band is the IR calculation [43].

a circularly polarized photon beam on a longitudinal polarized proton (butanol) target [32, 110], shown in figure 3.7 (purple dot, for proton γ_0).

The first results for the neutron γ_0 and δ_{LT} were obtained from E94-010 experiment in Jefferson Lab [93] (blue dot for proton γ_0 and δ_{LT} in figure 3.7). At the $Q^2 = 0.1 \text{ GeV}^2$ point, the experiment result for neutron agree with the $RB\chi PT$ calculation, but with significant discrepancy with the $HB\chi PT$ calculation. Since the γ_0 is sensitive with Δ resonance, it indicates that the Δ contribution should be considered properly in the χPT calculation. The higher Q^2 point is agree with the MAID model, while the lower one is significantly lower. The discrepancy δ_{LT} data indicates a significant disagreement with both heavy baryon χPT (blue dashed line in figure 3.7) and relativistic baryon χPT calculations (red dashed line in figure 3.7), which known as “ δ_{LT} puzzle”. The puzzle presents a challenge to the present theoretical prediction. However, the recent calculation using leading- and next-to-leading-order predictions of chiral perturbation theory shows that the δ_{LT} puzzle is gone [112] (red solid line and blue band in figure 3.7). The data has good agreement with MAID prediction. The proton data for δ_{LT} is needed to complete for further comparison.

3.5 Results for d_2

The experimental results for the higher twist moment d_2 are shown in figure 3.8. For the neutron data, the E94-010 data shows increased d_2 in low Q^2 and then decrease,

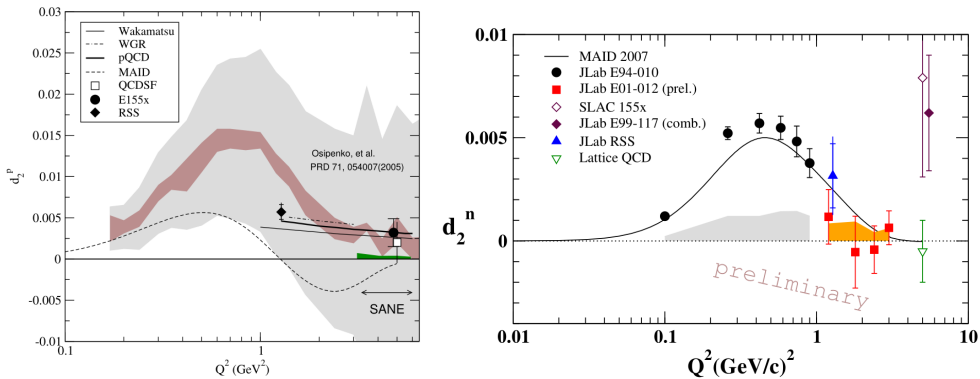


Figure 3.8 d_2 data for proton (left) and neutron (right). Proton data contains the results from RSS at JLab [106] and E155x at SLAC [101], compared with the calculation from the Lattice QCD [113], the PQCD [37], the MAID model [114], the chiral soliton models of WGR [104, 115] and Wakamatsu [105]. The expected SANE uncertainties are also included. The large shaded area is from Osipenko et al. [116]. Neutron results are from E94-010 [93], E01-012 [117], E99-117 [95], RSS experiments at JLab and E155x [24] at SLAC, compared with MAID 2007 and Lattice QCD.

while the result of Lattice QCD shows negative but close to 0 in $Q^2 = 5 \text{ GeV}^2$, but with large discrepancy with JLab E99-117 and SLAC E155x data. It is important to get high precision data at large Q^2 for testing of the lattice QCD and understanding of the quark-gluon correlations.

For the proton data the calculation of the Lattice QCD matched well with the RSS data and E155x data. But the data is scarce. The result of MAID model strongly disagree with data, which needs more g_2 experimental data to optimize [116].

Chapter 4

Inclusive Lepton-Nucleon Scattering

For the process of the lepton scattering, the reaction is divided into several classes:

- The inclusive scattering only refers to measure the scattered lepton. This is the simplest way.
- The semi-inclusive scattering refers to measure the scattered lepton and one or more final-state particles.
- The exclusive scattering refers to measure the scattered lepton, nucleon and all the reconstructed final particle produced in the interaction.

Here we only focus on the inclusive scattering.

4.1 Kinematic variables

The lowest order inclusive diagram for the lepton-nucleon scattering is:

$$l(p) + N(P) \rightarrow l(p') + X(P'). \quad (4.1)$$

The diagram is shown in figure 4.1. For the fixed-target, the cross section for the scattering of leptons is dominated by virtual photon exchange. We denote the k and s (k' and s') are the initial (final) four-momentum and spin four-vector of the lepton, respectively, $q = k - k'$ is the transferred four-momentum from the lepton to the nucleon, M is the nucleon mass, P and S are the nucleon four-momentum and spin four-vector, respectively.

Several invariant quantities are used:

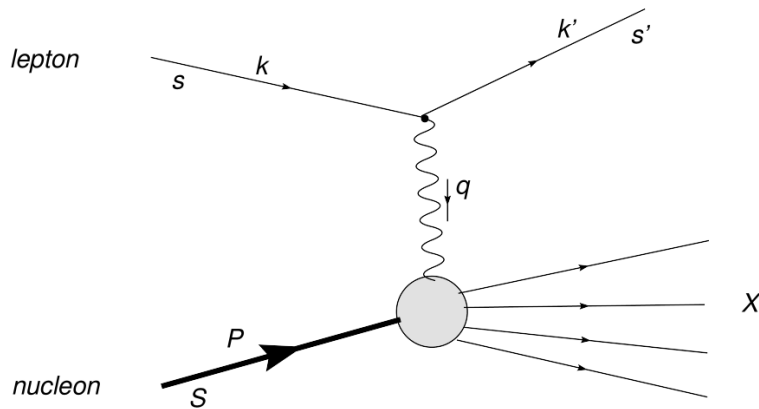


Figure 4.1 Feynman diagram for deep-inelastic lepton-hadron scattering

- Lepton's energy loss in the nucleon rest frame:

$$\nu = \frac{q * P}{M} = E - E', \quad (4.2)$$

where E and E' are the initial and final lepton energies.

- Squared four-momentum transfer:

$$Q^2 = -q^2 \approx 4EE' \sin^2\left(\frac{\theta}{2}\right), \quad (4.3)$$

where θ is the leptons scattering angle.

- Square of invariant mass:

$$W^2 = (P + q)^2 = M^2 + 2M\nu - Q^2, \quad (4.4)$$

- Bjorken scaling variable:

$$x = \frac{Q^2}{2M\nu}. \quad (4.5)$$

- The fraction of lepton energy loss:

$$y = \frac{\nu}{E}. \quad (4.6)$$

4.2 Types of the inclusive electron scattering

The cross section of the electron scattering is a function of the Q^2 and ν . The spectrum is shown in figure 4.2 [118]. It is splitted into several different kinematic regions: elastic, quasi-elastic, resonance, deep inelastic.

In elastic scattering the nucleon remain in the ground state. The ν is not high enough so that the nucleus stays intact. The invariant mass W is equal to the mass of the nucleon.

The quasi-elastic scattering happened when the ν is higher than the nuclear binding energy. The nucleon is knocked out of the nucleus and can be considered as quasi-free. The energy shift of the quasi-elastic peak is because of the energy absorption for the nucleon remove from the nucleus. If the target is nucleon like a proton target, then there is no quasi-elastic peak. Difference of them are shown in figure 4.3.

As the ν increase, the nucleon is excited to several different states known as the resonance region, which shows the composite structure system of the nucleon. The kinematic range of resonance is usually at $1.0 < W < 2.0 \text{ GeV}^2$. Several peaks in the resonance region show the different states of the nucleon. The first peak is the $\Delta(1232)$ resonance. The second peak consists of the $N(1520)$ and $N(1535)$ resonances. The third peak becomes more complicate since it contains many states. Also there is $N(1440)$ resonance exists between the peak of $\Delta(1232)$ and $N(1520)$. The properties of each resonance states such like the invariant mass (W), width (Γ), total angular momentum (J^P) and the orbital angular momentum (l) are shown in table (4.1).

When $Q^2 > 1-2 \text{ GeV}^2$ and $W > 2 \text{ GeV}^2$, the strong interaction becomes relatively weak. The quarks and gluons can be treated as free particles and the reaction can be

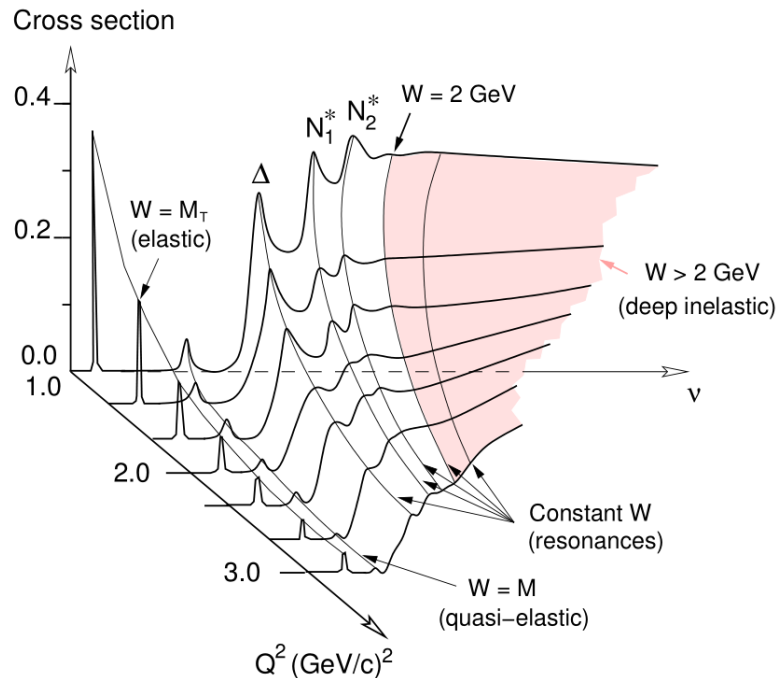


Figure 4.2 Spectrum of the electron scattering

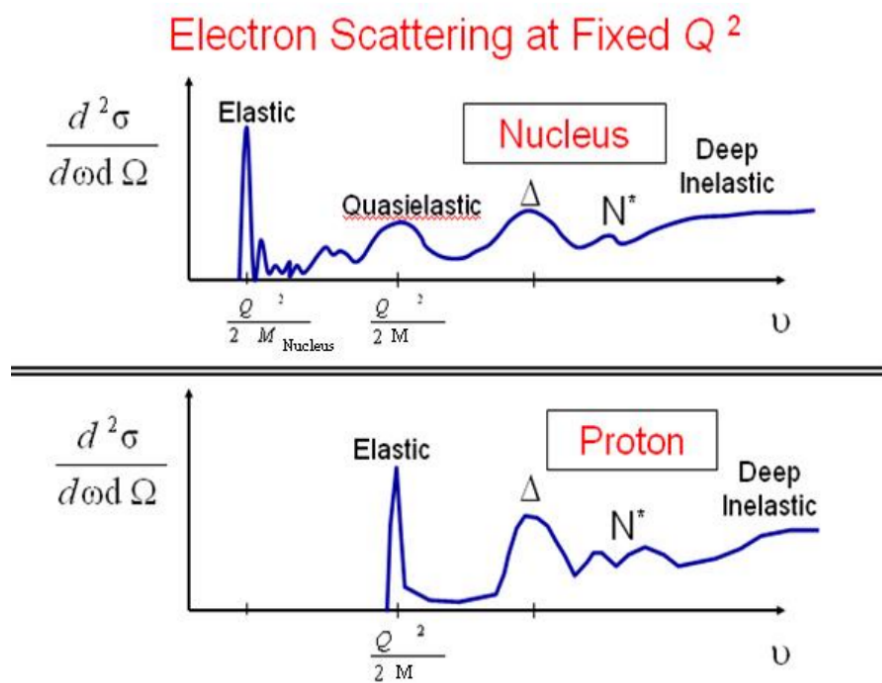


Figure 4.3 Spectrum of electron-nucleus scattering (up) and electron-nucleon scattering (down) [23]

Particle	Resonance	$W(MeV)$	$\Gamma(MeV)$	J^P	l
$\Delta(1232)$	P_{33}	1232	120	$\frac{3}{2}^+$	1
$N(1440)$	P_{11}	1440	300	$\frac{1}{2}^+$	1
$N(1520)$	D_{13}	1520	115	$\frac{3}{2}^-$	2
$N(1535)$	S_{11}	1535	150	$\frac{1}{2}^-$	0
$\Delta(1600)$	P_{33}	1600	320	$\frac{3}{2}^+$	1
$\Delta(1620)$	S_{31}	1620	140	$\frac{1}{2}^-$	0
$N(1650)$	S_{11}	1650	140	$\frac{1}{2}^-$	0
$N(1675)$	D_{15}	1675	150	$\frac{5}{2}^-$	2
$N(1680)$	F_{15}	1680	130	$\frac{5}{2}^+$	3
$\Delta(1700)$	D_{33}	1700	300	$\frac{3}{2}^-$	2
$N(1700)$	D_{13}	1700	150	$\frac{3}{2}^-$	2
$N(1710)$	P_{11}	1710	100	$\frac{1}{2}^+$	1
$N(1720)$	P_{13}	1720	250	$\frac{3}{2}^+$	1

Table 4.1 The properties of the nucleon resonance [119]

treated as the lepton-quark scattering with the quark-parton model. Deep inelastic scattering was used as a powerful tool to study the nucleon structure. QCD has been well tested in this region.

4.3 Differential cross section and structure functions

Considering of one photon exchange for detecting the final lepton in the solid angle $d\Omega$ and final energy range $(E', E' + dE')$, the differential cross section can be written as [14]:

$$\frac{d^2\sigma}{d\Omega dE'} = \frac{\alpha^2}{2Mq^4} \frac{E'}{E} L_{\mu\nu} W^{\mu\nu}, \quad (4.7)$$

where α is the electromagnetic coupling constant. The cross-section contains two part: The leptonic tensor $L_{\mu\nu}$ and the hadronic tensor $W_{\mu\nu}$. The $L_{\mu\nu}$ is known exactly and is given by:

$$L_{\mu\nu}(k, s; k', s') = [\bar{u}(k', s')\gamma_\mu u(k, s)]^*[\bar{u}(k', s')\gamma_\mu u(k, s)], \quad (4.8)$$

where $\mu(k, s)$ and $\bar{\mu}(k', s')$ are electron spinors. The leptonic tensor can be split into symmetry part (S) and anti-symmetry part (A) by interchanging the Lorentz indices μ and ν and on summing over s' :

$$L_{\mu\nu}(k, s, k') = L_{\mu\nu}^{(S)}(k; k') + iL_{\mu\nu}^{(A)}(k, s; k'), \quad (4.9)$$

$$L_{\mu\nu}^{(S)}(k; k') = 2[k_\mu k'_\nu + k'_\mu k_\nu - g_{\mu\nu}(kk' - m^2)], \quad (4.10)$$

$$L_{\mu\nu}^{(A)}(k, s; k') = 2[m\epsilon_{\mu\nu\alpha\beta}s^\alpha q^\beta], \quad (4.11)$$

where $g_{\mu\nu}$ is the metric tensor, $\epsilon_{\mu\nu\alpha\beta}$ is the Levi-Civita tensor. The Leptonic tensor is easy to calculate by using the QED formalism.

The hadronic tensor describes the interaction between the virtual photon and the nucleon, it is complicated to calculate directly. Four structure functions: unpolarized structure functions F_1 , F_2 and the spin related structure functions g_1 and g_2 are used to parametrize the quantity. The tensor $W_{\mu\nu}$ can also be split into symmetry and anti-symmetry part:

$$W_{\mu\nu}(q; P, s) = W_{\mu\nu}^{(S)}(q; P) + iW_{\mu\nu}^{(A)}(q; P, s), \quad (4.12)$$

where the symmetry part is:

$$\frac{1}{2M}W_{\mu\nu}^{(S)}(q; P) = (-g_{\mu\nu} + \frac{q_\mu q_\nu}{q^2})W_1(\nu, Q^2) + [(P_\mu - \frac{P \cdot q}{q^2}q_\mu)(P_\nu - \frac{P \cdot q}{q^2}q_\nu)]\frac{W_2(\nu, Q^2)}{M^2}, \quad (4.13)$$

and the anti-symmetry is:

$$\frac{1}{2M}W_{\mu\nu}^{(A)}(q; P, s) = \epsilon_{\mu\nu\alpha\beta}q^\alpha \{ M S^\beta G_1(\nu, Q^2) + [(P \cdot q)S^\beta - (S \cdot q)P^\beta]\frac{G_2(\nu, Q^2)}{M} \}, \quad (4.14)$$

Using the equations (4.9) and (4.12), the differential cross section can be rewritten as:

$$\frac{d^2\sigma}{d\Omega dE'} = \frac{\alpha^2}{2Mq^4} \frac{E'}{E} [L_{\mu\nu}^{(S)}W^{\mu\nu(S)} - L_{\mu\nu}^{(A)}W^{\mu\nu(A)}]. \quad (4.15)$$

It can be separately studied by considering the symmetry part $L_{\mu\nu}^{(S)}W_{\mu\nu}^{(S)}$ and the anti-symmetry part $L_{\mu\nu}^{(A)}W_{\mu\nu}^{(A)}$. The symmetry part is proportional to the unpolarized cross-section:

$$\begin{aligned} \frac{d^2\sigma^{unpol}}{d\Omega dE'}(k; P; k') &= 2\frac{\alpha^2}{2Mq^4} \frac{E'}{E} L_{\mu\nu}^{(S)}W_{\mu\nu}^{(S)} \\ &= \frac{4\alpha^2 E'^2}{q^4} [2W_1 \sin^2 \frac{\theta}{2} + W_2 \cos^2 \frac{\theta}{2}], \end{aligned} \quad (4.16)$$

where the $W_1(P \cdot q, Q^2)$ and $W_2(P \cdot q, Q^2)$ are the unpolarized structure functions. Note that the lepton mass is ignored. The anti-symmetry part can be extracted by using the differences of cross-sections with opposite target or beam spins:

$$\begin{aligned} &[\frac{d^2\sigma}{d\Omega dE'}(k, s, P, S; k') - \frac{d^2\sigma}{d\Omega dE'}(k, s, P, -S; k')] = \frac{\alpha^2}{2Mq^4} \frac{E'}{E} L_{\mu\nu}^{(A)}W_{\mu\nu}^{(A)} \\ &= \frac{8m\alpha^2 E'}{q^4 E} \{ [(q \cdot S)(q \cdot s) + Q^2(s \cdot S)]MG_1 + Q^2[(s \cdot S)(P \cdot q) - (q \cdot S)(P \cdot s)]\frac{G_2}{M} \}, \end{aligned} \quad (4.17)$$

where the $G_1(P \cdot q, Q^2)$ and $G_2(P \cdot q, Q^2)$ are two polarized structure functions. For the longitudinally polarized case, the spin of the initial lepton is along with or opposite to the nucleon polarization. One obtains:

$$\Delta\sigma_{||} = \frac{d^2\sigma^{\Rightarrow}}{d\Omega dE'} - \frac{d^2\sigma^{\Leftarrow}}{d\Omega dE'} = -\frac{4\alpha^2}{Q^2} \frac{E'}{E} [(E + E' \cos\theta) MG_1 - Q^2 G_2]. \quad (4.18)$$

For the transversely polarized case, the nucleon spin is perpendicular to the spin direction of the incoming lepton, and the azimuthal angle between the scattering plane (the plane between the incoming and outgoing lepton direction) and the polarization plane (the plane between the incoming lepton direction and the target polarization direction) is 0, one obtains:

$$\Delta\sigma_{\perp} = \frac{d^2\sigma^{\rightarrow\uparrow}}{d\Omega dE'} - \frac{d^2\sigma^{\rightarrow\downarrow}}{d\Omega dE'} = -\frac{4\alpha^2}{Q^2} \frac{E'^2}{E} \sin\theta [MG_1 + 2EG_2]. \quad (4.19)$$

In the deep inelastic region, with the Bjorken limit of:

$$Q^2 \rightarrow \infty, \nu \rightarrow \infty, \text{ and } x \text{ fixed}, \quad (4.20)$$

the structure functions W_1, W_2, G_1, G_2 are known to approximately scale [29]:

$$\lim_{Bj} MW_1(P \cdot q, Q^2) = F_1(x), \quad (4.21)$$

$$\lim_{Bj} \nu W_2(P \cdot q, Q^2) = F_2(x), \quad (4.22)$$

$$\lim_{Bj} \frac{(P \cdot q)^2}{\nu} G_1(P \cdot q, Q^2) = g_1(x), \quad (4.23)$$

$$\lim_{Bj} \nu (P \cdot q) G_2(P \cdot q, Q^2) = g_2(x), \quad (4.24)$$

where $F_{1,2}$ and $g_{1,2}$ vary very slow with Q^2 at fixed x , which means in the Bjorken limit the $F_{1,2}$ and $g_{1,2}$ are only the function of x . From the naive quark-parton model, the energy of the virtual photon is totally absorbed by the quark when x is equal to the momentum of the quark-parton, which is definitely independent with Q^2 . The experiments also confirmed that they are independent with Q^2 in a large x range. But later on people found that the Bjorken scale will be failed in the region of smaller x value [120], which needs to consider the gluon contribution using the QCD correction. The structure function $F_{1,2}$ and $g_{1,2}$ are then extended to $F_{1,2}(x, Q^2)$ and $g_{1,2}(x, Q^2)$:

$$g_1(x, Q^2) = M^2 \nu G_1(\nu, Q^2), \quad (4.25)$$

$$g_2(x, Q^2) = M \nu^2 G_2(\nu, Q^2), \quad (4.26)$$

$$F_1(x, Q^2) = MW_1(\nu, Q^2), \quad (4.27)$$

$$F_2(x, Q^2) = \nu W_2(\nu, Q^2). \quad (4.28)$$

The equations (4.16), (4.18), (4.19) are then expressed as:

$$d\sigma_{unpol} = \frac{d^2\sigma_{unpol}}{d\Omega dE'} = (\frac{d\sigma}{d\Omega})_{Mott} [\frac{2}{M}F_1(x, Q^2)\tan^2\frac{\theta}{2} + \frac{1}{\nu}F_2(x, Q^2)], \quad (4.29)$$

$$(\frac{d\sigma}{d\Omega})_{Mott} = \frac{\alpha^2 \cos^2 \frac{\theta}{2}}{4E^2 \sin^4 \frac{\theta}{2}}, \quad (4.30)$$

$$\Delta\sigma_{||} = -\frac{4\alpha^2 E'}{MQ^2 E \nu} [(E + E' \cos\theta)g_1(x, Q^2) - 2Mxg_2(x, Q^2)], \quad (4.31)$$

$$\Delta\sigma_{\perp} = -\frac{4\alpha^2 E'^2}{MQ^2 E \nu} \sin\theta [g_1(x, Q^2) + \frac{2E}{\nu} g_2(x, Q^2)], \quad (4.32)$$

where $(\frac{d\sigma}{d\Omega})_{Mott}$ is the Mott cross section, which describes the cross section when assuming the nucleon is a point-like particle.

Sometimes it is more convenient to measure the asymmetries than the cross sections in order to avoid some system error, which are ratios of the cross section difference to the unpolarized cross section. The longitudinal asymmetry $A_{||}$ and the transverse asymmetry A_{\perp} are expressed as:

$$A_{||} = \frac{\Delta\sigma_{||}}{2d\sigma_{unpol}}, \quad (4.33)$$

$$A_{\perp} = \frac{\Delta\sigma_{\perp}}{2d\sigma_{unpol}}. \quad (4.34)$$

4.4 Virtual photoabsorption cross section

Considering the inelastic scattering of polarized electrons off polarized target nucleons, the differential cross section can be expressed with the virtual photon absorption cross section. In the deep-inelastic region, it is a process that the quark absorb the virtual photon, as shown in figure 4.4. We denote the longitudinal polarization of the incoming electrons as $h = \pm 1$, and two polarization component of the target polarization as P_z and P_x . P_z and P_x are parallel and perpendicular to the lab momentum of the virtual photon, respectively. The differential cross section for the absorption of the virtual photon can be express in terms of a virtual photon flux factor Γ_v and four partial cross sections [41, 121]:

$$\frac{d\sigma}{d\Omega dE'} = \Gamma_v \sigma(\nu, Q^2), \quad (4.35)$$

$$\sigma = \sigma_T + \epsilon \sigma_L + hP_x \sqrt{2\epsilon(1-\epsilon)} \sigma'_{LT} + hP_z \sqrt{1-\epsilon^2} \sigma'_{TT}. \quad (4.36)$$

where the flux factor:

$$\Gamma_v = \frac{\alpha}{2\pi} \frac{E'}{E} \frac{K}{Q^2} \frac{1}{1-\epsilon}, \quad (4.37)$$

and its transverse polarization ϵ :

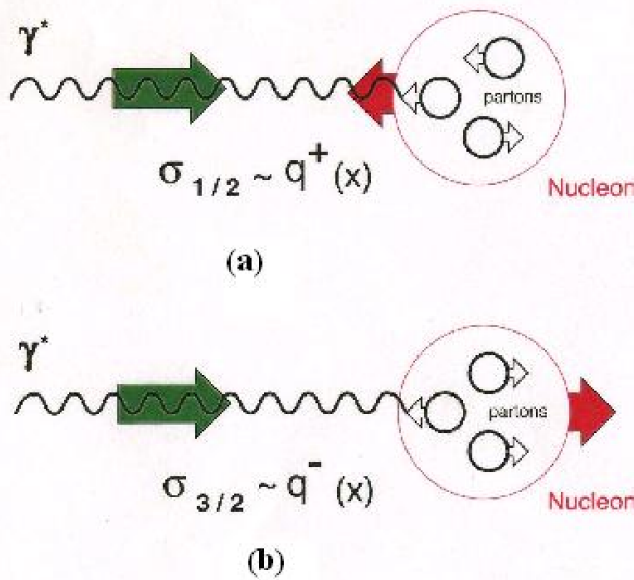


Figure 4.4 The interaction between the virtual photon and the polarized nucleon [23].

$$\epsilon = \frac{1}{1 + 2(1 + \frac{\nu^2}{Q^2}) \tan^2(\frac{\theta}{2})}. \quad (4.38)$$

The “equivalent photon energy” K is the laboratory photon energy producing a final state of total center-of-mass energy E upon absorption by a proton at rest defined by Hand [122]:

$$K = \nu(1 - x) = \frac{(W^2 - M^2)}{2M}. \quad (4.39)$$

The σ_T and σ_L are for the unpolarized experiment, while the σ'_{LT} and the σ'_{TT} are for the double polarization experiment. The σ_T and σ'_{TT} can be expressed in terms of the helicity cross sections $\sigma_{3/2}$ and $\sigma_{1/2}$, which are corresponded to excitation of intermediate states with spin $\frac{3}{2}$ and $\frac{1}{2}$, respectively:

$$\sigma_T = \frac{1}{2}(\sigma_{3/2} + \sigma_{1/2}), \quad (4.40)$$

$$\sigma'_{TT} = \frac{1}{2}(\sigma_{3/2} - \sigma_{1/2}). \quad (4.41)$$

The four virtual photoabsorption cross sections are related to the structure functions $F_{1,2}$ and $g_{1,2}$, which depend on ν and Q^2 :

$$\sigma_T = \frac{4\pi^2\alpha}{MK} F_1, \quad (4.42)$$

$$\sigma_L = \frac{4\pi^2\alpha}{K} \left(\frac{1+\gamma^2}{\gamma^2\nu} F_2 - \frac{1}{M} F_1 \right), \quad (4.43)$$

$$\sigma_{TT} = \frac{4\pi^2\alpha}{MK} (g_1 - \gamma^2 g_2), \quad (4.44)$$

$$\sigma_{LT} = \frac{4\pi^2\alpha}{MK} \gamma(g_1 + g_2). \quad (4.45)$$

The virtual Compton scattering asymmetries, A_1 and A_2 , are defined by the helicity dependent virtual photon-nucleon scattering cross sections [123, 124]. For spin $\frac{1}{2}$ targets (proton and neutron), the longitudinal asymmetry A_1 is expressed as:

$$A_1(x, Q^2) = \frac{\sigma_{1/2} - \sigma_{3/2}}{\sigma_{1/2} + \sigma_{3/2}}. \quad (4.46)$$

and the transverse asymmetry A_2 is expressed as:

$$A_2(x, Q^2) = \frac{2\sigma_{LT}}{\sigma_{1/2} + \sigma_{3/2}}. \quad (4.47)$$

It is customary to have the relationship between the virtual photon asymmetries and the structure functions:

$$A_1(x, Q^2) = \frac{\sigma_{TT}}{\sigma_T} = \frac{g_1(x, Q^2) - \gamma^2 g_2(x, Q^2)}{F_1}, \quad (4.48)$$

$$A_2(x, Q^2) = \frac{\sigma_{LT}}{\sigma_T} = \gamma \left(\frac{g_1(x, Q^2) + g_2(x, Q^2)}{F_1(x, Q^2)} \right), \quad (4.49)$$

where

$$\gamma = \frac{2Mx}{Q} = \frac{Q}{\nu}. \quad (4.50)$$

The asymmetries A_{\parallel} and A_{\perp} are expressed in terms of A_1 and A_2 following by equations (4.29, 4.31, 4.32):

$$A_{\parallel} = D(A_1 + \eta A_2), \quad (4.51)$$

$$A_{\perp} = d(A_2 - \xi A_1), \quad (4.52)$$

where

$$D = \frac{y[(1 + \frac{\gamma^2 y}{2})(2 - y) - \frac{2y^2 m^2}{Q^2}]}{y^2(1 - \frac{2m^2}{Q^2})(1 + \gamma^2) + 2(1 + R)(1 - y - \frac{\gamma^2 y^2}{4})}, \quad (4.53)$$

$$d = D \cdot \frac{[1 + \frac{\gamma^2 y}{2}(1 + \frac{2m^2 y}{Q^2})]\sqrt{1 - y - \frac{\gamma^2 y^2}{4}}}{(1 - \frac{y}{2})(1 + \frac{\gamma^2 y}{2}) - \frac{y^2 m^2}{Q^2}}, \quad (4.54)$$

$$\eta = \gamma \frac{[1 - y - y^2(\frac{\gamma^2}{4} + \frac{m^2}{Q^2})]}{(1 - \frac{y}{2})(1 + \frac{\gamma^2 y}{2}) - \frac{y^2 m^2}{Q^2}}, \quad (4.55)$$

$$\xi = \gamma \frac{1 - \frac{y}{2} - \frac{y^2 m^2}{Q^2}}{1 + \frac{\gamma^2 y}{2}(1 + \frac{2m^2 y}{Q^2})}, \quad (4.56)$$

where R is the ratio of the longitudinal and transverse cross section:

$$R = \frac{\sigma_L}{\sigma_T} = (1 + \gamma^2)\left(\frac{F_2}{2xF_1}\right) - 1. \quad (4.57)$$

When ignoring the mass of lepton with a small γ^2 , it becomes to [24]:

$$D = \frac{1 - E'\epsilon/E}{1 + \epsilon R}, \quad (4.58)$$

$$d = D \sqrt{\frac{2\epsilon}{1 + \epsilon}}, \quad (4.59)$$

$$\eta = \frac{\epsilon \sqrt{Q^2}}{(E - E'\epsilon)}, \quad (4.60)$$

$$\xi = \frac{\eta(1 + \epsilon)}{2\epsilon}. \quad (4.61)$$

The A_1 and A_2 can be extracted by measuring the longitudinal asymmetry $A_{||}$ and the transverse asymmetry A_{\perp} using the equation (4.33) and (4.34). The structure functions $g_{1,2}$ can then be extracted from the equation (4.48) and (4.49). With a series of measurement in different x and Q^2 , we can obtain the first moment of $\Gamma_1(Q^2)$ and $\Gamma_2(Q^2)$ with the structure functions $g_1(x, Q^2)$ and $g_2(x, Q^2)$. The A_{\perp} and g_2 are much smaller than $A_{||}$ and g_1 in the DIS region, thus the measurement needs more accuracy. In the high Q^2 region the term of g_2 is suppressed due to the factor of γ^2 , the equation (4.48) can be simplified as $A_1 = g_1/F_1$. Many experiments used this method to extract g_1 without measuring the transverse polarized cross section. But there is not enough reason to ignore the term of g_2 . For safety it is necessary to make a limit of it. There is a well-known condition established from the quark-parton model: $|A_2| \leq \sqrt{R}$. Later on people found that there exists a strong bound between A_1 and A_2 [125]:

$$|A_2| \leq \sqrt{R(1 + A_1)/2}. \quad (4.62)$$

Chapter 5

The E08-027 (g2p) Experiment

The E08-027 (g2p) experiment studied the spin structure function g_2 by measuring the cross section of the inclusive electron-proton scattering. The experiment successfully collected data from March to May, 2012 in Hall A at Jefferson Lab. This chapter will go through the experiment in detail.

5.1 Motivation

As discussed in the previous chapters, measurement of g_2 needs more precise data than g_1 . JLab has been at the forefront for measuring the nucleon spin structure over the wide kinematic range in the latest decades. With the high luminosity and high polarization electron beam and the high precision equipment in all of three Halls, JLab has been completed a number of precise experiments, which extended the data on spin structure significantly on both kinematic ranges and the precision. The data of g_2 for neutron has been collected precisely in both DIS and resonance region for neutron in the previous experiments, but the data for proton in the resonance region is still lacking. Comparing with the DIS region, studying in the resonance region can reveal more information on the internal structure of nucleon resonances and their excitation, which is important to check the related theory, such as the chiral perturbative theory and the lattice QCD.

In addition, the g_2 data can provide a test of the Burkhardt-Cottingham sum rule. Since the BC sum rule should apply at all values of $Q^2 > 0$, it can be tested by either at DIS region or at low Q^2 region. The data from the neutron shows agreement with the B-C sum rule, while the proton result from SLAC E155 shows large disagreement. Also a significant contribution to the g_2 integral comes from the nuclear resonance region. The precise g_2 data from low Q^2 is important to test the B-C sum rule.

A measurement of the longitudinal-transverse spin polarizability δ_{LT} is expected to be a good test for χPT . The resent neutron result shows significant disagreement with the χPT calculation. However, the δ_{LT} for the proton at low Q^2 does not exist yet.

The low Q^2 g_2 data will help to improve the precision in the hyperfine splitting of the hydrogen ground state, since the leading uncertainty in the measurement of the hyperfine splitting in the hydrogen ground state comes from the proton structure correction [126]. The data from this experiment may also help to improve the precision of the measurement for the proton charge radius.

5.2 Experiment Overview

The goal of the E08-027 experiment is to measure the g_2 structure function for the proton at low Q^2 . A measurement of the scattered electrons in the reaction $\vec{p}(\vec{e}, e')X$ at a

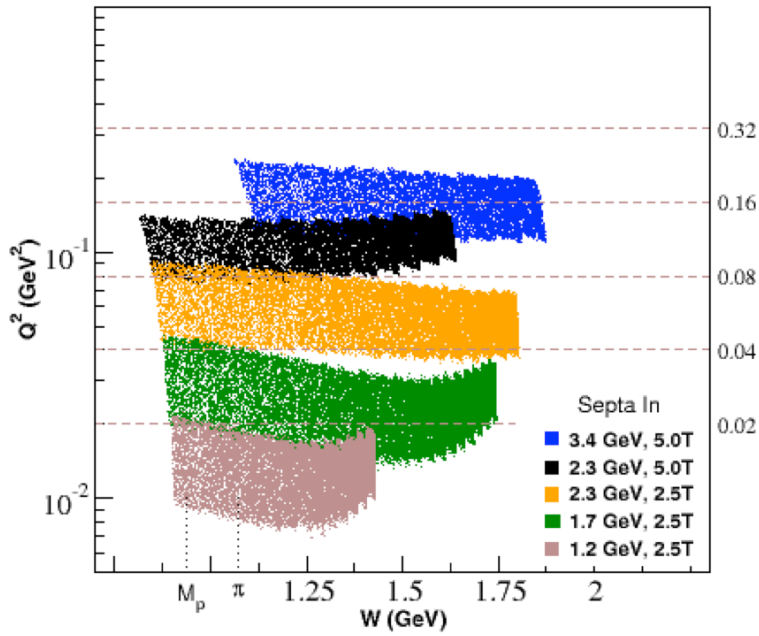


Figure 5.1 Kinematic coverage during the experimental run period. The numbers next to the vertical axis on the right side are the constant Q^2 values where the moments of the g_2 will be extracted.

scattering-angle of 5.69° in the low Q^2 region of $0.02 < Q^2 < 0.2 \text{ GeV}^2$ was performed to obtain the proton spin-dependent cross sections (see figure 5.1).

A polarized NH_3 target operating at 1 K was used as the proton target. The Dynamic Nuclear Polarization (DNP) process was used to polarize the solid NH_3 target. To avoid too much depolarization of the target, beam current was limited to $50 - 100 \text{ nA}$ during the experiment. New BPM and BCM receivers were designed and used for low current condition since the existing beam current monitors (BCMs), beam position monitors (BPMs) and calibration methods did not work at such a low current range. A pair of super-harps and a tungsten calorimeter were installed to calibrate the BPMs and BCMs, respectively. To compensate for the effect of the 2.5/5 T transverse target magnet field, two chicane dipole magnets were installed. A pair of slow rasters were installed for the first time in Hall A to spread the beam to a diameter of 2 cm, combining with a pair of fast rasters. To allow detection of scattered electrons at the scattering angle of 5.69° , the target was installed at 876.93 mm upstream from the pivot and a pair of septum magnets were installed. A new scintillator detector was developed and placed near the target to monitor the polarization of the beam and target. The schematic of experimental components is shown in figure 5.2.

The experiment measured the transversely polarized cross section difference $\Delta\sigma_\perp$ in 5 settings with different beam energy and target magnet field. Combining with the longitudinal polarized cross section difference $\Delta\sigma_\parallel$ from EG4 experiment, the g_2 is extracted as:

$$g_2 = \frac{1}{K_1 K_2} \left(\frac{\Delta\sigma_\perp}{K_3} - \frac{\Delta\sigma_\parallel}{K_4} \right), \quad (5.1)$$

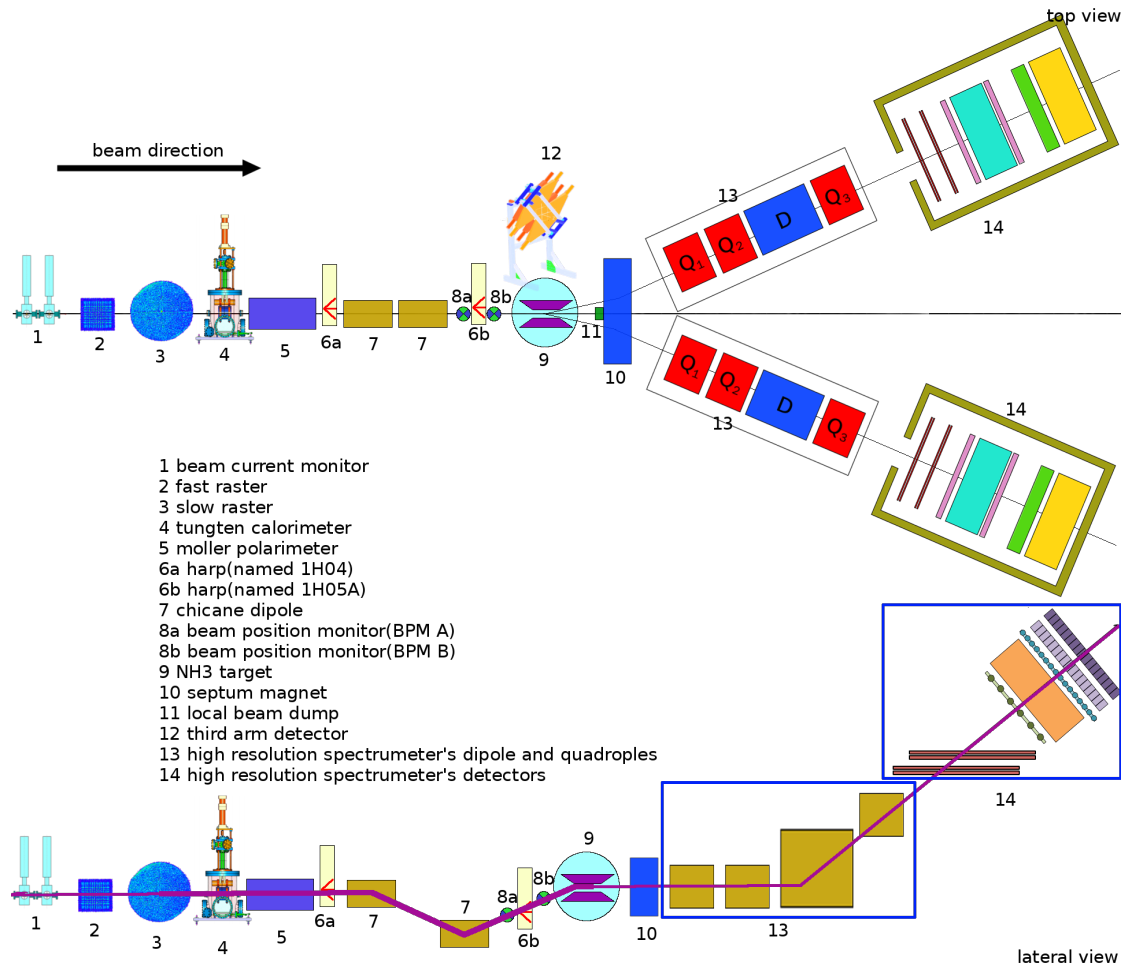


Figure 5.2 Schematic of components for g2p experiment

where

$$\begin{aligned}
 K_1 &= -\frac{4\alpha^2 E'}{MQ^2 E \nu}, \\
 K_2 &= \frac{2Mx}{E + E' \cos\theta} + \frac{2E}{\nu}, \\
 K_3 &= E' \sin\theta, \\
 K_4 &= E + E' \cos\theta,
 \end{aligned} \tag{5.2}$$

The experiment also measured the $\Delta\sigma_{||}$ in one beam energy setting with 5 T target magnet field for checking the results from EG4 experiment. Detail run summary is in appendix.

The projected results for the δ_{LT} and B-C sum rule are shown in figure 5.3. The data will provide benchmark tests of chiral perturbation theory calculations. In addition, the data will allow tests of the B-C sum rules and significantly impact ongoing calculations of the hydrogen hyperfine splitting.

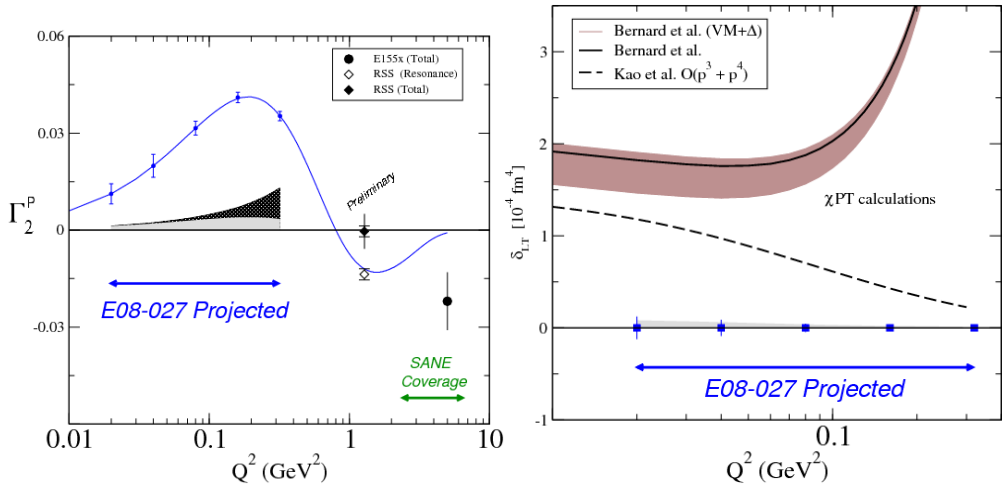


Figure 5.3 Projected uncertainties for Γ_2 (left) and δ_{LT} (right) for the E08-027 (g2p) experiment. The light and dark bands represent the experimental systematic, and the uncertainty arising from the unmeasured contributions to Γ_2 , respectively.

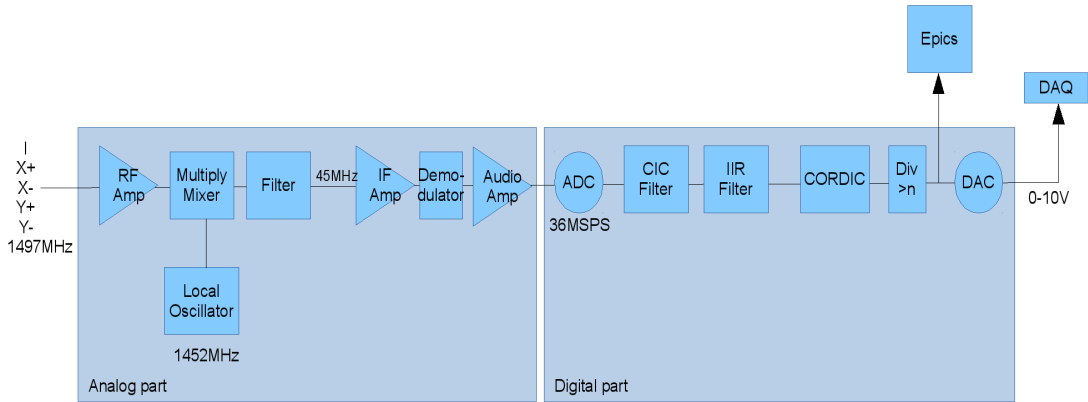


Figure 5.4 BPM and BCM receiver used for g2p experiment

5.3 The Beamline System

The beamline system for g2p experiment was rearranged for the special requirements of the NH_3 target. The 2.5/5T transverse target magnetic field bend down the beam. In order to offset this effect, two chicane dipole magnets were installed about 1 meter upstream of the target. Two beam position monitors (BPMs) were installed before the target in order to get the beam position and angle at the target. Two new super harps were installed for calibrating two BPMs. In addition to the fast raster system, a slow raster was installed for the first time in Hall A to minimize radiation damage to the target material. A tungsten calorimeter was installed for calibrating the beam current/charge monitor (BCM) in the low current environment. In order to get more accuracy beam position and beam charge, a new digital readout system was designed and built by the JLab instrumentation group [127]. A local beam dump was installed for the 5T target field settings which the beam was not going to the Hall A beam dump.

5.3.1 Beam Charge and Current

5.3.1.1 Beam Charge and Current Monitor (BCM)

The BCMs used for the g2p experiment are two RF cavities which are standard instrumentation during Hall A history. The whole BCM system in the beamline contains two RF cavities, an Unser monitor, and a BCM receiver with a data-acquisition system. The BCM cavities are located 23 m upstream of g2p target location, as the location shown in figure 5.2 (id.1). The two RF cavities were tuned to match the 1497 MHz beam frequency, resulting the output of the signal proportional to the beam current.

5.3.1.2 BCM and BPM receiver

Since the original RMS-to-DC converter [128] did not work in low current, a new BCM receiver and BPM receiver were designed by John Musson and his colleagues from JLab instrumentation group for the purpose of achieving enough signal/noise (S/N) ratio in the beam current environment from several nanoampere beam current to several microampere [127]. The design diagram is shown in figure 5.4.

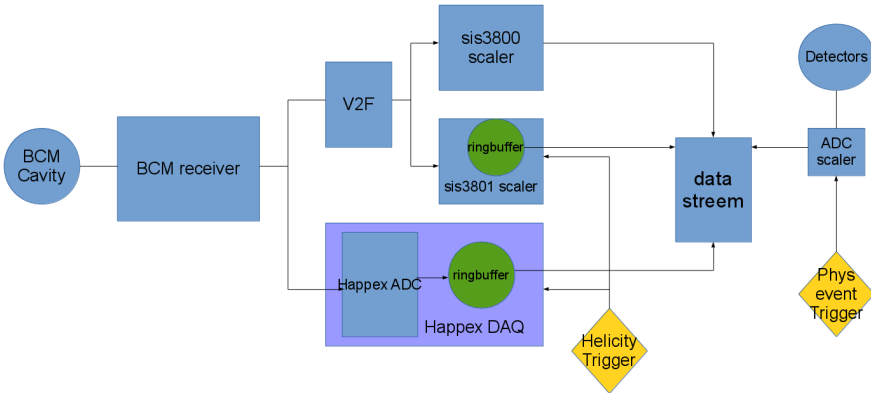


Figure 5.5 DAQ system for BCM

The receiver consists of analog part and digital part. The analog part converts the ratio frequency (RF) signal to the intermediate frequency (IF) signal and amplify it, while the digital part provides several digital filters to reduce the S/N ratio.

The RF wave from the beam is needed to convert to IF wave first for the suitable frequency for the next processing. The multiply mixer combines the 1497 MHz signal from beam and the sinusoidal 1452 MHz signal from a local oscillator, the equation can be simplified as:

$$\sin\theta\sin\phi = \frac{1}{2}\cos(\theta - \phi) - \frac{1}{2}\cos(\theta + \phi), \quad (5.3)$$

where θ and ϕ are the signals from beam and oscillator. Two signals with frequency of $\theta - \phi$ and $\theta + \phi$ are generated. The signal with frequency of $\theta + \phi$ is filtered by the filter after the mixer, only remain the $\theta - \phi = 45 \text{ MHz}$ signal.

The signal after two amplifier is digitized by a 36 MSPS ADC in order to apply two digital filters. The digital filter can achieve higher stop-band attenuation and faster transition, also more efficient than the analog one. For archiving enough S/N ratio and reaching enough resolution for the experiment, a 175Hz filter was used for the BPM receiver, which caused the BPM can only be used for getting average beam position. The filter was set to 10.4 kHz for the BCM receiver. The CORDIC system is used to calculate the amplitude and phase for the digital signal. The digital signal is converted back to 0~10 V analog signal to match the existed Hall A DAQ system. Since the signal is 20 bit, and the DAC is 18bit, the signal is needed to intercept before going to DAC. A div unit is used to do a bit shift and cut of the last several bits for the signal.

5.3.1.3 Data acquisition system for BCM

The BCM data from receiver was connected to the g2p data acquisition (DAQ) system as shown in figure 5.5. The output signal from receiver is a voltage analog signal, the V2F converts the voltage signal to the frequency signal in order to connect to scalers for counting. The HAPPEX ADC is an 18bit ADC with $875\mu\text{s}$ integration time which triggered by a 960 Hz helicity signal and expected higher resolution than scaler [129]. Both sis3801 scaler and HAPPEX ADC were triggered by helicity to get the helicity gated charge information, or the charge for each helicity status. The sis3800 scaler was

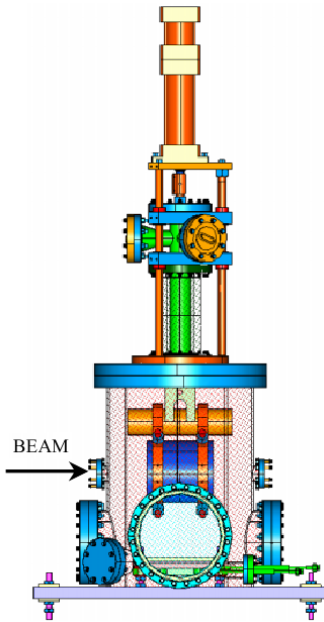


Figure 5.6 Tungsten Calorimeter

counting all of the time during a run for getting the total charge of the whole run. More details of the DAQ system are discussed in chapter [5.6](#).

5.3.1.4 Tungsten Calorimeter

The Unser monitor between two RF BCM cavities was used for double check the farady cup calibration result for the experiments ran in high current. The Unser in Hall A cannot work in the low current, and we cannot use the farady cup in the injector to calibrate our BCM since the beam loss can not be measured precisely in the low current. Therefore a tungsten calorimeter [\[130\]](#) was installed for calibrating our BCM by using the temperature arisen by the beam.

The tungsten calorimeter is shown in figure [5.6](#). The chamber hold the tungsten is pumped into vacuum to minimize heat loss. The tungsten is in three positions for the different purpose:

1. Beam charging. The tungsten is in the beam pipe, all the incoming beam electrons hit the tungsten. The temperature is arising during this period.
2. Equilibrating. The tungsten moves out the beam pipe but doesn't touch the cooling plate. The beam turns off. The temperature tend to stable. The measurement of the temperature is in this period.
3. Cooling. The tungsten moves to the cooling plate so that the tungsten can be cooled down.

For the temperature measurement, 6 thermometry devices (RTDs) are mounted on the outer surface at each end of the tungsten slug.

5.3.1.5 Calibrate the BCM

The calibration was taken for several times during the experiment for the different period. In order to get the uniform heat from beam in the tungsten surface, the rasters were turned on when taking the BCM calibration. The data acquisition system was busy working during the calibration to record the information from scaler and ADC. The scaler sis3801 and HAPPEX ADC data are helicity gated and saved in an array ringbuffer. The size of the ringbuffer is limited, when the ringbuffer is full, the front data will be overwritten and cause the data lost. For the dead-time consideration, the DAQ system only read 50 group data from ringbuffer for the maximum readout. An additional clock trigger with larger than 20 Hz ($\geq 960(\text{helicity frequency})/50$) was added to make sure there is no data lost in ringbuffer recorded in data-stream. Since the scaler and ADC have pedestal when there is no beam, the clock signal is needed for calculating the pedestal. For HAPPEX ADC since it is helicity triggered which is a periodic signal, the helicity entries is used for clock signal.

There are two type of clock signals, fast clock and slow clock. The frequency of the fast clock is ~ 103.7 kHz, while the frequency of the slow clock is ~ 1 kHz. The pedestal value is related the frequency of the clock signal, the calibration constants for using the slow clock and the fast clock are different.

A complete calibration period is shown in figure 5.7. The total temperature arise is used to calculate the total charge. The zero-order polynomial fits are taken before the beam charging and after the temperature become stable when tungsten in the equilibrating position. The temperature used is the average of the temperatures in 6 RTDs. The relationship between the total charge and the temperature arise is:

$$\text{Charge} = K \cdot \text{Temperature}, \quad (5.4)$$

where K is the heat capacity of tungsten, the value of it was measured by Ahamad Mahmoud before the experiment [131]. The value of K_{tungsten} he got is 8555.5 J/K , with at most 50 J/K uncertainty, as shown in figure . T is the average temperature from 6 RTDs.

There are several devices needed to be calibrated, each one has its own special condition. The detail calibration procedures for each device are as follows.

Calibration for sis3800 scaler

The sis3800 scaler is a VME implement. A reset signal was sent to the sis3800 scaler at the beginning of run to clean the counts. The HRS DAQ sampled the counts for each event. Since the scaler was found to cause high deadtime, only clock signals were sampled for each event, others were sampled for each 1000 events. Also the DAQ read the scaler once at the end of the run.

The third picture in the figure 5.7 is a calibration run for sis3800. The steep range is the period when the beam come, corresponding to the steep range in the first picture. To remove the pedestal from the scaler, the first-order polynomial fits are taken before and after beam. The pedestal value is defined as the slope from the fit. The total charge has the following relation with the counts:

$$\text{Charge} = \text{slope} \cdot (\Delta \text{counts} - \text{ped} \cdot \Delta \text{clockcounts}), \quad (5.5)$$

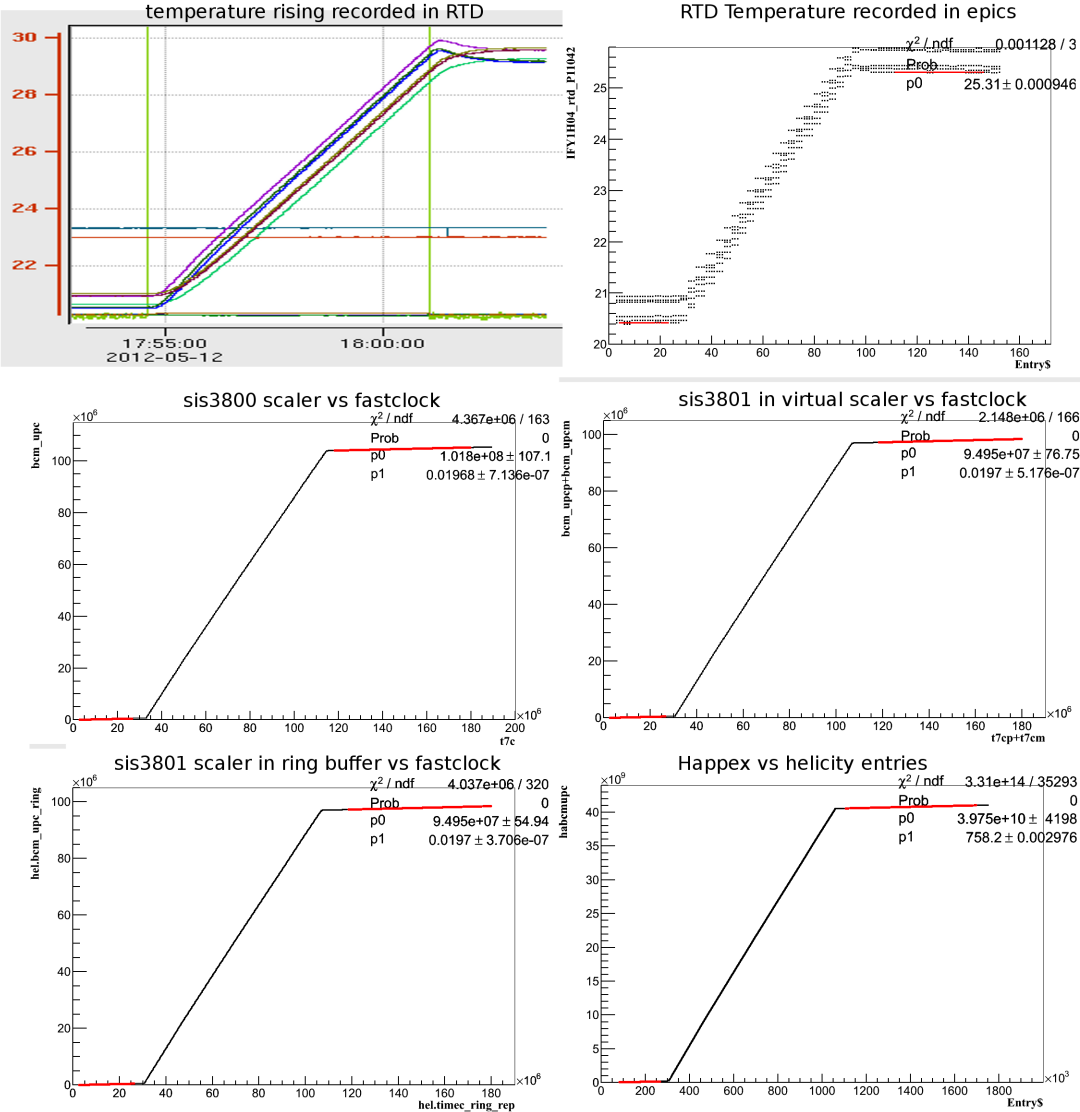


Figure 5.7 BCM Calibration, the first two pictures are the temperature arise for the RTDs, the last four pictures are the counts recorded in different devices at the same time.

where Δcounts is the total BCM counts accumulated in the scaler, $\Delta\text{clockcounts}$ is the total clock counts accumulated in the scaler. The *slope* and *ped* are two calibration constants which is calculated from calibration run. The *ped* is the pedestal value mentioned above. To get the *slope* value, two time points are chosen before and after the beam. Using the Δcounts and the $\Delta\text{clockcounts}$ between these two time points and combined with the charge calculated from the temperature, the *slope* value is then calculated.

Since the beam current is equal to Q/t , the calibration constants are used to calculate the beam current as below:

$$\text{Current} = \text{slope} \cdot (\text{rate} - \text{ped} \cdot \text{clockrate}), \quad (5.6)$$

where *rate* and *clockrate* are defined as the BCM counts and clock counts per second.

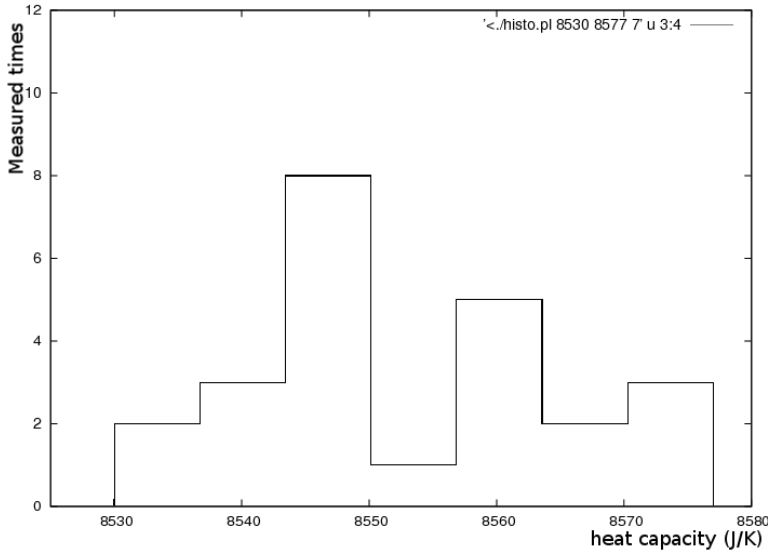


Figure 5.8 Tungsten calorimeter heat capacity determination

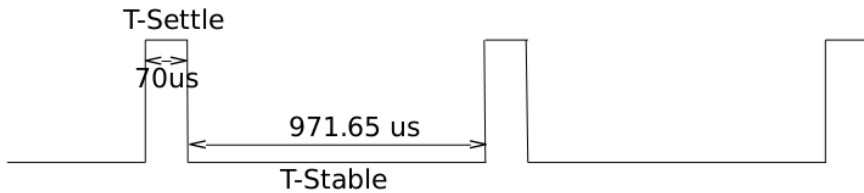


Figure 5.9 T-Settle signal from helicity control board, with $971.65 \mu s$ T-Stable time and $70\mu s$ T-Settle time.

Calibration for sis3801 scaler

A jumper in the sis3800 scaler is used to switch the scaler to sis3801 [132]. The sis3801 was controlled by the T-Settle signal which is one of the output from helicity control board [133] as shown in figure 5.9. The high-level T-Settle is $70 \mu s$ which indicates the helicity flips, or has unsure helicity status. The low-level T-Settle (or called T-Stable) means a stable helicity status. The rising edge of the T-Settle resets the scaler counts. The scaler stops counting during T-Settle, and recovers counting during T-Stable. The count for each helicity window was saved in a ringbuffer before merging to the standard DAQ system.

To calibrate the sis3801 scaler it is necessary to accumulate all of the counts for each helicity window, which needs no data lost. There are two methods to get the total counts. One is using the virtual scaler. The DAQ will automatically accumulate the total counts for positive helicity status and negative helicity status, which present two independent variables in the raw data, which named the virtual scaler. The total counts equal to the summary of the counts in the positive and negative scaler. Another is using the data from scaler ringbuffer, which is accumulating all of the counts from the ringbuffer, and using helicity decoder to check if data lost. The calculated calibration constants are same from two methods. The other procedures are the same as the sis3800. The total charge has the following relation with the counts:

$$Charge = slope \cdot (\Delta counts - ped \cdot \Delta clockcounts), \quad (5.7)$$

the $\Delta counts$ and $\Delta clockcounts$ are all from the sis3801 scaler. Since the sis3801 is not counting in $70 \mu s$ for each $1041.65 \mu s$, the slope calculated for sis3801 are larger than the slope for sis3800. The beam current is calculated by the following:

$$Current = Slope \cdot (rate - ped \cdot 103700/s \cdot 971.65\mu s)/1041.65\mu s, \quad (5.8)$$

where $103700/s$ is the frequency of the fast clock, $971.65 \mu s$ is the duration of T-Stable, $1041.65 \mu s$ is the duration of a helicity window.

Calibration for HAPPEX ADC

To calibrate the HAPPEX ADC, the values were accumulated for all of the events between two time points as the total counts. The entries in the HAPPEX DAQ was used as the time stamp since it is triggered by the periodic helicity signal. The total charge has the following relation with the counts:

$$Charge = slope \cdot 875\mu s \cdot (\Delta counts - ped \cdot \Delta entries), \quad (5.9)$$

where $875\mu s$ is the integration time of the ADC. The beam current is calculated by the following:

$$Current = slope \cdot (rate - ped) \cdot 875\mu s / 1041.65\mu s. \quad (5.10)$$

5.3.1.6 Uncertainty

The uncertainty of the calculated charge from the tungsten calorimeter came from the beam energy, RTD, measured tungsten heat capacity, and the heat loss. The accuracy of beam energy calculated from Arc measurement is 0.2MeV for range of 0.5 to 6 GeV [134], which contributes the uncertainty of calculated charge of 0.34 nC per 1K temperature rise (2.2GeV beam energy). The uncertainties of the RTDs are 12.5 mK [135], which contribute uncertainty of $0.046\text{ }\mu C$ (2.2GeV beam energy). The 50 J/K uncertainty of heat capacity contributes $0.18\text{ }\mu C$ per 1K temperature rise (2.2GeV beam energy). The Hall A calorimeter thermal and mechanical design limits heat losses to the $\sim 0.2\%$ level if the measurement within 20 min [130], which caused the uncertainty of calculated charge additional 0.2% . The total uncertainty is $\sim 0.68\%$ for the calculated charge from tungsten.

By comparing of the difference between upstream and downstream BCM, the fluctuations between upstream and downstream are below $0.19\text{ }\mu C$ for 90% runs. The relative differences between them for 90% runs are below 0.7% , as shown in figure 5.10. The differences indicate the uncertainty for the BCM is below 0.7% . Combining with the uncertainty of the tungsten calorimeter, the final uncertainty of BCM is below 1% .

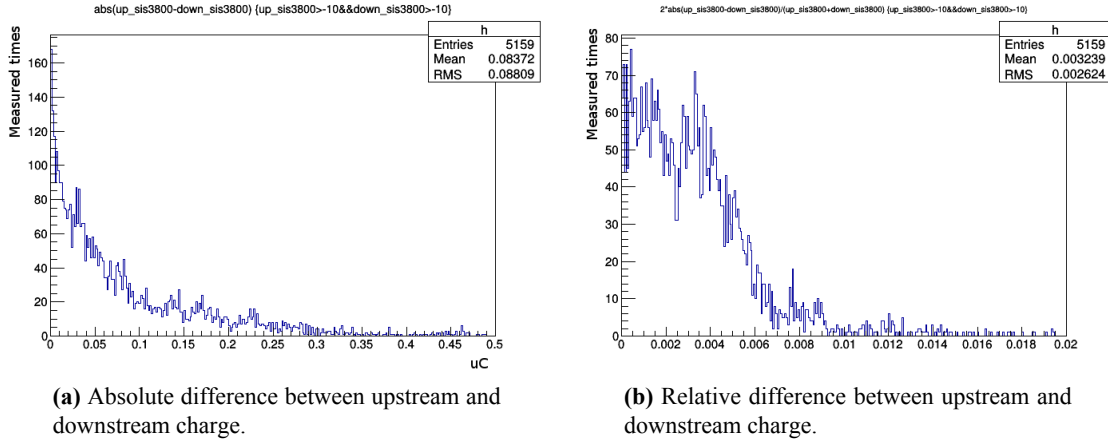


Figure 5.10 Comparing of the charge calculated from upstream and downstream. Each event in picture is the total charge calculated from one run from experiment.

#	date	polarization (%)	Syst.err.
1	03.03.2012	79.91 ± 0.20	$\pm 1.7\%$
2	03.30.2012	80.43 ± 0.46	$\pm 1.7\%$
3	03.30.2012	79.89 ± 0.58	$\pm 1.7\%$
4	04.10.2012	88.52 ± 0.30	$\pm 1.7\%$
5	04.23.2012	89.72 ± 0.29	$\pm 1.7\%$
6	05.04.2012	83.47 ± 0.57	$\pm 1.7\%$
7	05.04.2012	81.82 ± 0.59	$\pm 1.7\%$
8	05.04.2012	80.40 ± 0.45	$\pm 1.7\%$
9	05.15.2012	83.59 ± 0.31	$\pm 1.7\%$

Table 5.1 Summary of the Møller measurements for g2p experiment [136]

5.3.2 Beam polarization

The polarization of beam is measured by the Møller polarimeter which located in figure 5.2, id 5. The Hall A Møller polarimeter was built in 1997 [136] and was successfully used for many years. It uses the process of Møller scattering of $\vec{e}^- + \vec{e}^- = e^- + e^-$ with a ferromagnetic foil magnetized in a magnetic field of about 24 mT as a target of polarized electron [82]. The polarization of beam was extracted from measured asymmetry:

$$P_b = \frac{A_{measured}}{AnPow * P_t}, \quad (5.11)$$

where $AnPow$ is the analyzing power which depends on the beam position, P_t is the Møller target polarization. The measured asymmetry $A_{measured} = \frac{N_+ - N_-}{N_+ + N_-}$, which $+/-$ are the helicity status which the signal from helicity control board.

Nine measurements were taken during the experiment, as shown in table 5.1.

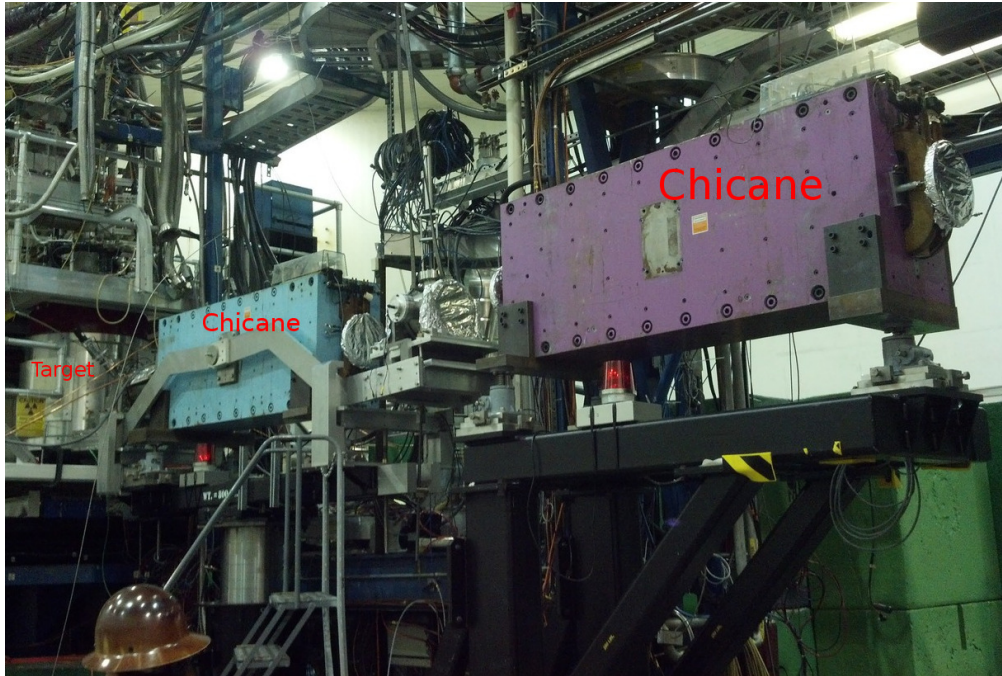


Figure 5.11 Chicane dipole magnet upstream of the target

5.3.3 Chicane dipole magnet

The transverse magnetic field in the target region would cause the beam deflected downward when the beam passes the target region. To compensate for this effect, two chicane magnets were placed in front of the target to pre-bend the beam upwards (figure 5.2, label 7). The first chicane magnet was installed 5.92 m upstream of the target which bend the beam down of the horizontal plane. The second chicane magnet, which was installed 2.66 m upstream of the target, bend the beam back to the target.

5.3.4 Beam Position and Angle

5.3.4.1 Beam Position Monitor

The BPM is designed to get the beam position information. There are several types of BPM using different methods. The cavity monitor uses the TM010 microwave in a resonant cavity to detect the beam current, and uses TM110 microwave to detect the beam position. The resolution of it can reach to $100 \mu\text{m}$ for 1 orbit/s measuring rate with 1 nA continuous wave beam [137], but it has a big frame that needs more than 1 meter space. The stripline BPM and antenna BPM used in Jefferson Lab contain 4 antennae placed symmetrically around the beam pipe. When beam passes through the BPM pipe, each antenna receives an induction signal. The both end of the output for each antenna in the stripline BPM are terminated by the same impedance, which only terminated in upstream end and kept open in downstream end in the antenna BPM [138]. The higher voltage sensitivity compared with the stripline BPM for open-ended antenna BPM was tested before experiment [139]. For the consideration of the test result and the limited space between the second chicane magnet and target (<1m), the open-ended antenna BPM was chosen for the experiment. The design diagram for the antenna BPM is shown in figure 5.12.

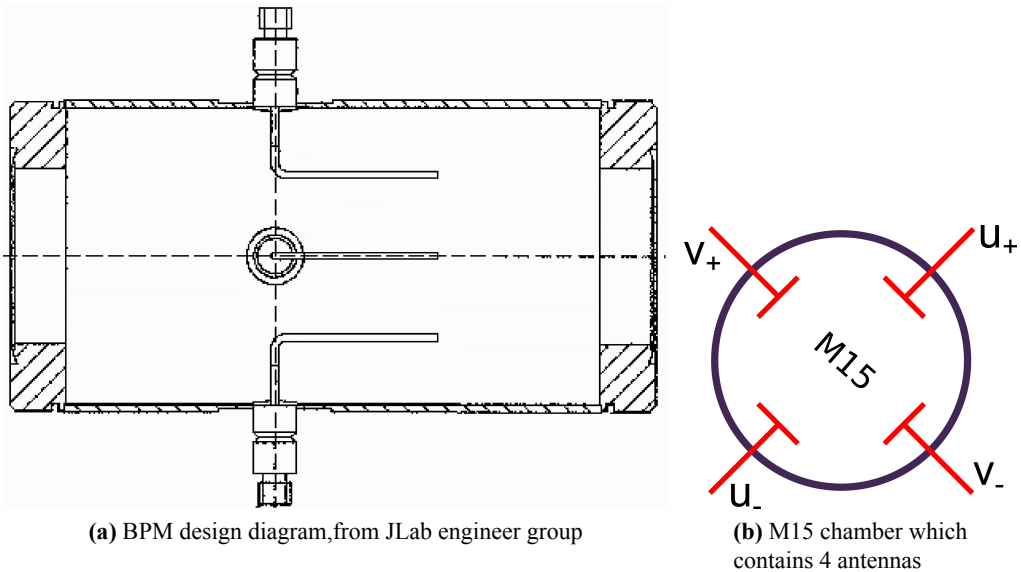


Figure 5.12 BPM Chamber

The BPM front-end receiver collects and sends the signal to the regular Hall A DAQ system and another DAQ system designed for parity violation experiments, the HAPPEX system. The new BPM receiver was designed by the JLab instrumentation group [127] in order to achieve the required precision at a level of 0.1 mm with a beam current as low as 50 nA. The regular DAQ system was connected to a 13-bit fastbus ADC (Lecroy ADC 1881) with an integration time of 50 ns, which was triggered by a scattered electron event. The HAPPEX system [129] was connected to an 18-bit ADC with an integration time of 875 μ s, which was triggered by a beam helicity signal at 1 kHz.

The BPM receiver generates a large time delay for the output signals. The digital filter used in the receiver contributes 1/175 s delay time, which was the inverse of the bandwidth setting chosen for the filter. There is a $\sim 4 \mu$ s delay as a result of finite processing times. The BPM cannot provide event by event position because of these time delays, due to the 25 kHz fast raster system.

Because of the space limitation on the beam-line, the two BPMs were placed very close to each other. One was placed 95.5 cm upstream of the target while the other was placed 69 cm upstream, making the distance between them only 26.5 cm. The short distance magnified the position uncertainty from the BPMs to target.

5.3.4.2 Super-Harp

The information achieved from BPM is relative since the BPM is a non-invasive device. A calibration is needed before using it. The harp is designed for doing this job.

Two super harps were designed and installed in the beam-line, as shown in figure 5.2 (label 6a - 1H04 and 6b - 1H05A), to provide an absolute measurement of the beam position for calibration of the BPMs. Because of the space limitation, only one harp (named 1H05A) was installed between the 2 BPMs. The other one was installed upstream of the first chicane magnet. For the space limit, the 1H05A harp was rotated 45° with respect to the beam pipe.

JLab's CEBAF can produce two types of beam, one is a continuous wave beam (CW) with 100% duty factor used for production runs, with high luminosity in excess of $10^{38} \text{ cm}^{-2} \text{s}^{-1}$ [82]. The other is a pulsed wave beam with 1% duty factor used for tuning the beam. For 50nA continuous wave beam (CW), harp scans were not reliable due to noisy signals. CW beam with higher current cannot be used due to the current limit of the target system. The harp used previously in Hall A was not suitable for either low current CW beam or high current pulsed beam, therefore the old harps were replaced by a new design. The new harps were able to work in pulsed beam with a current of several μA . A diagram for the harp is shown in figure 5.13, which consists of

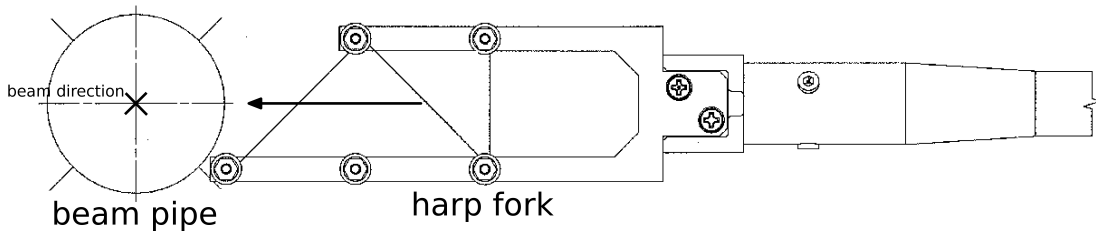


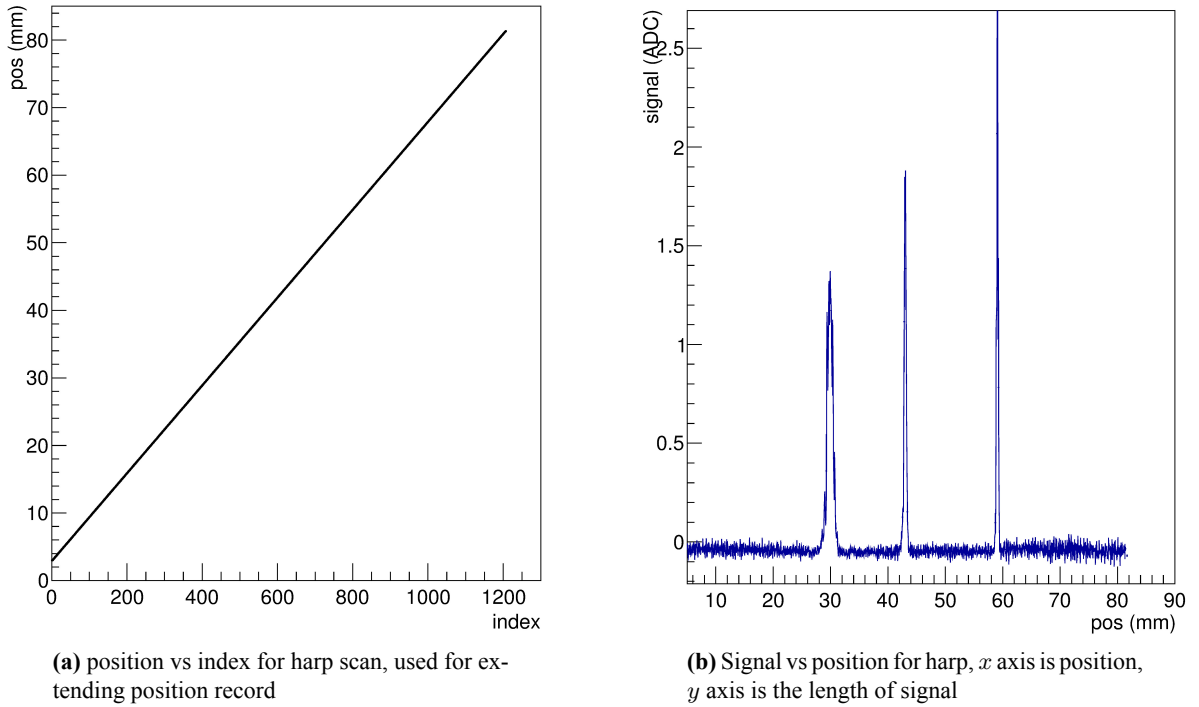
Figure 5.13 Harp diagram

three wires with a thickness of $50 \mu\text{m}$, a fork and a controller chassis. The harp chamber is perpendicular to the beam pipe and connected to the beam pipe as part of the vacuum chamber of the beamline. The two harps have different configurations of three wires: vertical(|), bank left(\), and bank right(/) for 1H04, and /, |, \ for 1H05. The angle of the / or \ wire is 45° relative to the wire dock frame. The wires are arranged in a fork (figure 5.13) controlled by a step motor [140] which can be moved in and out of the beam-line. The harps must be moved out of the beam-line when production data is being taken because they are invasive to the beam. The original position of the wires was surveyed before the experiment at a precision level of 0.1 mm. As the motor driver moved the fork through the beam, each wire received a signal, which was recorded for further analysis. The signals received from the wire and the step-counters from the motor driver were then sent to an amplifier and the DAQ. The amplification and the speed of the motor were adjustable for the purpose of optimizing the signals of each scan. Recorded data combined with the survey data was used to calculate the absolute beam position.

The signal from the | wire ($peak_{|}$) was used for getting the x position (x_{harp}) of the beam, and the signals from the /, \ wires ($peak_{/}$ and $peak_{\backslash}$) were used for getting the y position (y_{harp}):

$$\begin{aligned} x_{harp} &= survey_{|} - peak_{|} \\ y_{harp} &= \frac{1}{2}[(survey_{\backslash} - survey_{/}) - (peak_{\backslash} - peak_{/})] \end{aligned} \quad (5.12)$$

An example of a harp scan result is shown in figure 5.14. There are three groups of recorded data for each harp scan, which are “index”, “position”, and “signal”. The index is related to the moving steps of the fork during the scan. Each step of the index increases by 0.008-0.07 mm depending on the speed of the motor driver [140]. The position is the wire location for each index. The testing results show a good linear relation between the position and the index as shown in figure 5.14(a), because the motor speed is uniform.

**Figure 5.14** 1H05A harp scan data

The line is the fitted result with $pos = a * index + b$. According to this linear relation, interpolation or extrapolation can be applied when a few data points are missing, in some cases. The strength of signal vs. position is plotted in figure 5.14(b). Each peak represents the location when one of the three wires passed through the beam.

The positions measured by the two harps were used for calibrating the beam positions in the two BPMs. When the chicane magnets were on, beam did not pass straight through from the first harp to the second harp. BPM calibrations using two harps were only possible when the chicane magnets were off, i.e. in the straight-through settings. Since the BPM was calibrated in the local coordinate system, the calibration constants were independent from the settings of other instruments. To make sure that the calibration constants for the BPMs were still valid during the non-straight-through settings, the settings for the BPM receiver were kept the same as in the straight-through settings during production running.

The scan data from the harps was not reliable when the current of CW beam (100% duty factor) was lower than 100 nA due to the low signal-to-noise ratio. The harp scans were taken in pulsed mode at a current of a few μ A, while the BPMs were used for production data taking in CW mode at a beam current of 50-100 nA. For a BPM calibration run, a harp scan was done first in pulsed mode, then a DAQ run was taken immediately to record the ADC value in CW mode without changing the beam position. The harp scan was then taken again in the pulsed mode to double check the beam position. The harp scan data was discarded and the scan was taken again if the beam position changed.

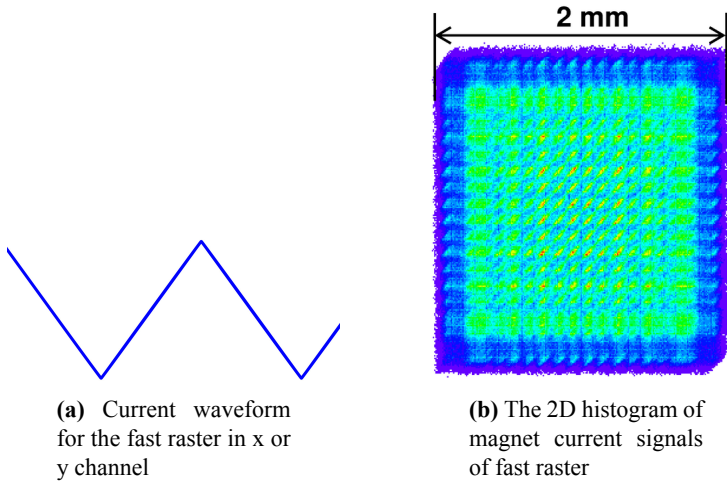


Figure 5.15 Fast raster pattern

5.3.4.3 Raster system

In order to minimize the depolarization, avoid damage to the target material from radiation, and reduce systematic error for the polarization measurement by NMR, two raster systems were installed at ~ 17 m upstream of the target, as shown in figure 5.2 (labels 2 and 3 for fast and slow rasters, respectively). Both the fast and slow rasters consist of two dipole magnets. The same triangular waveforms with frequency of 25 kHz were used to drive the magnet coils of the fast raster to move the beam in x and y directions, forming a rectangular pattern of $2\text{mm} \times 2\text{ mm}$, as shown in figure 5.15. The slow raster further spreads out the beam to a circle with a diameter of ~ 2 cm. When combined, the rastered beam has a diameter of ~ 2.2 cm, spread evenly over the most face of the 2.5 cm diameter target.

A dual-channel function-generator* was used to generate two independent waveforms to drive the magnet coils of the slow raster. The waveforms for the x and y directions are:

$$\begin{aligned} x &= A_x t^{1/2} \sin(\omega t), \\ y &= A_y (t + t_0)^{1/2} \sin(\omega t + \phi), \end{aligned} \quad (5.13)$$

where the A_x and A_y are the maximum amplitude, t_0 and ϕ are the AM and sin phase difference between x and y waveform, respectively. Both of them are sine functions modulated by a function $t^{1/2}$ in order to generate a uniform circular pattern [141], as shown in figure 5.16. The frequencies of the x and y waveforms kept same: $\omega = 99.412$ Hz. In order to cycle the amplitude modulation (AM) function, four piece-wise functions are combined together. The first term is $t^{1/2}$, and the second term is $\text{period} - t^{1/2}$, and so on for the third and fourth terms. The cycled function has the frequency of 30 Hz.

The ϕ was locked to $\frac{\pi}{2}$ by the function generator, while the t_0 was manually fixed

*agilent 33522A function generator, <http://www.home.agilent.com/en/pd-1871286-pn-33522A/function-arbitrary-waveform-generator-30-mhz>

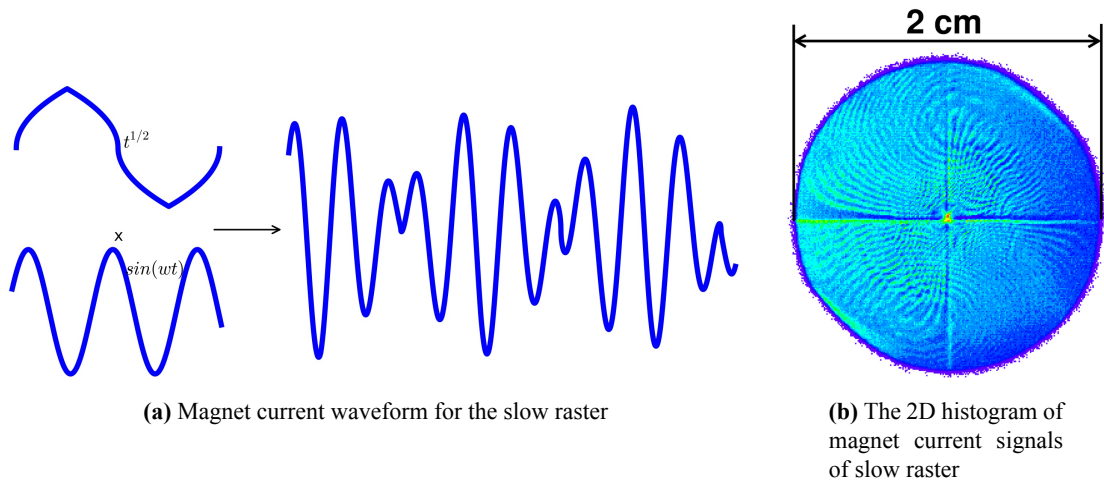


Figure 5.16 Slow raster pattern

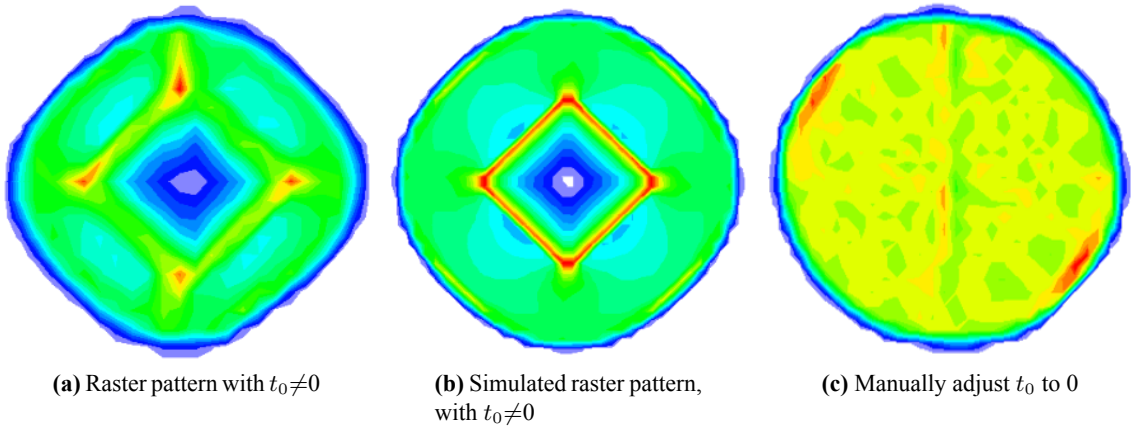


Figure 5.17 None-zero t_0 caused slow raster non-uniformity, (a) and (c) are from the data recorded in the ADC, (b) is simulated. The color palette shows the uniformity of the raster pattern.

to 0. Non-zero t_0 could cause a non-uniformity pattern, as shown in figure 5.17(a), which would cause non-uniformity beam distribution. A simulation was reproduced the non-uniformity by setting the t_0 to non-zero, as shown in figure 5.17(b). The t_0 was carefully adjusted and minimized before production data taking to avoid the non-uniformity. The pattern of the spread beam was relatively uniform after this adjustment during the experiment, as shown in figure 5.17(c).

5.3.4.4 BPM Calibration Coordinate System

There are three coordinate systems used for BPM calibration: Hall A coordinate system, BPM rotated coordinate system, BPM/Harp local coordinate system. The relation of them is shown in figure

The Hall coordinate is the global coordinate system in the hall, with the origin of the NH_3 target.

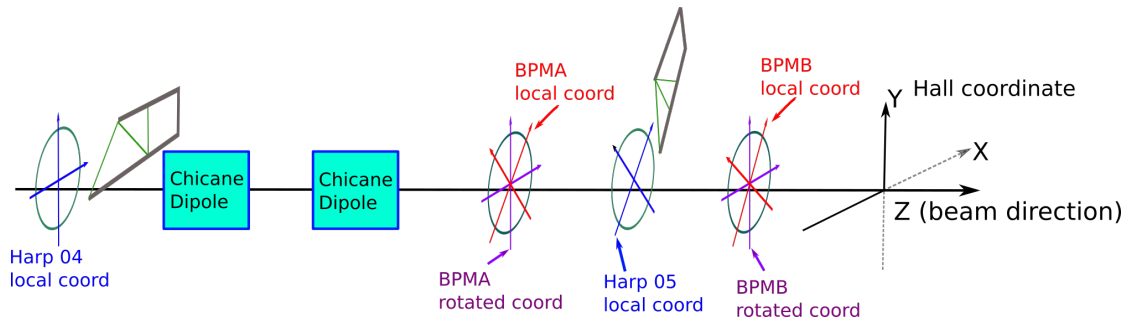


Figure 5.18 Coordinate system used for the BPM calibration

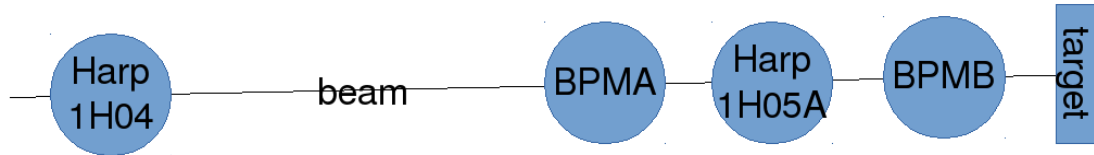


Figure 5.19 Position for 2 BPMs and 2 Harps

The origin of each local coordinate system is the surveyed location for each device. The angular components of survey data decide the orientation of each local coordinate system. The rotation between the BPMA local coordinate and the Hall coordinate is about 45° , while it is about 57° between the BPMB local coordinate and the Hall coordinate. To avoid confusion, the directions use u and v instead of x and y .

The harp scan data analysis was taken in the harp local coordinate. The calculated positions from two harps were transferred to the BPM local coordinate in order to calibrate the BPMs.

The BPM calibration was taken in the BPM local coordinate. In the straight through setting without the target magnet field, the positions calculated from the BPMs were transferred to the Hall coordinate in order to transport to the target location. For the settings with a transverse magnetic field, the input terms of the transport functions are the positions in the BPM rotated coordinate, which has the same origin with the BPM local coordinate but with the same directions with the Hall coordinate.

5.3.4.5 BPM Calibration

Transport the Absolute Beam Position from Harps to BPMs

The position calculated from equation 5.12 is the position in the harp local coordinate system. It is necessary to convert it to Hall coordinate system first and transport the position to the two BPMs. When the chicane magnet field is off, the absolute beam position at BPM can be linear transported from the harp.

During the experiment the BPM B receiver was not very stable, the receiver was replaced by another one during 4/26 and 5/3. The alternate receiver used a different gain setting, so calibrations for BPM B is not available for these runs. To determine the calibration for BPM B for these runs, the calibrated BPM A information is combined with the 1H05A harp data to get the absolute beam position at BPM B by using the linear transport method.

Get beam position from BPMs

The traditional difference-over-sum (Δ/Σ) method of calculating the beam position has the non-linearity effect at the position far away from the center of the beam pipe [138]. It is necessary to correct the equation of Δ/Σ since we have a slow raster with a large size of ~ 2 cm. With the assumption of an infinitely long chamber and neglecting the antenna influence on the electric field inside the chamber, the signal from each antenna excited by the beam can be calculated via image charge method (figure 5.20) [142, 143] :

$$\phi_i = \phi_0 I \frac{R^2 - \rho^2}{R^2 + \rho^2 - 2R\rho\cos(\theta_i - \theta_0)}, \quad (5.14)$$

where ϕ_i is the signal received in the antenna, and i is u_+ , u_- , v_+ and v_- , respectively, ϕ_0 is a constant related to the geometry of the BPM-chamber and the output resistance, I is the beam current, R is the radius of the BPM vacuum chamber, ρ is the radial position of the beam, and $\theta_i - \theta_0$ is the angle difference between the antenna and the beam in the polar coordinate .

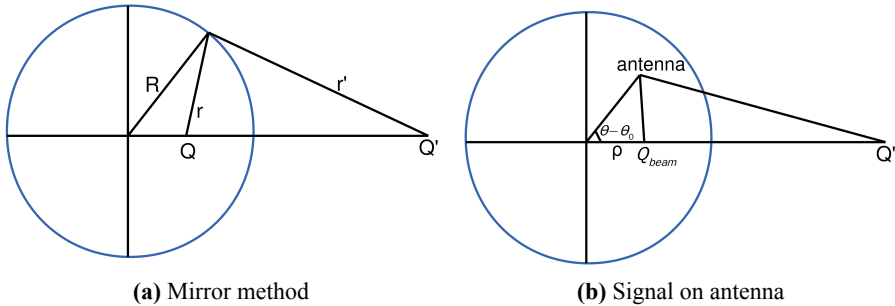


Figure 5.20 Signal for each antenna of BPM

The four antennas in the BPM chamber are used to determine the beam positions u and v in the BPM; u_+ and u_- for the u position, and v_+ and v_- for the v position. In order to extract the beam position information, and eliminate the dependence on the beam current in equation (5.14), the Δ/Σ method is used as follows:

$$D_U = \frac{\phi_{U+} - \phi_{U-}}{\phi_{U+} + \phi_{U-}}, \quad (5.15)$$

where U denotes u and v . Substituting equation (5.14) into equation (5.15), it can be rewritten as follows:

$$D_U = \frac{\phi_{U+} - \phi_{U-}}{\phi_{U+} + \phi_{U-}} = \frac{2}{R} \frac{\rho\cos(\theta - \theta_0)}{1 + \frac{\rho^2}{R^2}} = \frac{2}{R} \frac{U}{1 + \frac{\rho^2}{R^2}}, \quad (5.16)$$

where $\rho^2 = u^2 + v^2$. When $u^2 + v^2 \ll R^2$, equation (5.16) is simplified as:

$$U \approx \frac{R}{2} D_U = \frac{R}{2} \frac{\phi_{U+} - \phi_{U-}}{\phi_{U+} + \phi_{U-}}. \quad (5.17)$$

Equation (5.17) can be used in the simple case when the beam is near the center of the

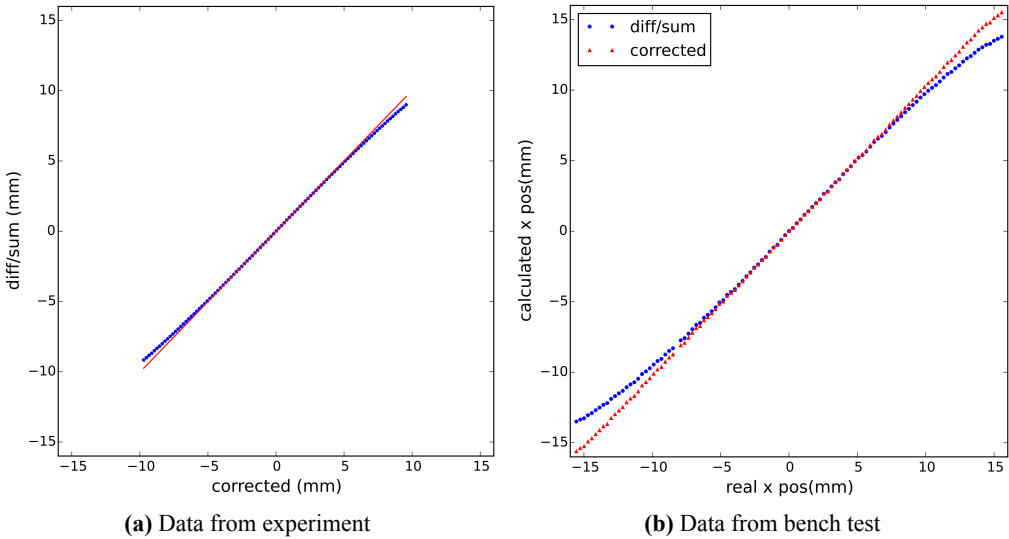


Figure 5.21 BPM non-linearity correction. (a) Comparison between the position calculated from Δ/Σ equation (5.17) (y axis) and the one from correction equation (5.18) (x axis). Red solid line is a reference line came from linear fit of the center points. Data is collected from the experiment. (b) Comparison between the Δ/Σ equation (5.17) and the correction equation (5.18) using the bench test data. The x axis is the real beam position. The red triangles are the positions calculated from correction equation (5.18). The blue circles are the positions calculated from Δ/Σ equation (5.17) .

beam pipe. When the beam is far from the center, equation (5.17) is no longer valid. For the g2p experiment, the beam was rastered to have a diameter of about 2 cm at the target. From equation (5.16) the beam position is calculated as:

$$U = RD_U \left(\frac{1}{D_u^2 + D_v^2} - \frac{1}{\sqrt{D_u^2 + D_v^2}} \sqrt{\frac{1}{D_u^2 + D_v^2} - 1} \right). \quad (5.18)$$

The correction equation is tested by using the experiment data and the bench test data. figure 5.21(a) shows the comparison between the position calculated from the correction equation (5.18) and the one from the Δ/Σ equation (5.17). The red solid line is a reference line came from linear fit of the center points. figure 5.21(b) shows the comparison with the real beam position from the bench test data. In this way the method using equation (5.18) can correct the non-linearity effect caused by the Δ/Σ method. The handling of the BPM information which only used for the center beam position also reduced this non-linearity effect.

The final information recorded in the data-stream was designed to have a linear response with the raw signal in the 50-100nA current range. The amplitude, A_i , recorded in the ADC has the following relation with the BPM signal, ϕ :

$$A_i \propto \phi_i * 10^{\frac{g_i}{20}}, \quad (5.19)$$

where g_i is the total gain for the BPM readout electronics. The ϕ_i in equation (5.16) can be rewritten as

$$\phi_i = a_i(A_i - A_{i_ped} + b_i), \quad (5.20)$$

where A_i and A_{i_ped} are the recorded ADC value and pedestal value, and a_i and b_i are the slope and intercept of the relationship between ϕ_i and $A_i - A_{i_ped}$. Equation (5.17) can be rewritten as:

$$D_U = \frac{(A_{U+} - A_{U+_ped} + b_{U+}) - h_U(A_{U-} - A_{U-_ped} + b_{U-})}{(A_{U+} - A_{U+_ped} + b_{U+}) + h_U(A_{U-} - A_{U-_ped} + b_{U-})}, \quad (5.21)$$

where $h_x = a_{x-}/a_{x+}$, and is related to the ratio of the signals for the x_+ and x_- antennas and the gain settings of the two channels. Similarly, $h_y = a_{y-}/a_{y+}$.

Combining the equations (5.20) and (5.14), the calibration constant b_i was obtained by taking the linear fit between the ADC values of BPM and the beam current:

$$I \propto (A_i - A_{i_ped} + b_i), \quad (5.22)$$

Besides, the linear fit used a group of runs which had the same beam position but different beam current. Figure 5.22 shows the $A_i - A_{i_ped}$ versus the beam current. It

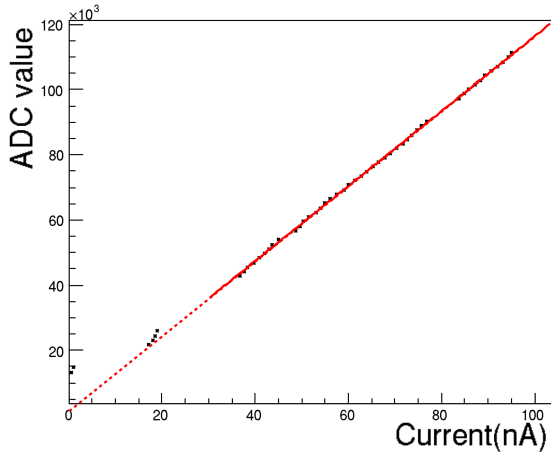


Figure 5.22 ADC value of BPM raw signal ($A - A_{ped}$) V.S. beam current

shows that the ADC values were linear with beam current in the considering current range of 50-100 nA. The intercept from the linear fit of figure 5.22 is the value b_i .

By transporting the position x_{harp} and y_{harp} in equation (5.12) from two harps to the BPM local coordinate u_{harp} and v_{harp} , a fit between the BPM data U and the harp data U_{harp} determined three calibration constants c_0 , c_1 and c_2 :

$$U_{harp} = U_c = c_0 + c_1 u + c_2 v, \quad (5.23)$$

where U_c is the calibrated BPM position. It was converted to Hall coordinate X_c for further transporting to the target location. An calibration example is shown in figure 5.23. The asterisks and the dots in figure 5.23 represent U_{harp} and U , respectively.

In order to reduce the noise and improve the resolution during data analysis, a software filter was applied. Since the 18 bit ADC was triggered by the helicity signal with a fixed frequency, it could be regarded as a sampling ADC. figure 5.24 shows the signal

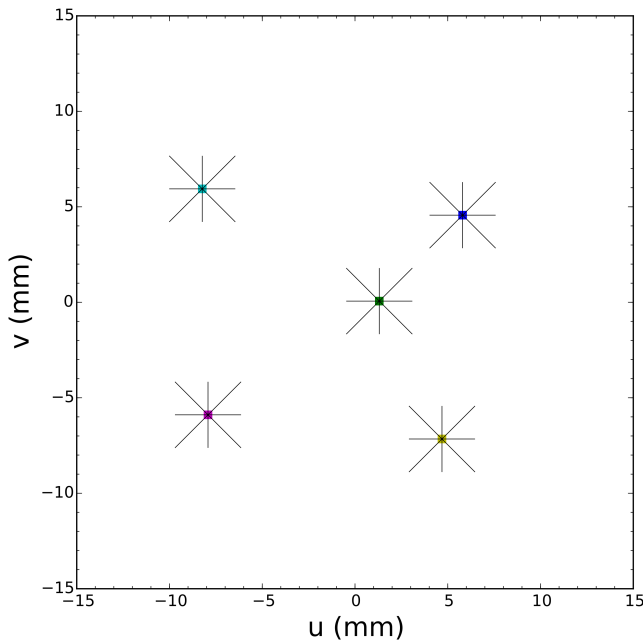


Figure 5.23 Harp scan data combined with BPM data, the asterisks are the positions from harp, while the dots are from BPM.

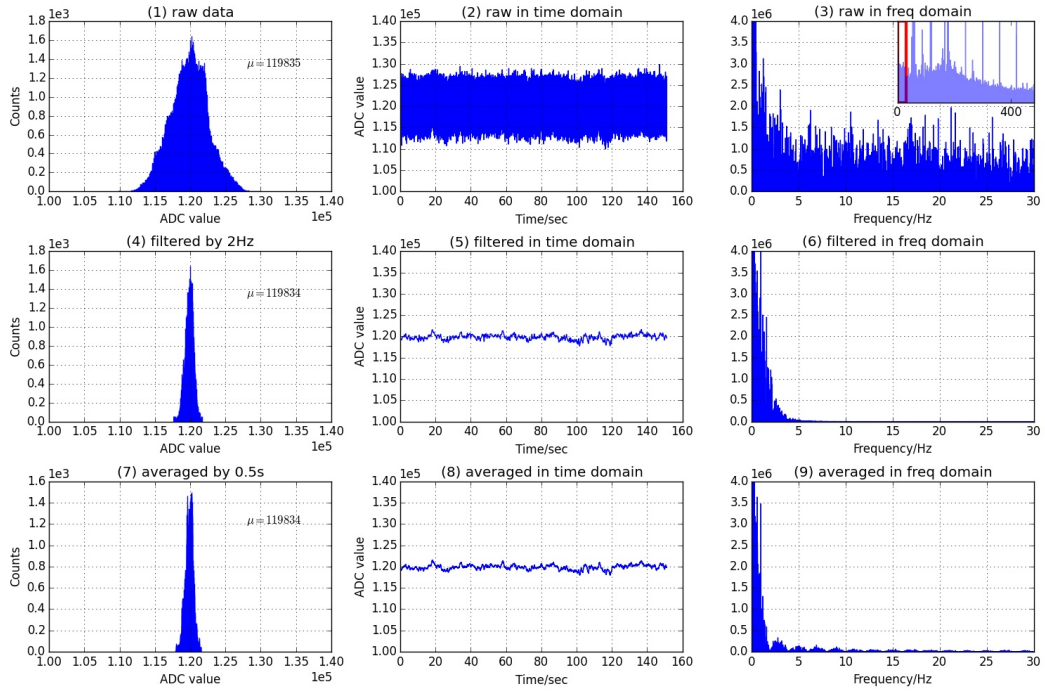
dealt with a 2 Hz low pass filter. Three plots at the bottom of figure 5.24 (a,b) are the averaged signal used for comparing with the filtered signal. The results show that the 2 Hz filter and the 0.5 s average are consistent within the required precision. The filter also erases the beam displacement caused by the rasters, which is necessary to extract the position of the beam center.

5.3.4.6 Beam position reconstruction at target

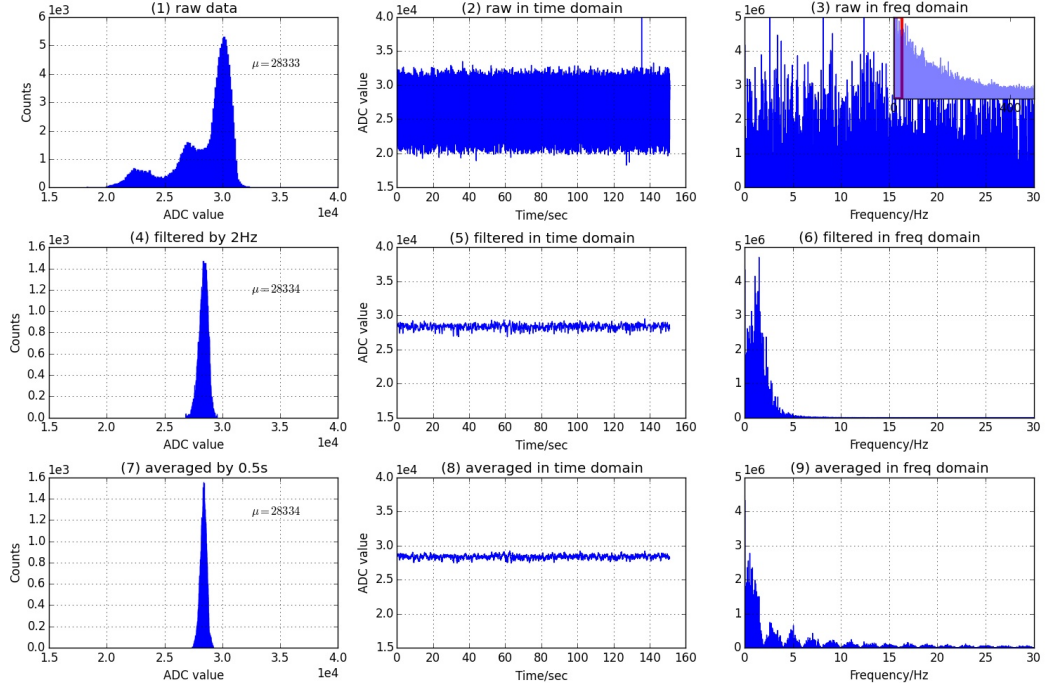
It is easy to transport the position from the BPMs to the target by using a linear transportation method for the straight through setting. For the settings with a transverse magnetic field at the target, the linear transportation method cannot be used since the beam is bent near the target. A simulation package was constructed to simulate the behavior of the beam. Polynomial curve fittings were used for simulated data to generate the transport functions in order to transport the beam from the two BPMs to the target (figure 5.25).

A target magnet field map [144] was generated from the TOSCA model. To test the accuracy of the TOSCA model, the target magnet field was measured before the experiment [145, 146]. The generated field map was used in the simulation. An event generator generated thousands of electrons with different initial positions and angles, with the energy of the electrons set to the same values as in the experiment. The Runge-Kutta method* with 0.02 mm step length was used to generate the trajectories from BPM A to the target by using the field map. The positions at BPM A, BPM B and the position and angle at the target was extracted from the simulated trajectory.

*http://en.wikipedia.org/wiki/Runge-Kutta_methods



(a) Normal run with beam



(b) Pedestal run without beam

Figure 5.24 Software filter applied to BPM signal. (a) is the signal with beam, (b) is the pedestal signal without beam. (1,2,3) in (a,b) are the raw signal without applying the filter, (4,5,6) are applied a 2 Hz finite-impulse-response filter with 4th order. (7,8,9) are averaged with 0.5 s. (1,4,7) are the 1-D histogram of the recorded signal, (2,5,8) are the signal in time domain, (3,6,9) are in frequency domain. Note all of the plots in (a) are from a single signal, same as in (b).

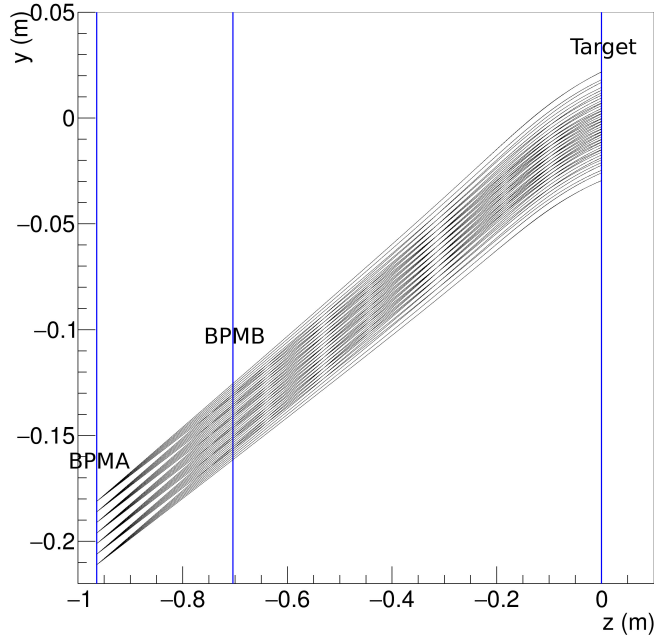


Figure 5.25 Transporting beam position from BPM to target with transverse target magnet field. Trajectories are from simulation. Blue lines show the z positions of BPMA, BPMB and target. y and z are in global Hall coordinate.

Data extracted from the simulation was used as input to a fitting program that determined the best-fit polynomial. In total, 24 different fits were taken for 4 different target positions and 6 configurations with different target magnetic field and beam energy settings. The validity of the transport functions was explored in the simulation using a new set of random trajectories generated in the same manner as those used in the fitting. The fits were compared with the full simulation and they are consistent with negligible difference.

The fitted transport functions were only used to transport the beam center position from the two BPMs to the target by applying the 2 Hz filter, which filtered out the fast raster and slow raster motion to keep only the beam center position. The transported position were expressed as X_{center} .

5.3.4.7 Determining the beam position event-by-event

The readout of the magnet current for the two rasters was connected to a series of ADCs. Two scintillator planes in the HRS form a DAQ trigger. This pulse signal triggered the ADC to record the magnet current for each event. The information from the rasters and the BPMs was combined to provide the beam position event-by-event. The position at the target was determined as:

$$X = X_{center} + X_{fstraster} + X_{slraster}, \quad (5.24)$$

where $X_{fstraster}$ and $X_{slraster}$ were the position displaced by the fast raster and slow raster, respectively, which were converted from the current values of the two raster

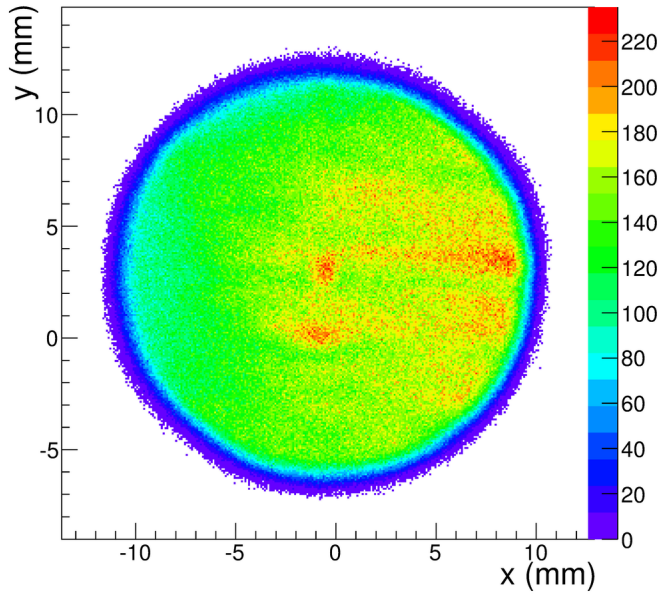


Figure 5.26 Reconstructed beam position at the target

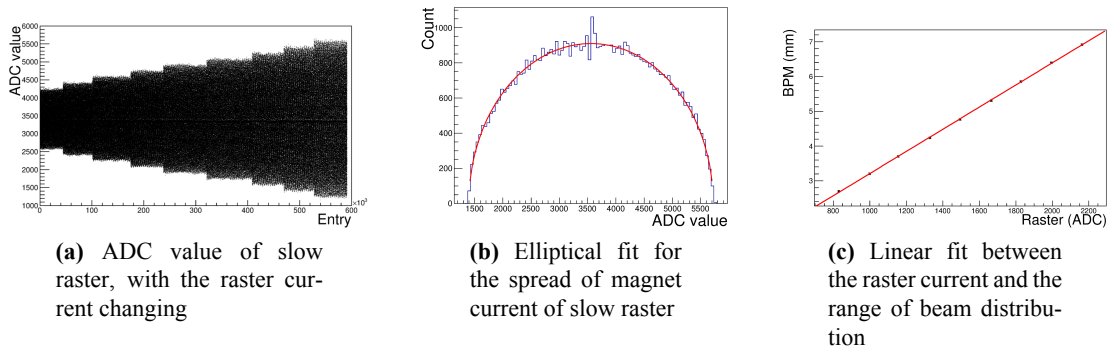


Figure 5.27 Converting the raster current to beam position shift

magnets. The calibration of the conversion factors between the magnet current of the rasters and the displaced position will be discussed in the next subsection. An example of reconstructed beam position is shown in figure 5.26.

Conversion factor for the slow raster

Two methods were used to calibrate the conversion factor for the slow raster. The first method used the calibrated BPM information, i.e., comparing the raster magnet current with the beam shape shown in the ADC of the BPMs. Several calibrations were taken during different run periods at a beam current of 100nA using different values of the raster magnet current, as shown in figure 5.27(a). The range of the beam distribution at the target was calculated from the ranges at the two BPMs without applying the filter, using the transport functions fitted previously. The range of the beam distribution at the two BPMs and the amplitude of the raster current was calculated from an elliptical fit, an example is shown in figure 5.27(b). Figure 5.27(c) shows a linear fit between the raster current and the range of the beam distribution at the target. The x axis in

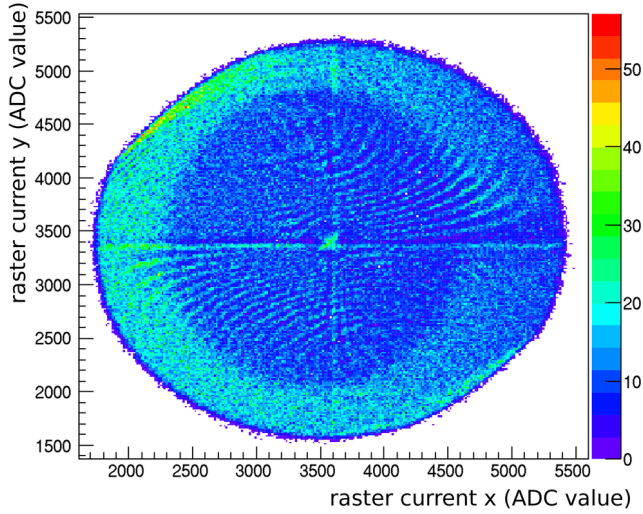


Figure 5.28 The shape of carbon hole in raster ADC, x and y axis are corresponding to the currents on x magnet and y magnet of slow raster, respectively.

figure 5.27(c) is the magnet current of the raster, and the y axis is the range of the beam distribution obtained from the BPMs.

The second method for calibrating the conversion factor used a target called “carbon hole” as shown in figure 5.38. The location of the carbon hole target is shown in figure 5.38. Scattered electrons were used as the trigger for recording the raster magnet current. Since the density of the target frame was much higher than that of the “hole”, which was submerged in liquid helium, the density of events triggered from the target frame was much higher than that of the hole itself. Recorded values reveal a hole shape as shown in figure 5.28. The size of the carbon hole was surveyed before the experiment, and a fit program was used to extract the radius of the recorded hole shape for that raster current. The conversion factor F was then calculated as the ratio of the size of the carbon hole S_{hole} and the radius of the hole shape R_{hole} in the ADC:

$$F = \frac{S_{hole}}{2 * R_{hole}}. \quad (5.25)$$

Conversion factor for the fast raster

The conversion for the fast raster was the same as for the slow raster. The low pass filter for the BPM was set to a higher value than the frequency of the fast raster to see the beam shape at the BPM formed by the fast raster. For a higher frequency filter, a larger beam current was needed to get a clear pattern. The beam current chosen for calibrating the fast raster was near 300 nA, which was the safety limit for the target. The beam shape formed by the fast raster is shown in figure 5.29.

5.3.4.8 Other improvements

Slow raster shape reconstruction

In order to improve the accuracy of the raster current value and minimize the uncertainty caused by the ADC resolution, a slow raster shape reconstruction was done using the fast

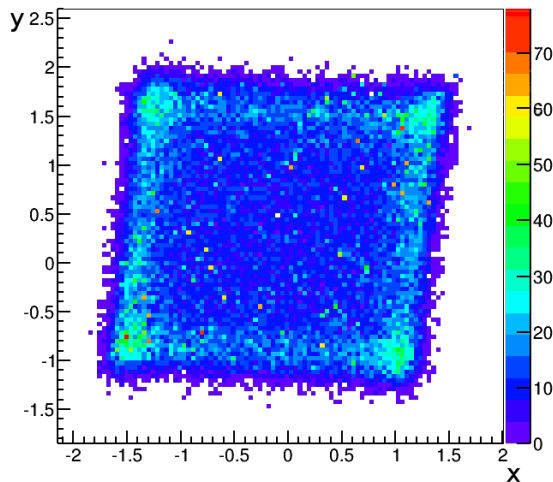


Figure 5.29 Beam shape formed by the fast raster at the BPM A location, the unit is millimeter

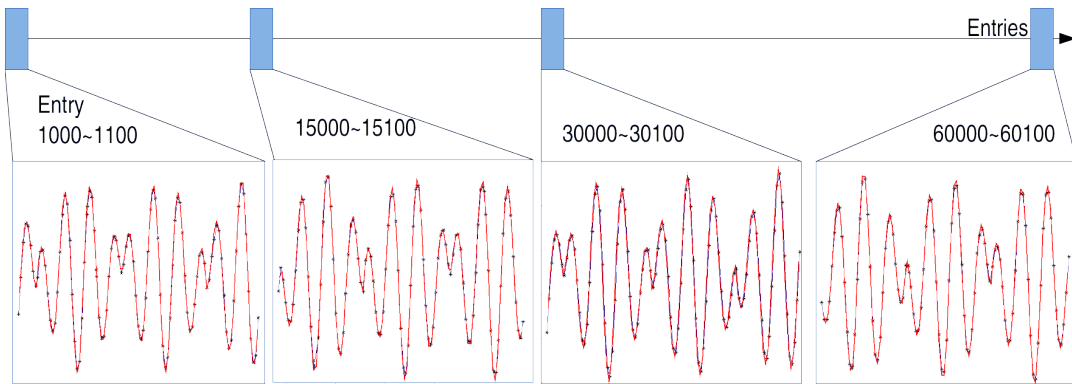


Figure 5.30 Slow raster phase reconstruction, the four pictures were using one fit result in one run, but in different time period of run. The asterisk is the real raster ADC data, and the line is the fit result.

clock signal. This signal was recorded in the scalers for each events, with a frequency of ~ 103.7 kHz. Since the slow raster function and the frequency setting was well known and controlled in the control room of Hall A, only phase information was needed to rebuild the shape.

Figure 5.30 is an example of the slow raster shape reconstruction. For the g2p experiment, there were about 7 million events in a production run with 20 minute duration. Unfortunately, the frequency of the fast clock signal was not stable, it was shifting during the experiment at a 40 Hz level (figure 5.31). A shift of 1 Hz during a run causes the shape to shift by 1.1 ms, corresponding to 1.1 cycles of the sine function. To avoid this shift, a fit was taken every 2000 events (1/3 second). The fit was also used to calculate the fast raster frequency, the result was matched with the one calculated with helicity.

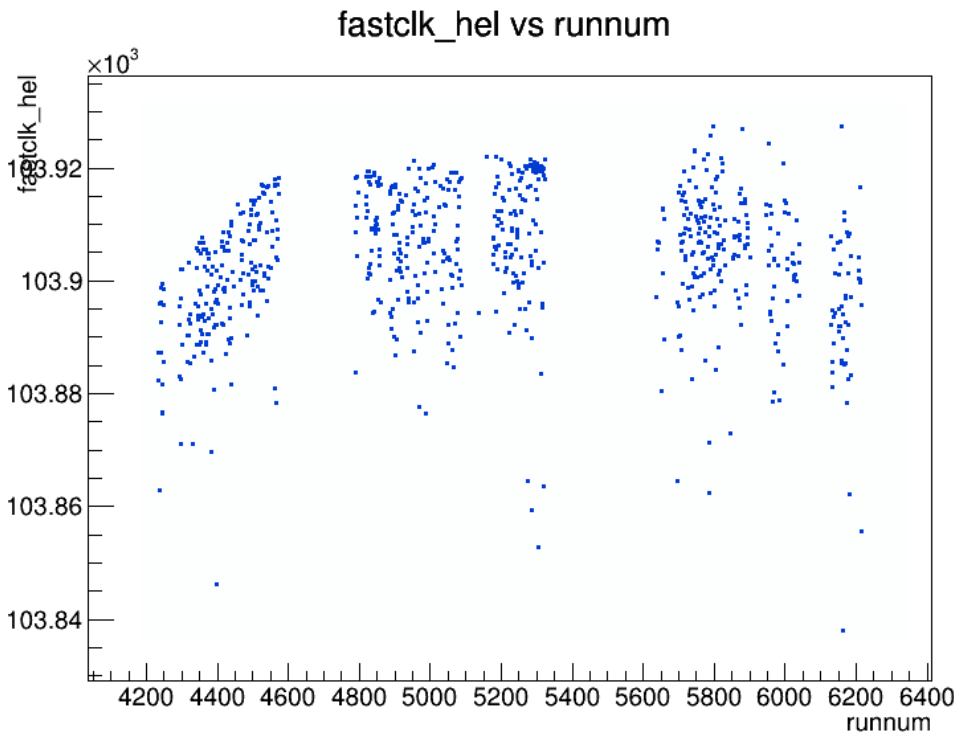


Figure 5.31 fast clock frequency change during experiment, x axis is run number, y axis is frequency (kHz) calculated by helicity signal

Beam motion determination

The determination of beam move was taken to split the run for several regions which have relatively stable beam position.

To judge if the beam moves, the root mean square (RMS) is looked at. A RMS deviation leaf for every 1000 events (0-1000,1-1001,2-1002,...) was calculated as shown in figure 5.32. Each entry in the figure 5.32 is the RMS of 1000 entries positions. When the beam suddenly moves there is a peak in the deviation histogram. When combined with another deviation leaf for every 300 entries, the baseline can be subtracted, leaving only the peak data. The peak positions were used for the first discontinuity point.

We use all of the beam trip points as the discontinuity points. Also, events that occurred during the beam trip, along with 2000 events after the beam came back were discarded. For case where the beam moved slowly, a discontinuity point was created when the beam position changed by more than 0.2mm, which is close to the BPM resolution. Combining all of the discontinuity points, the run was split in several regions which have a relatively stable position.

5.3.4.9 Uncertainty of the beam position and angle

Auto-gain and Fixed gain mode

Since the g2p experiment ran in 50 nA, the uncertainty of it should be carefully calculated. At the beginning of g2p experiment during 3/1/2012 and 3/29/2012, the BPM setting use the auto-gain mode which was used for several experiments before the g2p

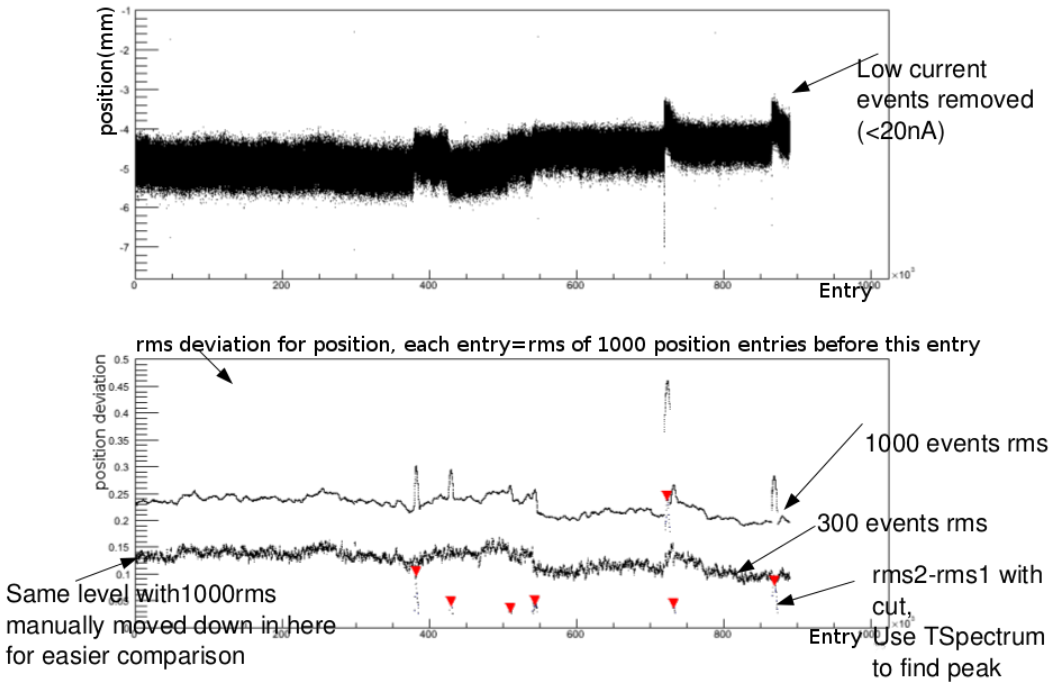


Figure 5.32 Using RMS to check if beam move, x axis is entry, y axis on top pad is x position, on bottom there is rms calculated from above pad

experiment. As shown in figure 5.4, the BPM receiver have 4 channels, each antenna connected its own channel and the gain of each one can be adjusted independently. Combining the equation (5.19) and equation (5.14), equation (5.15) can be rewritten as :

$$D_U = k \frac{I \cdot \phi'_+ \cdot 10^{\frac{g_+}{20}} - I \cdot \phi'_- \cdot 10^{\frac{g_-}{20}}}{I \cdot \phi'_+ \cdot 10^{\frac{g_+}{20}} + I \cdot \phi'_- \cdot 10^{\frac{g_-}{20}}} = k \frac{\phi'_+ \cdot 10^{\frac{g_+ - g_-}{20}} - \phi'_-}{\phi'_+ \cdot 10^{\frac{g_+ - g_-}{20}} + \phi'_-}. \quad (5.26)$$

Auto-gain mode means the gain setting automatically changes with the current, but fix the $g_+ - g_-$ value. Because the difference between g_+ and g_- is fixed, the result D_U in equation (5.26) will not be changed when gain and current is changing. The advantage of auto-gain mode is the BPM receiver can work in a large current range and don't need to change the gain by hand. But during the first range runs for g2p experiment we found that the auto-gain mode cannot work well since the beam current g2p used was only around 50 nA, the signal/noise ratio became low enough that auto-gain mode didn't work anymore. After the date 3/29/2012, we changed to dual gain mode, that is use one fixed gain setting below 500 nA for CW beam mode and use another fixed gain setting above 500 nA for tuning beam.

Pedestal

From equation (5.22) it is necessary to get the pedestal value A_{ped} . For auto-gain mode since the gain is always changing, the pedestal value is always changing too. For auto-gain mode the value D_U in equation (5.21) is calculated directly using $\frac{A_+ - A_-}{A_+ + A_-}$, the un-

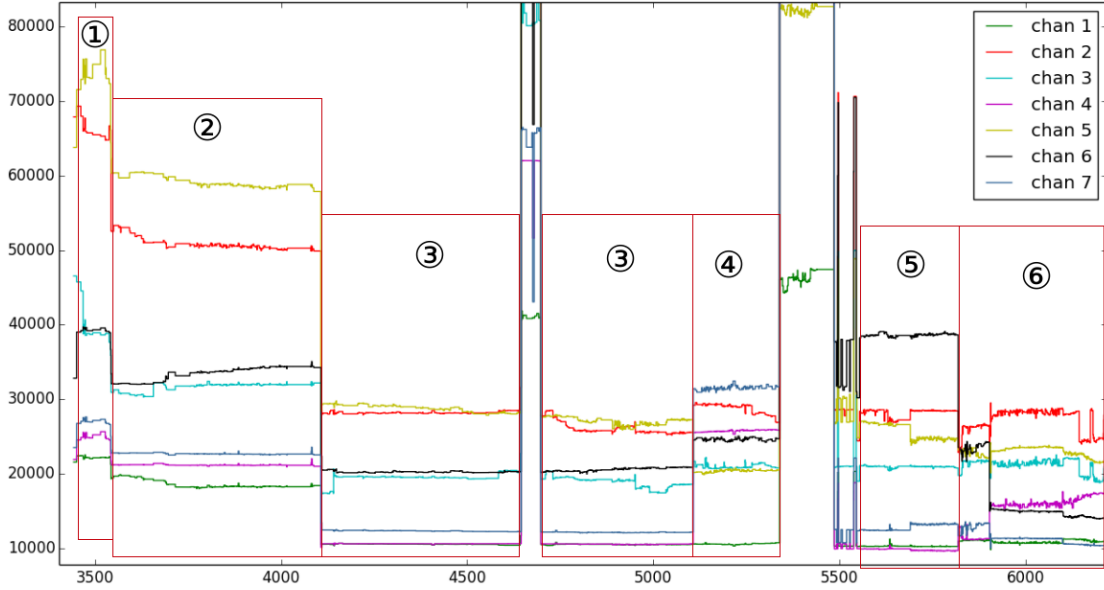


Figure 5.33 Pedestal change during experiment for left arm

certainty of it is calculated by using another method and will discuss in next section. Here we only discuss about the fixed gain setting.

During 3/29 and 5/18 we have 6 different gain settings. Figure 5.33 is the pedestal change for each settings during experiment. The data came from two parts, one is from the real pedestal run that the beam kept off, another from the beam trip events in production runs. The reason to use beam trip events as pedestal value is that the number of the run with beam trip is much more than the pure pedestal run so that we can get more closed value. The data shows there is few different between pure pedestal run and beam trip pedestal, and the pedestal is changing during the time. The pedestal values in figure 5.33 are saved were the sqlite database. The pedestal value for each run choice the one closest for that run and have the same gain setting. The uncertainty of pedestal calculated from two part: One is the root-mean-square of 2 Hz filtered histogram for each pedestal run; The other part is from the pedestal database that split several relatively stable range in figure 5.33, and calculate root mean square for all of the pedestal values in that range. The final pedestal uncertainty used the larger one from those two parts.

Pedestal uncertainty for auto gain mode

As mentioned above, the gain setting was always changing when in auto gain mode. Unfortunately the gain setting was only recorded at the beginning of run and not recorded in epics file for each change. For the reason above it is impossible to get pedestal uncertainty directly. Since the gain was not fixed, the value of the calculated position changed when the gain changed (Pedestal changed) is the most important one we should consider and it is the meaning of pedestal uncertainty. Luckily we don't have many runs in auto gain mode, most of them are optics runs, and just a few of them are production runs. All of the optics runs ran in 80~100 nA in auto gain period and that have less pedestal disturbance than in 50 nA.

The main idea to estimate the pedestal uncertainty in auto gain mode is, choose some relatively stable position ranges (no manual change, beam is stable), check the position deviation between each range. Since there is no way to know how large the gain waggled during a run and between runs, and how large calculated position change when the gain wags, even in the same gain setting the pedestal is still not stable (see [5.3.4.9](#)). For the reason above the maximum position deviation is used for position uncertainty caused by pedestal.

Total Uncertainty

The uncertainty of the final beam position at the target for each event contains several contributions:

- The first part comes from the uncertainty of the calibration constant. It includes the BPM resolution for the DAQ runs used for the calibration, the uncertainty of the harp data corresponding to each calibration, and the survey uncertainties for the BPMs and harps. It contributes about 0.7 mm for the uncertainty of the position and 0.7 mrad for the uncertainty of the angle.
- The uncertainty on the pedestal is the largest uncertainty for the beam position measurement, contributing about 0.7~1.5 mm to the uncertainty of the position and 0.7~1.5 mrad to the uncertainty of the angle.
- The uncertainties from the BPM survey need to be included, since the production data and the calibration data were taken at different beamline settings when the equipment was moved. They contribute 0.5 mm to the uncertainty of the position.
- The uncertainty from the magnetic field map of the target was considered for the settings with the target magnet field.
- The uncertainties due to the size conversion of the rasters were also included.

The position uncertainty was magnified by a factor of 5 at the target because of the short distance between the two BPMs. For example, in the straight through setting, if the uncertainty at BPM A is 0.2 mm, and at BPM B is 0.27 mm, the uncertainty at the target is 1.1 mm for position and 1.3 mrad for angle. The uncertainty for the position at the target was around 1~2 mm, while the uncertainty for the angle was 1~2 mrad. More detail position and uncertainty can be found in g2p sql database.

5.3.5 Local beam dump

For the settings with 5 T transverse target magnet field, the chicane magnet cannot bend the beam to the Hall A beam dump. The low beam current for the experiment allow for the use of a local beam dump, which was installed downstream the NH_3 target and upstream the septum magnet, as shown in figure [5.34](#). The local beam dump worked great during the experiment without any high radiation recorded.

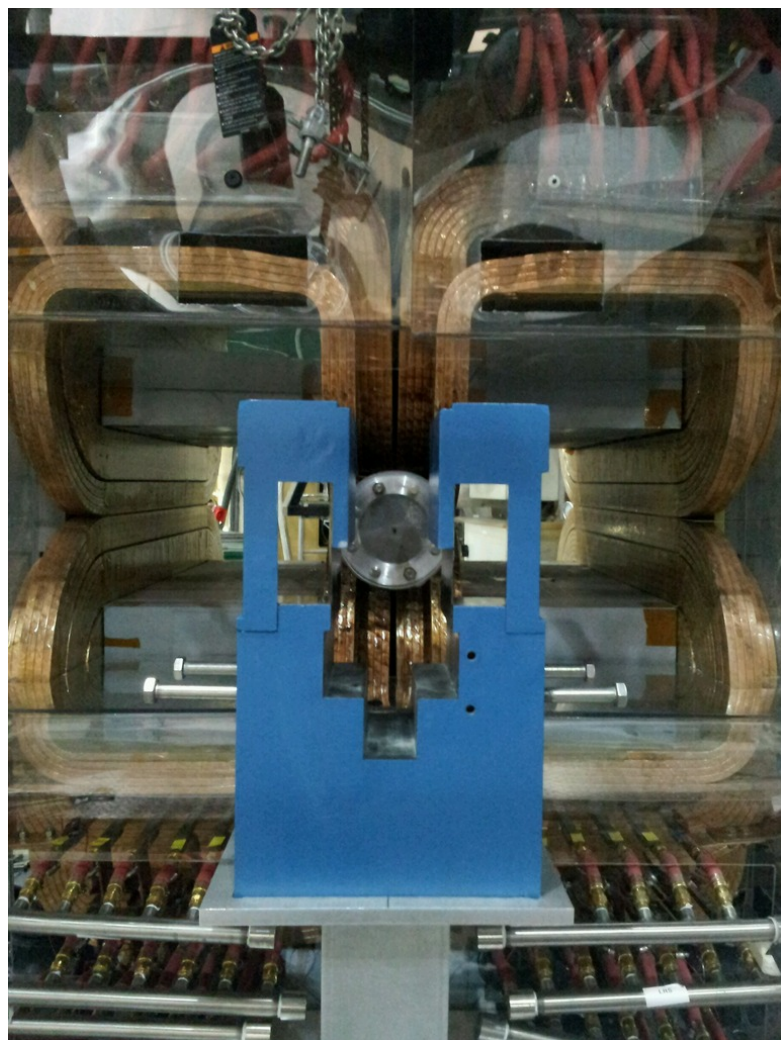


Figure 5.34 The local beam dump (blue one) and the septum magnet (back of the local beam dump).

5.4 The Polarized Target System

Polarized target was widely used to extract the polarized neutron and proton data in order to study the nucleon structure in the spin degree of freedom in nuclear and particle experiments. There are several types of polarized target system used in Jefferson Lab. The polarized ammonia (NH_3) target is used to study the spin of proton, while the polarized 3He target acts as an neutron target.

5.4.1 Polarized NH_3 target

The polarized proton target used during the g2p experiment is from UVa target group, which uses solid ammonia as the proton material. It has been used for many experiments before, like SANE, RSS in Hall C and EG1-4 in Hall B at Jefferson Lab, and E143, E155, E155x in SLAC. The dynamic nuclear polarization (DNP) method is used to polarize the target, which is using low temperature down to 1 K and 140 GHz microwave to pump the polarization into a high level up to 94 %. The nuclear magnetic resonance (NMR) is used for measuring the polarization, while the thermal equilibrium (TE) polarization is used for calibrating it.

5.4.1.1 Polarization mechanisms

Dynamic Nuclear Polarization

The dynamic nuclear polarization (DNP) was used to achieve high polarization for the NH_3 target. A microwave generator emits the microwaves at the splitting energy of ν_{NMR} . The energy splitting between two electron sublevel $m_e = \frac{1}{2}$ and $m_e = -\frac{1}{2}$ is about 140 GHz at 5 T and 70 GHz at 2.5 T, and the energy splitting between two proton sublevels $m_p = \frac{1}{2}$ and $m_p = -\frac{1}{2}$ is about 200 MHz at 5T. Thanks for the granular control of the microwave technology, we can obtain any frequency we want use in microwave section accurately by using the cavity. The “positive” polarization from the state of $e_{-\frac{1}{2}}p_{-\frac{1}{2}}$ to $e_{\frac{1}{2}}p_{\frac{1}{2}}$ needs 140.2 GHz microwave and the “negative” polarization from the state of $e_{\frac{1}{2}}p_{\frac{1}{2}}$ to $e_{-\frac{1}{2}}p_{-\frac{1}{2}}$ needs 140.5 GHz microwave for the 5T magnet.

Thermal Equilibrium (TE) Polarization

A Zeeman splitting because of the high magnet field causes 2 sublevels which the proton’s spin is $I = \frac{1}{2}$. The population of these two sublevels is calculated by the Boltzmann law:

$$N_{\frac{1}{2}} = N_{-\frac{1}{2}} e^{-\frac{\Delta E}{k_B T}}, \quad (5.27)$$

where $N_{\frac{1}{2}}$ and $N_{-\frac{1}{2}}$ are the population of two sublevels, T is the temperature of the environment, k_B is the Boltzmann constant, ΔE is the energy difference of two sublevels in the magnetic field of B . As defined polarization by $P(\frac{1}{2}) = \frac{N_{\frac{1}{2}} - N_{-\frac{1}{2}}}{N_{\frac{1}{2}} + N_{-\frac{1}{2}}}$, the thermal equilibrium polarization is calculated as:

$$P(\frac{1}{2}) = \tanh(\frac{\mu B}{k_B T}) \quad (5.28)$$

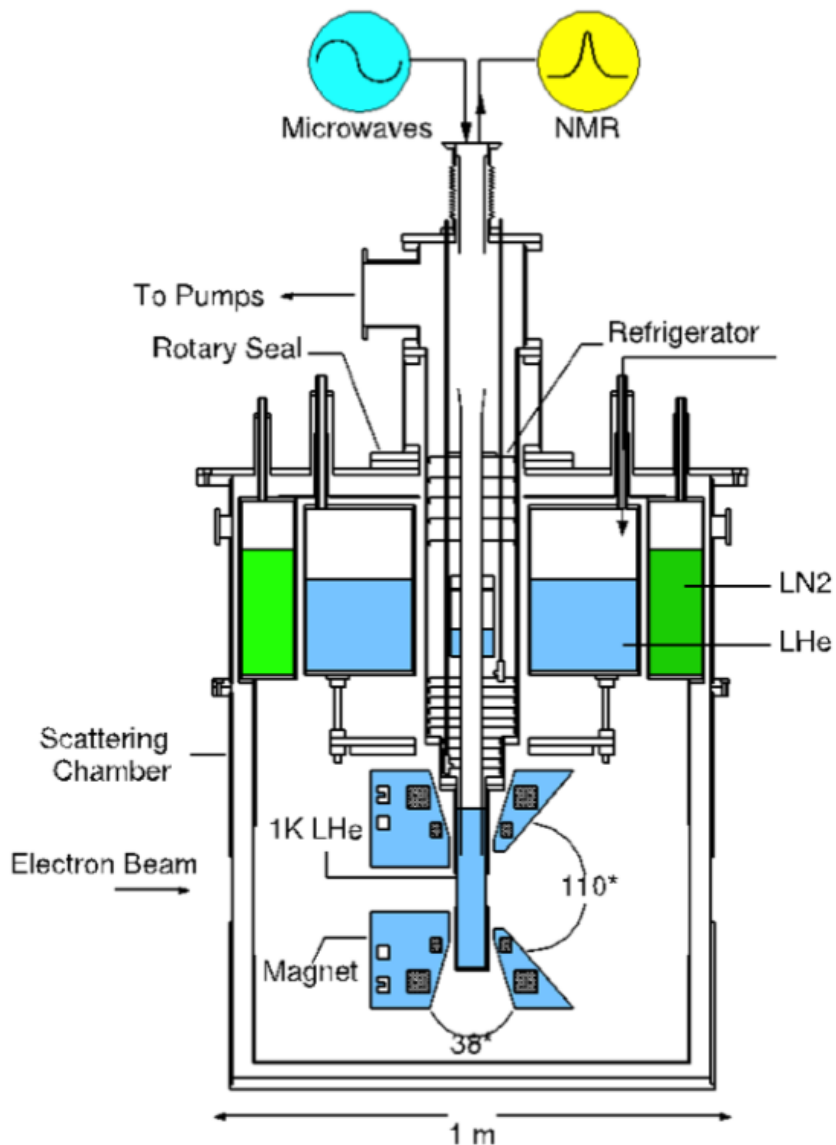


Figure 5.35 Polarized NH_3 target system

which is only the function of magnetic field B and temperature T . The proton's thermal polarization is about 0.5% at 5 T magnet field and 1 K temperature. It is used for calibrating the NMR measurement.

5.4.1.2 Target system

Target magnet

The original 5 T oxford superconducting magnet was burned before the experiment during a quench while the target was being tested in preparation for installation. The superconducting magnet from the Hall B polarized target was replaced and installed in the g2p cryostat. Because of the power and construction limit for the chicane dipole magnet, also for the reason of getting smaller Q^2 , the 2.5 T magnet field was used in addition to the 5 T magnet field.

The NH_3 target system is shown in figure 5.35. The open geometry of the target

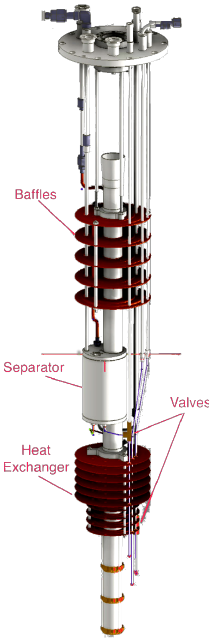


Figure 5.36 1K refrigerator

magnet allows the beam to pass through longitudinal or transverse. The magnet allows to generate a uniform field region of less than 10^{-4} over a cylindrical volume with 2 cm in diameter and 2 cm long [147].

Refrigerator

A 4He evaporation refrigerator was used to cool down the temperature of the target to 1 K, as shown in figure 5.36. It is installed vertically along the center of the magnet. The liquid helium is siphoned from the magnet to the separator via a transfer line. The vapor is pumped away by a small diaphragm pump and cools the baffles. The liquid helium in the bottom of the separator is delivered to the target nose via a copper tube. The vapor is pumped away from the target nose by a $12000 m^3 h^{-1}$ roots pump set to reach the temperature to about 0.9 K [147].

Target Material

There are many requirements used to select the material: the polarization that can be obtained, the dilution factor (ratio of the free polarizable nucleons to the total), the build-up time of polarization, the simplicity for the preparation and handling, and the radiation damage resistance [148]. Butanol has less polarized background than ammonia and higher dilution factor than propanediol, ammonia and propanediol can achieve higher polarization.

The most important thing that can reduce the polarization is radiation damage. The radiation can produce additional radicals that the Larmor frequency of it is different as the material. As the increasing of these radicals, the relax time of nucleon is shortened and the polarization of it is reduced. The ammonia is chosen because of its high resistance of radiation damage and low temperature ($\sim 77 K$) for annealing to recover. Even so, the target material was changed for many times during the g2p experiment.

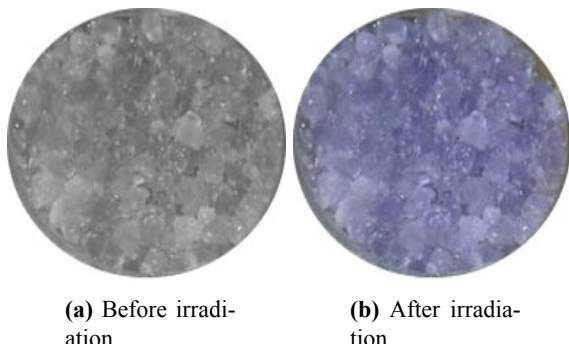


Figure 5.37 NH_3 beads before and after the irradiation.

The material was processed granularity in order to averagely cool the material. The equal size of the beads is about 1 mm. The rapid freezing process is used to create a glassy state in order to achieve the hypodispersion of paramagnetic radicals. In order to get more paramagnetic radicals, the irradiation process is necessary. The high temperature irradiation at ~80 K was taken in NIST before the g2p experiment.

Target insert

The target insert consists of several cells, as shown in figure 5.38. From up to down in the picture, it is NH_3 cell, CH_2 hole, carbon hole, NH_3 cell, dummy cell and carbon cell. Two NH_3 cells were used during the production runs, with the ammonia beads filled and the aluminum foil covered. The dummy cell was used to calculate the dilution factor of the target, with the same structure as the NH_3 cell but without the ammonia beads. The carbon cell was used for the optics study. The CH_2 hole and the carbon hole were designed to load the CH_2 foil and the carbon foil in order to do the optics study. But at the most of the time they didn't load anything.

The position of the target insert is in the center of the refrigerator, it moved vertically to different target positions by a remote controlled stepper motor.

Microwave

The microwave generator contains: a microwave chamber (EIO tube) used to generate the microwave, a motor and motor control used to change the length of the chamber in order to change the frequency of microwave, a water cooling system, high voltage and power supply, a power meter used to measure the frequency, and a circular waveguide used to lead the microwave to the target insert. Both 70 GHz and 140 GHz EIO tube has a tunable frequency of about 1% [149]. Due to the lower attenuation in the waveguide at 70 GHz, the microwave power was delivered to the target cells more than 2W at 70 GHz, while it is 1W at 140 GHz [147]. Figure 5.39 shows a 140 GHz microwave system.

NMR system - Q meter

The NMR coil is a short coil of CuNi capillary. It was installed inside the NH_3 cell, as shown in figure 5.40 (a). The signal of the NMR coil was connected to the Q-meter



Figure 5.38 Target insert

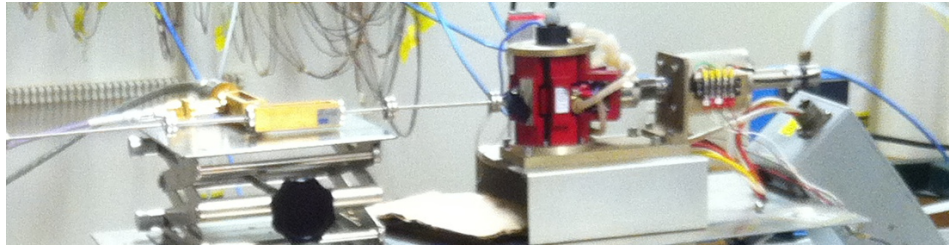


Figure 5.39 Microwave system

circuit [150] which is used measure the polarization of target in NMR system.

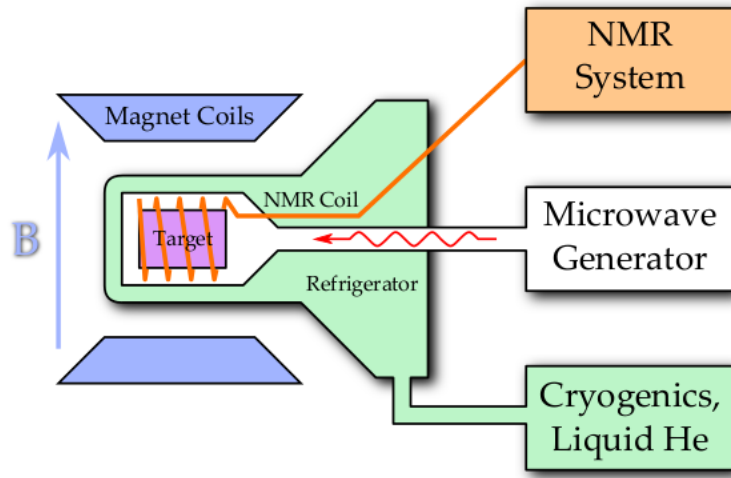
The circuit of the Q-meter is shown in figure 5.40 (b). The polarization P of the target is related to the susceptibility caused by the polarized nucleons as:

$$P = K \int_0^{\infty} \chi''(\omega) d\omega, \quad (5.29)$$

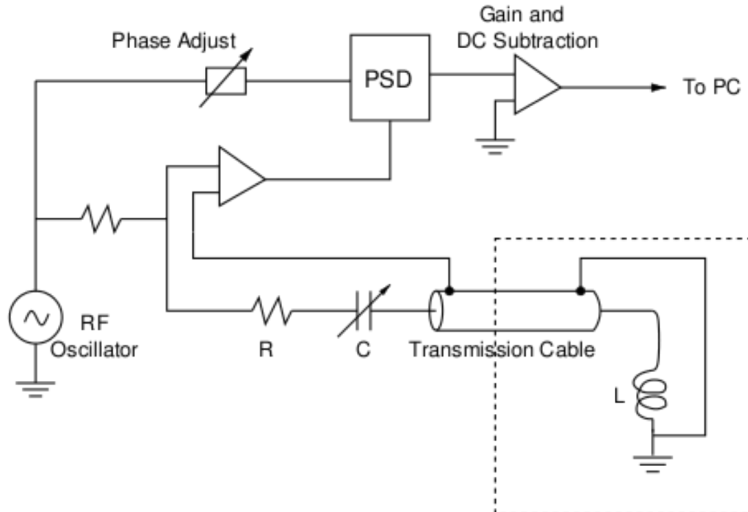
where the polarized nucleons caused susceptibility $\chi(\omega) = \chi'(\omega) - i\chi''(\omega)$. The $\chi'(\omega)$ and the $\chi''(\omega)$ are the dispersive and the absorptive part of the susceptibility. K is a constant related to the properties of the concerned nucleus (polarized proton). The NMR coil itself has a inductance L_0 , the target material changes the inductance as:

$$L(\omega) = L_0(1 + 4\pi\eta\chi(\omega)), \quad (5.30)$$

where the η is the filling factor of coil. For proton, the value of $\chi(\omega)$ is 0 in all frequency range except near of the larmor resonance frequency ω_0 , causing a peak in the output



(a) Overview of the NMR system



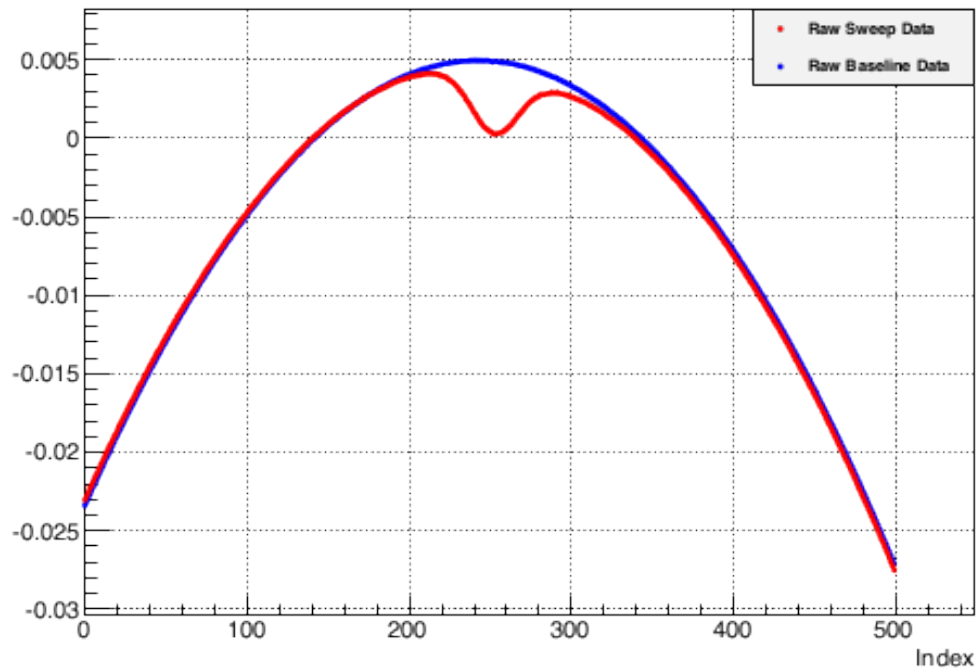
(b) Overview of the NMR system

Figure 5.40 NMR system for NH_3 target

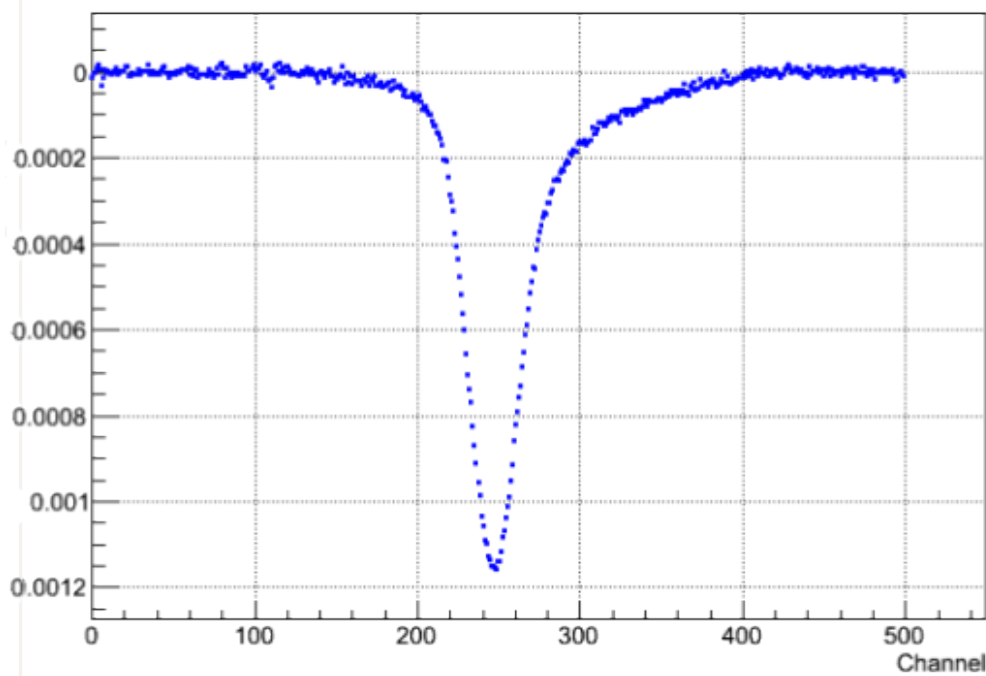
of the Q-meter circuit, as shown in figure 5.41 (a). Figure 5.41 (b) shows the signal after removing the baseline, which was measured at the same setting when the ω moved away from ω_0 .

5.4.1.3 Polarization

The uncertainty of the calculated polarization was from the polynomial fit of raw NMR signal and the uncertainty from the TE measurement. The uncertainty from the fit was largely based on the quality of the NMR signal, but never larger than 3%. The uncertainty from the TE measurement was from the target field reading and the temperature reading. The former was provided as 2% dictated by the precision of the magnet power supply. The temperature in the target nose was measured using both manometer that measured the pressure in the target nose and convert it to temperature. The final uncertainty of the polarization was around 3.5%~4%.



(a) NMR peak, Blue is the baseline when the ω moved away from ω_0 .



(b) NMR signal after subtracting the baseline

Figure 5.41 NMR signal for the Q-meter

Figure 5.42 (3rd/4nd) shows the polarization when using the 5 T magnet field during the experiment. About 70% polarization was gotten by average [151]. The figure shows the polarization drop caused from the radiation damage by the beam, and the polarization recovered after taking anneal or replacing the material. Figure 5.42 (1st/2nd) shows the polarization when using the 2.5 T magnet field, which shows the average of 15% polarization.

5.4.2 Polarized 3He target

Free neutrons are hardly achieved due to the short lifetime (under 15 minutes), other materials are used instead. 3He has one neutron and two protons. The spin of neutron is aligned with the spin of the 3He nucleus since the spins of two protons are paired. A polarized 3He target lab was built in 1998 at Jefferson Lab and has been undergoing upgrade and improvement continuously. A mount of experiments have successfully run with the 3He target. Several experiments after JLab 12 GeV upgrade are proposed to use the 3He target. Although the 3He target was not used for the g2p experiment, I also worked on testing the 3He target for several months.

5.4.2.1 Polarization mechanisms

Since the density of 3He is too low, the spin exchange optical pumping was used instead of direct optical pumping [153]. The $K - Rb$ mixture is first polarized by optical pumping. Three diode lasers were installed to generate right circular light. The ground state of $^{85}Rb\ 5S_{1/2}$ splits to $F = 2$ and $F = 3$ hyperfine status with the nuclear spin $I = \frac{5}{2}$ and electron spin $S = \frac{1}{2}$. Each F splits to $2F + 1$ fine status as shown in figure 5.43. The first excited state $5P_{1/2}$ and the other alkalis split to a similar pattern. The right circular light causes m_F plus 1 for every excitation. Most of the electrons stay in the $m_F = +3$ state at last. The polarization of alkali reaches more than 90%. The collision transfer of polarization between the polarized alkali and the 3He causes the 3He polarized at a high record of 65% [153].

5.4.2.2 Target Setup

Figure 5.44 is the equipment construction of 3He target in target lab. Three pairs of orthogonal Helmholtz coils provide the holding field of target. The wavelength of diode laser has good monochromaticity and is true to the absorption spectrum of Rb and K. The laser will be leaded into the oven via the optics. The Rb and K in the oven will be polarized. The NMR and EPR part is used for measuring the polarization of 3He . The holding field control is used for controlling the magnitude and direction of holding field. The data is collected by GPIB to PC for control and analysis.

Laser Optics

In order to get high brightness, three diode lasers and six light roads has been used. The laser optics is shown in figure 5.45 . There are two quarter wave plates, one lens, one cube and two mirrors in every three roads. The laser is lead into optics with fiber first, and then passes through the lens in order to be focused into parallel. When the laser passes through the cube, it is splitted to two roads, most part of P wave passes through

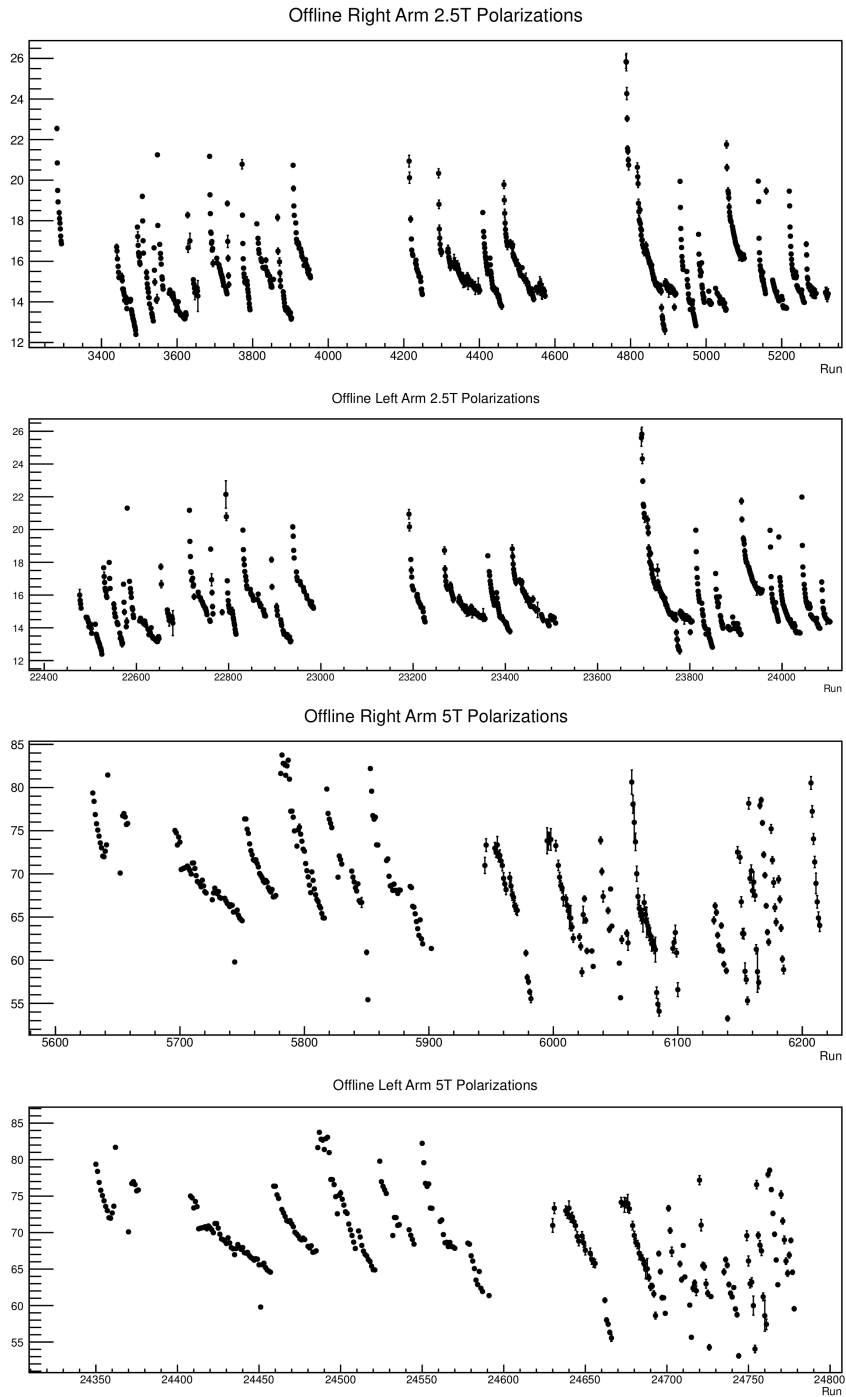


Figure 5.42 Target polarization for 2.5 T magnet field (1st/2nd) and 5.0 T magnet field (3rd/4th) during experiment [152]

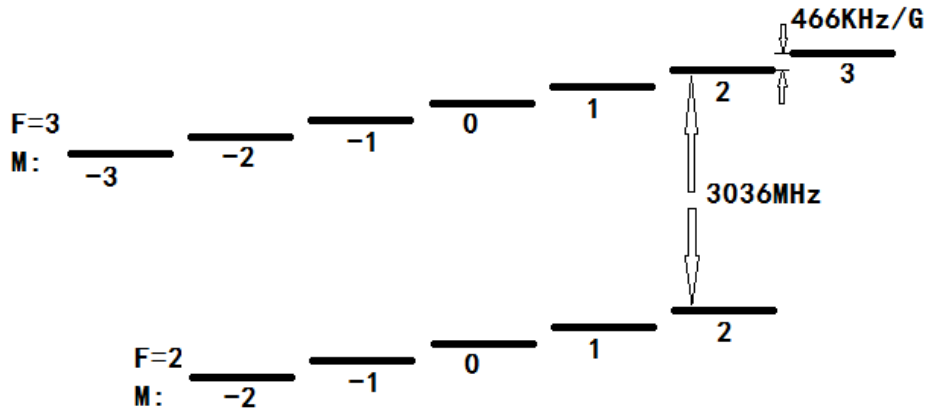


Figure 5.43 Ground state energy levels for ^{85}Rb , as 466 kHz/G of Zeeman splitting and 3036 MHz of hyperfine splitting

and is reflected by the 3" mirror. All of the S wave and about 10% P wave are reflected to the direction of quarter wave plate by cube, then they pass through the quarter wave plate twice. The laser is transformed into right circular polarized light after the optics. Totally 6 roads of laser are extracted by the optics. About 10% of laser is reflected back to fiber, and the necessary protection for fiber is needed.

5.4.2.3 The principle of polarization measurement

Two methods are used for measuring the polarization of ^3He , one is NMR, the other is EPR.

Nuclear Magnetic Resonance (NMR)

The technique of adiabatic Fast Passage (AFP) is the key method in NMR Sweep. The NMR signal is received with NMR pick-up coils when the spin reversal happened since the holding field or frequency sweeping across resonance. Combining with the same measurement performed for a water sample, the polarization of ^3He is obtained. Both the field sweep and the frequency sweep are used for the NMR measurement. The NMR field sweep is described as follows. The frequency sweep has similar principle.

Classically, a torque is exerted by the magnetic field if a ^3He nucleus is in a static magnetic field:

$$\frac{d\vec{M}}{dt} = \gamma \vec{M} \times \vec{H}_0, \quad (5.31)$$

where \vec{M} is the ^3He nucleus magnetic moment, \vec{H}_0 is the holding field, and γ is the gyromagnetic ratio. The $\frac{d\vec{M}}{dt}$ is written in rotating frame as:

$$\frac{d\vec{M}}{dt} = \frac{\partial \vec{M}}{\partial t} + \vec{\omega} \times \vec{M}, \quad (5.32)$$

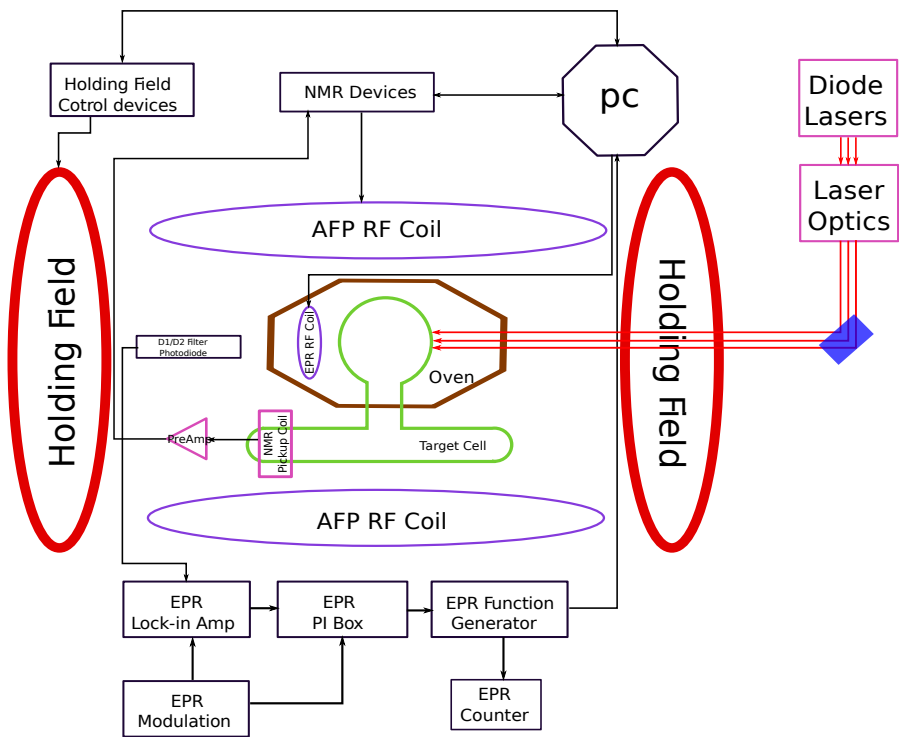


Figure 5.44 ${}^3\text{He}$ target setup

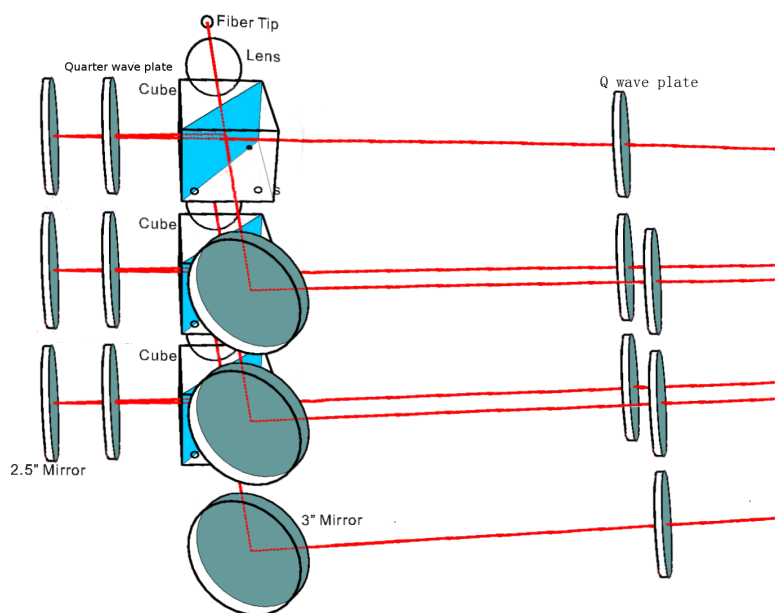


Figure 5.45 Laser optics

where $\vec{\omega}$ is the frequency of the rotating frame. Combining (5.31) with (5.32), the following formula is obtained:

$$\frac{\partial \vec{M}}{\partial t} = \gamma \vec{M} \times (\vec{H}_0 + \frac{\vec{\omega}}{\gamma}). \quad (5.33)$$

If we make comparisons about (5.31) and (5.33), the holding field \vec{H}_0 in (5.31) has been changed as effective field $(\vec{H}_0 + \frac{\vec{\omega}}{\gamma})$ in (5.33). We can choose a rotating frame that make the effective field vanished, i.e. let $\omega_0 = -\gamma H_0$. The holding field is in z direction in all time, and we can write \vec{H}_0 as $H_0 \vec{e}_z$. In x direction a RF field of $\vec{H}_{RF} = 2H_1 \cos(\omega t) \vec{e}_z = H_1 \hat{e}'_+ + H_1 \hat{e}'_-$ is applied, where $\hat{e}'_{\pm} = \cos(\omega t) \hat{e}_x \pm \sin(\omega t) \hat{e}_y$ which only needs one of them. In the rotating frame the effective field can be written as:

$$\vec{H}_e = (H_0 + \frac{\omega}{\gamma}) \vec{e}_z + H_1 \hat{e}'_+, \quad (5.34)$$

where $H_1 \vec{i}$ is perpendicular to \vec{H}_0 and have a frequency ω to rotate it. The absolute value, i.e. the magnitude of \vec{H}_e is written as:

$$H_e = \sqrt{(H_0 + \frac{\omega}{\gamma})^2 + H_1^2}. \quad (5.35)$$

The angle θ between the holding field \vec{H}_0 and effective field \vec{H}_e can be written as:

$$\tan \theta = \frac{H_1}{H_0 + \frac{\omega}{\gamma}} = \frac{\omega_1}{\omega_0 - \omega} \quad (5.36)$$

As the H_1 is much smaller than H_0 , the angle θ can be regarded as 0 unless $\omega_0 - \omega$ close to 0. Once the ω_0 is passed to ω , the nuclear magnetic resonance could be happened and the magnetic moment of 3He becomes anti-parallel to the holding field by following the effective field.

The 3He average magnetic moment $\langle \vec{M} \rangle$ is proportional to the signal height. Because the polarization of 3He is proportional to $\langle \vec{M} \rangle$, the relationship between signal height and polarization is obtained by taking the calibration process.

The water calibration is used to calibrate the NMR signal by measuring the thermal polarization of the proton in water.

Electron paramagnetic resonance

When the 3He nucleus are polarized, a small magnet field at a level of ~ 0.1 Gauss [118] was generated by their spins. In addition to the holding magnet field of 25 Gauss, the EPR frequency is decomposed as:

$$\nu_{EPR} = \nu_0 \pm \Delta\nu_{EPR}, \quad (5.37)$$

where ν_0 is caused by holding field, $\Delta\nu_{EPR}$ is related to the polarization of 3He , and \pm corresponds to the direction of polarization. Since the $\Delta\nu_{EPR}$ is much smaller than ν_0 , the adiabatic fast passage (AFP) sweep [154] was taken to reverse the polarization of 3He periodically. The $\Delta\nu_{EPR}$ is extracted from the EPR frequency calculated before and after spin reversal:

$$\Delta\nu_{EPR} = \frac{\nu_{EPR,\uparrow\uparrow} - \nu_{EPR,\downarrow\downarrow}}{2}, \quad (5.38)$$

where \uparrow and \downarrow are two spin directions of the 3He nucleus, $\uparrow\uparrow$ are the direction of holding field.

The polarization P_{He} has the following relation with the $\Delta\nu_{EPR}$ [155]:

$$P_{He} = \frac{3}{8\pi} \frac{(2I+1)}{g_s\mu_B} \frac{h}{\mu_K} \frac{\Delta\nu_{EPR}}{(1+\epsilon)\kappa_0\rho_{He}}, \quad (5.39)$$

where g_s is the electron g factor, μ_B is Bohr magneton, I is the nuclear spin, $\frac{\mu_K}{h}$ is the magnetic moment of 3He , ϵ is the magnetic moment correction factor, κ_0 is the frequency shift enhancement factor depending on temperature[156, 157], ρ_{He} is the density of 3He .

Frequency lock

The frequency modulation (FM) sweep is used to find the EPR resonance frequency in order to lock it to do the AFP sweep. If a magnetic field with EPR resonance frequency is added, two splitted states between $5P_{1/2}$ and $5P_{3/2}$ are mixed. More electrons in state of $5P_{3/2}$ causes decay from $5P_{3/2}$ to $5S_{1/2}$ and emit 785nm light which called D_2 light. In the meantime the D_1 absorption spectrum happens caused by $5S_{1/2} \rightarrow 5P_{1/2}$. Because of the narrow laser we used, the laser light absorbed cleanly with little noise of background, which means we can get a clean D_1 absorption spectrum. The original gaussian peak of D_1 light is almost absorbed. Either D_1 or D_2 light could be used to lock the EPR resonance frequency. The D_1 and D_2 light are picked by photodiode and exported by fiber. In order to get maximum signal, the best place was found for photodiode. The photodiode for D_2 was placed in the top of the oven, and for D_1 was placed in the front of the oven. A D_2 filter was used for the D_2 photodiode to detect the increase in D_2 light. Since D_1 light is much brighter than D_2 , no filter was added for D_1 photodiode. Figure 5.46 shows an example of EPR FM sweep by either using D_1 or D_2 .

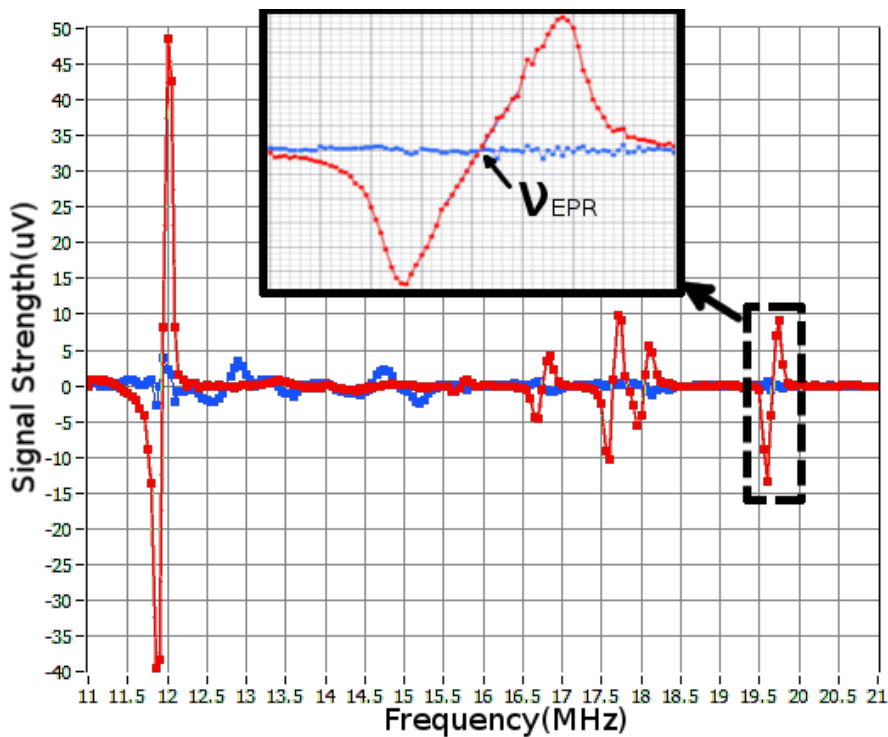
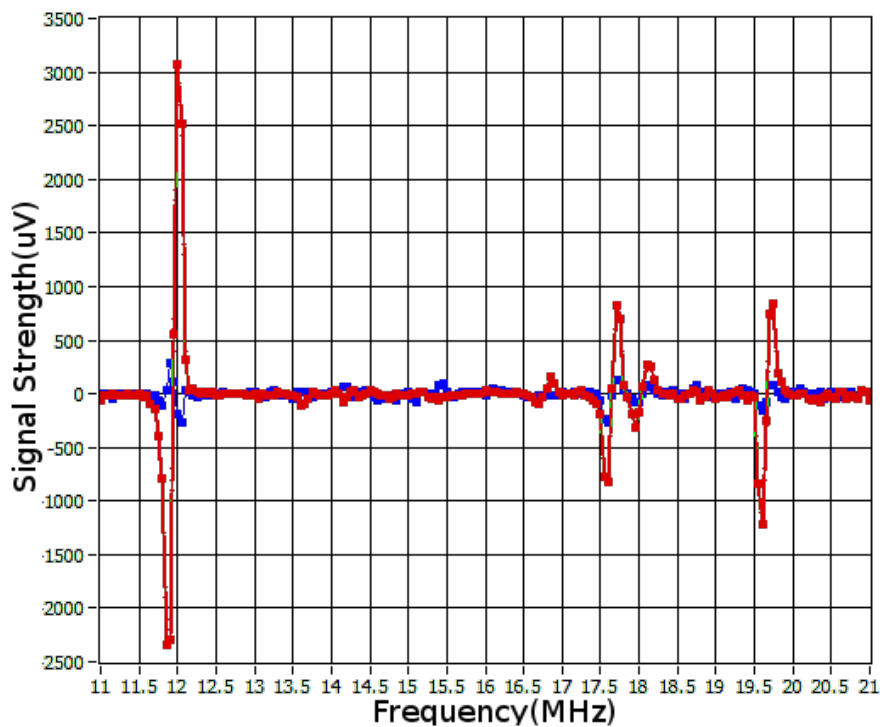
(a) FM sweep using D_2 light(b) FM sweep using D_1 light

Figure 5.46 Frequency modulation sweep, x axis is the frequency, y axis is the signal after Fourier transformer. Each peak indicate one alkali nuclide. The red lines are the real part, while the blue lines are the imaginary part.

5.5 The Hall A High Resolution Spectrometers

The g2p experiment uses the standard Hall A high resolution spectrometers (HRS) and their detector package to detect the scattered electrons, as shown in figure 5.2, id 13 and 14. Since the g2p experiment is an inclusive experiment, two arms, left arm and right arm, did the same job for the reason of increasing the statistic and independent with each other. Each arm has a group of Q1-Q2-D-Q3 super conducting magnets set. The Q1, Q2 and Q3 are three quadrupoles for focusing. The D is a dipole magnet to select the electrons with chosen momentum value. It bends the electron to the detector set with a vertical bend of 45° in a small range of momenta and scattering angles, which provides the momentum resolution at the level of 10^{-4} [82]. Other characteristics of HRS are shown in table 5.2.

Optical length	23.4 m
Momentum range	0.3-4.0 GeV/c
Momentum acceptance	$-4.5\% < \delta p/p < +4.5\%$
Momentum resolution	1×10^{-4}
Left arm HRS angular range	$12.5 - 150^\circ$
Right arm HRS angular range	$12.5 - 130^\circ$
Horizontal angular acceptance	± 30 mrad
Vertical angular acceptance	± 60 mrad
Horizontal angular resolution	0.5 mrad
Vertical angular resolution	1 mrad
Solid angle at $\delta p/p = 0, y_0 = 0$	6 msr
Transverse length acceptance	± 5 cm
Transverse position resolution	1 mm

Table 5.2 Characteristics of the Hall A HRS [82]

5.5.1 Septum magnet

The g2p experiment measured the scattered electron in 6° forward angle. However, the minimum achievable angle for the HRS is 12.5° . The septum magnets were installed in front of the spectrometer to reach the angle to 6° for two arms. The target was placed 87.693 cm upstream of the traditional Hall A center to accommodate the magnets. The schematic of the septum is shown in figure 5.47. Combining with the septum and the HRS, the angular acceptance is ~ 2 msr, and the momentum resolution is $\sim 2 \times 10^{-4}$.

5.5.2 Detector package in HRS

The detector package for the HRS is installed in a shield hut with the data acquisition electronics (DAQ) at the end of the magnet group as shown in figure 5.2, id 14. The layout of the detector package is shown in figure 5.48. The detector package contains a set of vertical drift chambers used for tracking information, a gas Cerenkov detector and a set of lead glass calorimeter used for particle identify, two sets of scintillators used for the DAQ trigger. The efficiencies of the detectors were studied in detail.

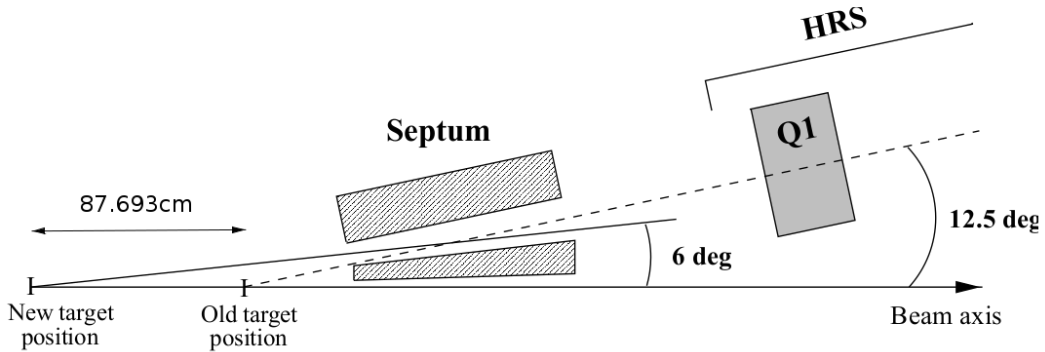


Figure 5.47 Schematic diagram of the septum magnet

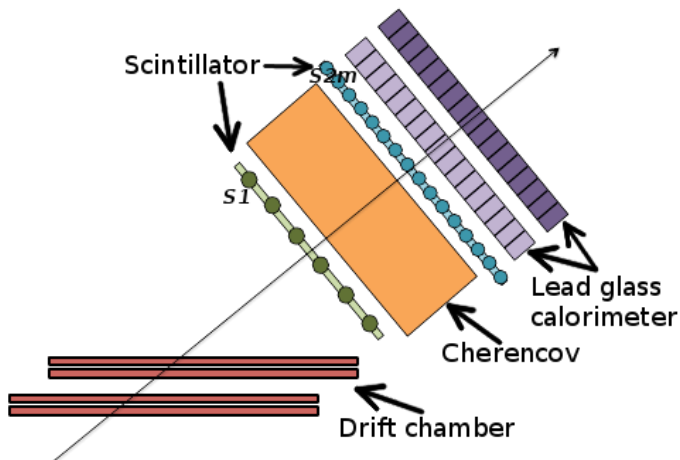


Figure 5.48 Layout of the detector package

5.5.2.1 Vertical drift chambers

The vertical drift chambers (VDC) were used to measure the position and angle of incidence electrons at the spectrometer focal plane at a level of $\pm 125 \mu\text{m}$ and 0.5 mrad, respectively [158]. The diagram of the VDC is shown in figure 5.49. The VDC is composed of two wire planes with 0.335 m vertical separation, each plane contains 368 sense wires [159]. Each plane is selected a perpendicular UV wires configuration, which are inclined angle of 45° respect to the dispersive and non-dispersive directions. The chambers are filled with the gas mixture of argon and ethane. The electric field is generated by a high voltage with the nominal operating voltage of -4 kV. Each wire is connected to the Time-to-Digital Converter (TDC) to reconstruct the track. The timing is used to determine the drift distances for each wire. A linear fit of drift distances versus wire position is used to determine the cross-over point of the track.

The VDC's track efficiency is defined as [160]:

$$Eff_{VDC} = \frac{N_{good}}{N_{total}}, \quad (5.40)$$

where N_{total} is the total events, N_{good} is the number of good events which have at least one track reconstructed in VDC and verified by the lead glass calorimeters. Usually we

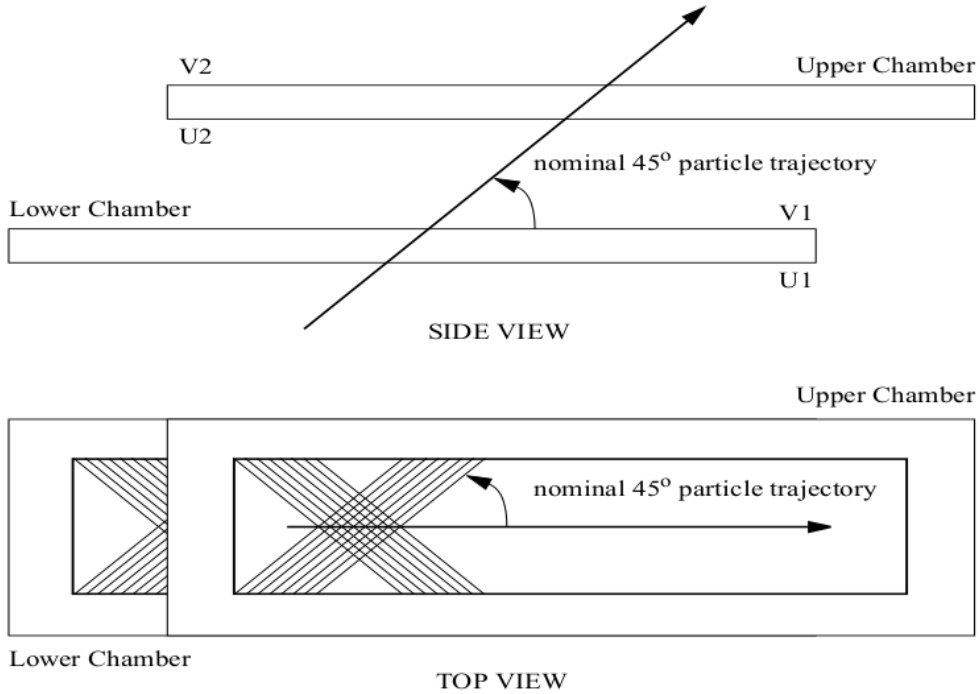


Figure 5.49 Schematic diagram of the VDC

use the single-track efficiency instead:

$$Eff_{VDC_single} = \frac{N_{single}}{N_{total}}, \quad (5.41)$$

where N_{single} is the number of events which only have one good track. Figure 5.50-5.51 (a) show the single-track efficiencies for the g2p experiment, and (b) shows the multi-track probabilities. The figures clearly show that in some momentum ranges (near the elastic) the probability for an event with multi-tracks can reach 30%. The multi-track events were carefully distinguished using the information from lead glass. The total track efficiencies can be reached to more than 99% after the correction (figure 5.50-5.51 (c)).

5.5.2.2 Trigger scintillators

A pair of plastic scintillator planes (S1 and S2m) separated by 2 m triggers the data acquisition system. The S1 has six $0.5\text{ cm} \times 30\text{ cm} \times 36\text{ cm}$ paddles in a 1×6 arrangement. The S2m has sixteen $43.2\text{ cm} \times 5.1\text{ cm} \times 14\text{ cm}$ paddles in a 1×16 arrangement. Each paddle is read out via two photomultiplier tubes (PMTs) on two sides. Detail of the DAQ system will be described in chapter 5.6.

5.5.2.3 Gas Cherenkov detector

In order to distinguish between electrons and pions, a threshold gas Cherenkov detector is installed with a pair of electromagnetic lead glass calorimeter in each HRS. The gas Cherenkov is mounted between two scintillators and operated at atmospheric pressure with CO_2 with an index of refraction of 1.0004. It is based on the detection of the

Cherenkov light, which is produced by a particle passing through faster than light in the medium. A heavier particle such as a pion needs the momentum threshold of 4.87 GeV/c to produce the Cherenkov light, compared with the threshold of 18 MeV/c for an electron. None of the g2p momentum settings are higher than 3.3 GeV, the gas Cherenkov can suppress most of the pions.

Ten spherical mirrors with the radius of curvature of 90 cm [161] and the focal length of 80 cm [82] are installed. Each mirror is viewed by a PMT. The signals from the PMTs are sent to the analog-to-digital converter (ADC) and summed. The signal of the gas Cherenkov also provides the efficiency trigger for the DAQ system.

The detector efficiency of gas Cherenkov was determined by selecting a sample of events that were seen in the lead-glass calorimeter, and counting the number of these events that also fired the gas Cherenkov. The detector efficiency for gas Cherenkov was found above 99.8%, as shown in figure 5.52 [162].

5.5.2.4 Lead glass calorimeter

The pion can produce the knocked electrons from the materials, which can excite the signal in the Cherenkov detector. It can be suppressed by two layers of lead glass calorimeters in each HRS as shown in figure 5.53. The first layer for the right arm is composed of 48 $10\text{ cm} \times 10\text{ cm} \times 35\text{ cm}$ lead glass blocks which oriented perpendicular to the particle track, whereas the second layer is composed of 80 $15\text{ cm} \times 15\text{ cm} \times 35\text{ cm}$ lead glass blocks which oriented parallel to the particle track for the right arm. For the left arm the first layer is composed of $34\text{ }15\text{ cm} \times 15\text{ cm} \times 30(35)\text{ cm}$ lead glass blocks, and the second layer is composed of 34 similar blocks. Each block is viewed by a PMT and connected to the ADC.

To determine the detector efficiency for the lead glass calorimeter, a selection of electrons that triggered the gas Cherenkov is made. The number of these events that also trigger the lead glass calorimeter are then counted. The detector efficiency for the lead glass calorimeter was found above 98.8% in all kinematic ranges, as shown in figure 5.54 [162].

5.5.2.5 Cut efficiency and pion suppression

Three cuts are used for particle identification: a gas Cherenkov threshold cut, a cut on the first layer of lead glass, and a cut on the total energy deposited in the calorimeter. The purpose of these cuts is maximum suppressing the pion contamination and minimum cutting out the good electron events. The gas Cherenkov threshold cut can maintains a high electron detection efficiency greater than 99.5% percent for most of the kinematic settings, as shown in figure 5.55 [162].

The cuts on the lead glass calorimeter are momentum dependent, which were determined separately for each kinematic settings. They are chosen that the overall electron detection efficiency does not fall below 99%. The first layer cut was placed a conservative cut, while the summed energy in both layers were placed a separate cut. The overall pion suppression was determined by applying all of these three cuts. The level of residual pion contamination is below 0.0052 for π/e for all kinematic settings, as shown in figure 5.56 [162].

5.5.3 Simulation package

A new Monte-Carlo simulation package was developed to study the spectrometer acceptance and the optics calibration with the target field. It has been tuned to work with the effect of the target and septum fields. The package was developed with an optimized Runge-Kutta method with self-adjusting step length to improve the speed and accuracy, based on the hall A Single Arm Monte-Carlo (SAMC) package. Several different cross-section models and energy-loss models are included in the elastic and resonance kinematic regions. The simulation results are also used to compare with the results in the packing fraction study.

5.5.4 Spectrometer optics

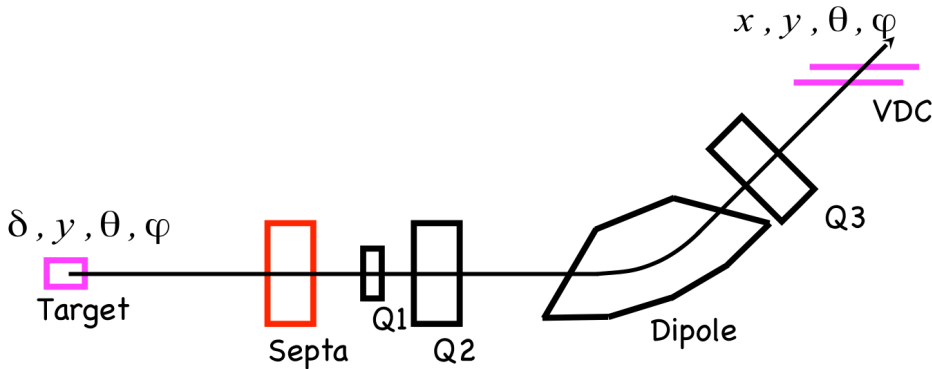


Figure 5.57 Schematic of the components related in the optics study

The purpose of the HRS optics study is to reconstruct the kinematic variables of the scattered electrons at the reaction point with a set of optics matrix elements, as shown in figure 5.57. The relationship between the variables at the reaction point (target) and at the focal plane for the first order approximation is:

$$\begin{pmatrix} \delta \\ \theta \\ y \\ \phi \end{pmatrix}_{tg} = \begin{pmatrix} <\delta|x> & <\delta|\theta> \\ <\theta|x> & <\theta|\theta> \\ & <y|y> & <y|\phi> \\ & <\phi|y> & <\phi|\phi> \end{pmatrix} \begin{pmatrix} x \\ \theta \\ y \\ \phi \end{pmatrix}_{focal}, \quad (5.42)$$

where δ is defined as:

$$\delta = \frac{P - P_0}{P_0}, \quad (5.43)$$

where P is the measured momentum for scattered electron, and P_0 is the spectrometer central momentum. The variables $(\delta, \theta, y, \phi)_{tg}$ are defined in the target coordinate system, as shown in figure 5.58. The z direction of the target coordinate system is defined by the direction of spectrometer central ray. The optics data with no target field has been optimized for both the left and right HRS, which allows us to remove the additional complexity of the target field and focus on the septa and HRS magnets.

The angles θ and ϕ related optics matrix elements are calibrated with the standard sieve slit method [163]. A single carbon foil target and the point beam (without raster) were used for this purpose. The sieve slit (figure 5.59(a)) was located between the target and the septum. The θ_{tg} and ϕ_{tg} were calculated from the known geometry of sieve slit and the survey data. The reconstructed sieve slit histogram after the calibration is shown in figure 5.59(b).

The δ was calibrated by using the elastic peak of carbon data. The reconstructed momentum after the calibration is shown in figure 5.60.

At the very forward scattering angle of 5.69° , foil targets with a large z position separation are needed to calibrate the y_{tg} related optics matrix elements. A single foil carbon target and the aluminum entrance window of the target chamber are used for this purpose. This will make the resolutions slightly worse but still satisfy our requirement. The calibrated result is shown in figure 5.61.

In addition to the calibration of the optics matrix, the central angle of the spectrometer system is studied with two different methods: using survey information or using double elastic peaks [164]. The survey information provides smaller systematic uncertainty and is the one being used. The central angle, together with the relative scattering angle reconstructed by the optics matrix, is used to calculate the scattering angle of the out-going electrons.

The resolutions for the optics without the target field are close to the nominal performance of the HRS system as shown in table 5.3.

RMS	LHRS	RHRS	Nominal performance [163]
$\delta[dp]$	1.5×10^{-4}	2.4×10^{-4}	1.1×10^{-4}
$\theta[\text{out of plane angle}]$	1.59 mrad	1.57 mrad	2.55 mrad
y	3.3 mm	2.9 mm	1.7 mm
$\phi[\text{in plane angle}]$	0.99 mrad	0.82 mrad	0.85 mrad

Table 5.3 Performance summary of RMS values for optics study without target field

In g2p setting, the strong transverse target field makes the optics study more challenging. To deal with this target field, the reconstruction process is separated into two parts. The first part, containing the septum magnet and HRS, is assumed to be represented by the matrix with no target field which has been described above. Unfortunately, the configuration changes during the experiment because of the broken septum magnet, which requires the matrix elements to be re-calibrated. The simulation package mentioned above is used to calculate the reference angles of the fits for the recalibration. The second part, the target field region, is treated only with a ray-tracing method. The same simulation package is also used here to calculate the trajectory of the scattered electrons.

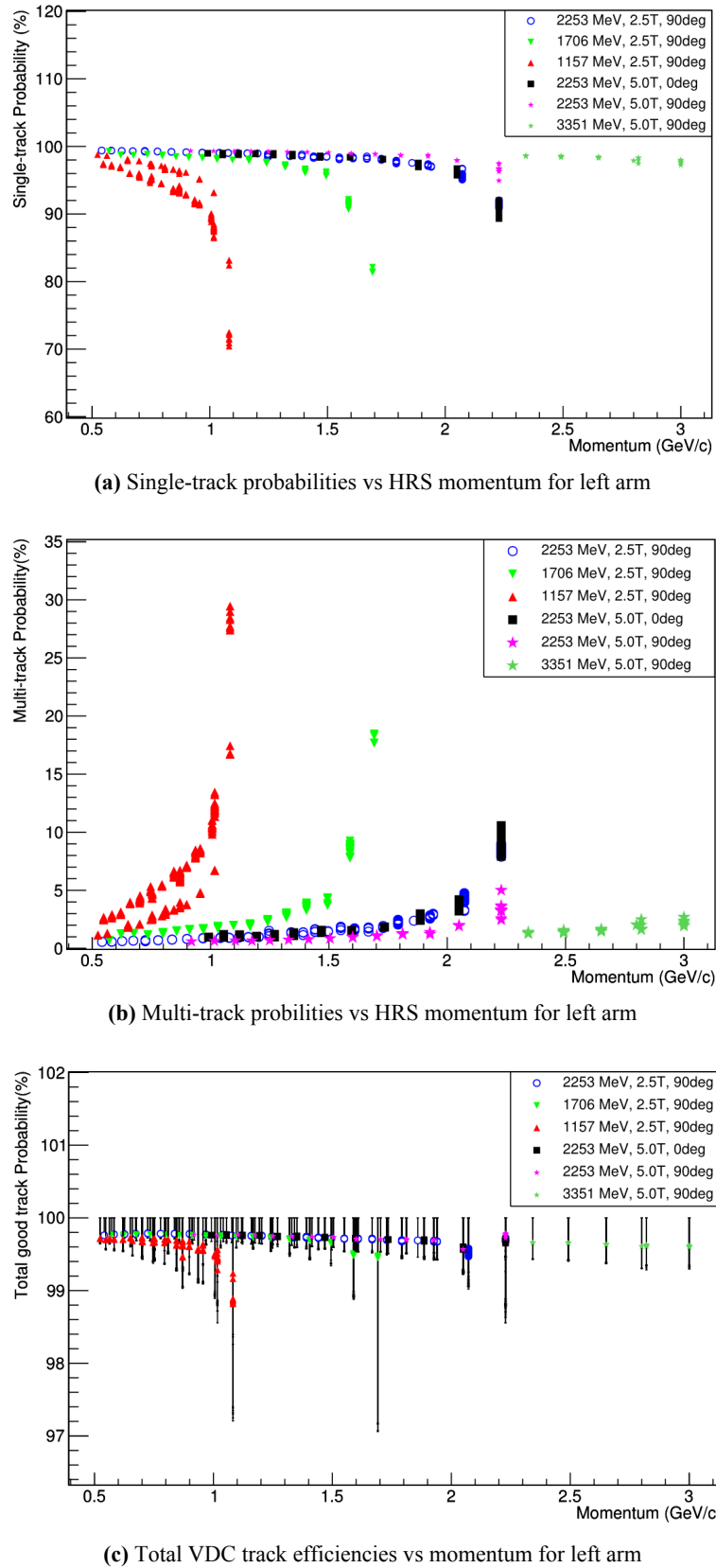
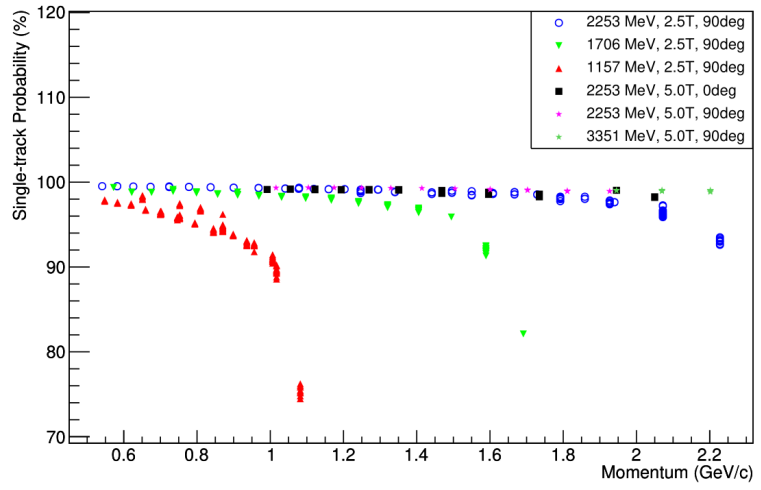
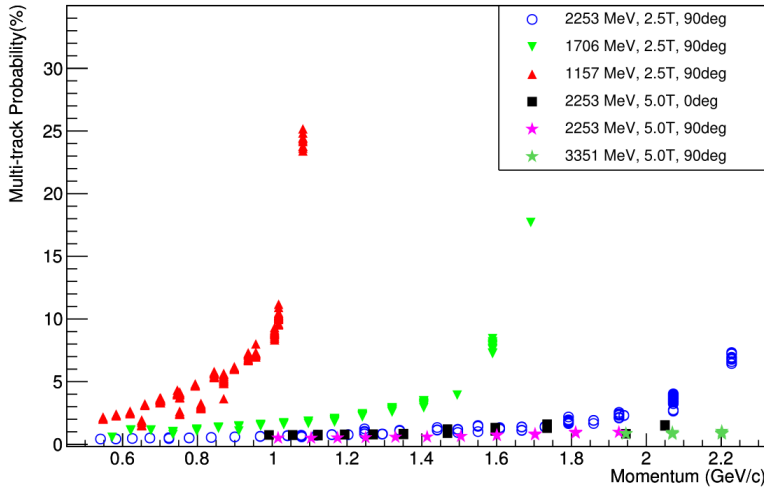


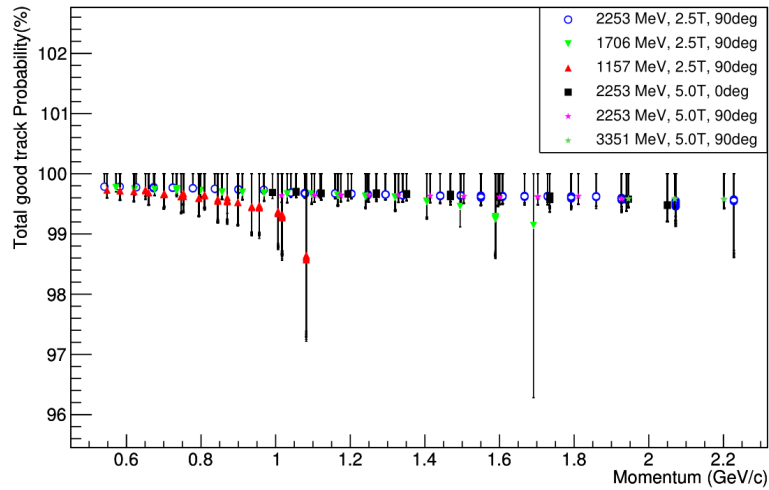
Figure 5.50 VDC track efficiencies for left arm [160]



(a) Single-track probabilities vs HRS momentum for right arm



(b) Multi-track probabilities vs HRS momentum for right arm



(c) Total VDC track efficiencies vs momentum for right arm

Figure 5.51 VDC track efficiencies for right arm [160]

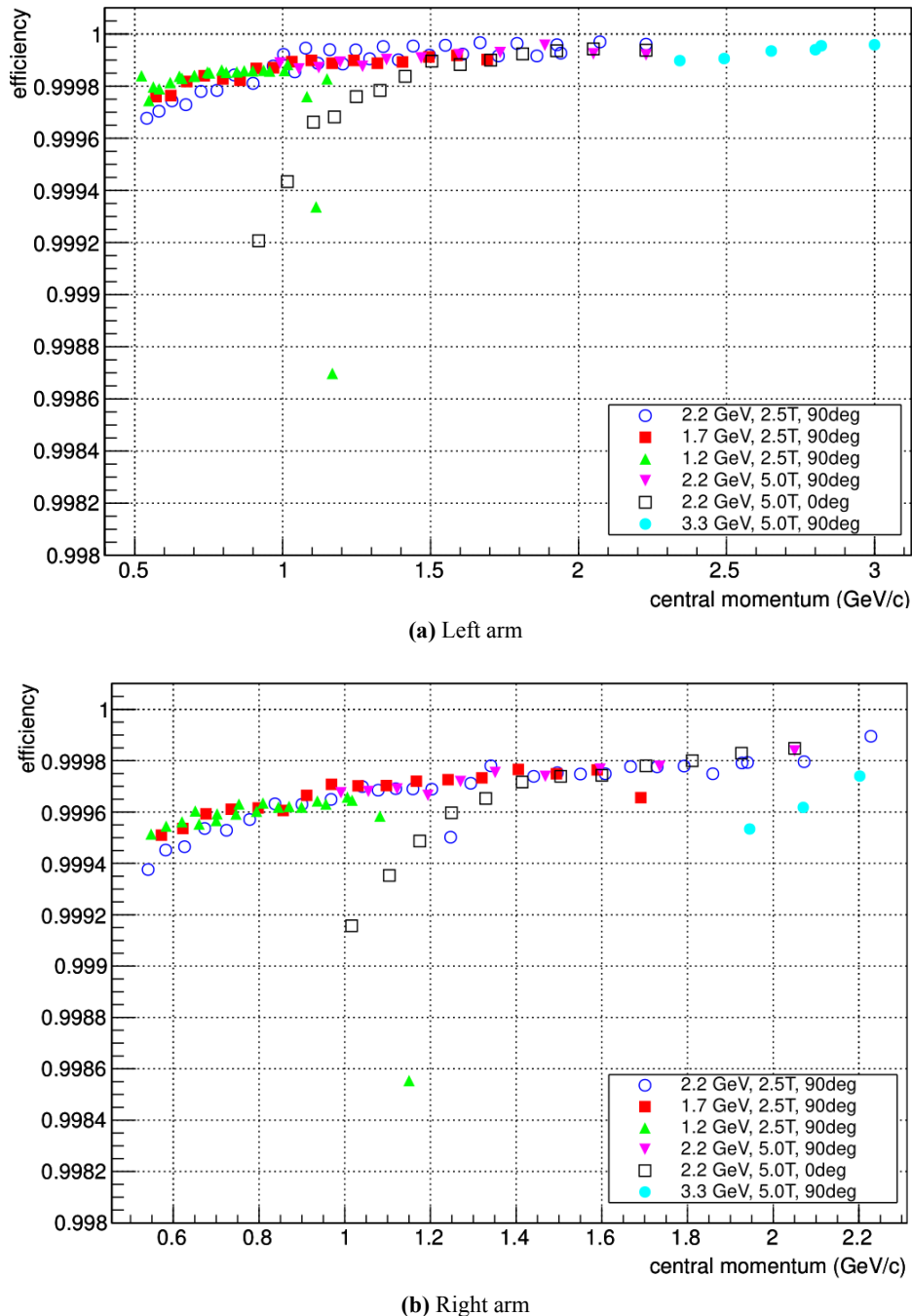


Figure 5.52 Detector efficiency for gas Cherenkov detector [162]

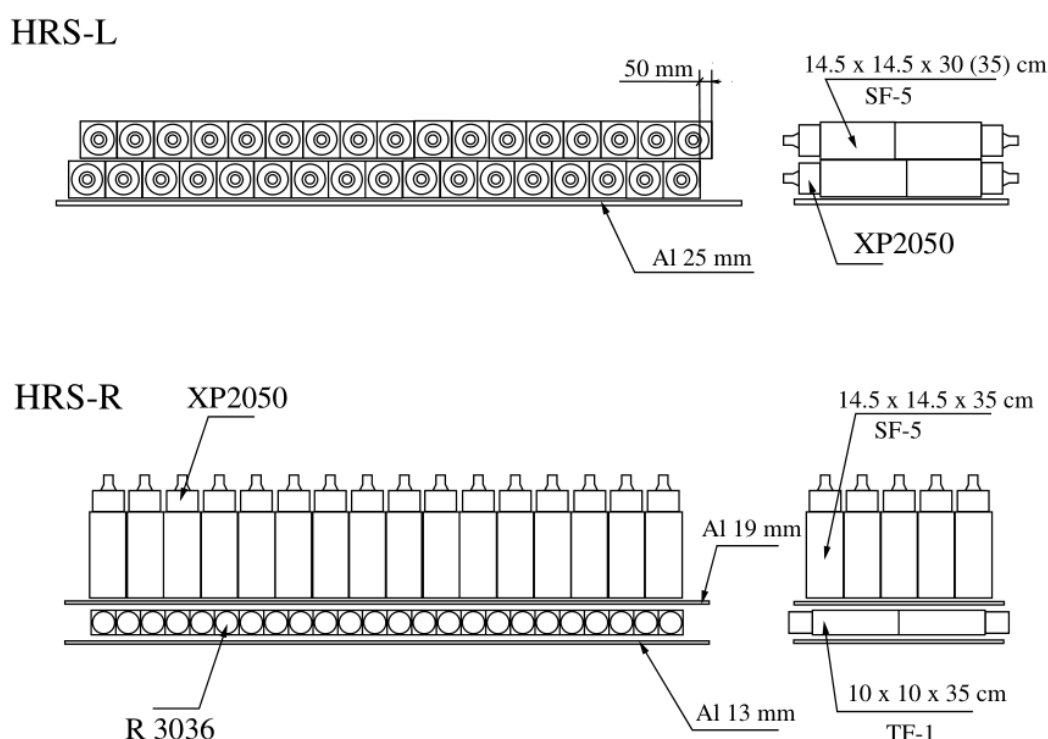


Figure 5.53 Layout for the lead glass calorimeters for two arms[82]. HRS-L for left arm, HRS-R for right arm.

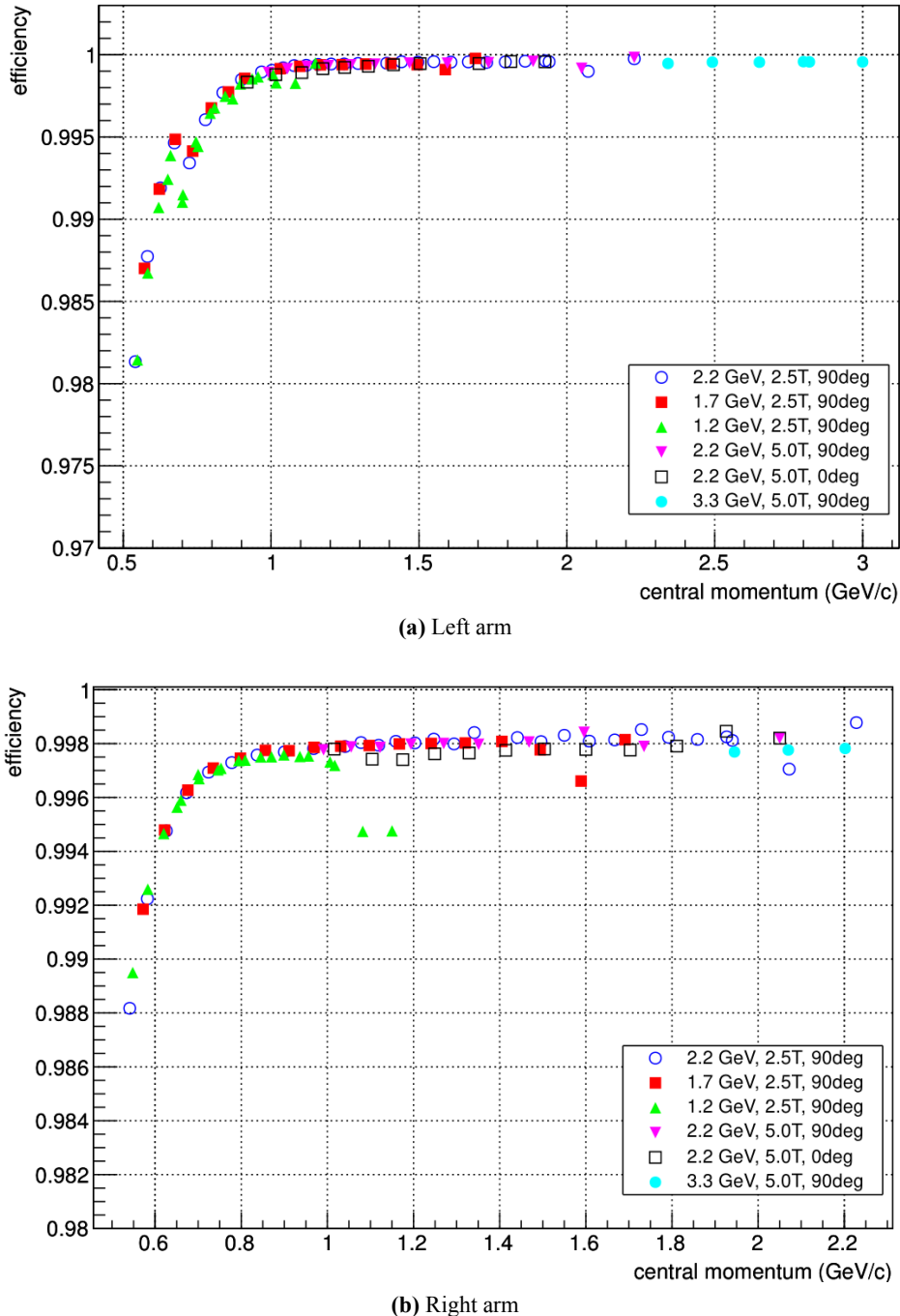


Figure 5.54 Detector efficiency for lead glass calorimeter [162]

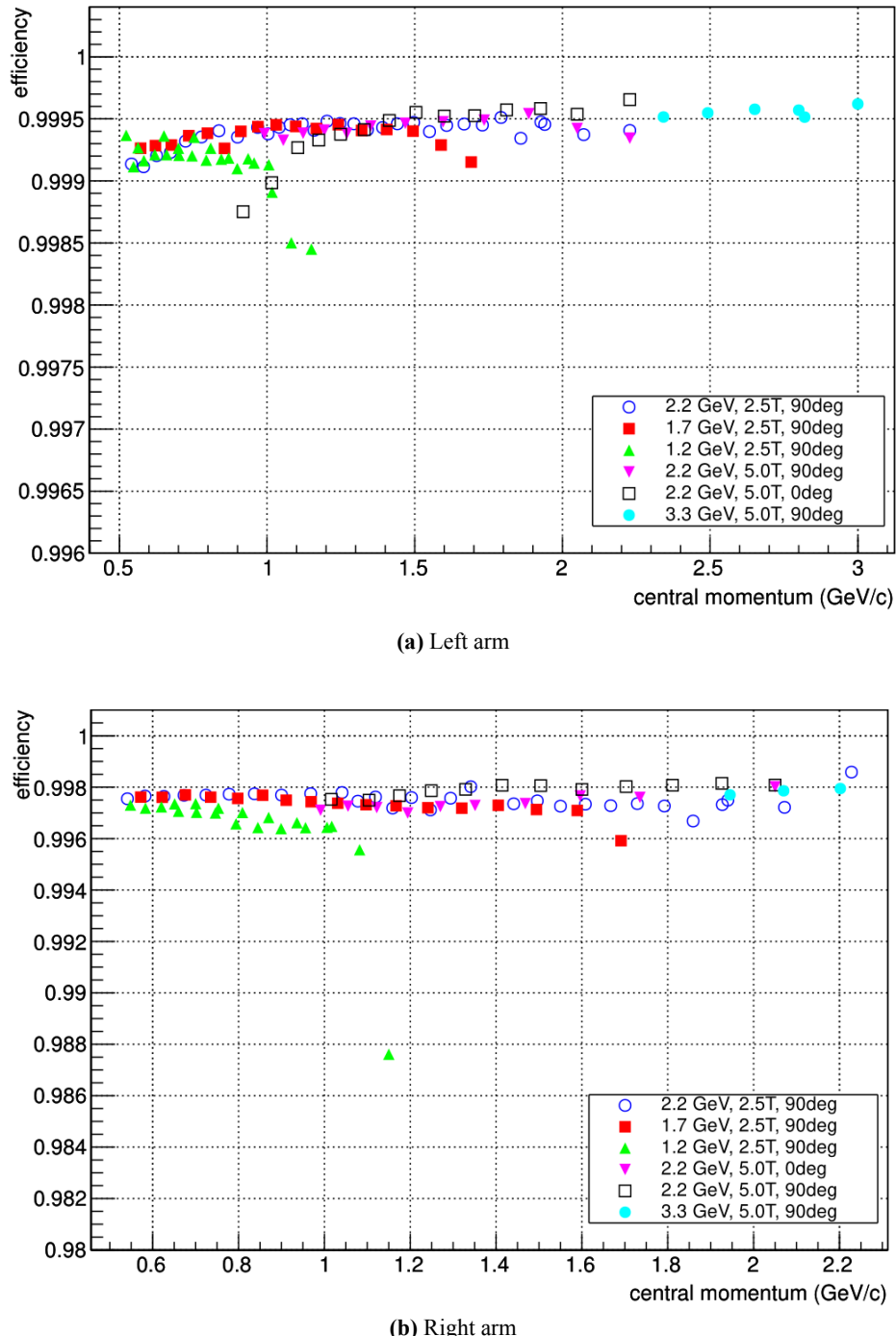
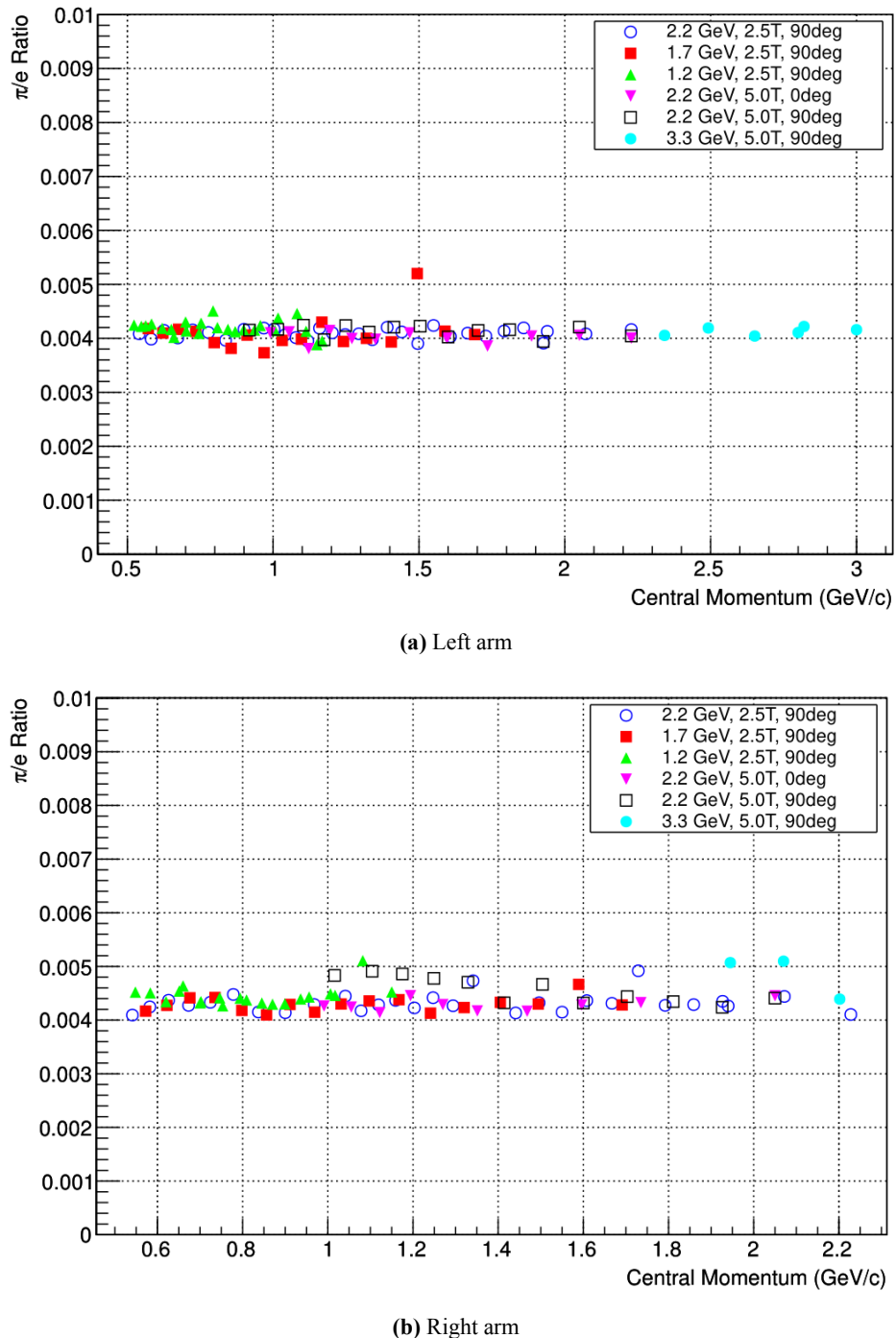


Figure 5.55 Cut efficiency for gas Cherenkov detector [162]

**Figure 5.56** Pion suppression [162]

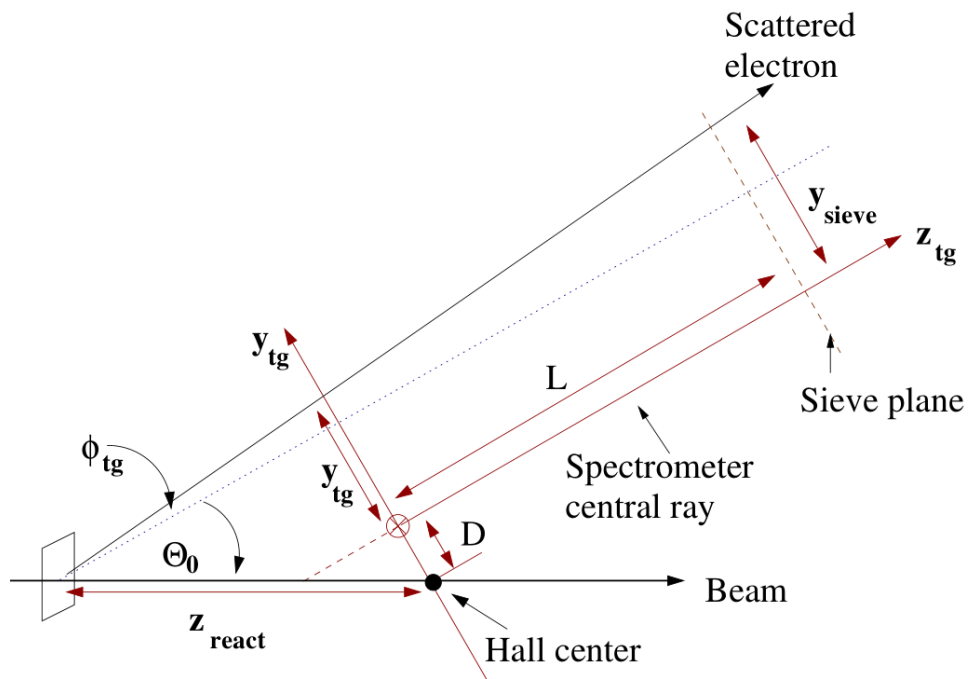
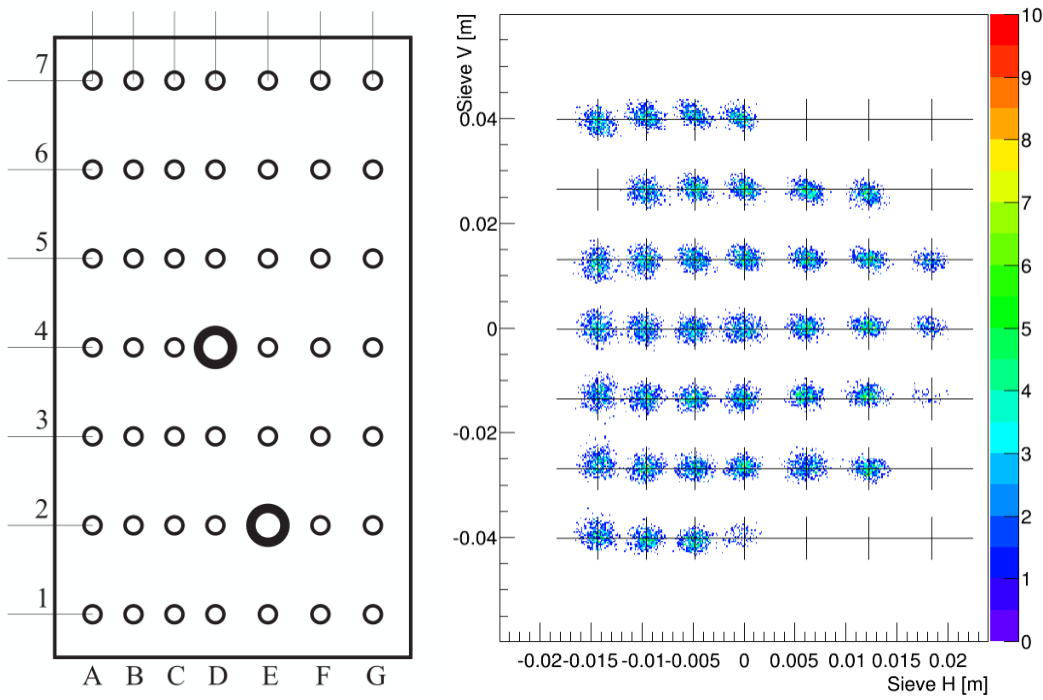


Figure 5.58 Target coordinate system



(a) Sieve slit. Labels on the left and button are for convenient during the study. Two of the holes are large holes which used to determine the orientation.

(b) Reconstructed sieve slit

Figure 5.59 Sieve slit and its reconstructed histogram

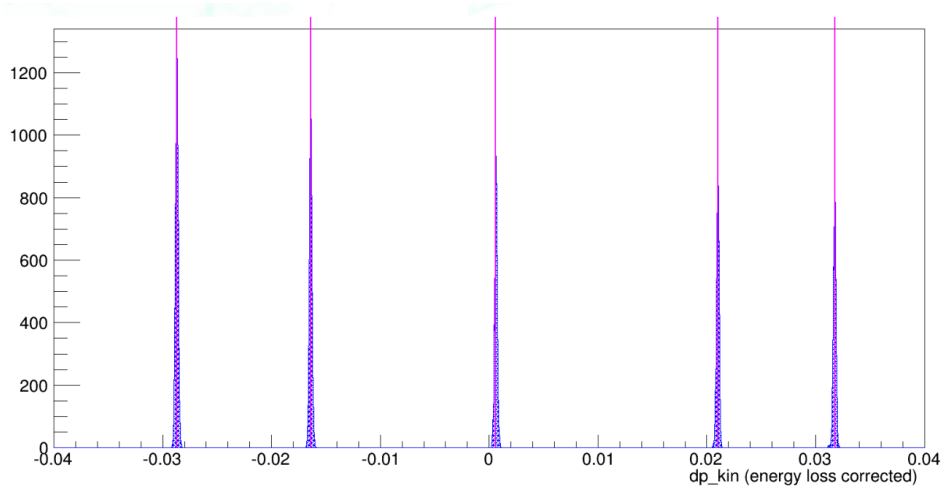


Figure 5.60 Reconstructed momentum after calibration, red line is calculated from carbon elastic.

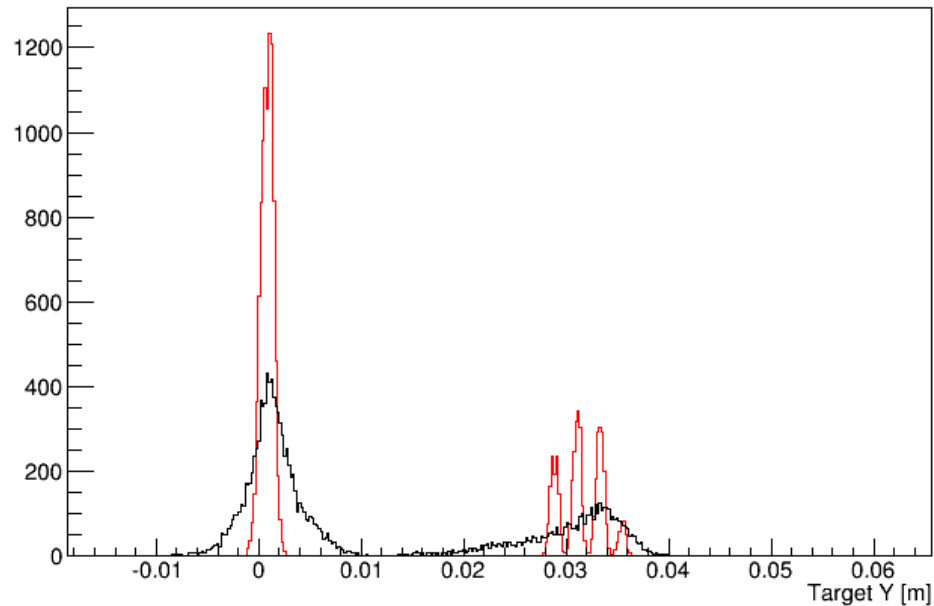


Figure 5.61 Reconstructed y after calibration. The red histograms are calculated from survey, the black one are from reconstruction.

5.6 The Data Acquisition System

The standard HRS DAQ system was used for recording the detector information. The helicity based DAQ systems, scaler ringbuffer and HAPPEX DAQ, were installed for getting the helicity related information, such as the charge and the helicity for each event. For the double check of $P_b P_t$ measurement, an independent DAQ system which called third arm DAQ was built by a measurement of the proton's elastic asymmetry.

5.6.1 Single arm HRS DAQ

5.6.1.1 Event trigger

When the scattered electron passed through two scintillators, the logical signal of S1&S2m (means both scintillator have signal) was used for the main trigger. The gas Cherenkov counter was used for checking the trigger efficiency, the logical signal of (S1 xor S2m)&cer was defined for the efficiency trigger, which means one of two scintillators have signal, but not both, and at the same time gas Cherenkov have signal. The trigger efficiency was defined as:

$$E_{ff} = \frac{T_{main}}{T_{main} + T_{eff}}, \quad (5.44)$$

where T_{main} and T_{eff} are total accounts of main trigger and efficiency trigger [165].

The trigger efficiency for both arms are shown in figure 5.62. The results show most of runs the efficiency is higher than 99.1%.

5.6.1.2 Connection

There are 3 fastbus crates, 1 trigger supervisor scaler crate, 1 HAPPEX crate for each arm. The main trigger and the efficiency trigger was connected to the trigger supervisor after several logic modules and trigger the ADC and TDC in fastbus crate to collect the data from detectors (figure 5.63). The trigger supervisor is the device distributes triggers and maintains system busy signals. The charge information from BCM and the trigger count was recorded in scaler.

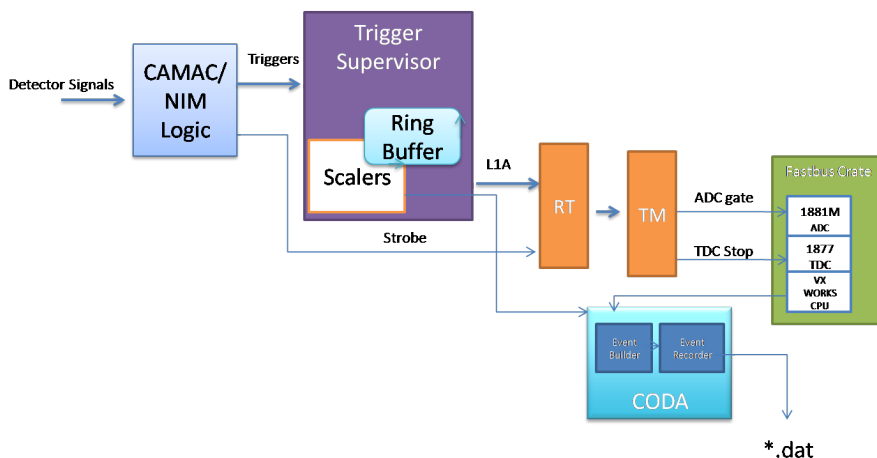


Figure 5.63 Hall A standard DAQ system

5.6.1.3 Scaler

The scaler sis38xx have two mode, sis3800 and sis3801. The former is a counter, each trigger caused to read the count once. The sis3800 was used to save the information of charge, clock and trigger signal for each event; the latter is a ring buffer triggered by helicity, each event trigger pulse caused to read out the buffered data saved in FIFO and clean it. The sis3801 was used to save the helicity dependent charge, clock and trigger signal.

5.6.1.4 Dead time

When DAQ cannot accept another trigger, the deadtime occurs. Since g2p ran in low Q^2 level, the physics rate was large even if the beam current kept in a low level of 50 nA. The deadtime includes two part: the readout deadtime (D_r) and the conversion deadtime (D_c , or front-end deadtime). The conversion deadtime occurs when a trigger come and ADC/TDC is still busy dealing the signals from last trigger [166]. The readout deadtime occurs when the read out control (ROC) cannot accept new event. The total deadtime is the sum of them: $D_r + D_c$. To reduce the dead time for the HRS DAQ system, the buffered mode was used, which means the event is buffered before readout and the trigger supervisor can process a new event while reading out the previous event, and readout time is separated with the conversion time. During the whole experiment, the deadtime kept near 25% (figure 5.64) when the prescale set to 1 and running 6.5 kHz of production run, this was a new record in Hall A at Jefferson Lab.

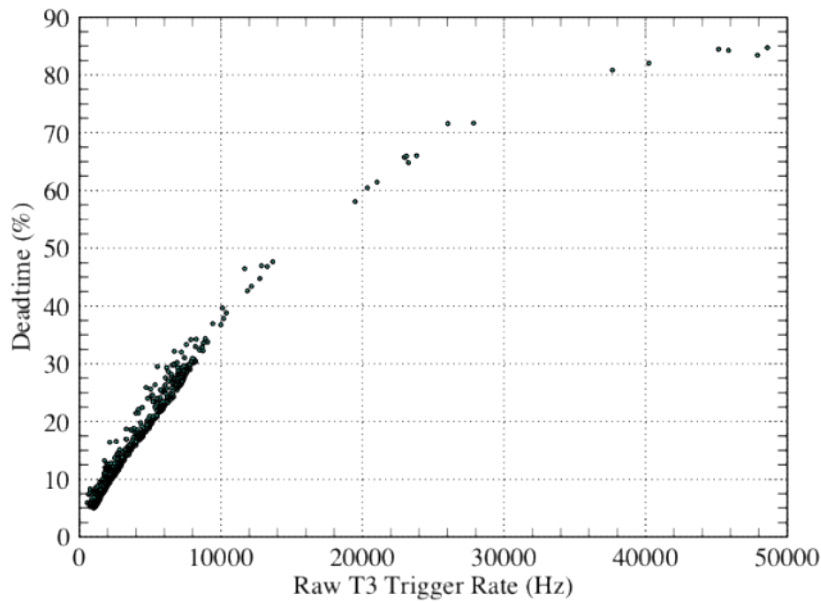


Figure 5.64 DAQ deadtime during production run, T3 is the main trigger in left arm.
The trigger rate was kept around 6~7 kHz after the prescale during the experiment.

5.6.2 Helicity

The beam was polarized in injector before going to CEBAF accelerator and controlled by a helicity control board, which is a NIM board. The helicity control board generate

Mode	Free clock
T-Settle	$70 \mu s$
T-Stable	$971.65 \mu s$
Helicity Pattern	+ - -+ or - + +-
Reporting delay	8 window
Helicity board frequency	960.015 Hz

Table 5.4 Helicity configuration

several signals which relative to each other. It controls the high voltage supply to change the orientation of laser's polarization, which was used to generate the polarized electron beam with GaAs photogun by using the method of optical pumping. Meanwhile the helicity control board send four waves to the DAQ system in Hall. During the g2p experiment the helicity setting is the same as QWEAK experiment in Hall C, as shown in table 5.4.

5.6.2.1 helicity signals

Four waves sent to hall during experiment by fiber which named T-Settle (or MPS), pattern_sync (or QRT), pair_sync, delayed helicity (figure 5.65). The quartet helicity pattern is used for experiment to minimize the system error, which is “+ - -+” or “- + +-”, one pattern is composed with four helicity windows. The pattern_sync shown the first window of one pattern. The T-Settle signal is used for judging if helicity is reliable and triggering the helicity related DAQ like sis3801 scaler and HAPPEX DAQ. The pair sync signal flipped in each helicity window, which was used as the redundancy information. The helicity flip signal sent to hall is 8 windows delayed with the real helicity flip signal, and need to further dealt for use.

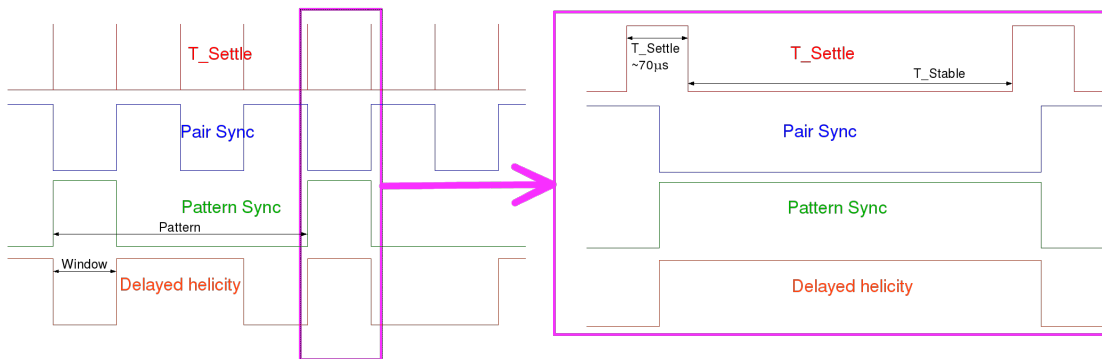


Figure 5.65 Helicity signal

5.6.2.2 storage

The helicity signal sent to hall A was connected to several places: trigger interface register (TIR) to record the helicity status for each physics event; sis3801 scaler's ring buffer to record the charge for each helicity status; HAPPEX DAQ (will discuss below) for the more precise current and position record for each helicity status. The helicity gated sis3801 scaler and HAPPEX DAQ was triggered by T-Settle signal.

5.6.2.3 helicity decoder

The helicity control board uses a 30 bit register generate pseudo-random bits to control the pattern of helicity, the prediction program is needed to regenerate the actual helicity. We built a new helicity decoder package to regenerate the actual helicity in offline analysis. The main idea is to use 30 continuous helicity pattern as pseudo-random seed to predict the actual helicity. Since the beam tripped during run, each trip caused the helicity needed to be predicted again if the trip time is too long. The events before helicity successfully predicted might not usable for the data analysis. To get more efficiency decoder and recover more events, we did two times of prediction, one predict from the start of the events, one predict reversed from the end of event.

There are three devices recorded the helicity signal, the TIR, scaler ringbuffer, HAPPEX ringbuffer. The advantage of using three devices to record is we can predict each devices and compare of them, and we can recover more events even if one device failed to predict. The scaler ringbuffer and HAPPEX ringbuffer was triggered by helicity, the ringbuffer is an array saved in FIFO for former and CPU's register for latter. Each element in array includes the information of helicity, charge, clock signals for this helicity status (figure 5.66). In order to let all ringbuffer data recorded in data-stream, and not be affected with beam trip, the minimum DAQ rate was set as 20 Hz by using of the clock signal combined with prescale, since the maximum ringbuffer readout is 50 buffers considered about the dead time and the helicity frequency is about 1 KHz. The ringbuffer worked much stable and didn't have any problems during experiments. The prediction for ringbuffer helicity is easy and don't have additional treatment.

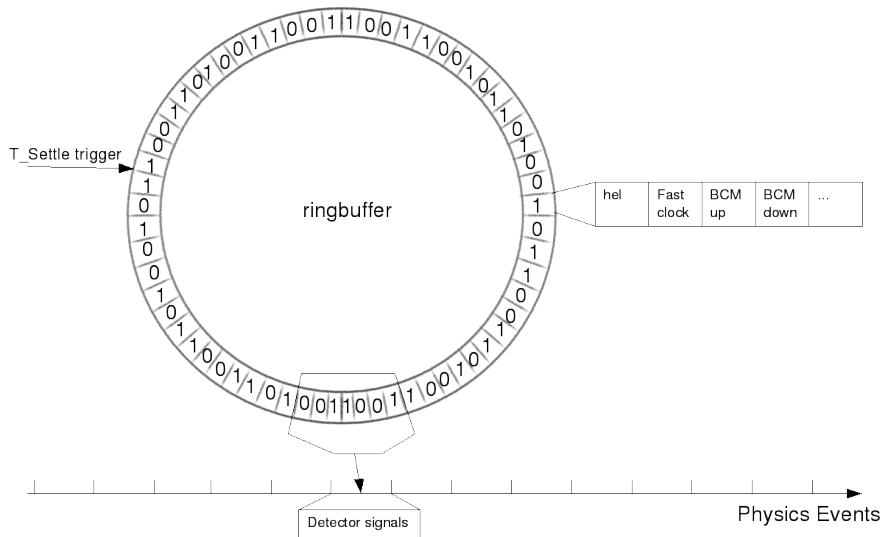


Figure 5.66 Ringbuffer

Since TIR uses physics trigger, there might have several events that have same helicity status, or some helicity status may lose. The direct prediction may fail for these situations. The solution is using the fast clock signal recorded in TIR as time stamp, compare the time stamp to judge if there are multiple physics events in one helicity status or there are helicity status lost.

5.6.3 HAPPEX DAQ

The HAPPEX DAQ uses 18bit ADC which designed for the parity violation experiments. The reason to use it is because of its high bit resolution, it is important to get high precise charge asymmetry. It was reprogrammed and reassembled for g2p experiment.

The HAPPEX DAQ contains a timing board (NIM) [167], several pieces of HAPPEX ADC [129], a flexible IO (FLEXIO,NIM) [168] , a trigger interface, and a vxworks CPU. The diagram for HAPPEX DAQ is shown in figure 5.67.

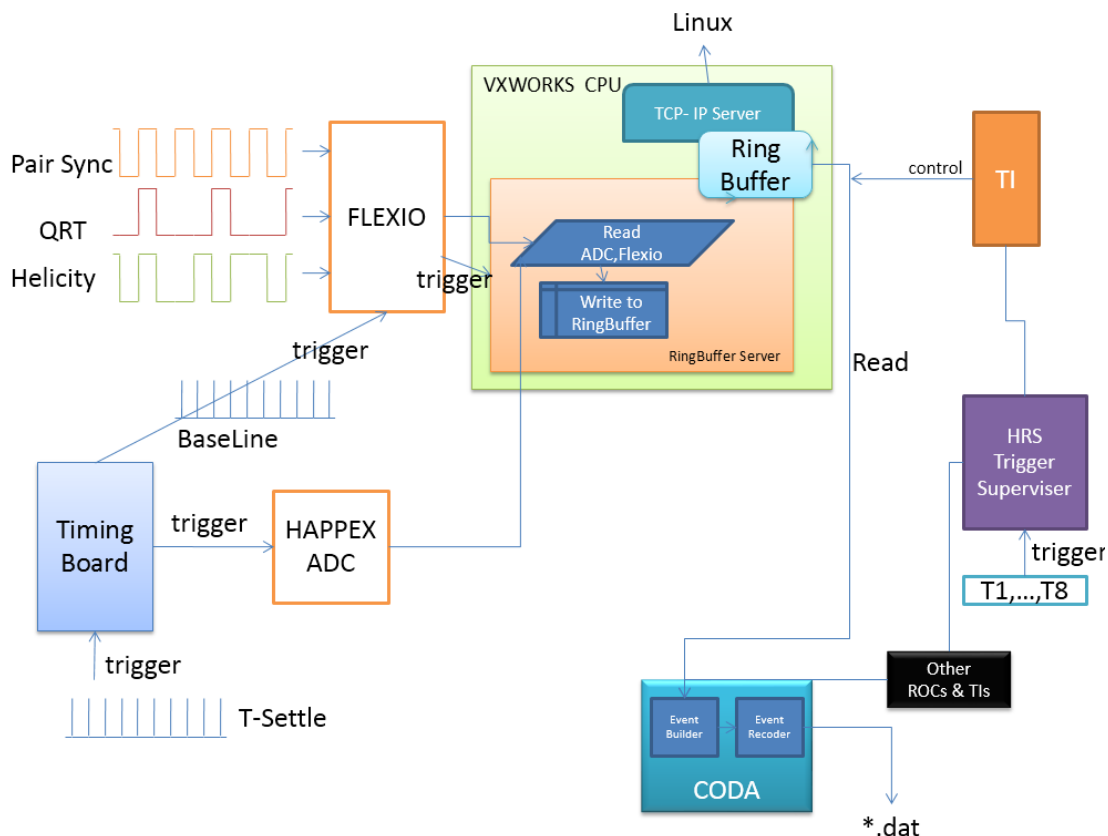


Figure 5.67 HAPPEX DAQ diagram

5.6.3.1 Timing board

The timing board is a NIM board that generate several time information to control when ADC start and stop integrating. The T-Settle signal is used as trigger source for timing board. Based on the trigger signal, the timing board generated a group of signals (figure 5.68). The reset signal controls the ADC integrating, the delay time between the baseline signal and the peak signal is used as integrated time, and the digital value difference between them is used as integrated result. The DAC module in timing board is also useful for debugging during the experiment.

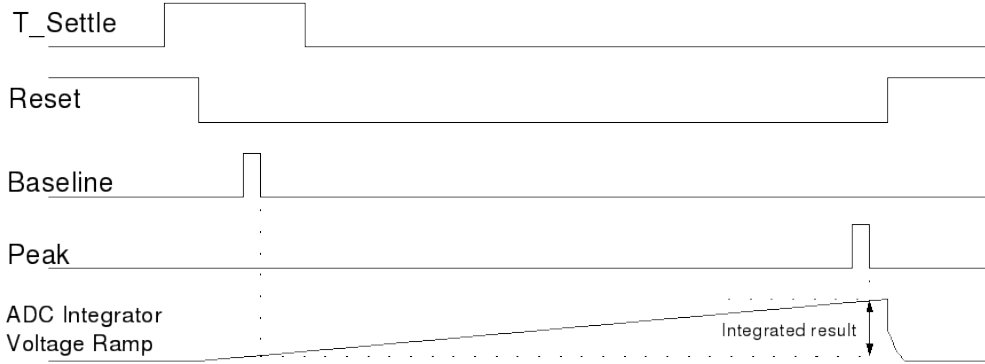


Figure 5.68 Timing board signals. [168]

5.6.3.2 HAPPEX ADC

The HAPPEX ADC was designed for high bit resolution (18 bit) and small non-linearity ($\leq 2 \times 10^{-5}$). From the asymmetry measurement test (figure 5.69), the bit resolution for HAPPEX ADC is much better than scaler. The integration time for HAPPEX ADC controlled by timing board for g2p is $875\mu s$, a little bit lower than helicity period ($1041.65\mu s$). This caused very precise record for position and current information.

5.6.3.3 Flexible IO

The flexible IO is a NIM board that used to record the digital information. In HAPPEX DAQ it was used to record the helicity signals. When a baseline signal peak came from timing board, the flexible IO recorded one group information. It also provides a trigger signal for further usage.

5.6.3.4 Ring Buffer

A vxworks CPU controls the data reading from HAPPEX ADC and flexible IO to the ringbuffer server in CPU's register. For more reliable performance and less CPU occupation, a trigger was used instead of checking pair sync polarity all of the time. The trigger information came from flexible IO with the same period as T-Settle. Each trigger caused CPU readout the data from flexible IO and ADC one time. To mix the data to the data-stream with detector data, a trigger interface controlled by HRS trigger supervisor was used for reading the data from ringbuffer server in CPU to the data-stream. For the debug usage online, a TCP-IP server was running in CPU in order to readout the data from ringbuffer from any linux computer at any time.

5.6.4 Third arm DAQ

The main purpose of third arm is to provide additional measurement of beam and target polarization and cross-checking the result from Møller and NMR measurement. The main idea is measuring e-p elastic asymmetry and compare with well-known physics asymmetry:

$$A_{raw} = P_b * P_t * D * A_{phy}, \quad (5.45)$$

where A_{raw} is measured e-p raw asymmetry, A_{phy} is physics asymmetry, D is dilution factor. P_b and P_t are the polarization of beam and target.

The third arm was located near target (figure 5.2, id 12). Due to low rates of elastic electrons at 42° scattering angle for the beam energy of 2.2/3.3 GeV, the proton's elastic peak at 72° scattering angle was measuring instead. The third arm DAQ uses two scintillator trackers for dE plane, which used in SANE experiment, one for X plane, another for Y plane; a proton array counters with four scintillators for E plane, which used in DVCS experiment. The trigger signal was set as coincidence between dE1 and dE2 plane, which is dE1&dE2. The energy deposition for each E plane is about 9.96~10.27MeV.

Due to the large scattering angle for elastic proton peak measurement, the third arm is very sensitive with the reactive status change. The slow raster's magnet current was connected to the third arm DAQ. If the beam hit the beam pipe or the target pipe, the histogram of x:y for slow raster will show the hot spot in the picture, and the rate for third arm will arise. Due to this feature, the third arm was also used for beam quality check during experiment. Figure 5.70 shows the third arm used for tuning beam using the carbon hole target.

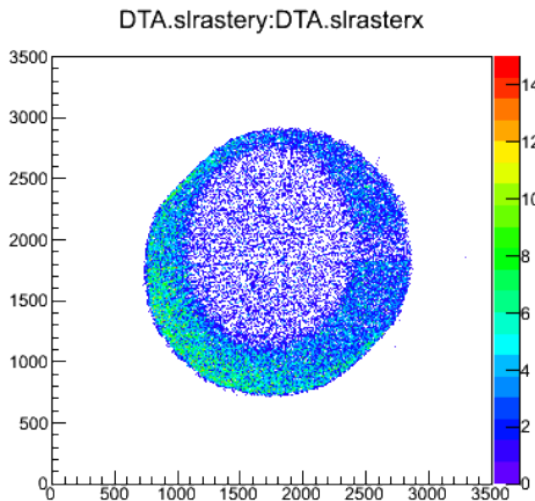


Figure 5.70 The slow raster current histogram in third arm DAQ. The hole in center shows less events in there, which reveals the carbon hole in the target stick. Since the scattered proton from hole region is much less than from target stick region.

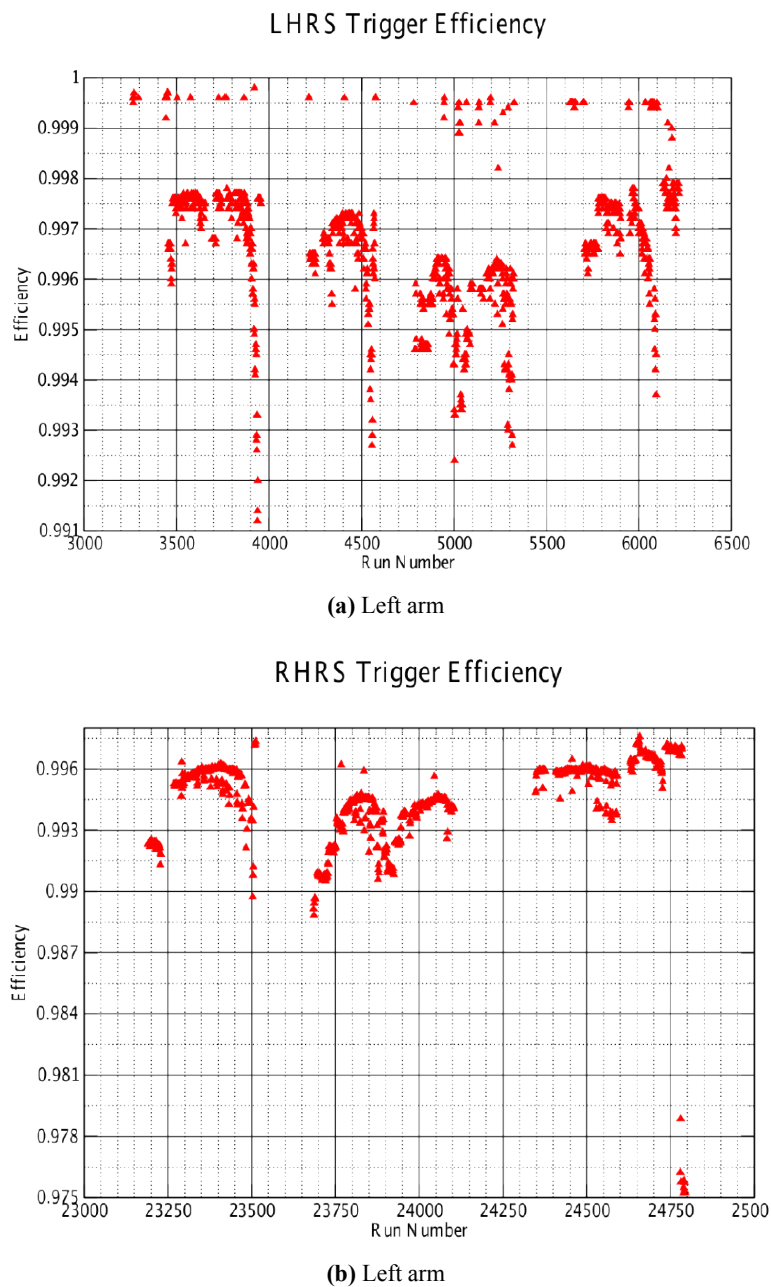


Figure 5.62 Trigger efficiency [165].

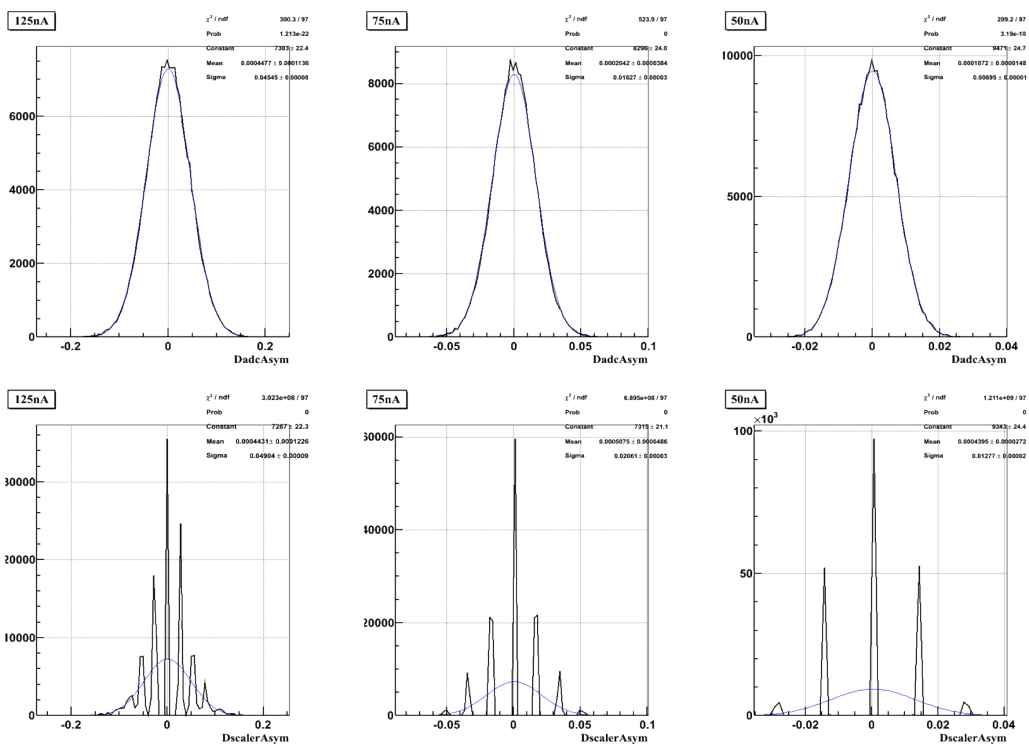


Figure 5.69 Comparison for charge asymmetry measurement histogram between using HAPPEX and scaler, up three use HAPPEX, down three use scaler. From left to right the current used are 125nA, 75nA, 50nA. The total events are same.

Chapter 6

Results

6.1 Extract asymmetry from data

The calculation of asymmetry is the first step to extract the spin structure functions. In order to get the asymmetry, the study of the polarization of beam and target, the packing fraction, the dilution factor and the radiative correction are needed. This section presents the physics asymmetries extracted from the data.

6.1.1 Asymmetry method

The physics asymmetry in either longitudinal or transverse setting is defined as:

$$A_{phys} = \frac{1}{P_b \cdot P_t \cdot D_f} A_{meas}, \quad (6.1)$$

where :

- P_b is the beam polarization,
- P_t is the target polarization,
- D_f is the dilution factor,
- A_{meas} is the measured asymmetry, which is calculated by:

$$A_{meas} = \frac{Y_+ - Y_-}{Y_+ + Y_-}, \quad (6.2)$$

where Y_{\pm} are the normalized yield in either helicity status. The yield is calculated as:

$$Y = \frac{p_s \cdot N}{Q \cdot L \cdot \epsilon_{det}}, \quad (6.3)$$

where:

- N is the number of counts,
- p_s is the prescale factor,
- ϵ_{det} is the detector efficiency which is equal to:

$$\epsilon_{det} = \epsilon_{VDC} \cdot \epsilon_{trig} \cdot \epsilon_{Cer} \cdot \epsilon_{cal}, \quad (6.4)$$

where ϵ_{VDC} is the VDC efficiency, ϵ_{trig} is the trigger efficiency, ϵ_{Cer} is the gas Cherenkov efficiency and ϵ_{cal} is the lead glass calorimeter efficiency,

- L is the livetime of the DAQ system, which is equal to $1 - \text{deadtime}$,
- Q is the total charge. Y_{\pm} , Q_{\pm} and L_{\pm} are the total charge and livetime in either helicity status, respectively.

The uncertainty of the physics asymmetry caused by the statistic is calculated as:

$$\delta A = \frac{2Y_+ Y_-}{(Y_+ + Y_-)^2} \sqrt{\frac{S_+^2}{N_+} + \frac{S_-^2}{N_-}}, \quad (6.5)$$

where S is the statistical fluctuation due to the prescale factor, which can be calculated as:

$$S = \sqrt{1 - Lf(1 - \frac{1}{p_s})}, \quad (6.6)$$

where f is the acceptance for useful events:

$$f = \frac{N_{\text{accepted}}}{N_{\text{recorded}}}. \quad (6.7)$$

6.1.2 Charge asymmetry

The charge asymmetry is defined as:

$$A_Q = \frac{Q_+ - Q_-}{Q_+ + Q_-}. \quad (6.8)$$

It is typically from the injector, such as from the pocket cell or half-wave plate. Checking the charge asymmetry is necessary to find the potential problems which will cause additional uncertainties. Figure 6.1 shows the charge asymmetries for the production runs during the whole experiment period. The average charge asymmetry for the whole run period is $83 \pm 187 \text{ ppm}$, which is very small.

6.1.3 False asymmetry

The false asymmetry is defined as the raw asymmetry for the unpolarized target. A lot of potential sources may cause abnormal false asymmetry, such as charge, livetime, the power-supply for each electronics, or even the commercial electricity. It is important to check it in detail. The false asymmetry was checked by using the carbon target or the dummy target which is unpolarized. The results are shown in figure 6.2. The average false asymmetry during the experiment is $-96 \pm 48 \text{ ppm}$, which will be used in the systematic error calculation.

6.1.4 Packing fraction

The NH_3 target cell is comprised of ammonia beads and liquid helium. The packing fraction, or the ratio of the length of ammonia to the total target length, must be understood for dilution analysis. The packing fraction was extracted from data using the NH_3 target, the dummy target and the carbon target.

The diagram of the target nose is shown in figure 6.3. The l_{tg} is the length of the

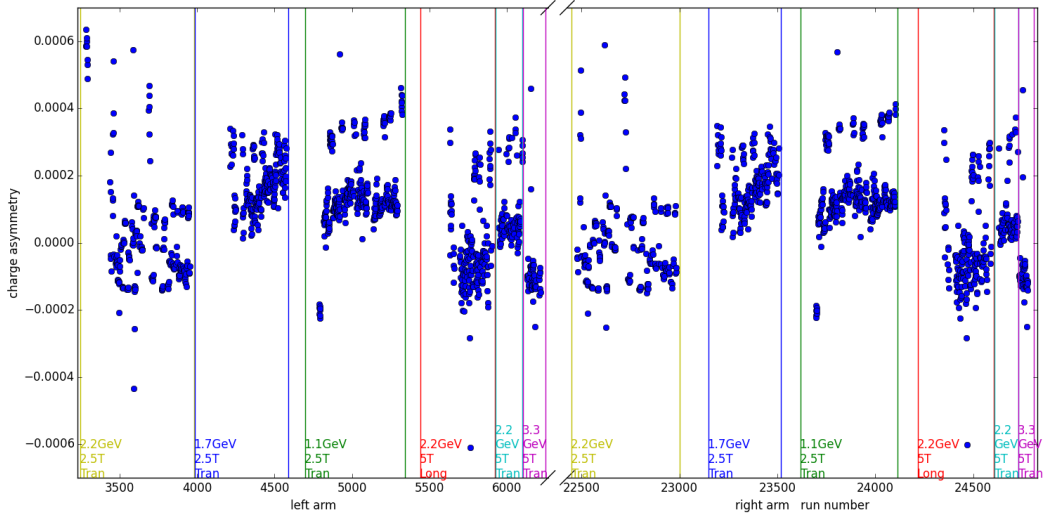


Figure 6.1 Charge asymmetries for the production runs during the whole experiment period

target chamber, while the l_{tot} is the total length of the target nose. Both of them were surveyed before the experiment. The NH_3 target chamber is shown in figure 5.38. The yield of production data using the NH_3 target can be exploded by [169]:

$$Y_{prod} = Y_{He}^{out} + (1 - p_f)Y_{He}^{full} + p_f Y_{NH_3}^{full}, \quad (6.9)$$

where:

- Y_{He}^{out} is the yield for helium outside the target chamber,
- Y_{He}^{full} is the yield for helium inside the target chamber if the target chamber is full of helium,
- $Y_{NH_3}^{full}$ is the yield for ammonia if the target chamber is full of the target material,
- p_f is the packing fraction.

The Y_{He}^{out} and Y_{He}^{full} can be obtained from the dummy target, where the target cell is filled only with liquid helium:

$$Y_{He}^{out} = \frac{l_{tot} - l_{tg}}{l_{tot}} Y_{dummy}, \quad (6.10)$$

$$Y_{He}^{full} = \frac{l_{tg}}{l_{tot}} Y_{dummy}, \quad (6.11)$$

The packing fraction can be extracted from the ratio of yield instead of calculating the absolute cross section which needs the additional acceptance factors from equations (6.9-6.11):

$$p_f = \frac{l_{tot}}{l_{tg}} \left(\frac{Y_{prod}}{Y_{dummy}} - 1 \right) \left(\frac{Y_{NH_3}^{full}}{Y_{He}^{full}} - 1 \right), \quad (6.12)$$

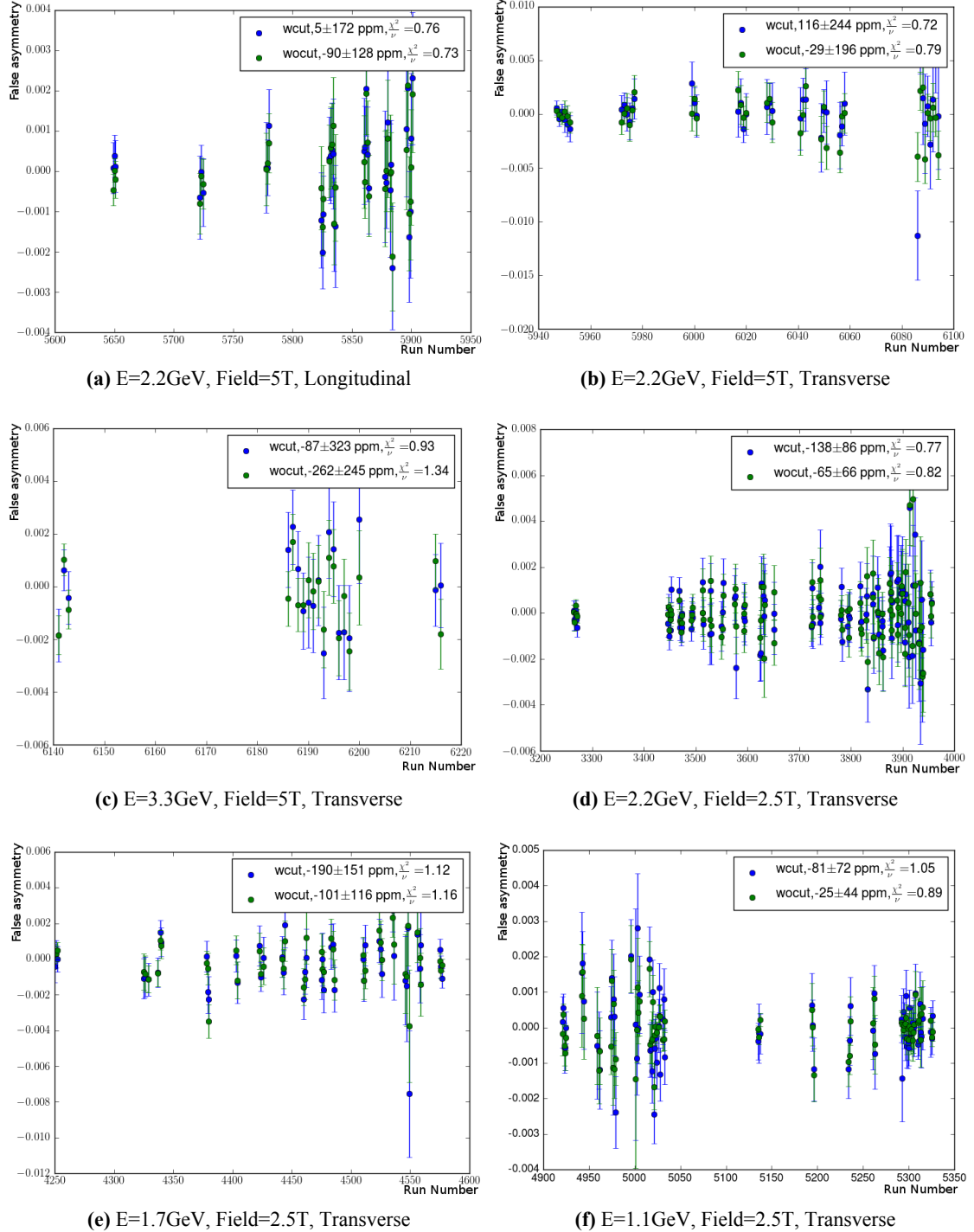


Figure 6.2 False asymmetries for different beam energy settings. Blue dots are without the detector cut, while green dots are with the detector cut.

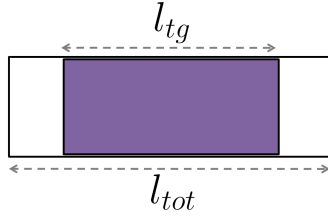


Figure 6.3 Diagram for the comparison of the l_{tg} and l_{tot} , where the former is the length of the target cell, and the latter is the length of the target nose [169].

It is not possible to extract the $Y_{NH_3}^{full}$ from the data. The elastic form factors are used to extract the ratio of $Y_{NH_3}^{full}/Y_{He}^{full}$. The yield has the relation with the cross section as:

$$Y = \sigma \frac{A_{cc} \cdot N_A \rho l}{M}, \quad (6.13)$$

where M is the molar mass, ρ is the density, A_{cc} is the acceptance, and l is the length. The equation (6.12) can then be written as:

$$p_f = \frac{l_{tot}}{l_{tg}} \left(\frac{Y_{prod}}{Y_{dummy}} - 1 \right) \left(\frac{\sigma_N}{\sigma_{He}} \frac{\rho_N M_{He}}{\rho_{He} M_N} + \frac{\sigma_H}{\sigma_{He}} \frac{\rho_H M_{He}}{\rho_{He} M_H} - 1 \right). \quad (6.14)$$

The cross section ratios σ_N/σ_{He} and σ_H/σ_{He} are determined from the elastic form factors [170], while the yield ratio Y_{prod}/Y_{dummy} is obtained from data. The fits to the elastic peak of N , H and He are used to extract the Y_{prod}/Y_{dummy} , as shown in figure 6.4. The quasi-elastic contamination is need to be removed. For the dummy target, two fits were taken: Landau-Gaussian fit for elastic peak and a Gaussian fit for quasi-elastic peak. For the production data, it is more complicated, since the first peak contains the nitrogen and helium elastic peak, and the second peak contains the nitrogen and helium quasi-elastic peak and the hydrogen elastic peak. The hydrogen elastic peak was predicted from the elastic factors. The QFS model [171] was used to predict the quasi-elastic peak. For the helium quasi-elastic peak, the parameters of model were adjusted in the dummy target. For the nitrogen quasi-elastic peak, the parameters were first adjusted using the data from carbon target since there is no pure nitrogen data collected in the experiment, and second adjusted in the ammonia target. The final yield ratio is extracted from the fitted areas:

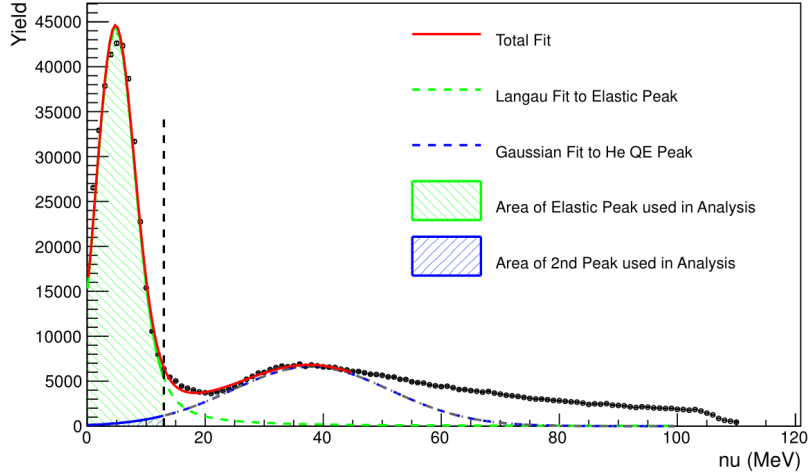
$$\frac{Y_{prod}}{Y_{dummy}} = \frac{S_{e-He} + S_{e-N} + S_{e-H}}{S_{e-He}}, \quad (6.15)$$

where S_{e-He} , S_{e-N} and S_{e-H} is the area of the elastic peak for He , N and H after subtracting the quasi-elastic contamination, respectively.

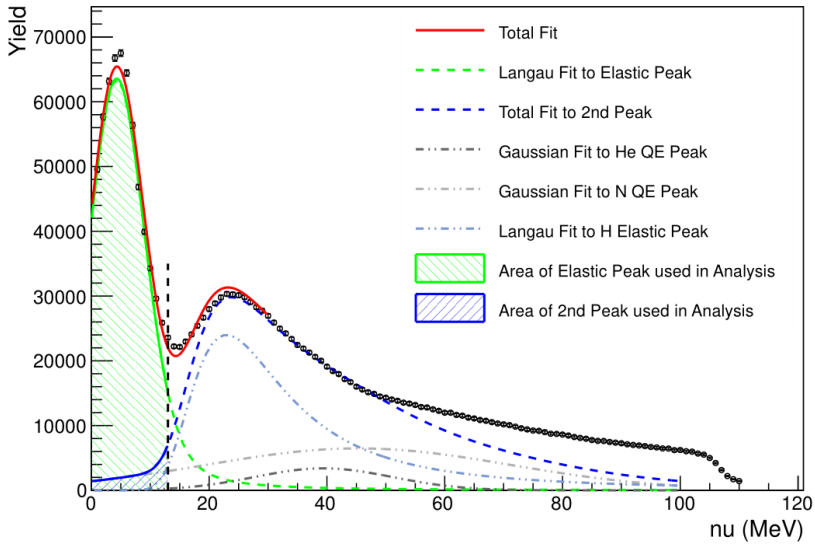
The preliminary results for each settings during the experiment can be found in Melissa's technote [169].

6.1.5 Dilution

The measured asymmetry is diluted by contributions from the nitrogen in the ammonia target material, helium used to cool the target, and the aluminum target end caps. It can be rewritten as:



(a) Fit for the dummy target. Dotted line represents the elastic region



(b) Fit for the production run

Figure 6.4 Fit to elastic and quasi-elastic peak in order to extract the yield ratio. Figures are from Melissa [169].

$$A_{meas} = \frac{Y_{H+} - Y_{H-}}{Y_{H+} + Y_{H-} + Y_{bg}}, \quad (6.16)$$

where Y_{bg} is the background yield caused by the elements other than hydrogen:

$$Y_{bg} = Y_N + Y_{He} + Y_{Al}. \quad (6.17)$$

The dilution factor is extracted from equation (6.16):

$$D_f = 1 - \frac{Y_{bg}}{Y_{prod}}. \quad (6.18)$$

Besides the NH_3 target, three other targets were used for dilution study: the empty target which is full of liquid helium, the dummy target, and the carbon target. Each

yield can be expressed by the cross sections:

$$Y_{prod} = A_{cc}N_A \left(\frac{p_f l_{tg} \rho_N}{M_N} \sigma_N + \frac{p_f l_{tg} \rho_H}{M_H} \sigma_H + \frac{(l_{tot} - p_f l_{tg}) \rho_{He}}{M_{He}} \sigma_{He} + \frac{l_{Al} \rho_{Al}}{M_{Al}} \sigma_{Al} \right), \quad (6.19)$$

$$Y_{bg} = A_{cc}N_A \left(\frac{p_f l_{tg} \rho_N}{M_N} \sigma_N + \frac{(l_{tot} - p_f l_{tg}) \rho_{He}}{M_{He}} \sigma_{He} + \frac{l_{Al} \rho_{Al}}{M_{Al}} \sigma_{Al} \right), \quad (6.20)$$

$$Y_{dummy} = A_{cc}N_A \left(\frac{l_{tot} \rho_{He}}{M_{He}} \sigma_{He} + \frac{l_{Al} \rho_{Al}}{M_{Al}} \sigma_{Al} \right), \quad (6.21)$$

$$Y_{empty} = A_{cc}N_A \left(\frac{l_{tot} \rho_{He}}{M_{He}} \sigma_{He} \right), \quad (6.22)$$

$$Y_{carbon} = A_{cc}N_A \left(\frac{(l_{tot} - l_C) \rho_{He}}{M_{He}} \sigma_{He} + \frac{l_C \rho_C}{M_C} \sigma_C \right), \quad (6.23)$$

where l_C is the length of the carbon target. The aluminum contamination is extracted from the dummy yield and the empty yield:

$$Y_{Al} = Y_{dummy} - Y_{empty}, \quad (6.24)$$

and the helium contamination is extracted from the empty yield:

$$Y_{He} = Y_{empty} \cdot \left(1 - \frac{l_{tg}}{l_{tot}} p_f \right). \quad (6.25)$$

The nitrogen contamination is more complicated since there is no pure nitrogen data. The carbon data was used in terms of the cross section ratio σ_N/σ_C from the P.Bosted model [172]. Since the Small Angle GDH experiment has similar kinematics to g2p, we can use the nitrogen data set from the saGDH experiment to tune the P.Bosted model for use at the g2p kinematics. Elastic and inelastic radiative corrections have been completed on the saGDH nitrogen data and the P.Bosted model has been tuned to $\pm 5\%$ level [173]. The actual nitrogen background is scaled by using the tuned P.Bosted model with the g2p carbon data:

$$Y_N = (Y_{carbon} - Y_{empty} \cdot \frac{l_{tot} - l_C}{l_{tot}} p_f K_{CN} \frac{\sigma_N}{\sigma_C}), \quad (6.26)$$

where

$$K_{CN} = \frac{l_{tg} \rho_N M_C}{l_C \rho_C M_N}. \quad (6.27)$$

Combining with the equation (6.17-6.26), the dilution factor is extracted by:

$$D_f = 1 - \left(\frac{Y_{dummy}}{Y_{prod}} + p_f K_{CN} \frac{\sigma_N}{\sigma_C} \frac{Y_{carbon}}{Y_{prod}} - p_f \frac{l_{tg} + (l_{tot} - l_C) K_{CN} \frac{\sigma_N}{\sigma_C}}{l_{tot}} \frac{Y_{empty}}{Y_{prod}} \right), \quad (6.28)$$

The dilution factor can also be extracted from the cross section model:

l_{tg}	2.8307 cm
l_{tot}	3.7045 cm
l_{Al}	0.0004 cm
ρ_{NH_3}	0.817 g/cm ³
ρ_{He}	0.145 g/cm ³
ρ_{Al}	2.7 g/cm ³

Table 6.1 Parameters used in dilution calculation

$$D_f = \frac{3 \frac{\rho_{NH_3} p_f l_{tg}}{M_{NH_3}} \sigma_H}{\frac{\rho_{NH_3} p_f l_{tg}}{M_{NH_3}} (3\sigma_H + \sigma_N) + \frac{\rho_{He} (l_{tot} - p_f l_{tg})}{M_{He}} \sigma_{He} + \frac{\rho_{Al} l_{Al}}{M_{Al}} \sigma_{Al}}. \quad (6.29)$$

Before the dilution factor from the data becomes available, the one from the model was used instead. Figure 6.5 shows the dilution factors for materials ID 17-20 calculated from the P.Bosted model. The dilution factor is related to the kinematic variables W and Q^2 .

6.1.6 Radiative correction

The Feynman diagram shown in figure 4.1 only considered the Born process, which is assumed for theoretical analyses. The data from experiment contains the higher order effect which is necessary to be corrected in order to compare with the Born process in the theory. The analysis of it is called radiative correction.

The radiative correction was considered into several categories: the virtual photon one-loop corrections, the internal and external bremsstrahlung, and the ionization energy loss. With the classification of the interaction material, the radiative correction was considered into internal and external correction, while the former was happened when the electrons interact with the target material (proton), and the latter was happened when the electrons passing through the target and HRS components before arriving to the detectors. The external radiative correction was always considered as the unpolarized situation, while the internal radiative correction was considered separately for the unpolarized cross section and the polarized cross section.

The next-to-leading order processes for the radiative correction are shown in figure 6.6. It includes the vacuum polarization correction (figure 6.6(a)) which the virtual photon spontaneously splits into a e^+ / e^- pair, the electron self-energy (figure 6.6(b,c)), the vertex correction (figure 6.6(d)), and the real photon bremsstrahlung emission before and after the electron-proton scattering (figure 6.6(d,e)). The main processes by which this happens are bremsstrahlung. Figure 6.7 shows the internal and external bremsstrahlung emissions. The t_b and t_a are the radiation length before and after the scattering, respectively.

In addition of the bremsstrahlung, the ionization energy loss also happened when the electrons pass through the materials. The collision loss is mostly from the collisions between the scattered electrons and the atomic electrons, which results in the ionization of the struck atom. It contributes a few MeV loss per g/cm² material.

6.1.6.1 Formalism of the unpolarized radiative correction

For the unpolarized cross section, the internal and external radiative corrections are predicted from the energy peaking approximation using Stein's formalism [174]. It is calculated from the following formula [174, 175]:

$$\begin{aligned}
 \sigma_{inrad} = & \left(\frac{d^2\sigma}{d\Omega dE_p} \right)_{in} = \left(\frac{R\Delta E}{E_s} \right)^{b(t_b+t_r)} \left(\frac{\Delta E}{E_p} \right)^{b(t_a+t_r)} \left[1 - \frac{\xi/\Delta E}{1 - b[t_a + t_b + 2t_r]} \right] \bar{\sigma}_{in}(E_s, E_p) \\
 & + \int_{E_s \text{ min}}^{E_s - R\Delta E} \bar{\sigma}_{in}(E'_s, E_p) \left(\frac{E_s - E'_s}{E_p R} \right)^{b(t_a+t_r)} \left(\frac{E_s - E'_s}{E_s} \right)^{b(t_b+t_r)} \\
 & \times \left[\frac{b(t_b + t_r)}{E_s - E'_s} \phi \left(\frac{E_s - E'_s}{E_s} \right) + \frac{\xi}{2(E_s - E'_s)^2} \right] dE'_s \\
 & + \int_{E_p + \Delta E}^{E_p \text{ max}} \bar{\sigma}_{in}(E_s, E'_p) \left(\frac{E'_p - E_p}{E'_p} \right)^{b(t_a+t_r)} \left(\frac{(E'_p - E_p)R}{E_s} \right)^{b(t_b+t_r)} \\
 & \times \left[\frac{b(t_a + t_r)}{E'_p - E_p} \phi \left(\frac{E'_p - E_p}{E'_p} \right) + \frac{\xi}{2(E'_p - E_p)^2} \right] dE'_p,
 \end{aligned} \tag{6.30}$$

where

$$R = \frac{M_T + 2E_s \sin^2(\frac{\theta}{2})}{M_T - 2E_p \sin^2(\frac{\theta}{2})},$$

$$\Delta E = 5 \text{ MeV},$$

$$\phi(v) = 1 - v + \frac{3}{4}v^2,$$

$$\bar{\sigma}_{in}(E_s, E_p) = \tilde{F}(Q^2) \sigma_{in}(E_s, E_p),$$

$$b = \frac{4}{3} \left\{ 1 + \frac{1}{9} [(Z+1)/(Z+\eta)] [\ln(183Z^{-1/3})]^{-1} \right\},$$

$$t_r = \frac{\alpha}{b\pi} [\ln(\frac{-q^2}{m^2}) - 1],$$

$$E_s \text{ min} = \frac{E_p}{1 - \frac{E_p}{M_T} (1 - \cos\theta)},$$

$$E_p \text{ max} = \frac{E_s}{1 + \frac{E_s}{M_T} (1 - \cos\theta)},$$

$$\xi = \frac{\pi m}{2a} \frac{t_a + t_b}{(Z + \eta) \ln(183/Z^{1/3})},$$

$$T = t_a + t_b,$$

$$\begin{aligned}\tilde{F}(Q^2) &= 1 + 0.5772bT + \frac{2\alpha}{\pi} \left[\frac{-14}{9} + \frac{13}{12} \ln\left(\frac{Q^2}{m^2}\right) \right] \\ &\quad - \frac{\alpha}{2\pi} \ln^2\left(\frac{E_s}{E_p}\right) + \frac{\alpha}{\pi} \left[\frac{1}{6}\pi^2 - \Phi\left(\cos^2\frac{\theta}{2}\right) \right],\end{aligned}$$

and σ_{in} is the unradiated inelastic cross section, m is the mass of electron, M_T is the mass of target nuclei, t_b and t_a are the radiation length before and after the scattering point, respectively, θ is the scattering angle, Z is the atomic number, E_s and E_p are the energies of the incoming and outgoing electrons. The spence function Φ is defined as:

$$\Phi(x) = \int_0^x \frac{-\ln|1-y|}{y} dy. \quad (6.31)$$

If only considered the external radiative correction, just set t_r to 0 and set $\tilde{F}(Q^2) = 1 + 0.5772bT$.

6.1.6.2 Elastic tail

The elastic tail must be considered for the data, since it becomes relatively large in the resonance region. The elastic cross section without the energy loss is calculated as [174]:

$$\sigma_{el}(E_0) = \left(\frac{d\sigma}{d\Omega}\right)_{el} = \sigma_{Mott} \frac{E'_{el}}{E_0} [W_2^{el} + 2\tan^2\frac{\theta}{2} W_1^{el}], \quad (6.32)$$

where E_0 is the energy of incoming electron, and E'_{el} is the elastic peak:

$$E'_{el} = \frac{2}{1 + (2E_0/M_T) \sin^2(\frac{\theta}{2})}. \quad (6.33)$$

The W_1^{el} and W_2^{el} are two elastic form factors, and they have the relationship with two elastic form factors G_E and G_M :

$$\begin{aligned}W_1^{el} &= \tau G_M^2, \\ W_2^{el} &= \frac{G_E^2 + G_M^2}{1 + \tau},\end{aligned} \quad (6.34)$$

where

$$\tau = \frac{Q^2}{4M_T^2}. \quad (6.35)$$

The form factors G_E and G_M are from [176]. The radiative tail caused from the external bremsstrahlung and the ionization loss can be calculated as [174]:

$$\begin{aligned}\sigma_{el_extern} = & \frac{M_T + (2E_s - \omega_s)sin^2(\frac{\theta}{2})}{M_T - 2E_p sin^2(\frac{\theta}{2})} \times \bar{\sigma}_{el}(E_s - \omega_s)[\frac{bt_b}{\omega_s}\phi(\nu_s) + \frac{\xi}{2\omega_s^2}] \\ & + \bar{\sigma}_{el}(E_s)[\frac{bt_a}{\omega_p}\phi(\nu_s) + \frac{\xi}{2\omega_p^2}],\end{aligned}\quad (6.36)$$

where $\bar{\sigma}_{el} = \tilde{F}(Q^2)\sigma_{el}$, and

$$\omega_s = E_s - \frac{E_p}{1 - (2E_p/M_T)sin^2(\frac{\theta}{2})}, \quad (6.37)$$

$$\omega_p = \frac{E_s}{1 + (2E_s/M_T)sin^2(\frac{\theta}{2})} - E_p, \quad (6.38)$$

$$\nu_s = \omega_s/E_s, \quad (6.39)$$

$$\nu_p = \omega_p/(E_p + \omega_p). \quad (6.40)$$

The radiative tail caused from the internal bremsstrahlung can be calculated by the integration from equation (B.5) in MO. and THAI.'s paper [177]. It can also be extracted from the angle-peaking approximation by assuming the majority of bremsstrahlung photons are emitted in the same direction as the incident and scattered electrons [174]:

$$\begin{aligned}\sigma_{el_intern} = & \frac{M_T + (2E_s - \omega_s)sin^2(\frac{\theta}{2})}{M_T - 2E_p sin^2(\frac{\theta}{2})} \times \bar{\sigma}_{el}(E_s - \omega_s)[\frac{bt_r}{\omega_s}\phi(\nu_s)] \\ & + \bar{\sigma}_{el}(E_s)[\frac{bt_r}{\omega_p}\phi(\nu_s)].\end{aligned}\quad (6.41)$$

The correction from the equation (6.36) and (6.41) is only for single-photon emission. It is corrected by multiplying a factor for multiple-soft-photon radiation [174]:

$$F_{soft} = (\frac{\omega_s}{E_s})^{b(t_b+t_r)}(\frac{\omega_p}{E_p + \omega_p})^{b(t_a+t_r)}. \quad (6.42)$$

6.1.6.3 Radiative correction for the polarized cross section

The internal radiative correction for the polarized cross section is different as the unpolarized cross section. Akushevich described the correction method in detail in his paper [178] and built a fortran code POLRAD [179]. Karl Slifer and Seonho Choi improved the code to allow an interative procedure which built a model based on the measured data from experiment [180].

6.1.7 Acceptance cut

Since the acceptance study is still ongoing, rough acceptance cuts are applied. Figure 6.8-6.10 show the acceptance cuts for three different beam settings.

Three variables are used for acceptance cut, which are calculated from optics study:

settings	bins	normalized χ^2
2.2GeV,5T,longitudinal	17	1.32
2.2GeV,5T,transverses	16	0.53
3.3GeV,5T,transverses	16	0.89

Table 6.2 Normalized χ^2 for the comparison of the asymmetries with and without the acceptance cut

- dp , or δ , is defined in equation (5.43). Figure 6.8-6.10 (a) show the yield for dp . The x axis is dp , and the y axis is the total counts (or events) for each bin in this beam energy setting. It is clear to distinguish the acceptance edge for dp from the picture.
- ϕ , or the in plane angle (the angle in the scattered plane). The Mott cross section was weighted for the ϕ yield in figure 6.8-6.10 (c) in order to eliminate the cross section factor. The acceptance edge for ϕ is also clearly distinguished.
- θ , or the out of plane angle (the angle perpendicular to the scattered plane). There is no clear acceptance edge for θ yield in figure 6.8-6.10 (b). The cut is taken near the tail of the histogram.

6.1.8 Asymmetry result

The physics asymmetries are calculated using the equation 6.1, with the detector cuts and the acceptance cuts. Figure 6.11 (a,b,c) are the asymmetries for the settings of 2.2 GeV beam energy with 5 T longitudinal target magnet field, 2.2 GeV beam energy with 5 T transverse target magnet field, and 3.3 GeV beam energy with 5 T transverse target magnet field, respectively. The error bar of asymmetry is calculated from the equation 6.5, which only includes the statistic error. The results are compared with the model in the following sections.

6.1.9 Asymmetry with different acceptance cuts

The differential cross section $\Delta\sigma_{||/\perp}$ was calculated from the asymmetry and the unpolarized cross section. The uncertainty of the unpolarized cross section is dominated by the systematic error, while the uncertainty of the asymmetry is dominated by the statistic error. It is important to compare the calculated asymmetries with and without the acceptance cuts, so that we can use the most events. Figure 6.12 shows the asymmetries compared with and without the acceptance cut. The normalized χ^2 are shown in table 6.2. The comparison shows the asymmetry results are consistent before and after applying the acceptance cuts in figure 6.8-6.10. Similar studies are needed to be taken when the acceptance study is done.

6.2 Model prediction

6.2.1 MAID

The unitary isobar model MAID2007 [181] uses phenomenological fits to the photo-production and electro-production data for the nucleon from the pion-production threshold to $W=2$ GeV. The major resonances contributions (table 4.1) are included by assuming the resonance contributions have Breit-Wigner forms with contributions to the transverse cross sections given by:

$$\sigma_{\frac{1}{2}(\frac{3}{2})} = \frac{4M}{W_{res}\Gamma_{res}} A_{\frac{1}{2}(\frac{3}{2})}^2 B(\nu, Q^2), \quad (6.43)$$

where $B(\nu, Q^2)$ represents the generalization to electroproduction of the Breit-Wigner form, W_{res} is the mass of the resonance, Γ_{res} is the resonance width, and $A_{\frac{1}{2}(\frac{3}{2})}$ is the relevant photo-coupling helicity amplitude. A non-resonant background and contributions from vector mesons are also included.

6.2.2 Peter Bosted Model

The P.Bosted model utilizes an empirical fit to the measurements of inclusive inelastic electron-proton cross sections in the kinematic range of $0 \leq Q^2 \leq 8$ GeV^2 and $1.1 < W < 3.1$ GeV [182]. The fit covers the data from the high precision longitudinal/transverse separated cross section measurements from E94-110, E00-116, E00-002 at JLab Hall C and SLAC DIS, a smooth transition to the photonproduction point from DAPHNE, and use of Breit-Wigner forms for all resonances. The model also makes the empirical fits to the electron-nucleus scattering for the cross sections $A > 2$ [183].

The P.Bosted model has been updated fairly regularly in the recent years to include all available unpolarized data. There is also some attempt to address nuclear effects in Bosted's fit. The P.Bosted model is used for the unpolarized cross section for the further analysis, which includes extracting the $\Delta\sigma_{||/\perp}$ from the data and the dilution factors.

6.2.3 Asymmetry from the models

The cross section from the model is the Born cross section. It is needed to be radiated before comparing the data. The radiated cross section is calculated as:

$$\sigma_{rad} = \sigma_{inrad} + \sigma_{elrad}, \quad (6.44)$$

where σ_{inrad} is the radiated inelastic cross section and the σ_{elrad} is the radiated elastic tail. For unpolarized P.Bosted model, the σ_{inrad} is calculated from equation (6.30) and the σ_{elrad} is calculated from the sum of the σ_{el_extern} and σ_{el_intern} . For polarized $\Delta\sigma_{||/\perp}$ the internal part of the σ_{inrad} and σ_{elrad} are dealt using Karl's code which mentioned in section 6.1.6.3. Figure 6.13 shows the comparison of unradiated P.Bosted model cross section (red curve), σ_{rad} (cyan curve), σ_{inrad} (blue curve) and σ_{elrad} (green curve), which shows a large influence from the radiation procedure.

Figure 6.14 shows the unpolarized cross section from P.Bosted model before and after the radiation with the same kinematic settings as the data. Figure 6.15 shows the $\Delta\sigma_{||/\perp}$ from MAID model before and after the radiation. The asymmetry is calculated by the ratio of $\Delta\sigma_{||/\perp}$ from MAID and $d\sigma_{unpol}$ from P.Bosted model:

$$A = \frac{\Delta\sigma_{||/\perp_MAID}}{d\sigma_{unpol_Bosted}}. \quad (6.45)$$

The asymmetries before and after the radiation are shown in figure 6.16.

6.3 Asymmetry Comparison

Figure 6.17 shows the asymmetries calculated from data in section 6.1.8 compare with the one calculated from model in section 6.2.3. The Q^2 is around $0.02 \sim 0.045 \text{ GeV}^2$ for the setting of $E=2.2\text{GeV}$, field=5T, longitudinal, $0.066 \sim 0.084 \text{ GeV}^2$ for the setting of $E=2.2\text{GeV}$, field=5T, transverse, and $0.88 \sim 0.1 \text{ GeV}^2$ for the setting of $E=3.3\text{GeV}$, field=5T, transverse. The data is not radiative corrected and the model is radiated.

6.4 g_1 and g_2

The longitudinal and transverse differential cross sections $\Delta\sigma_{||/\perp}$ are extracted from both the asymmetries and the unpolarized cross section $d\sigma_{unpol}$ from equations (4.33,4.34):

$$\Delta\sigma_{||/\perp} = A_{||/\perp} \cdot d\sigma_{unpol}. \quad (6.46)$$

The unpolarized cross section $d\sigma_{unpol}$ from data needs the absolute acceptance value. Before it becomes available, the radiated P.Bosted model is used instead to get the $\Delta\sigma_{||/\perp}$. Figure 6.18 shows the $\Delta\sigma_{||/\perp}$ from data (error bar) compared with the model (solid line). Note the data is not radiative corrected and the model is radiated in the picture.

The g_1 and g_2 without the radiative correction are then extracted from the $\Delta\sigma_{||/\perp}$. The g_1 is calculated from the equation 4.31, with the $\Delta\sigma_{||}$ from the data of longitudinal setting and $\Delta\sigma_{\perp}$ from the MAID. The g_2 is calculated from the equation 4.32, with the $\Delta\sigma_{\perp}$ from the transverse setting and $\Delta\sigma_{||}$ from the MAID.

6.5 Conclusion

The physics asymmetries for both longitudinal and transverse calculated from the data were mostly matched the one calculated from the MAID/P.Bosted model. From the both longitudinal and transverse asymmetries we can see a clear $\Delta(1232)$ resonance peak, and the blurred $N^*(1520/1535)$ and $N^*(1680)$ peaks. The values in the $\Delta(1232)$ resonance matched very well with the model, while the deviation appeared in the $N^*(1440)$ resonance, which shows the potential incorrect for the model. More precise cross section from data is needed for further comparison.

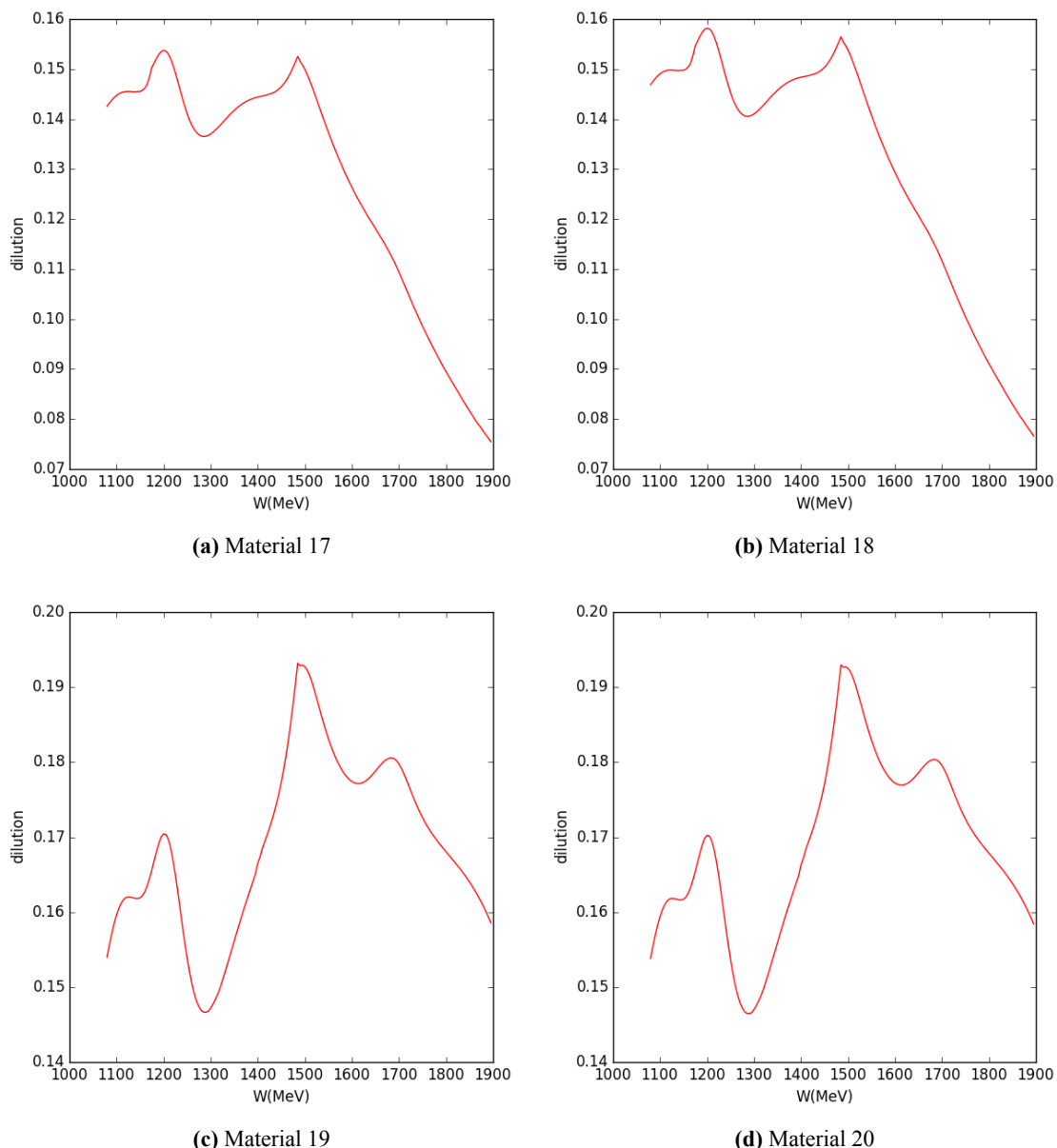


Figure 6.5 Dilution factors for material 17-20, calculated from the P.Bosted model

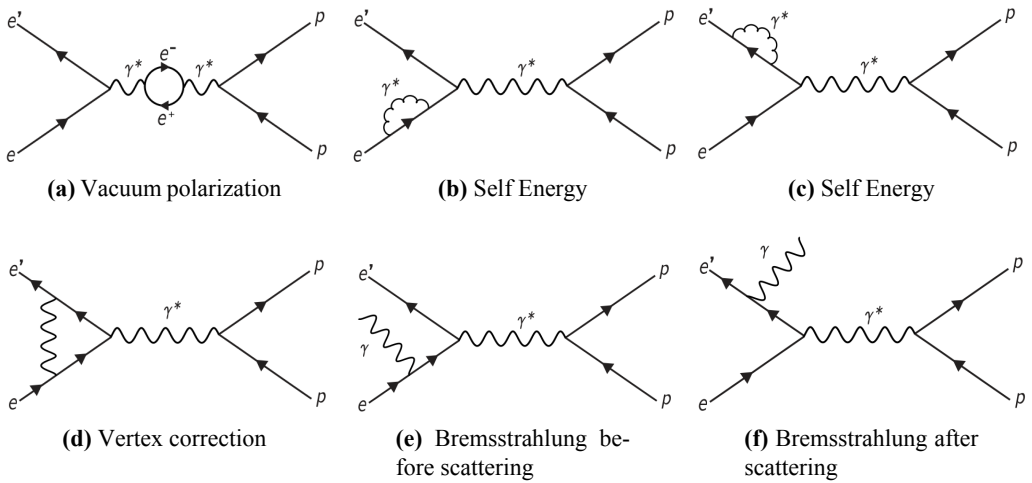


Figure 6.6 Next to leading order internal radiative correction

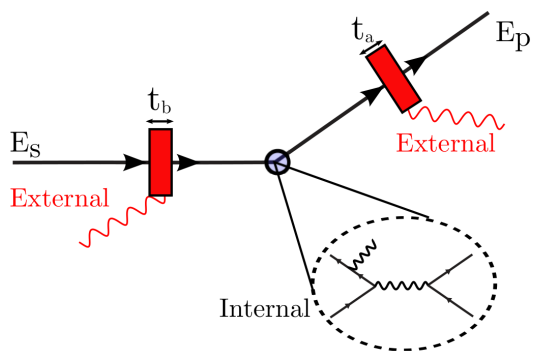


Figure 6.7 Internal and external bremsstrahlung emission. The t_a and t_b are the radiation length before and after the scattering, respectively.[173]

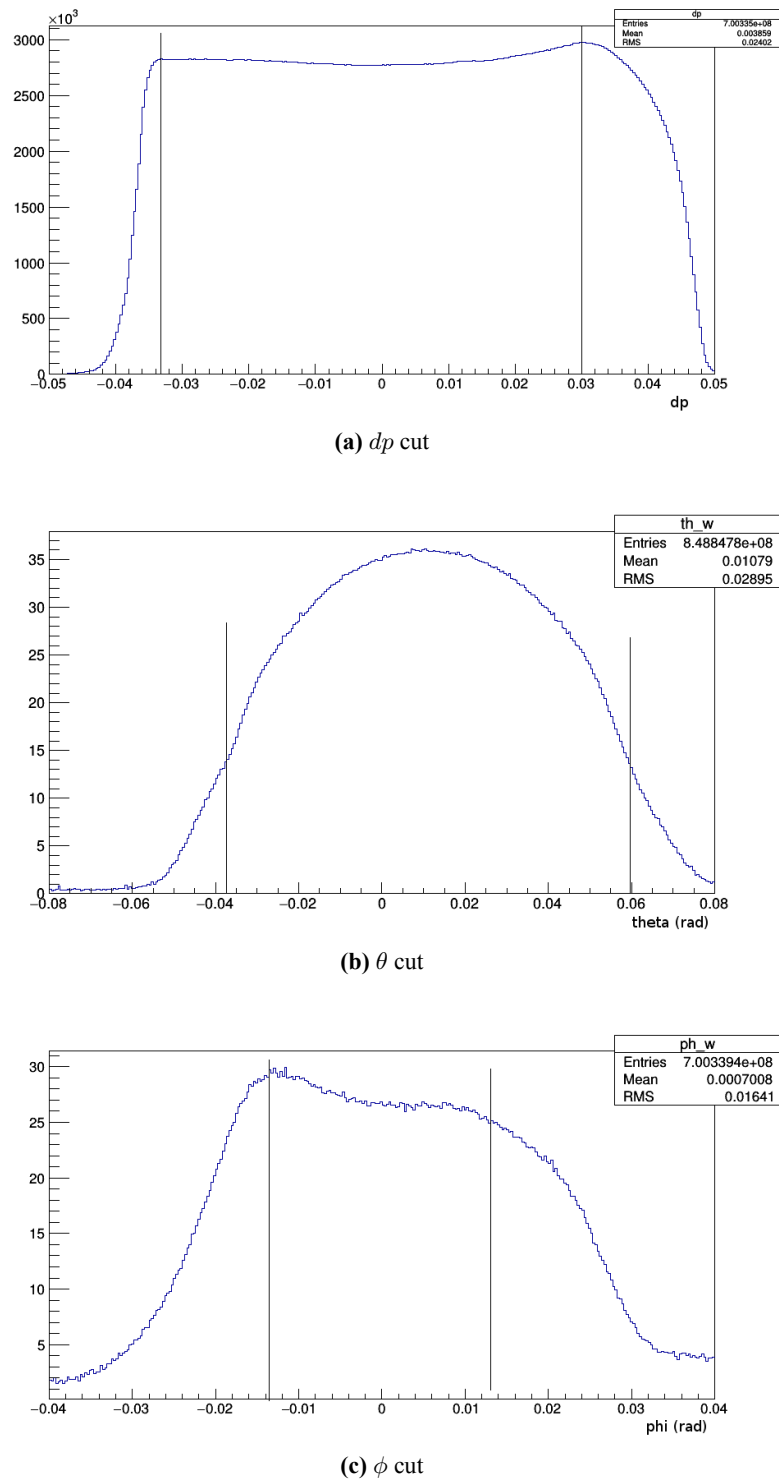


Figure 6.8 Acceptance cut for E=2.2GeV, Field=5T, longitudinal

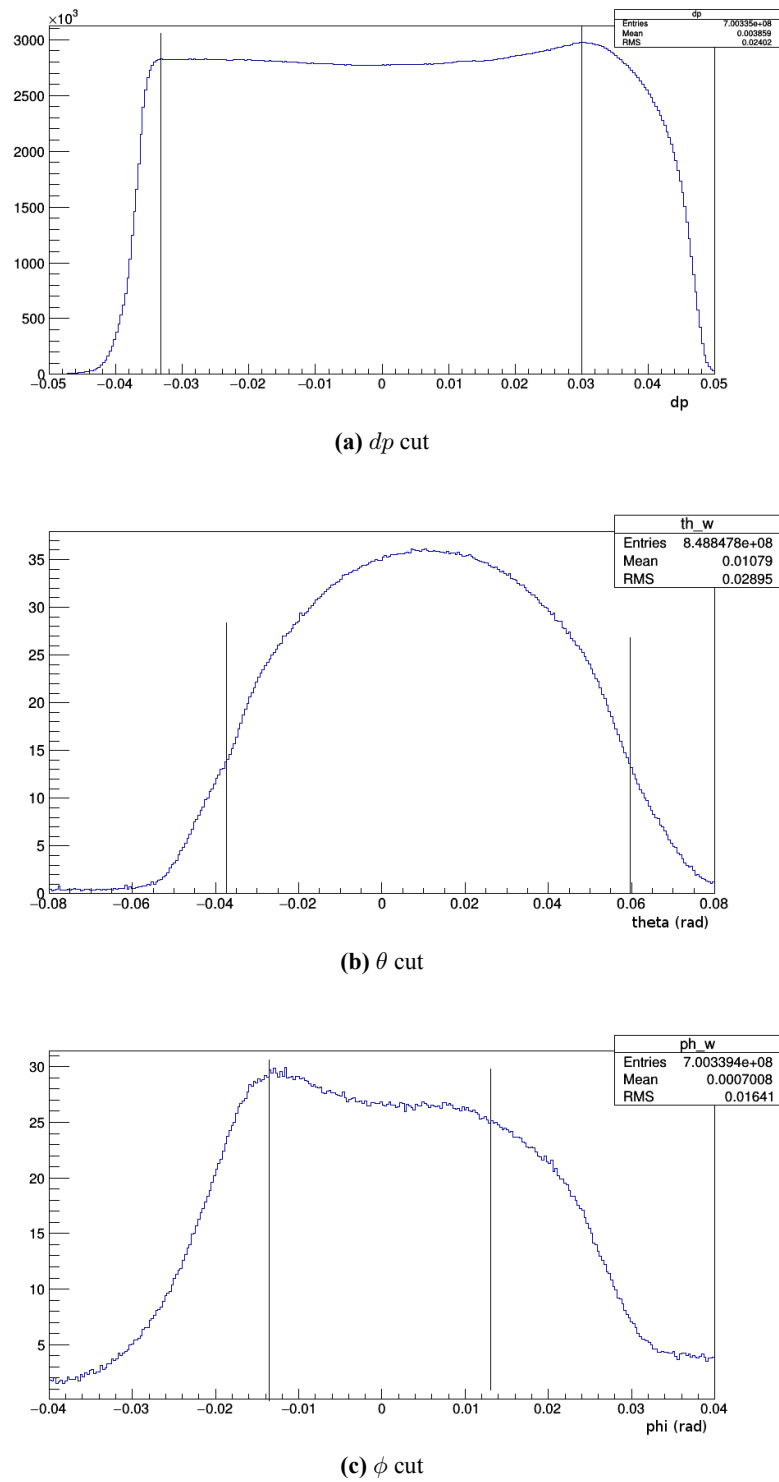


Figure 6.9 Acceptance cut for $E=2.2\text{GeV}$, Field=5T, transverse

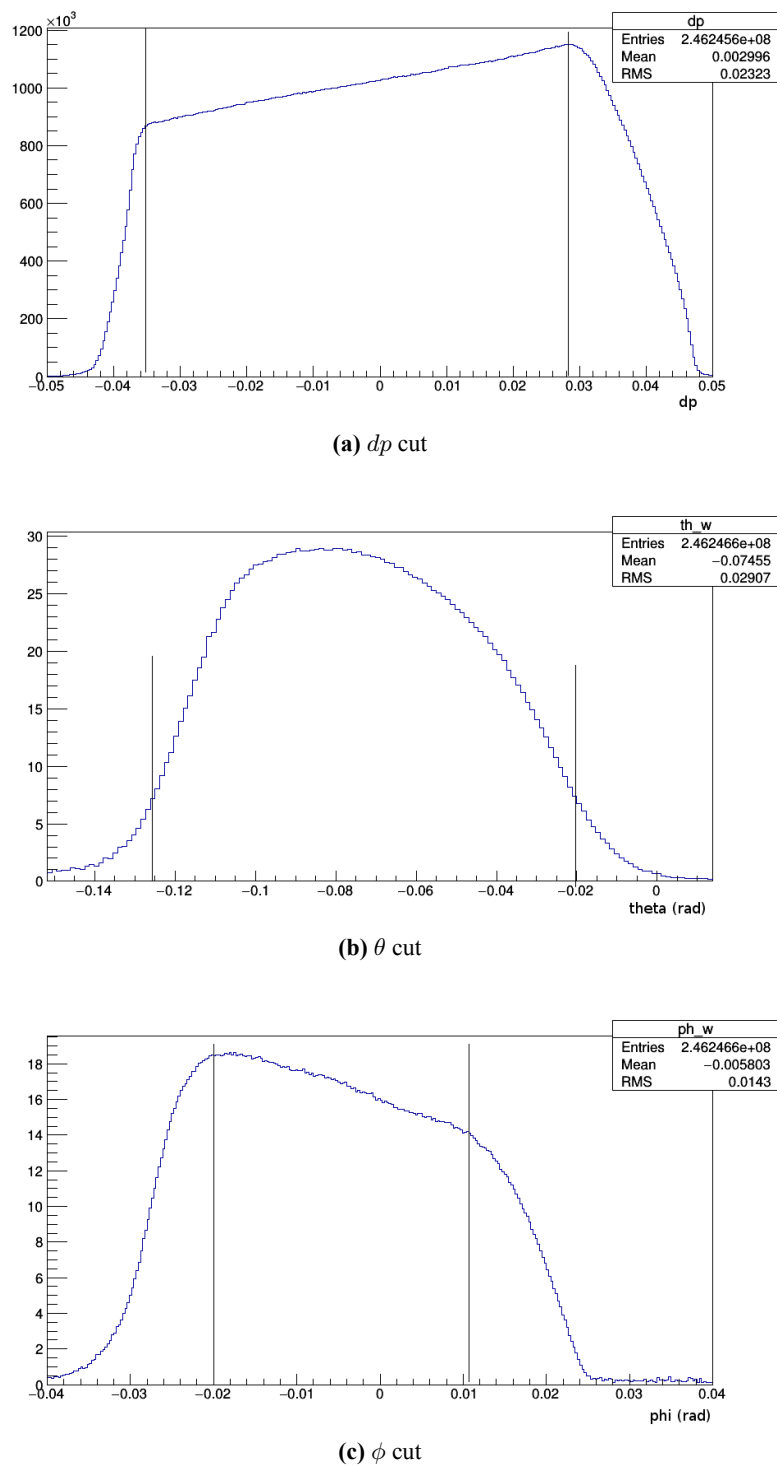


Figure 6.10 Acceptance cut for $E=3.3\text{GeV}$, Field=5T, transverse

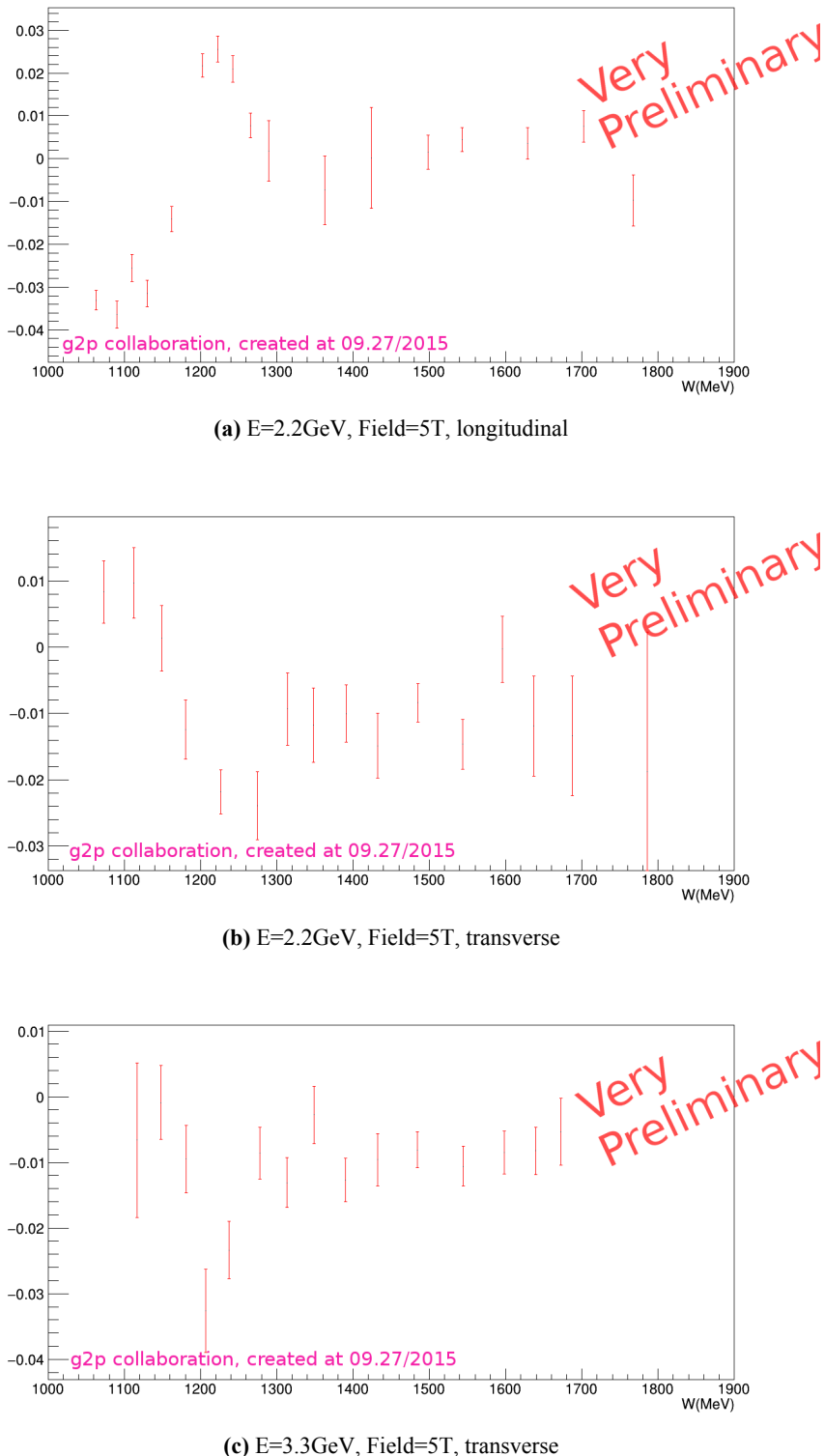


Figure 6.11 Physics Asymmetry (without the radiative correction). Only considered the statistic error. The dilution factor was calculated from the radiated P.Bosted model, with the scattering angle fitted from the data. The packing fraction was averaged from Melissa's result [169] for each material.

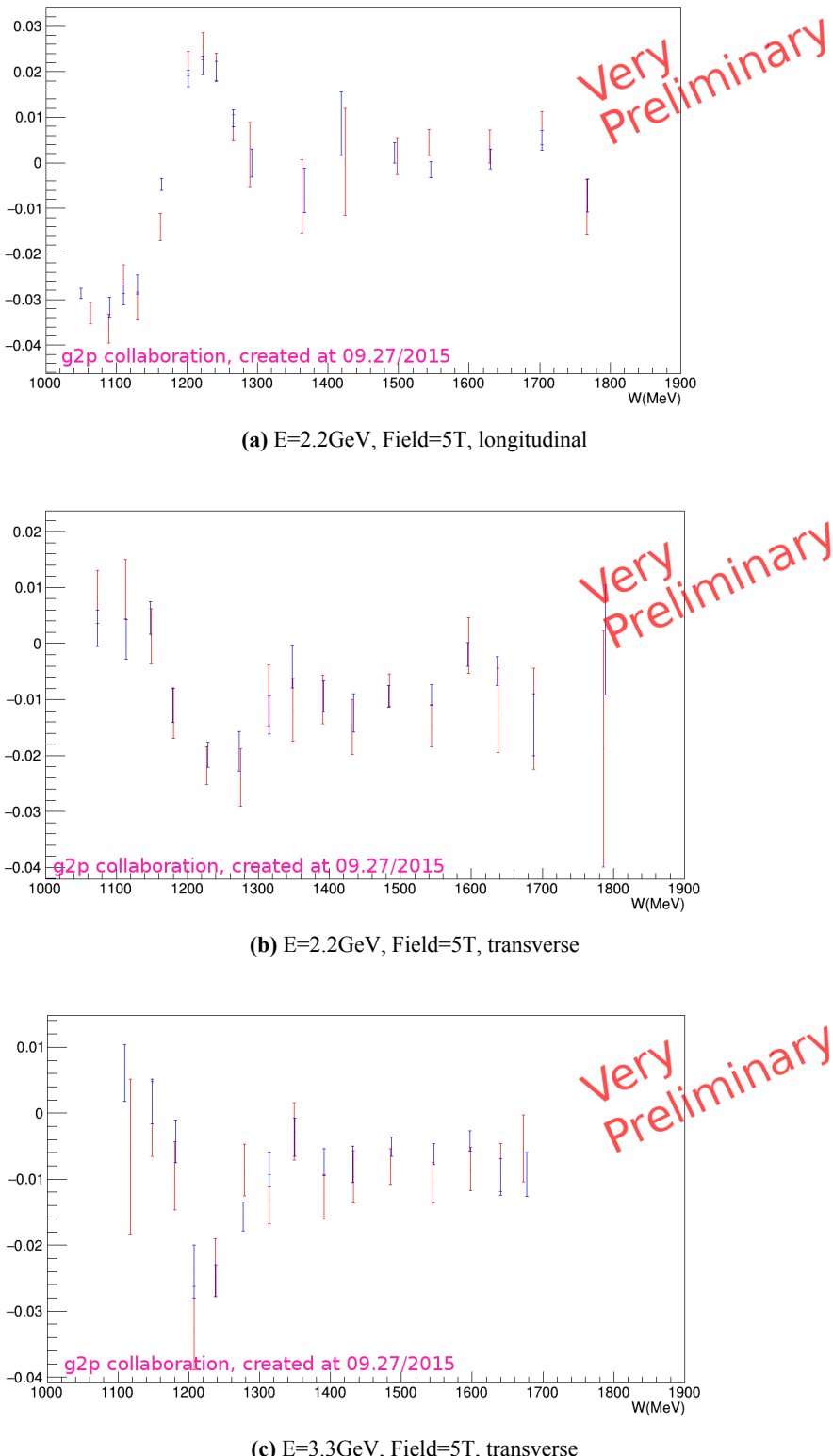


Figure 6.12 Physics Asymmetries with the different acceptance cuts (without the radiative correction). The red error bars are with the acceptance cuts, while The blue error bars are without the acceptance cuts. Only considered the statistic error. The dilution factor was calculated from the radiated P.Bosted model, with the scattering angle fitted from the data. The packing fraction was averaged from Melissa's result [169] for each material.

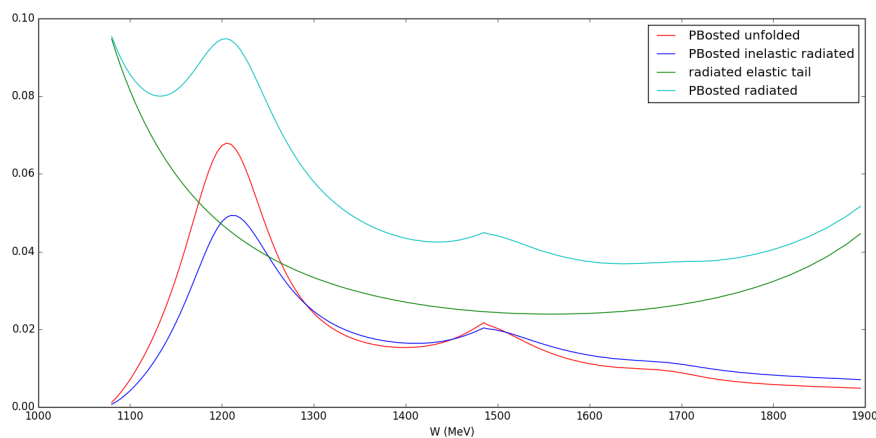
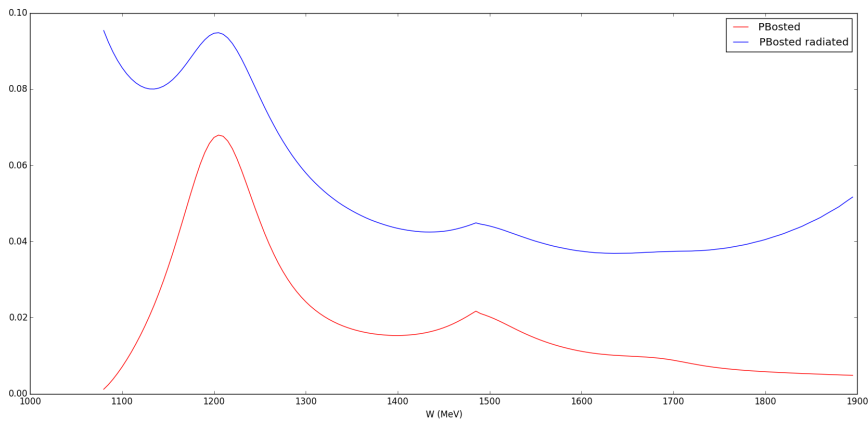
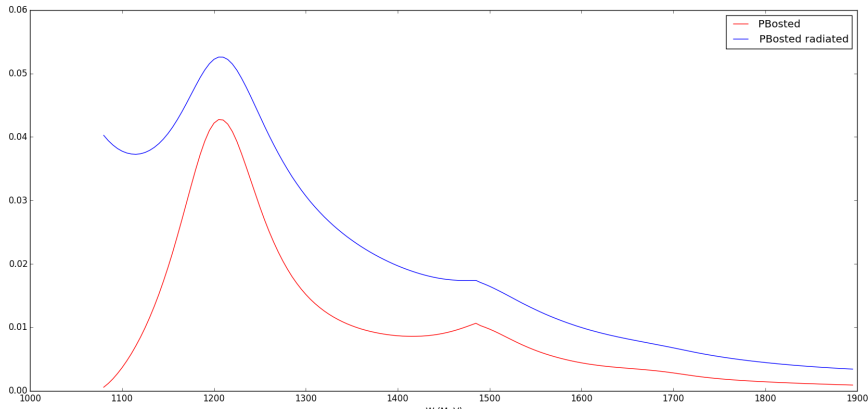


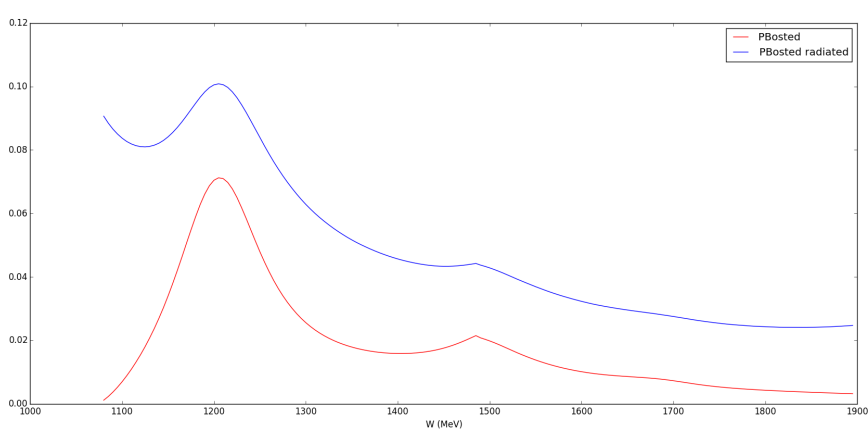
Figure 6.13 Unradiated P.Bosted model (red curve) compare with σ_{rad} (cyan curve), σ_{inrad} (blue curve) and σ_{elrad} (green curve).



(a) Same kinematic settings as $E=2.2\text{GeV},\text{Field}=5\text{T},\text{longitudinal}$

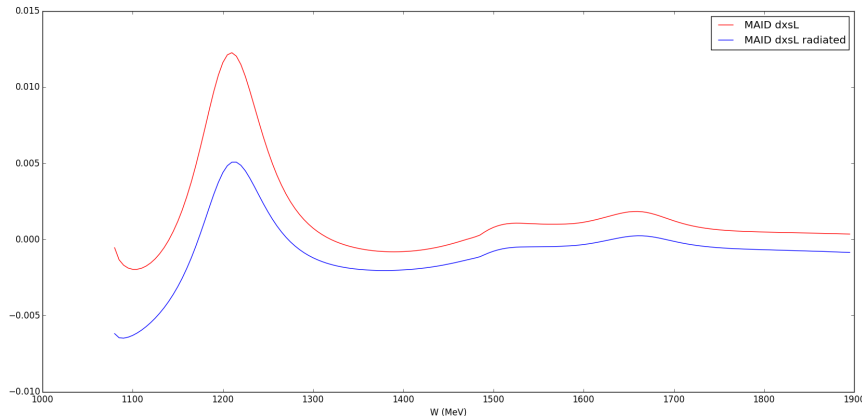


(b) Same kinematic settings as $E=2.2\text{GeV},\text{Field}=5\text{T},\text{transverse}$

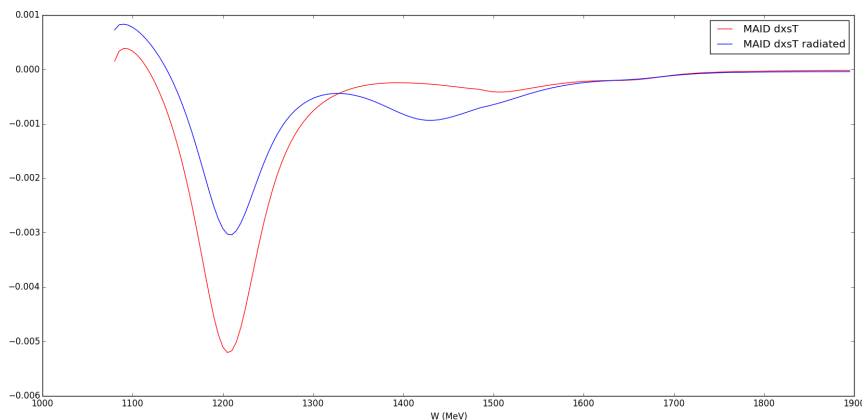


(c) Same kinematic settings as $E=3.3\text{GeV},\text{Field}=5\text{T},\text{transverse}$

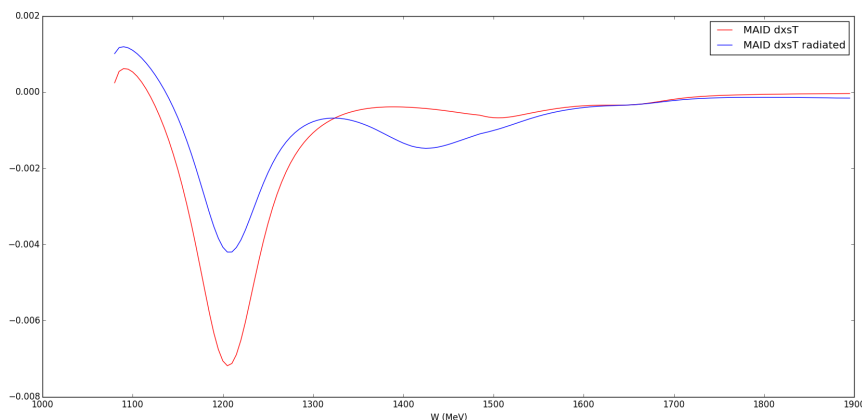
Figure 6.14 Radiated P.Bested model (blue solid line) compared with the unradiated P.Bested model (red solid line)



(a) Radiated vs unradiated $\Delta\sigma_{||}$, Same kinematic settings as E=2.2GeV,Field=5T, longitudinal

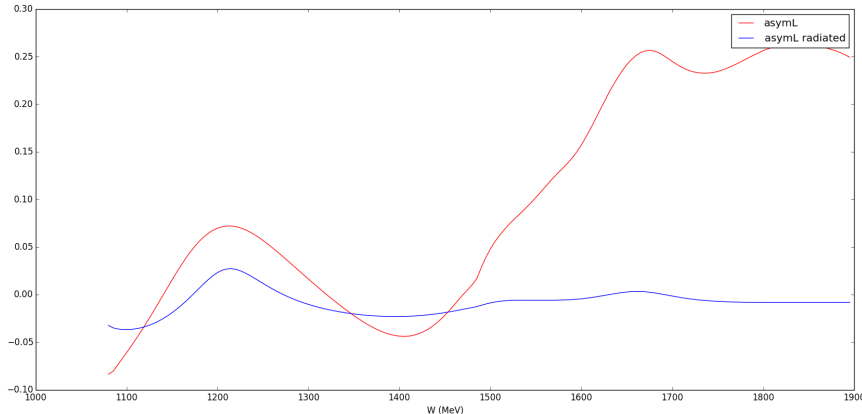


(b) Radiated vs unradiated $\Delta\sigma_{\perp}$, Same kinematic settings as E=2.2GeV,Field=5T, transverse

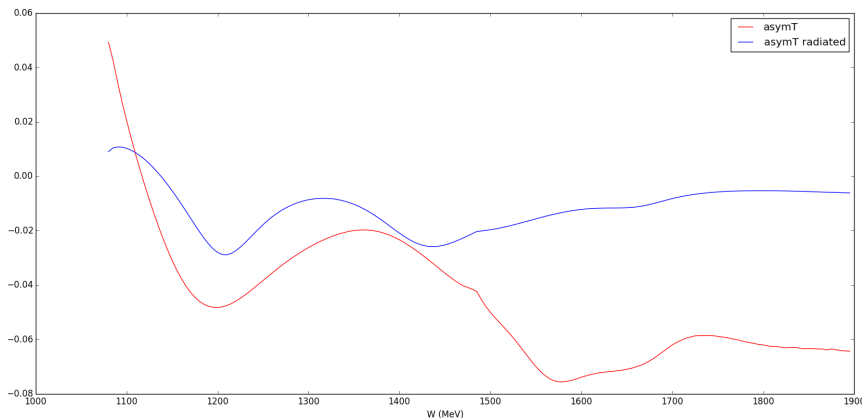


(c) Radiated vs unradiated $\Delta\sigma_{\perp}$, Same kinematic settings as E=3.3GeV,Field=5T, transverse

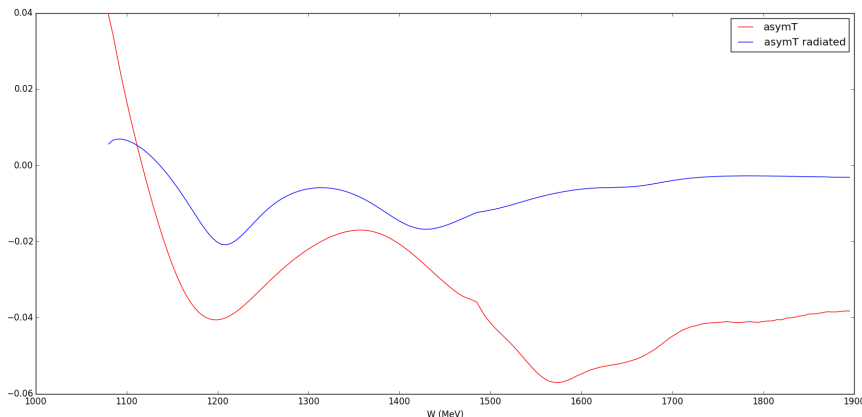
Figure 6.15 Radiated $\Delta\sigma_{||/\perp}$ (blue solid line) compared with the unradiated $\Delta\sigma_{||/\perp}$ from MAID (red solid line)



(a) Radiated vs unradiated A_{\parallel} , Same kinematic settings as $E=2.2\text{GeV}, \text{Field}=5\text{T}, \text{longitudinal}$



(b) Radiated vs unradiated A_{\perp} , Same kinematic settings as $E=2.2\text{GeV}, \text{Field}=5\text{T}, \text{transverse}$



(c) Radiated vs unradiated A_{\perp} , Same kinematic settings as $E=3.3\text{GeV}, \text{Field}=5\text{T}, \text{transverse}$

Figure 6.16 Radiated $A_{\parallel/\perp}$ (blue solid line) compared with the unradiated $A_{\parallel/\perp}$ (red solid line), calculated from Model

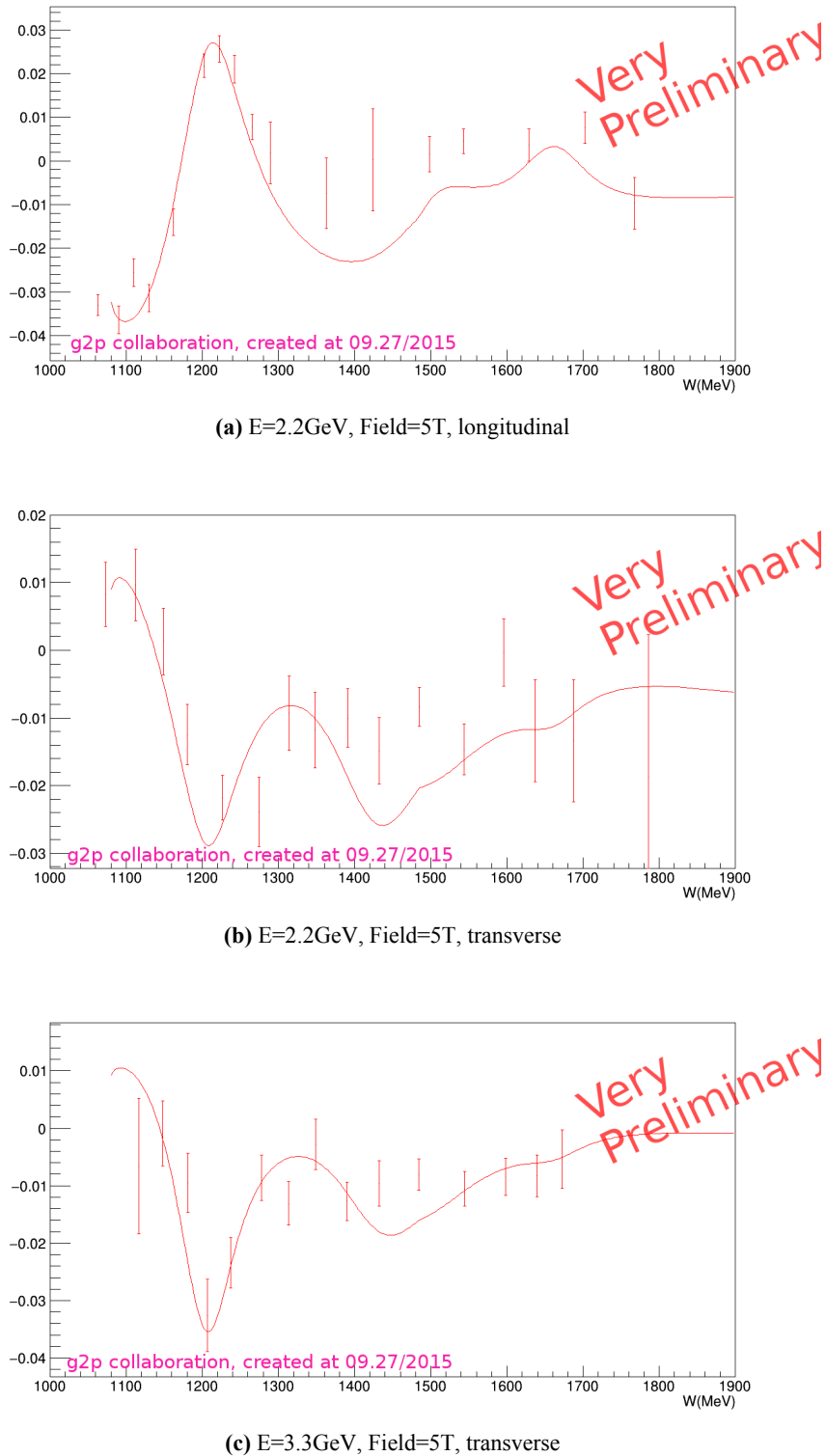


Figure 6.17 Physics asymmetry compared with model (without the radiative correction). Only considered the statistic error. The dilution factor was calculated from the radiated P.Bosted model, with the scattering angle fitted from the data. The packing fraction was averaged from Melissa's result [169] for each material. The asymmetry from model was calculated from the radiated MAID/P.Bosted model.

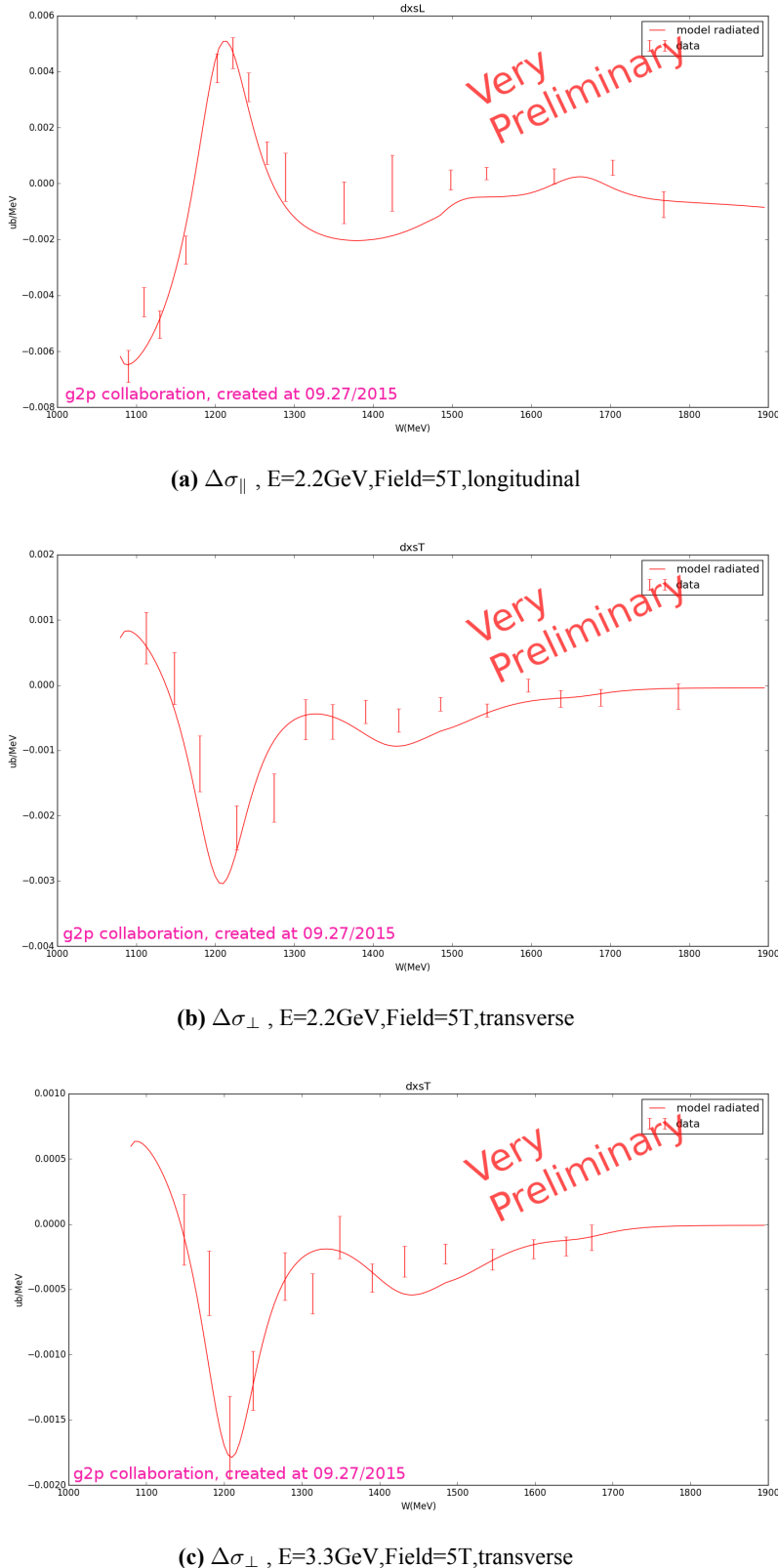
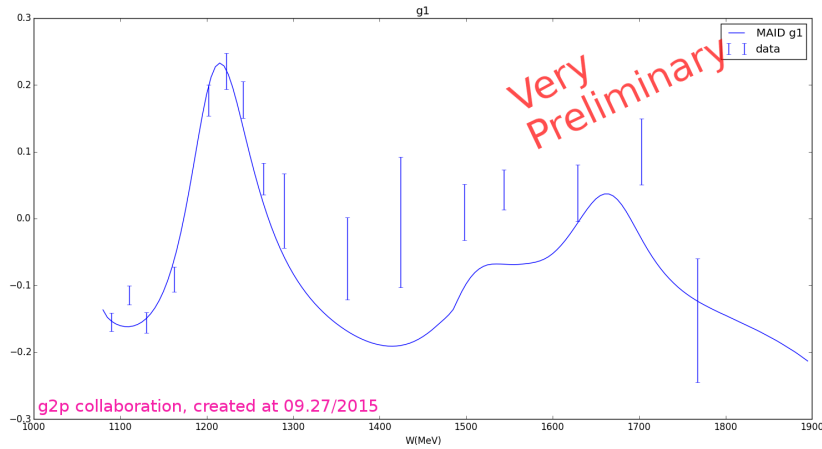
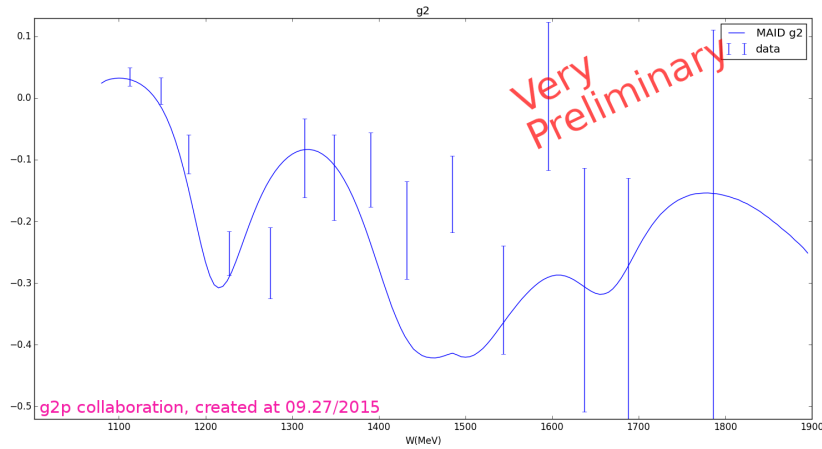


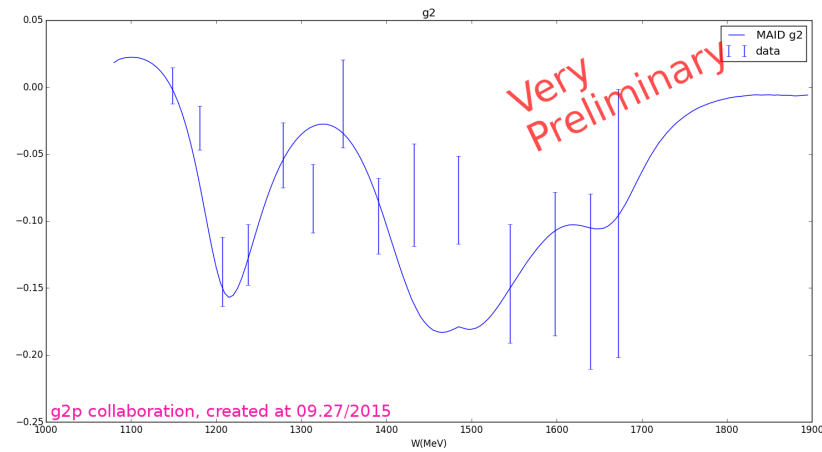
Figure 6.18 $\Delta\sigma_{||/\perp}$ from data (error bar, before radiative correction, calculated by the asymmetry from data with the help of radiated P.Bosted model) compared with the model (solid line, from radiated MAID model). Only considered the statistic error. The dilution factor was calculated from the radiated P.Bosted model, with the scattering angle fitted from the data. The packing fraction was averaged from Melissa's result [169] for each material.



(a) g_1 , $E=2.2\text{GeV}$, Field=5T, longitudinal. Q^2 is around $0.02 \sim 0.045\text{ GeV}^2$



(b) g_2 , $E=2.2\text{GeV}$, Field=5T, transverse. Q^2 is around $0.066 \sim 0.084\text{ GeV}^2$



(c) g_2 , $E=3.3\text{GeV}$, Field=5T, transverse. Q^2 is around $0.088 \sim 0.1\text{ GeV}^2$

Figure 6.19 g_1 and g_2 (before radiative correction, calculated by the asymmetry from data with the help of P.Bosted and MAID model) compared with model (from radiated MAID model). Only considered the statistic error. The dilution factor was calculated from the radiated P.Bosted model, with the scattering angle fitted from the data. The packing fraction was averaged from Melissa's result [169] for each material.

Chapter 7

Summary

The experiment E08-027 successfully measured the transverse cross section difference $\Delta\sigma_{\perp}$ at several kinematic settings in the Q^2 range of $0.02 - 0.2 \text{ GeV}^2$. The experiment also measured the longitudinal cross section difference $\Delta\sigma_{\parallel}$ at one beam energy setting for checking the EG4 result. The structure function g_2 is going to be extracted from the measured $\Delta\sigma_{\perp}$ with the combination of $\Delta\sigma_{\parallel}$ from EG4 experiment. The very preliminary results from the asymmetry shows a obvious $\Delta(1232)$ resonance peak. The data also shows several peaks from other resonances. Compared with the asymmetry calculated from the models, the data matched well with the models in the $\Delta(1232)$ resonance, while the comparison indicates some deviation from other resonance peaks. More careful data analysis is needed for the further study.

The data analysis is still ongoing, including the acceptance study and the dilution study, which are needed to obtain final cross section and final asymmetry. The optics study is nearly complete. The radiated model compared with the unirradiated model indicates that the radiative correction is very important for the final result. The radiative correction for the data must be carefully studied after extracting the cross section differences. The data analysis for the EG4 experiment in Hall B at JLab is also ongoing, the final physics results need to wait for their result. Because of the different Q^2 range between the data of $\Delta\sigma_{\parallel}$ and the $\Delta\sigma_{\perp}$, a data fit is necessary for the result of $\Delta\sigma_{\parallel}$ in order to cover the kinematic range of $\Delta\sigma_{\perp}$. Once the studies mentioned above is done, the spin structure function g_2 can be extracted. The integrated g_2 in x will give us a test for the B-C sum rule, with some assumptions and extensions in the unmeasured x range. The longitudinal-transverse spin polarizability δ_{LT} will finally be extracted to test the χPT calculation.

Appendix

Run summary during the experiment for the production run

Beam Energy (GeV)	Target Field	Target Orien	Run range (Left)	Run range (Right)	HRS Momentums		
					GeV	Runs (Left)	Runs (Right)
2.2	0	Straight	2000-2854	20000-21931			
2.2	2.5 T	\perp	2855-2997	21932-22071			
2.2	0	Straight	3167-3199	22248-22272			
2.2	2.5 T	\perp	3200-3956	22273-22987	540	2	2
					582	4	3
					625	3	2
					672	4	3
					723	4	4
					777	4	1
					836	5	4
					900	4	4
					968	3	3
					1002	8	
					1040	4	3
					1078	3	11
					1118	3	2
					1159	10	9
					1202	7	6
					1246	14	13
					1294	7	7
					1340	10	10
					1390	6	6
					1440	9	8
					1495	6	9
					1549	11	12
					1607	10	10
					1666	8	7
					1728	7	7
					1792	21	18
					1858	1	3
					1926	25	24
					1940	12	7
					2017	27	25
					2228	16	4

1.7	2.5 T	⊥	3957-4582	22988-23517	571	5	5
					621	6	5
					675	6	5
					734	10	10
					798	13	12
					856	10	10
					910	10	8
					968	15	13
					1030	16	14
					1096	13	13
					1166	19	18
					1240	19	17
					1320	19	17
					1404	21	17
					1493	6	1
1.1 GeV	2.5 T	⊥	4696-5326	23619-24104	1588	25	26
					1690	4	1
					523	2	
					547	8	7
					563	2	
					582	9	8
					620	7	7
					650	8	18
					659	11	10
					700	36	34
					746	11	9
					752	30	28
					794	18	14
					809	20	30
					844	22	18
2.2 GeV	5 T		5441-5902	24217-24591	870	34	32
					898	24	21
					935	18	18
					956	22	21
					1006	18	18
					1017	28	26
					1081	9	10
					1113	1	
					1151	1	1
					1168	1	
					991	1	1
					1054	6	10
					1121	5	10
					1193	6	7
					1269	6	9
					1350	5	13

					1468	13	26
					1596	2	49
					1734	2	46
					1885	40	
					2049	65	
					2227	27	
2.2 GeV	5 T	\perp	5903-6100	24592-24727	918	1	
					1015	1	2
					1103	1	4
					1174	2	4
					1249	3	3
					1329	4	4
					1413	5	5
					1504	7	6
					1600	7	7
					1702	6	6
					1811	9	9
					1926	8	7
					2049	9	11
					2227	27	
3.3 GeV	5 T	\perp	6101-6300	24728-25000	1945		9
					2069		15
					2201		14
					2342	8	
					2491	11	
					2650	9	
					2800	4	
					2820	12	
					3000	9	

Research Achievements

Received

1. Pengjia Zhu, *et al.* Beam Position Reconstruction for the g2p Experiment in Hall A at Jefferson Lab, Nuclear Instruments and Methods in Physics Research Section A

Technical Reports

1. Pengjia Zhu, Beam Charge Measurement for g2p experiment, g2p technical report, E08-027 Collaboration (unpublished), http://hallaweb.jlab.org/experiment/g2p/technotes/bcm_technote.pdf
2. Pengjia Zhu, Uncertainty on g2 due to target spin misalignment, g2p technical report, E08-027 Collaboration (unpublished), http://hallaweb.jlab.org/experiment/g2p/technotes/E08027_TN2011_02.pdf
3. Pengjia Zhu, Summaries of Experimental Activities - E08-027, Hall A collaboration work report, Jefferson Lab

Talks and Presentations

1. g2p&GEp analysis status, Hall A Winter Collaboration Meeting, Jefferson Lab, Newport News, VA, US, 2014
2. Instrumentation and analysis progress for g2p experiment, International workshop on hadron physics, Huangshan, China, June 2013
3. Instrumentation for the g2p experiment, International workshop on Chiral Dynamics, Newport News, VA, US, 2012
4. Beamline improvement, Hall A collaboration meeting, Jefferson Lab, Newport News, VA, US, 2012
5. Hardware for g2p experiment, Hampton University Graduate Studies Summer School, Newport News, VA, US, 2012

Bibliography

- [1] Bloom E D, Coward D H, DeStaebler H, et al. High-Energy Inelastic $e - p$ Scattering at 6° and 10° . *Phys. Rev. Lett.*, 1969, 23:930–934.
- [2] Breidenbach M, Friedman J I, Kendall H W, et al. Observed Behavior of Highly Inelastic Electron-Proton Scattering. *Phys. Rev. Lett.*, 1969, 23:935–939.
- [3] Close F. On the transformation between current and constituent quarks and consequences for polarised electroproduction structure functions. *Nuclear Physics B*, 1974, 80(2):269 – 298.
- [4] Alguard M J, Ash W W, Baum G, et al. Deep Inelastic Scattering of Polarized Electrons by Polarized Protons. *Phys. Rev. Lett.*, 1976, 37:1261–1265.
- [5] Alguard M J, Ash W W, Baum G, et al. Deep-Inelastic $e - p$ Asymmetry Measurements and Comparison with the Bjorken Sum Rule and Models of Proton Spin Structure. *Phys. Rev. Lett.*, 1978, 41:70–73.
- [6] Baum G, Bergström M R, Bolton P R, et al. New Measurement of Deep-Inelastic $e - p$ Asymmetries. *Phys. Rev. Lett.*, 1983, 51:1135–1138.
- [7] Ellis J, Jaffe R. Sum rule for deep-inelastic electroproduction from polarized protons. *Phys. Rev. D*, 1974, 9:1444–1446.
- [8] Ashman J, Badelek B, Baum G, et al. A measurement of the spin asymmetry and determination of the structure function g_1 in deep inelastic muon-proton scattering. *Physics Letters B*, 1988, 206(2):364 – 370.
- [9] Ashman J, Badelek B, Baum G, et al. An investigation of the spin structure of the proton in deep inelastic scattering of polarised muons on polarised protons. *Nuclear Physics B*, 1989, 328(1):1 – 35.
- [10] Jaffe R, Manohar A. The g_1 problem: Deep inelastic electron scattering and the spin of the proton. *Nuclear Physics B*, 1990, 337(3):509 – 546.
- [11] Feynman R P. Very High-Energy Collisions of Hadrons. *Phys. Rev. Lett.*, 1969, 23:1415–1417.
- [12] Filippone B, Ji X D. The Spin structure of the nucleon. *Adv.Nucl.Phys.*, 2001, 26:1.
- [13] Callan C G, Gross D J. Crucial Test of a Theory of Currents. *Phys. Rev. Lett.*, 1968, 21:311–313.
- [14] Anselmino M, Efremov A, Leader E. The Theory and phenomenology of polarized deep

- inelastic scattering. *Phys.Rept.*, 1995, 261:1–124.
- [15] Leader E. Nucleon Spin. In: Pötz W, Hohenester U, Fabian J, (eds.). *Proceedings of Modern Aspects of Spin Physics*. Springer Berlin Heidelberg, 2007: 95–128.
- [16] Leader E, Anselmino M. A crisis in the parton model: where, oh where is the proton's spin? *Zeitschrift für Physik C Particles and Fields*, 1988, 41(2):239–246.
- [17] Wilson K G. Non-Lagrangian Models of Current Algebra. *Phys. Rev.*, 1969, 179:1499–1512.
- [18] Kuhn S, Chen J P, Leader E. Spin Structure of the Nucleon - Status and Recent Results. *Prog.Paupr.Nucl.Phys.*, 2009, 63:1–50.
- [19] Vogelsang W. Rederivation of the spin-dependent next-to-leading order splitting functions. *Phys. Rev. D*, 1996, 54:2023–2029.
- [20] Ball R D, Forte S, Ridolfi G. Next-to-leading order determination of the singlet axial charge and the polarized gluon content of the nucleon. *Physics Letters B*, 1996, 378(1–4):255 – 266.
- [21] Carlitz R, Collins J, Mueller A. The role of the axial anomaly in measuring spin-dependent parton distributions. *Physics Letters B*, 1988, 214(2):229 – 236.
- [22] Larin S. The next-to-leading {QCD} approximation to the Ellis-Jaffe sum rule. *Physics Letters B*, 1994, 334(1–2):192 – 198.
- [23] Yun-Xiu Y, Hai-Jiang L, Xin-Hu Y, et al. Progress in experimental studies on longitudinal spin structure of nucleon. *Progress in Physics*, 2012, 32:294–334.
- [24] Abe K, Akagi T, Anthony P L, et al. Measurements of the proton and deuteron spin structure functions g_1 and g_2 . *Phys. Rev. D*, 1998, 58:112003.
- [25] Bernard V. Chiral perturbation theory and baryon properties. *Progress in Particle and Nuclear Physics*, 2008, 60(1):82 – 160.
- [26] Bernard V, Kaiser N, Meissner U G. Chiral dynamics in nucleons and nuclei. *Int. J. Mod. Phys.*, 1995, E4:193–346.
- [27] Bernard V, Kaiser N, Meissner U G. Small momentum evolution of the extended Drell-Hearn-Gerasimov sum rule. *Phys. Rev. D*, 1993, 48:3062–3069.
- [28] Bernard V, Hemmert T R, Meißner U G. Novel analysis of chiral loop effects in the generalized Gerasimov–Drell–Hearn sum rule. *Physics Letters B*, 2002, 545(1–2):105 – 111.
- [29] Bjorken J D. Asymptotic Sum Rules at Infinite Momentum. *Phys. Rev.*, 1969, 179:1547–1553.
- [30] Sulkosky V A. THE SPIN STRUCTURE OF ${}^3\text{He}$ AND THE NEUTRON AT LOW Q₂ : A MEASUREMENT OF THE GENERALIZED GDH INTEGRAND[D]. 2007.
- [31] Drell S D, Hearn A C. Exact Sum Rule for Nucleon Magnetic Moments. *Phys. Rev. Lett.*, 1966, 16:908–911.

- [32] Ahrens J, Altieri S, Annand J R M, et al. First Measurement of the Gerasimov-Drell-Hearn Integral for 1H from 200 to 800 MeV. *Phys. Rev. Lett.*, 2001, 87:022003.
- [33] Amarian M, Auerbach L, Averett T, et al. Q^2 Evolution of the Generalized Gerasimov-Drell-Hearn Integral for the Neutron using a ^3He Target. *Phys. Rev. Lett.*, 2002, 89:242301.
- [34] JPChen, ADeur, FGaribaldi, spokesperson. JLab E97-110 experiment. Proposal, Jefferson Lab, 1997..
- [35] M Anghinolfi e a. The GDH Sum Rule with Nearly-Real Photons and the Proton g1 Structure Function at Low Momentum Transfer. Proposal, Jefferson Lab, 2003..
- [36] Wandzura S, Wilczek F. Sum rules for spin-dependent electroproduction- test of relativistic constituent quarks. *Physics Letters B*, 1977, 72(2):195 – 198.
- [37] Shuryak E, Vainshtein A. Theory of power corrections to deep inelastic scattering in quantum chromodynamics: (II). Q-4 effects; polarized target. *Nuclear Physics B*, 1982, 201(1):141 – 158.
- [38] Ji X. The nucleon structure functions from deep-inelastic scattering with electroweak currents. *Nuclear Physics B*, 1993, 402(1–2):217 – 250.
- [39] Stein E, Górnicki P, Mankiewicz L, et al. {QCD} sum rule calculation of twist-4 corrections to Bjorken and Ellis-Jaffe sum rules. *Physics Letters B*, 1995, 353(1):107 – 113.
- [40] Chen J P, Deur A, Meziani Z E. Sum rules and moments of the nucleon spin structure functions. *Mod.Phys.Lett.*, 2005, A20:2745–2766.
- [41] Drechsel D, Pasquini B, Vanderhaeghen M. Dispersion relations in real and virtual Compton scattering. *Physics Reports*, 2003, 378(2–3):99 – 205.
- [42] Kao C, Spitzenberg T, Vanderhaeghen M. Burkhardt-Cottingham sum rule and forward spin polarizabilities in heavy baryon chiral perturbation theory. *Phys. Rev. D*, 2003, 67:016001.
- [43] Bernard V, Hemmert T R, Meiñner U G. Spin structure of the nucleon at low energies. *Phys. Rev. D*, 2003, 67:076008.
- [44] Bernard V, Epelbaum E, Krebs H, et al. New insights into the spin structure of the nucleon. *Phys. Rev. D*, 2013, 87:054032.
- [45] Burkhardt H, Cottingham W. Sum rules for forward virtual compton scattering. *Annals of Physics*, 1970, 56(2):453 – 463.
- [46] Soffer J, Teryaev O V. Bjorken sum rule at low $\{Q^2\}$. *Physics Letters B*, 2002, 545(3–4): 323 – 328.
- [47] Anthony P L, Arnold R G, Band H R, et al. Deep inelastic scattering of polarized electrons by polarized ^3He and the study of the neutron spin structure. *Phys. Rev. D*, 1996, 54:6620–6650.
- [48] Abe K. Precision Measurement of the Proton Spin Structure Function g1p. SLAC-PUB-6508,

1994..

- [49] Incerti S. Measurement of the neutron spin structure functions using polarized electrons and a polarized He-3 target: The SLAC E154 experiment. *Nucl.Phys.Proc.Suppl.*, 1998, 64:162–166.
- [50] King P. Spin Structure Functions of the Proton and Deuteron from SLAC Experiments E155 and E155X. *SLAC-PUB-9741*, 2002..
- [51] Ackerstaff K, Airapetian A, Akushevich I, et al. Measurement of the neutron spin structure function g_{n1} with a polarized ^3He internal target. *Physics Letters B*, 1997, 404(3–4):383 – 389.
- [52] Airapetian A, Akopov N, Akushevich I, et al. Measurement of the proton spin structure function g_{1p} with a pure hydrogen target. *Physics Letters B*, 1998, 442(1–4):484 – 492.
- [53] Stewart J, Collaboration T H. The HERMES polarized hydrogen internal gas target. *AIP Conference Proceedings*, 1998, 421(1):69–78.
- [54] Airapetian A, Akopov N, Akopov Z, et al. Precise determination of the spin structure function g_1 of the proton, deuteron, and neutron. *Phys. Rev. D*, 2007, 75:012007.
- [55] Airapetian A, Akopov N, Akopov Z, et al. Quark helicity distributions in the nucleon for up, down, and strange quarks from semi-inclusive deep-inelastic scattering. *Phys. Rev. D*, 2005, 71:012003.
- [56] Airapetian A, Akopov N, Amarian M, et al. Measurement of the Spin Asymmetry in the Photoproduction of Pairs of High- p_T Hadrons at HERMES. *Phys. Rev. Lett.*, 2000, 84:2584–2588.
- [57] Kunne F. Results from the SMC experiment at CERN. The COMPASS experiment at CERN. *Nucl. Phys. Proc. Suppl.*, 2002, 105:34–39. [,34(2002)].
- [58] Adeva B, Ahmad S, Arvidson A, et al. Measurement of the spin-dependent structure function $g_{1(x)}$ of the deuteron. *Physics Letters B*, 1993, 302(4):533 – 539.
- [59] Adams D, Adeva B, Arik E, et al. Spin asymmetry in muon-proton deep inelastic scattering on a transversely-polarized target. *Physics Letters B*, 1994, 336(1):125 – 130.
- [60] Adams D, Adeva B, Arik E, et al. Measurement of the spin-dependent structure function $g_{1(x)}$ of the proton. *Physics Letters B*, 1994, 329(2–3):399 – 406.
- [61] Adams D, Adeva B, Arik E, et al. A new measurement of the spin-dependent structure function $g_{1(x)}$ of the deuteron. *Physics Letters B*, 1995, 357(1–2):248 – 254.
- [62] Adams D, Adeva B, Arik E, et al. Spin structure of the proton from polarized inclusive deep-inelastic muon-proton scattering. *Phys. Rev. D*, 1997, 56:5330–5358.
- [63] Adeva B, Akdogan T, Arik E, et al. Spin asymmetries A_1 and structure functions g_1 of the

- proton and the deuteron from polarized high energy muon scattering. *Phys. Rev. D*, 1998, 58:112001.
- [64] Adeva B, Akdogan T, Arik E, et al. Polarised quark distributions in the nucleon from semi-inclusive spin asymmetries. *Physics Letters B*, 1998, 420(1–2):180 – 190.
- [65] Adeva B, Arik E, Arvidson A, et al. Spin asymmetries A_1 of the proton and the deuteron in the low x and low Q^2 region from polarized high energy muon scattering. *Phys. Rev. D*, 1999, 60:072004.
- [66] Adeva B, Arik E, Arvidson A, et al. Polarisation of valence and non-strange sea quarks in the nucleon from semi-inclusive spin asymmetries. *Physics Letters B*, 1996, 369(1):93 – 100.
- [67] Adeva B, Arik E, Arvidson A, et al. The spin-dependent structure function $g1(x)$ of the proton from polarized deep-inelastic muon scattering. *Physics Letters B*, 1997, 412(3–4):414 – 424.
- [68] Adeva B, Arik E, Arvidson A, et al. Spin asymmetries for events with high p_T hadrons in DIS and an evaluation of the gluon polarization. *Phys. Rev. D*, 2004, 70:012002.
- [69] Alexakhin V, Alexandrov Y, Alexeev G, et al. The deuteron spin-dependent structure function and its first moment. *Physics Letters B*, 2007, 647(1):8 – 17.
- [70] Alexakhin V, Alexandrov Y, Alexeev G, et al. Spin asymmetry and the spin-dependent structure function of the deuteron at low values of x and. *Physics Letters B*, 2007, 647(5–6):330 – 340.
- [71] Alekseev M, Alexakhin V, Alexandrov Y, et al. The polarised valence quark distribution from semi-inclusive {DIS}. *Physics Letters B*, 2008, 660(5):458 – 465.
- [72] Adler S S, Afanasiev S, Aidala C, et al. Improved measurement of double helicity asymmetry in inclusive midrapidity π^0 production for polarized $p + p$ collisions at $\sqrt{s} = 200$ GeV. *Phys. Rev. D*, 2006, 73:091102.
- [73] Adare A, Afanasiev S, Aidala C, et al. Inclusive cross section and double helicity asymmetry for π^0 production in $p + p$ collisions at $\sqrt{s} = 200$ GeV: Implications for the polarized gluon distribution in the proton. *Phys. Rev. D*, 2007, 76:051106.
- [74] Abelev B I, Aggarwal M M, Ahammed Z, et al. Longitudinal Double-Spin Asymmetry and Cross Section for Inclusive Jet Production in Polarized Proton Collisions at $\sqrt{s} = 200$ GeV. *Phys. Rev. Lett.*, 2006, 97:252001.
- [75] Abelev B I, Aggarwal M M, Ahammed Z, et al. Longitudinal Double-Spin Asymmetry for Inclusive Jet Production in $\vec{p} + \vec{p}$ Collisions at $\sqrt{s} = 200$ GeV. *Phys. Rev. Lett.*, 2008, 100:232003.
- [76] Adamczyk L, Adkins J K, Agakishiev G, et al. Measurement of Longitudinal Spin Asymmetries for Weak Boson Production in Polarized Proton-Proton Collisions at RHIC. *Phys. Rev.*

- Lett., 2014, 113:072301.
- [77] Adamczyk L, Adkins J K, Agakishiev G, et al. Precision Measurement of the Longitudinal Double-Spin Asymmetry for Inclusive Jet Production in Polarized Proton Collisions at $\sqrt{s} = 200$ GeV. Phys. Rev. Lett., 2015, 115:092002.
- [78] Aschenauer E C, et al. The RHIC SPIN Program: Achievements and Future Opportunities. 2015..
- [79] Florian D, Sassot R, Stratmann M, et al. Evidence for Polarization of Gluons in the Proton. Phys. Rev. Lett., 2014, 113:012001.
- [80] Aggarwal M M, Ahammed Z, Alakhverdyants A V, et al. Measurement of the Parity-Violating Longitudinal Single-Spin Asymmetry for W^\pm Boson Production in Polarized Proton-Proton Collisions at $\sqrt{s} = 500$ GeV. Phys. Rev. Lett., 2011, 106:062002.
- [81] Adare A, Afanasiev S, Aidala C, et al. Cross Section and Parity-Violating Spin Asymmetries of W^\pm Boson Production in Polarized $p + p$ Collisions at $\sqrt{s} = 500$ GeV. Phys. Rev. Lett., 2011, 106:062001.
- [82] Alcorn J, al. Basic instrumentation for Hall A at Jefferson Lab. Nuclear Instruments and Methods in Physics Research Section A: Accelerators, Spectrometers, Detectors and Associated Equipment, 2004, 522(3):294 – 346.
- [83] Mecking B, Adams G, Ahmad S, et al. The {CEBAF} large acceptance spectrometer (CLAS). Nuclear Instruments and Methods in Physics Research Section A: Accelerators, Spectrometers, Detectors and Associated Equipment, 2003, 503(3):513 – 553.
- [84] JLab webpage, <https://www.jlab.org/Hall-C/equipment/HMS/performance.html..>
- [85] Rondón O A. The RSS and SANE experiments at Jefferson Lab. AIP Conference Proceedings, 2009, 1155(1):82–92.
- [86] Adams D, Adeva B, Akdogan T, et al. The spin-dependent structure function $g_1(x)$ of the deuteron from polarized deep-inelastic muon scattering. Physics Letters B, 1997, 396(1–4): 338 – 348.
- [87] Bosted P. Very preliminary results for the spin structure function g_2 from {SLAC} {E155x}. Nuclear Physics A, 2000, 663–664(0):297c – 300c.
- [88] Abe K, Akagi T, Anderson B, et al. Measurement of the neutron spin structure function g_{n2} and asymmetry A_{n2} . Physics Letters B, 1997, 404(3–4):377 – 382.
- [89] Abe K, Akagi T, Anthony P L, et al. Measurements of the Proton and Deuteron Spin Structure Function g_2 and Asymmetry A_2 . Phys. Rev. Lett., 1996, 76:587–591.
- [90] Abe K, Akagi T, Anthony P L, et al. Measurement of the Proton and Deuteron Spin Structure Function g_1 in the Resonance Region. Phys. Rev. Lett., 1997, 78:815–819.

- [91] Anthony P, Arnold R, Averett T, et al. Measurement of the proton and deuteron spin structure functions g_2 and asymmetry $\{A_2\}$. *Physics Letters B*, 1999, 458(4):529 – 535.
- [92] Amarian M, Auerbach L, Averett T, et al. Q^2 Evolution of the Neutron Spin Structure Moments using a ${}^3\text{He}$ Target. *Phys. Rev. Lett.*, 2004, 92:022301.
- [93] Amarian M, Auerbach L, Averett T, et al. Measurement of the Generalized Forward Spin Polarizabilities of the Neutron. *Phys. Rev. Lett.*, 2004, 93:152301.
- [94] Slifer K, Amarian M, Auerbach L, et al. ${}^3\text{He}$ Spin-Dependent Cross Sections and Sum Rules. *Phys. Rev. Lett.*, 2008, 101:022303.
- [95] Zheng X, Aniol K, Armstrong D S, et al. Precision measurement of the neutron spin asymmetries and spin-dependent structure functions in the valence quark region. *Phys. Rev. C*, 2004, 70:065207.
- [96] Kramer K, Armstrong D S, Averett T D, et al. Q^2 Dependence of the Neutron Spin Structure Function g_2^n at Low Q^2 . *Phys. Rev. Lett.*, 2005, 95:142002.
- [97] Nilanga Liyanage, Jian-Ping Chen, Seonho Choi, spoksperson. JLab E01-012 experiment. Proposal, Jefferson Lab, 2001..
- [98] SChoi, XJiang, Z-E Meziani, Brad Sawatzky, spoksperson. JLab E06-014(d2n) experiment. Proposal, Jefferson Lab, 2005..
- [99] Wesselmann F R, et al. Proton spin structure in the resonance region. *Phys. Rev. Lett.*, 2007, 98:132003.
- [100] G Warren, spokesperson. JLab E07-103 (SANE) experiment. 2006..
- [101] Anthony P L. Precision measurement of the proton and deuteron spin structure functions g_2 and asymmetries A_2 . *Physics Letters B*, 2003, 553(1-2):18 – 24.
- [102] Stratmann M. Bag model predictions for polarized structure functions and their Q^2 evolutions. *Zeitschrift für Physik C Particles and Fields*, 1993, 60(4):763–771.
- [103] Song X. Polarized structure function g_2 in the c.m. bag model. *Phys. Rev. D*, 1996, 54:1955–1966.
- [104] Weigel H, Gamberg L. Hadron structure functions within a chiral quark model. *Nuclear Physics A*, 2001, 680(1–4):48 – 51. Quark Nuclear Physics 2000.
- [105] Wakamatsu M. Polarized structure function $g_2(x)$ in the chiral quark soliton model. *Physics Letters B*, 2000, 487(1–2):118 – 124.
- [106] Wesselmann F, Slifer K, Tajima S, et al. Proton Spin Structure in the Resonance Region. *Phys. Rev. Lett.*, 2007, 98:132003.
- [107] Sulkosky V A. Neutron (${}^3\text{He}$) Spin Structure Functions at Low Q^2 . *AIP Conference Proceedings*, 2009, 1155(1):93–100.

- [108] Solvignon P. Quark-Hadron Duality in Neutron Spin-Structure and g2 moments at intermediate Q2. AIP Conference Proceedings, 2009, 1155(1):101–111.
- [109] Chen J. Moments of Spin Structure Functions: Sum Rules and Polarizabilities. Int.J.Mod.Phys., 2010, E19:1893–1921.
- [110] Dutz H, Helbing K, Krimmer J, et al. First Measurement of the Gerasimov-Drell-Hearn Sum Rule for ${}^1\text{H}$ from 0.7 to 1.8 GeV at ELSA. Phys. Rev. Lett., 2003, 91:192001.
- [111] Prok Y, Bosted P, Burkert V, et al. Moments of the spin structure functions and for $0.05 < Q^2 < 3.0 \text{GeV}^2$. Physics Letters B, 2009, 672(1):12 – 16.
- [112] Lensky V, Alarcón J M, Pascalutsa V. Moments of nucleon structure functions at next-to-leading order in baryon chiral perturbation theory. Phys. Rev. C, 2014, 90:055202.
- [113] Göckeler M, Horsley R, Kürzinger W, et al. Lattice calculation of the nucleon's spin-dependent structure function g_2 reexamined. Phys. Rev. D, 2001, 63:074506.
- [114] Drechsel D, Kamalov S, Tiator L. The GDH sum rule and related integrals. Phys. Rev. D, 2001, 63:114010.
- [115] Weigel H, Gamberg L, Reinhardt H. Polarized nucleon structure functions within a chiral soliton model. Phys. Rev. D, 1997, 55:6910–6923.
- [116] Osipenko M, Simula S, Melnitchouk W, et al. Global analysis of data on the proton structure function g_1 and the extraction of its moments. Phys. Rev. D, 2005, 71:054007.
- [117] Solvignon P, Liyanage N, Chen J P, et al. Quark-Hadron Duality in Neutron (${}^3\text{He}$) Spin Structure. Phys. Rev. Lett., 2008, 101:182502.
- [118] Zheng X. Precision Measurement of Neutron Spin Asymmetry A_1^n at Large x_{Bj} using CEBAF at 57GeV[D]. Massachusetts Institute of Technology, 2002.
- [119] KA Olive e a P D G. 2014 Review of Particle Physics. Chin. Phys. C, 2014, 38:090001.
- [120] Stein S, Atwood W B, Bloom E D, et al. Electron scattering at 4° with energies of 4.5-20 GeV. Phys. Rev. D, 1975, 12:1884–1919.
- [121] Drechsel D, Kamalov S S, Tiator L. Gerasimov-Drell-Hearn sum rule and related integrals. Phys. Rev. D, 2001, 63:114010.
- [122] Hand L N. Experimental Investigation of Pion Electroproduction. Phys. Rev., 1963, 129:1834–1846.
- [123] Roberts R G. The Structure of the Proton. New York: Cambridge University Press, 1990.
- [124] Leader E, Sridhar K. An Introduction to Gauge Theories and Modern Particle Physics. New York: Cambridge University Press, 1985.
- [125] Soffer J, Teryaev O. Improved positivity bound for deep inelastic scattering on transversely polarized nucleon. 1999..

BIBLIOGRAPHY

- [126] Nazaryan V, Carlson C, Griffioen K. Experimental Constraints on Polarizability Corrections to Hydrogen Hyperfine Structure. *Phys. Rev. Lett.*, 2006, 96:163001..
- [127] Musson J. Functional Description of Algorithms Used in Digital Receivers. 2012..
- [128] Denard J C. HIGH ACCURACY BEAM CURRENT MONITOR SYSTEM FOR CEBAF'S EXPERIMENTAL HALL A. 2001. 2326 – 2328.
- [129] Michaels R. Precision Integrating HAPPEX ADC. Technical report, Jefferson Lab, 2003.
- [130] M Bevins A D. Mechanical and thermal design of the CEBAF Hall A beam Calorimeter. 2005..
- [131] G2P Elog, <https://hallaweb.jlab.org/dvcsllog/g2p/173..>
- [132] SIS3801 VME Multiscaler User Manual.
- [133] Roger Flood S H, Suleiman R. Helicity Control Board User's Guide. Jefferson Lab, 2010.
- [134] JLab webpage, http://hallaweb.jlab.org/equipment/beam/absol_beam.html..
- [135] rousseau. Calibration of the calorimeter. Technical report, Jefferson Lab.
- [136] Møller Measurements for E08-027 (g2p) and E08-007, <http://hallaweb.jlab.org/equipment/moller/e08-027.html>. 2012..
- [137] Rok Ursic C P, Edward Strong L T. 1 nA BEAM POSITION MONITORING SYSTEM. Technical report, Jefferson Lab, 1998.
- [138] Barry W . A general analysis of thin wire pickups for high frequency beam position monitors. *Nuclear Instruments and Methods in Physics Research A*, 1991, 301:407–416.
- [139] g2p/GEp Beam Transport Meeting Minutes 2010.11.23, 2010.11.23.
- [140] Yan C, Adderley P, Barker D, et al. Superharp - A wire scanner with absolute position read-out for beam energy measurement at CEBAF. *Nuclear Instruments and Methods in Physics Research A*, 1995, 365:261–267.
- [141] Yan C. Hall C Polarized Target Raster System Upgrade. Technical report, Jefferson Lab, 2005.01.
- [142] CRCarman, Pellegrin J L. The Beam Positions of the spear storage ring. SLAC-PUB-1227, 1973.4..
- [143] PPoit. Evaluation and correction of nonlinear effects in FNPL beam position monitors. FNPL Technical report No.Beams-doc-1894-v1, 2005.07.05..
- [144] R. Wines, private communication.
- [145] Liu J. Magnetic field mapping on a translation table. Technote, Jefferson Lab, 2011..
- [146] Gu C. Target Field Mapping and Uncertainty Estimation. Technote, Jefferson Lab, 2015..
- [147] Pierce J, Maxwell J, Badman T, et al. Dynamically polarized target for the and experiments at Jefferson Lab. *Nuclear Instruments and Methods in Physics Research Section A: Accelerators*,

- Spectrometers, Detectors and Associated Equipment, 2014, 738(0):54 – 60.
- [148] Crabb D G, Meyer W. Solid polarized targets for nuclear and particle physics experiments. Annu. Rev. Nucl. Part. Sci., 1997, 47:67–109.
- [149] Crabb D G, Day D. The Virginia/Basel/SLAC polarized target: operation and performance during experiment E143 at SLAC. Nuclear Instruments and Methods in Physics Research A, 1995, 356:9–19.
- [150] Court G, Gifford D, Harrison P, et al. A high precision Q-meter for the measurement of proton polarization in polarised targets. Nuclear Instruments and Methods in Physics Research Section A: Accelerators, Spectrometers, Detectors and Associated Equipment, 1993, 324(3): 433 – 440.
- [151] Badman T. Proton Polarization Studies and Uncertainty Analysis for E08-027. Technote, Jefferson Lab, 2013..
- [152] Badman T. Proton Polarisation Studies and Uncertainty Analysis for E08-027. Technote, Jefferson Lab, 2013..
- [153] Jian-Ping Chen Y Q. Polarized ^3He Target used in Jefferson Lab Hall A. Technote, Jefferson Lab, 2010..
- [154] Abagam A. The principles of nuclear magnetism. University Press, Oxford, 1961.
- [155] Babcock E, Nelson I A, Kadlec S, et al. ^3He polarization-dependent EPR frequency shifts of alkali-metal- ^3He pairs. Phys. Rev. A, 2005, 71:013414.
- [156] Kelleher A M. A measurement of the neutron electric form factor at very large momentum transfer using polarized electrons scattering from a polarized Helium-3 target[D]. the College of William and Mary, 2010.
- [157] Romalis M V, Cates G D. Accurate ^3He polarimetry using the Rb Zeeman frequency shift due to the Rb- ^3He spin-exchange collisions. Phys. Rev. A, 1998, 58:3004–3011.
- [158] Fissum K. VDC Manual. Technote, Jefferson Lab, 1997..
- [159] Fissum K, Bertozzi W, Chen J, et al. Vertical drift chambers for the Hall A high-resolution spectrometers at Jefferson Lab. Nuclear Instruments and Methods in Physics Research Section A: Accelerators, Spectrometers, Detectors and Associated Equipment, 2001, 474(2):108 – 131.
- [160] Liu J. VDC Multi-track Efficiency Study for E08-027. Technote, Jefferson Lab, 2013..
- [161] Iodice M, Cisbani E, Colilli S, et al. The {CO2} gas Cherenkov detectors for the Jefferson Lab Hall-A spectrometers. Nuclear Instruments and Methods in Physics Research Section A: Accelerators, Spectrometers, Detectors and Associated Equipment, 1998, 411(2–3):223 – 237.

BIBLIOGRAPHY

- [162] Cummings M. Efficiency Studies and Cut Optimization for E08-027. Technote, Jefferson Lab, 2013..
- [163] Liyanage N. Optics Calibration of the Hall A High Resolution Spectrometers using the new optimizer. Technote, Jefferson Lab, 2002..
- [164] Huang M. Central Scattering Angle Measurement. Technote, Jefferson Lab, 2014..
- [165] Zielinski R. Determining the Trigger Efficiency for E08-027. Technote, Jefferson Lab, 2012..
- [166] DKirby. Hall A Readout and Conversion Deadtime. Technical report, Jefferson Lab, 2012.
- [167] Specification of HAPPEX II ADC Timing Board, Revision 1. Technical report, Jefferson Lab.
- [168] Jastrzembski E. A Flexible vme Input/Output module. Technical report, Jefferson Lab, 1999.
- [169] Cummings M. Packing Fraction Analysis for E08-027. Technote, Jefferson Lab, 2015..
- [170] Venkat S, Arrington J, Miller G A, et al. Realistic transverse images of the proton charge and magnetization densities. *Phys. Rev. C*, 2011, 83:015203.
- [171] Lightbody J W J, Connell J S O. Modeling single arm electron scattering and nucleon production from nuclei by GeV electrons. *Computers in Physics*, 1988, 2:57.
- [172] Bosted P E, Fersch R, Adams G, et al. Ratios of $^{15}\text{N}/^{12}\text{C}$ and $^4\text{He}/^{12}\text{C}$ inclusive electroproduction cross sections in the nucleon resonance region. *Phys. Rev. C*, 2008, 78:015202.
- [173] Zielinski R. Unpolarized Radiative Corrections. Technote, Jefferson Lab, 2014..
- [174] S Stein e. Electron scattering at 4' with energies of 4.5-20 Gev. *Physical Review D*, V12, No.7, 1975..
- [175] Slifer K. Modifications to the QFS and RADCOR codes. Technote, Jefferson Lab, 2003..
- [176] Arrington J. Implications of the discrepancy between proton form factor measurements. *Phys. Rev. C*, 2004, 69:022201.
- [177] MO L W, TSAI Y S. Radiative Corrections to Elastic and Inelastic ep and up Scattering. *Rev. Mod. Phys.*, 1969, 41:205–235.
- [178] Akushevich I, Ilyichev A, Shumeiko N. Radiative effects in scattering of polarized leptons by polarized nucleons and light nuclei. *Proceedings of Lepton and photon interactions at high energies. Proceedings, 20th International Symposium, LP 2001, Rome, Italy, July 23-28, 2001*, 2001.
- [179] Akushevich I, Ilyichev A, Shumeiko N, et al. POLARD 2.0 FORTRAN code for the radiative corrections calculation to deep inelastic scattering of polarized particles. *Comput. Phys. Commun.*, 1997, 104:201–244.
- [180] Slifer K. Spin Structure of ^3He and the Neutron at Low Q2; A Measurement of the Extended

BIBLIOGRAPHY

- GDH Integral and the Burkhardt-Cottingham Sum Rule[D]. Temple University, 2004.
- [181] Drechsel D, Kamalov S S, Tiator L. Unitary Isobar Model - MAID2007. *Eur. Phys. J.*, 2007, A34:69–97.
- [182] Christy M E, Bosted P E. Empirical fit to precision inclusive electron-proton cross- sections in the resonance region. *Phys. Rev.*, 2010, C81:055213.
- [183] Bosted P, Mamyan V. Empirical Fit to electron-nucleus scattering. 2012..